

---

# Entanglement of Single Rubidium Atoms: From a Bell Test Towards Applications

Kai Stefan Matthias Redeker

---



München 2020



---

# Entanglement of Single Rubidium Atoms: From a Bell Test Towards Applications

Kai Stefan Matthias Redeker

---

Dissertation  
an der Fakultät für Physik  
der Ludwig-Maximilians-Universität  
München

vorgelegt von  
Kai Stefan Matthias Redeker  
aus Bonn

München, den 27.02.2020

Erstgutachter: Prof. Dr. Harald Weinfurter  
Zweitgutachter: Prof. Dr. Ulrich Schollwöck  
Tag der mündlichen Prüfung: 29.04.2020

# Zusammenfassung

Mit der Entwicklung der Quantenmechanik wurden neuartige Konzepte in der Beschreibung der Natur eingeführt. Der quantenmechanische Formalismus, basierend auf Wellenfunktionen von Teilchen und Systemen, führte zu überraschenden und außergewöhnlichen Erkenntnissen. Ein bemerkenswertes Beispiel dafür ist die Möglichkeit der Verschränkung mehrerer quantenmechanischer Systeme. Aufgrund der einzigartigen Eigenschaften solcher verschränkter Systeme, die einer intuitiven lokal-realistischen Beschreibung der Welt widersprechen, entbrannte eine Diskussion, ob die Quantenmechanik eine komplette Beschreibung der physikalischen Realität liefern kann. Die Verfechter einer lokal-realistischen Weltansicht, unter ihnen Albert Einstein, schlugen eine Erweiterung der Quantenmechanik durch so genannte lokale versteckte Parameter (im Englischen *local-hidden variables* kurz LHV) vor, um den Widerspruch zwischen der Quantenmechanik und ihrem lokal-realistischen Weltbild zu lösen. Nach über dreißigjähriger Kontroverse, ob so eine Erweiterung möglich und sinnvoll sei, schlug John Bell ein Experiment vor, in dem die Vorhersagen der Quantenmechanik denen auf LHVs basierenden Vorhersagen widersprechen. Er formulierte dies 1964 in der berühmten Bellschen Ungleichung.

In den letzten 50 Jahren wurden daraufhin zahlreiche Experimente zur Überprüfung der Bellschen Ungleichung durchgeführt, die alle eine Verletzung der Ungleichung zeigten und damit das lokal-realistische Weltbild widerlegten. In diesen Experimenten war es jedoch aufgrund technischer und konzeptueller Limitierungen nötig, zusätzliche Annahmen zu machen, die mögliche „Schlupflöcher“ für LHV Theorien öffnen. Die drei bekanntesten sind das Detektionsschlupfloch, das Lokalitätsschlupfloch und das Entscheidungsschlupfloch: Das Detektionsschlupfloch öffnet sich, wenn aufgrund unzureichender Detektionseffizienz eine fair verteilte Auswahl der Detektionsereignisse angenommen werden muss. Das Lokalitätsschlupfloch entsteht durch die Annahme von unabhängigen Messungen. Es kann durch raumartige Trennung der Messungen geschlossen werden. Das Entscheidungsschlupfloch betrifft die Unabhängigkeit der Messungsrichtungswahl.

Da das Ausschließen der lokal-realistischen Theorien eine sehr grundsätzliche Aussage über die Natur ist, neben den experimentellen Herausforderungen, eine sehr sorgsame Analyse der Messdaten notwendig. In den üblichen Methoden zur Auswertung experimenteller Daten wird unter anderem angenommen, dass die wiederholte Messungen unabhängigen und identisch verteilten Ergebnisse liefern. Diese Annahme für zum „Erinnerungsschlupfloch“ in dem LHV Theorien die Ergebnisse vorheriger Messungen nutzen können. Deshalb sind speziell entwickelte Auswertemethoden notwendig. Erst seit kurzem ist es möglich auf alle Extraannahmen in einem Experiment zu verzichten und so ein schlupflochfreies Experimentes durchzuführen. Die ersten Experimente die alle Schlupflöcher auf einmal schließen konnten, wurden parallel zu den Experimenten in dieser Dissertation entwickelt und durchgeführt.

Jenseits von den fundamentalen Überlegungen kann die quantenmechanische Verschränkung für neue vielversprechende Anwendungen genutzt werden. Dazu zählen unter anderem Quantencomputer und neue Protokolle in der Quantenkommunikation. In dieser Arbeit werden beide Bereiche sowohl die Konsequenzen der Verschränkung für das fundamentale Verst-

ändnis der Welt als auch die sich ergebenden Möglichkeiten für neue quantentechnologische Anwendungen betrachtet.

Dies wird experimentell am Beispiel zweier verschränkter Rubidiumatome, die 398 m voneinander entfernt sind, untersucht. Zunächst werden dazu zwei einzelne  $^{87}\text{Rb}$ -Atome in separaten Atomfallen gefangen. Um jetzt beide Atome über die große Entfernung miteinander zu verschränken, wird das sogenannte „entanglement swapping“ Protokoll angewandt. Hierzu wird zunächst jedes Atom mit einem Photon verschränkt, welches dann in einer optische Glasfaser zu einem Bellzustandsanalysator geleitet wird. Hier werden die beiden Photonen auf einen gemeinsamen verschränkten Zustand projiziert und gemessen. So wird die Verschränkung auf die Atome übertragen, wobei das Messergebnis der Photonenmessung die erfolgreiche Erzeugung der Verschränkung verkündet. Nachdem nun die Atome miteinander verschränkt sind, ist es möglich, eine Messung an jedem Atom vorzunehmen und so den verschränkten Zustand zu untersuchen.

Mit den verschränkten Atomen kann ein experimenteller Test der Bellschen Ungleichung durchgeführt werden. Hierzu wird die Clauser-Horne-Shimony-Holt (CHSH)-Ungleichung, die bekannteste von mehreren äquivalenten Formulierungen der Ungleichung, verwendet. Sie bezieht sich auf ein Experiment mit Teilchenpaaren und zwei Messapparaturen: Die beiden Messapparaturen erhalten jeweils ein Teilchen eines Paares, um unabhängig voneinander eine von zwei möglichen (lokalen) Messungen durchzuführen. Die Messergebnisse für die vier verschiedenen Messungskombinationen werden in den Korrelatoren  $E_{ab}$  zusammengefasst ( $a, b \in \{0, 1\}$ ) und diese in der folgenden Art zusammengezählt  $S = |E_{00} + E_{01}| + |E_{10} - E_{11}|$ . Die CHSH-Ungleichung besagt  $S \leq 2$  für LHV basierte Theorien, Quantenmechanik erlaubt jedoch für verschränkte Teilchenpaare Werte von  $S \leq 2\sqrt{2}$ . Die obengenannten Schlupflöcher werden wie folgt geschlossen: Zunächst wird durch die Verwendung des „entanglement swapping“ Protokoll zusammen mit der Verkündung der Verschränkung eine Messung für jedes verschränkte Paar durchgeführt und das Detektionsschlupfloch ist automatisch geschlossen. Um das Entscheidungsschlupfloch zu schließen wird die Messrichtung für jedes Atom von zwei unabhängigen und schnellen Quantenzufallszahlengeneratoren gewählt. Außerdem wird ein schnelles Messverfahren angewandt, das mit einer maximalen Dauer von 1.1  $\mu\text{s}$  (inklusive der Messrichtungswahl) eine raumartige Trennung der Messungen an den Atomen sichergestellt. Eine Messung mit 10000 Messereignissen lieferte mit einem  $S = 2.222 \pm 0.033$  eine nahezu eindeutige Verletzung der Ungleichung. Eine genauere Analyse der Daten mittels eines extra an das Experiment angepassten Hypothesentest ergibt eine Wahrscheinlichkeit von  $p \leq 1.739 \cdot 10^{-10}$ , dass ein Experiment in einer durch LHV Theorien beschriebenen Welt vergleichbare Messdaten produziert. Dies erlaubt eine Zurückweisung der lokal-realistischen Weltansicht.

Eine der wenigen Annahmen, die gemacht wurden, um das Experiment durchzuführen, ist, dass die Quantenzufallszahlengeneratoren, die auf einem spezifischen physikalischen Modell basieren, wirklich unabhängige und unvorhersagbare Zufallszahlen liefern. Die Tatsache, dass es unmöglich ist, die Zufälligkeit von Zufallszahlen zu beweisen, ist ein grundsätzliches Problem der experimentellen Tests der Bellschen Ungleichung. Um dieses Problem anzugehen, wurden in Zusammenarbeit mit 12 anderen Forschungsgruppen unter der Führung des ICFO Instituts, Barcelona, zeitgleich 13 Experimente durchgeführt, wobei Messrichtungen durch von Menschen erzeugten Zufallszahlen bestimmt wurden. So ersetzt der freie Wille der Menschen das physikalische Modell der Zufallszahlen. Der hier beschriebene Münchener Beitrag ist ein Test der CHSH Ungleichung mit Atom-Photon-Verschränkung, welcher  $S = 2.427 \pm 0.022$  ergab und damit den lokal-realistischen Theorien widerspricht.

Auf der Anwendungsseite ist diese experimentelle Atom-Atom-Verschränkung ein Demonstrator für ein simples Quantennetzwerk: Die Atome sind die Quantenspeicher an den beiden Knoten, die durch einen auf Photonen basierenden Kanal verbunden sind. Solch eine elementare Verbindung ist ein notwendiger Baustein für zukünftige Quantenrepeater und somit auch für größere Quantennetze. Mittels der vorher gezeigten quasi schlupflochfreien Verletzung der Bellschen Ungleichung ist es möglich, diese Verbindung in einem „Black-Box-Szenario“ zu zertifizieren. Das bedeutet, dass die Verschränkung zwischen den beiden Netzwerkknoten mit minimalen Annahmen über das physikalische System und insbesondere ohne Vertrauen in die benutzten Aufbauten quantifiziert werden kann. Dieses Verfahren nennt man „Self-Testing“ oder „device-independent state certification“. Auf diese Weise konnte in Zusammenarbeit mit der Forschungsgruppe von Nicolas Sangouard von der Universität Basel eine mittlere (device-independent) Quantenzustandstreue des Atom-Atom-Zustands von  $F = 51.24\%$  mit einer statistischen Sicherheit von 99% gezeigt werden. So war es zum ersten Mal möglich, eine Quantennetzwerkverbindung, die zwei Knoten miteinander verbindet, welche sich nicht in ein und demselben Raum befinden, zu zertifizieren.

Um die Qualität des verschränkten Zustandes und damit der Quantennetzwerkverbindung in künftigen Experimenten zu verbessern, wurde abschließend untersucht, wie sich die Erzeugung der Atom-Photon-Verschränkung für das „entanglement-swapping“ verbessern lässt. Dazu wurde ein detailliertes Modell von optischer Anregung und Photoemission der Atome unter Berücksichtigung mehrerer angeregter Zustände erstellt und die Zeitabhängigkeit der einzelnen Emissionskanäle berechnet. Basierend auf diesen ist es möglich, die Verschränkungsqualität abhängig von den Photondetektionszeitpunkten im Bellzustandsanalysator zu berechnen. Mit verbesserten Zeitfenstern und optischen Anregepulsen ist es möglich, den zu erwartenden  $S$ -Wert einer Bellmessung auf  $S \approx 2.3$  und auch die durchschnittliche Quantenzustandstreue in der Zertifizierung auf  $F \approx 0.58$  zu steigern. Zusammen mit Verbesserungen bezüglich der zeitlichen Kohärenz des verschränkten Zustandes, sowie der zustandserhaltenden Wellenlängenumwandlung der Photonen in Telekommunikationsbereich wird es in Zukunft möglich sein, die Distanz zwischen den Atomen zu vergrößern und weitere „device-independent“-Anwendungen zu realisieren.

# Abstract

The development of quantum mechanics introduced new concepts to describe the world. Its formalism, based on wave functions for particles, lead to surprising and unique consequences. One particular noteworthy example is the possibility to entangle quantum mechanical systems. The features of entanglement oppose the more intuitive local-realistic world view, which lead to a controversy about the completeness of quantum mechanics itself. Yet, once established, entanglement was not only seen as mere curiosity of quantum mechanics, but instead its vast potential for possible quantum technologies was investigated. Today, it is a valuable resource for, e.g., quantum computing and quantum communication. This thesis focuses on how quantum entanglement challenges and expands our fundamental understanding of nature, as well as its implementation in quantum technologies.

Among others, Albert Einstein (in the famous EPR paper from 1935) opposed the non local-realistic concept of quantum mechanics. This criticism resulted in the demand for an extension of quantum mechanics with so called local-hidden variables (LHV), serving the sole purpose of converting quantum mechanics into a local-realistic theory. In 1964 John Bell proposed an experimental test, involving a pair of entangled particles, for which quantum mechanics and local-realistic theories predict different results. Bell formulated this in form of an inequality, called Bell's inequality. The most known and more general formulation of this inequality was derived by Clauser, Horne, Shimony, and Holt (CHSH) in 1969. They proposed an experiment consisting out of a pair of entangled particles and two measurement devices. From each pair one of the particles is send to each of the measurement deceives. Subsequently, both measurement devices perform a local measurement on their particle, using one of two possible measurement settings. Here, the correlators  $E_{a,b}$  for all setting combinations  $a, b \in \{0, 1\}$  are evaluated and used to calculated the CHSH  $S$  value via  $S = |E_{00} + E_{01}| + |E_{10} - E_{11}|$ . For all local realistic theories  $S \leq 2$ , while quantum mechanics allows for a violation of the inequality up to the value of  $S = 2\sqrt{2}$ .

Over the last 50 years experiments testing Bell's theorem showed a violation of the inequality, contradicting local-realism. However, extra assumptions needed to be made for the evaluation of those Bell tests since the experiments were limited by technical imperfections as well as conceptual limitations. This opens so called "loopholes" that can be exploited by more complex local-realistic theories, which do not comply to these extra assumptions. Three major loopholes exist: the detection loophole, the locality loophole and the freedom of choice loophole. First, in case of insufficient detection efficiency, only a fraction of the entangled particles is detected. Therefore, it is necessary to assume that the measured fraction constitutes a fair representation of all particles (fair sampling assumptions). This opens the to called detection loophole. The second loophole is related to the necessity of performing local measurements on each particle. This can only be ensured by space-like separation of the two measurements on one entangled pair. If this is not the case, the local measurements have to be assumed not to influence each other, opening the locality loophole. The last one is called "the freedom of choice loophole", demanding an independent and unpredictable setting choice for each measurement. Until recently, it was not possible to close all major loopholes in one

experiment.

In addition to the requirements on the experimental setup, there are also requirements on the experimental procedure and the evaluation of the recorded data. Since a possible rejection of local-realism is a fundamental statement, it is necessary to perform both the experiment as well as the evaluation with great care. In standard methods for evaluating experiments independent and identically distributed (i.i.d.) measurement outcomes are assumed. This assumption opens the so called memory loophole, which can be exploited by LHV theories with a history dependence. The first experiments complying with all requirements on the experiment and using rigorous evaluation method were conducted parallel to the work presented in this thesis.

In this work, entanglement of two single  $^{87}\text{Rb}$  atoms is investigated. For this, single atoms are trapped in two setups 398 m apart . To create entanglement between the atoms, the spin state of each atom is entangled with the polarization of a single photon employing excitation and spontaneous photon emission. The emitted photons are coupled into single mode optical fibers and guided to a photon measurement setup. Then the entanglement of the atom-photon pairs is swapped to the atoms by a joint Bell state projection measurement of the two photons, heralding the atom-atom entanglement allowing for an event ready measurement of the atomic state. The atomic state measurement is based on a state selective ionization and a subsequent detection of the ionization fragments and allows for an efficient projection of the atomic state in less than 1.1  $\mu\text{s}$ , enabling space like separation of parallel atomic measurement. Additionally employing quantum random number generators (QRNG) to chose the measurement setting, this setup enabled for a loophole free Bell experiment. The measurement of 10000 entangled atom pairs yielded  $S = 2.222 \pm 0.033$  showing a clear violation of the CHSH inequality. Using the collected data for a hypothesis test of local-realism showed a probability for the same data produced in an experiment described by LHV theories of  $p = 1.739 \cdot 10^{-10}$ . This allows for a rejection of local-realism.

Additionally, Atom-atom entanglement over 398 m demonstrates a real world implementation of a basic quantum network link. Such a link constitutes a basic building block for a quantum repeater that are necessary for future large scale quantum networks. Furthermore, the quality of the entangled state, in conjunction with the absence of the loopholes enable the implementation of certain device-independent protocols. Therefore, self-testing can be applied for certifying the quantum network link. With the improved self-testing formalism, developed in a collaboration with Nicolas Sangouard's group at the University of Basel, it is possible to show the first fully device-independent certification of a quantum link. The link has an average fidelity of  $F = 51.24\%$  with a confidence level of 99%.

For future experiments, a higher quality of the entangled atom-atom state is desirable. Therefore, the atom-atom state generation based on entanglement swapping from atom-photon entanglement, is thoroughly investigated. First the excitation process, which creates the atom-photon entanglement, is investigated and possible effects of experimental imperfections and the effect of the actual multilevel atom are identified. A time dependence for different excitation processes is obtained. Now the dependence of the atom-atom state on the detection times of both photons is calculated. Based on this model optimized parameters for the excitation pulse and the acceptance time window for the photon detection for future experiments are obtained. Together with other improvements, e.g., increasing the temporal coherence of the atomic state and frequency conversion of the photon wavelength into telecom range, this enables to create entanglement over even longer distances.

# Contents

<b>1. Introduction</b>	<b>1</b>
<b>2. Long Distance Entanglement of Atomic Qubits</b>	<b>5</b>
2.1. Qubit Encoding in Interior States of $^{87}\text{Rb}$	5
2.2. Trapping Single Atoms	8
2.3. State Preparation, Control, and Measurement of Single Atoms	12
2.3.1. Creation of atom-photon entanglement	12
2.3.2. Measurement of the atomic state	17
2.3.3. Coherence of the atomic states	21
2.4. Creation of long Distance Atom-Atom Entanglement	28
2.4.1. Heralded entanglement via entanglement swapping	29
2.4.2. Operation of the two-trap setup	33
<b>3. Bell’s theorem: Testing Local-Realism</b>	<b>38</b>
3.1. Local-Realism and Quantum Mechanics	38
3.2. CHSH Inequality	39
3.2.1. Bound for LHV theories	41
3.2.2. Bound for Quantum Mechanics	42
3.3. Bell experiments and “Loopholes” for local-realism	44
3.3.1. “Loopholes” in experiments	45
3.3.2. Statistical analysis of a Bell experiment	52
3.3.3. Requirements for a robust Bell experiment	54
3.3.4. A short history of Bell experiments	55
<b>4. Violation of Bell’s Inequality with Entangled Atoms</b>	<b>58</b>
4.1. Design of the experiment	58
4.1.1. Closing the detection and the locality loophole	59
4.1.2. Generation of random inputs	63
4.1.3. Residual assumptions made for the Bell test	68
4.2. Evaluation with Hypothesis Testing	70
4.2.1. Bound based on martingales and concentration inequalities	71
4.2.2. Bound derived from a non-local game	74
4.2.3. Applying the hypothesis test	76
4.3. Avoiding expectation bias	76
4.4. Experimental violation of Bell’s inequality	77
4.4.1. Runs with 10000 events	78
4.4.2. Evaluation of all collected events and further analysis	81
<b>5. Addressing Assumptions for the Choice of Random Inputs</b>	<b>84</b>
5.1. Separating input generation from the experiment	84

5.2.	Human free will as sources for randomness: “The Big Bell Test” . . . . .	86
5.2.1.	The Munich contribution . . . . .	86
5.2.2.	Experimental Results “Humans vs QRNG” . . . . .	88
5.2.3.	Model of the Bell test using atom-photon entanglement . . . . .	91
<b>6.</b>	<b>Towards Applications and Quantum Networks with Atom-Atom Entanglement</b>	<b>96</b>
6.1.	Quantum Networks . . . . .	96
6.2.	Device-independent quantum protocols . . . . .	97
6.2.1.	Scenario for DI protocols . . . . .	97
6.2.2.	Examples of DI applications . . . . .	99
6.3.	Self-testing: A device-independent characterization of entanglement . . . . .	101
6.3.1.	Self-testing with a Bell state fidelity . . . . .	101
6.3.2.	DI certification of an elementary quantum network link . . . . .	103
<b>7.</b>	<b>Improving the Atom-Atom State Preparation</b>	<b>107</b>
7.1.	Detailed model for photon emission from a single atom . . . . .	107
7.1.1.	Deviations from the ideal excitation process . . . . .	107
7.1.2.	Unconditioned Atom-photon state . . . . .	108
7.1.3.	Atom-photon state conditioned on photon detection . . . . .	111
7.2.	Possible reduction of unwanted processes . . . . .	114
7.2.1.	Model of the excitation process . . . . .	114
7.2.2.	Time dependence of the excitation process . . . . .	115
7.2.3.	Time filtering and optimizing pulse parameters . . . . .	117
7.3.	Effect of the photon emission on the two atom state fidelity . . . . .	119
7.3.1.	Two photon interference . . . . .	119
7.3.2.	Detection time dependent atom-atom state . . . . .	122
7.4.	Optimizing the two photon coincidence time window . . . . .	125
7.4.1.	Model for the $S$ value dependence on the detection times . . . . .	125
7.4.2.	Optimal acceptance time windows for different applications . . . . .	130
7.5.	Optimal excitation parameters for future experiments . . . . .	134
<b>8.</b>	<b>Conclusion and Outlook</b>	<b>136</b>
<b>A.</b>	<b>Physical Constants and Properties of <math>^{87}\text{Rb}</math></b>	<b>138</b>
<b>B.</b>	<b>Definition of the Coordinate System, Polarization, and Atomic States</b>	<b>141</b>
<b>C.</b>	<b>On the Entangled Atom-Photon State</b>	<b>148</b>
<b>D.</b>	<b>Light field of the ODT near its focus</b>	<b>152</b>
<b>E.</b>	<b>Hong Ou Mandel effect for unpolarized photons</b>	<b>156</b>
<b>F.</b>	<b>Technical Details of the Experimental Setup</b>	<b>164</b>
<b>G.</b>	<b>Formulary</b>	<b>167</b>

# 1. Introduction

With the development of quantum mechanics new concepts for the description of the world were introduced. Its formalism, as it is based on wave functions for particles, lead to surprising and unique consequences. One particular noteworthy example is the possibility of entanglement of quantum mechanical systems. Its features oppose the more intuitive local-realistic world view, and thus lead to a controversy about the completeness of quantum mechanics itself [1, 2]. Yet, once established, entanglement was not only seen as mere curiosity of quantum mechanics and, instead, its vast potential for possible quantum technologies was investigated. Today, it is a valuable resource for, e.g., quantum computing [3, 4] and quantum communication [5]. This thesis will focus on how quantum entanglement challenges and expands our fundamental understanding of nature, as well as its implementation in quantum technologies.

Among others, Albert Einstein opposed the non local and non realistic concept of quantum mechanics [1], which surfaces most prominent for entangled particles. This criticism resulted in the demand for an extension of quantum mechanics with so called local-hidden variables (LHV), serving the sole purpose of converting quantum mechanics into a local-realistic theory. The controversy, whether such an extension is necessary and possible, was open for more than three decades [6, 7, 8]. Finally, in 1964 John Bell formulated his famous no-go theorem on local-realistic theories. Along the theorem he also described a possible scenario for and experimental test, involving a pair of entangled particles, where quantum mechanics and local-realistic theories predict different results [2]. Bell's theorem is usually stated in the form of an inequality, called Bell's inequality, of which the CHSH inequality is the most prominent form [9]. Here, the possible experiment consists of a pair of particles and two measurement devices. From each pair one of the particles is sent to each of the measurement devices. Subsequently, both devices perform a local measurement on their particle, using one of two possible measurement settings. The correlators  $E_{a,b}$  for all setting combinations  $a, b \in \{0, 1\}$  are evaluated and used to calculate the needed CHSH  $S$  value via  $S = |E_{00} + E_{01}| + |E_{10} - E_{11}|$ . For all local realistic theories it is smaller or equal than 2. Crucially, in quantum mechanics  $S$  values up to  $2\sqrt{2}$  are possible. Therefore, it is possible to disprove local-realism by violating the CHSH inequality  $S \leq 2$ .

The first experiments testing Bell's theorem showed a violation of the inequality and thus, in a sense, contradicted local-realism [10, 11, 12]. However, the experiments were limited by technical imperfections as well as conceptual limitations. Thus assumptions need to be made for the evaluation. This opens so called "loopholes" for more complex local-realistic theories, which do not comply to these extra assumptions. There are three major loopholes [13]: First, in case of insufficient detection efficiency only a fraction of the entangled particles is detected. Here, it is necessary to assume that the measured fraction constitutes a fair representation of all particles (fair sampling assumptions). This opens the so called "detection loophole". The second loophole is related to the necessity of performing local measurements on each particle. This can only be ensured by space-like separation of the two measurements on one entangled pair. If this is not the case, the local measurements have to be assumed not to influence each other, opening the "locality loophole". The last one is called "the freedom of choice loophole",

demanding an independent and unpredictable setting choice for each measurement.

In addition to the requirements on the experimental setup, there are also requirements on the experimental procedure and the evaluation of the recorded data. Since a possible rejection of local-realism is a very fundamental statement, it is necessary to perform both the experiment as well as the evaluation with great care. To avoid a possible bias introduced by the experimenter [14], the duration, the measurement procedure, and the analysis method need to be fixed before the actual experiment starts. Furthermore, no data may be discarded in Bell test experiments. There is only one exception: if a predefined objective criterium independent of the measurement results, is fulfilled before the excluded result was recorded, e.g., malfunction of a crucial device, it is possible to discard events during the malfunction. Violating these rules will diminish or even make the result of the experiment void. The evaluation process is even more delicate, since in standard methods for evaluating experiments independent and identically distributed (i.i.d.) measurement outcomes are assumed. This assumption opens the so called memory loophole, which can be exploited by LHV theories with a history dependence [15]. However, it is possible to avoid this loophole by using evaluation methods without assuming i.i.d. measurement results [16, 17]. Only experiments that follow all of the mentioned requirements and rules allow for a valid test of local realism. Until recently, it was not possible to close all major loopholes in one experiment. The first experiments complying with all requirements were conducted parallel to the work presented in this thesis [18, 19, 20].

Beyond providing a clever method disproves local realism, quantum entanglement also enables a whole field of new applications in quantum technology. Not only is it the backbone of quantum computing, but also enables novel “device-independent” protocols for secure quantum communication as well as random number generation [21, 22, 23]. In such protocols, a test of Bell’s inequality is used to verify that the respective devices create entanglement. In case of a successful verification, the protocols allow for trusted results, e.g., a secret key, even from imperfect not trustworthy devices. A downside of these protocols is that, due to the Bell test, the technical requirements are much higher than for standard device-dependent protocols. But with the demonstration of the loophole free Bell test experiments, the first device independent protocols can now be implemented.

Moreover, entanglement of separated stationary qubits, which serve as quantum memories, is the key ingredient for future, large scale quantum networks [24], enabled by using quantum repeater protocols. These can not only extend the range of quantum connections but can also include quantum error correction protocols, e.g., state purification [25]. Such networks are key to enable distributed quantum computation, secure communication over long distance, and precise clock synchronization [26]. In this context the device-independent protocol for self-testing verifies connections between quantum nodes [22, 27]. Thus, it will be possible to certify in a device-independent manner that a quantum network can be used for the quantum communication tasks it is designed for.

In this work, entanglement of two single  $^{87}\text{Rb}$  atoms is investigated. For this, single atoms are trapped [28] in two setups 398 m apart. To create entanglement between the atoms, each atom is entangled with a single photon employing excitation and spontaneous photon emission [29, 30]. Then the entanglement of the atom-photon pairs is swapped to the atoms by a joint Bell state projection measurement of the two photons [31, 32, 33]. The emitted photons are coupled into single mode optical fibers and guided to photon measurement setup. The measurement outcome of the two-photon measurement heralds the atom-atom entanglement and allows for an event ready measurement of the atomic state. This measurement is based on a state selective ionization and a subsequent detection of the ionization fragments [34, 35, 36]

and allows for an efficient projection of the atomic state in less than  $1.1 \mu\text{s}$  [37], enabling space like separation of parallel atomic measurement [38].

With this atom-atom entanglement setup, a Bell test experiment is performed. By additionally employing physical random number generators [39] for the setting choices, it is possible to close all major loophole and to refute local-realism. While the design of the experiment, allowing to close the detection and locality loophole, is described in [38], the present work focuses on the characterization of the employed random number generators as well as the evaluation methods. For a sound analysis of a Bell test, it is necessary to state all used assumptions for the experiment and the evaluations. Since it is impossible to prove randomness without extra assumptions, employing random number generators result in residual assumptions for the Bell test which LHV theories could exploit. Although, such theories are very specific and not very likely, a different way for choosing independent and unpredictable settings is desirable. One possible solution is employing randomness stemming from distant stars [40, 41, 42, 43]. In this work a different approach based on human free will is pursued [44]. In “The Big Bell Test” collaboration 13 experiments were performed parallel on November 30th 2016 to test local realism [45]. The setting choices were based on random bits generated by people around the world via a browser game during the experiments. This work contributed to the Big Bell Test by testing the CHSH inequality based on atom-photon entanglement. Here, the settings for the atom state read-out were determined by human made random bits, while photon settings were chosen by a beam splitter.

Atom-atom entanglement over 398 m additionally demonstrates a basic quantum network link. By connecting two laboratories in different buildings of the university, with a fiber connection that crosses through public space, i.e, a four lane main street, it is a clear proof that quantum networks can be implemented in the real world. Also, this link constitutes a basic building block for a quantum repeater that will be needed for future large scale quantum networks [46]. Furthermore, the quality of the entangled state, in conjunction with the absence of the loopholes enable the implementation of certain device-independent protocols. Thereby, the device-independent generation of random bits can be shown. More importantly, since the connection between the two atoms forms a quantum network link, self-testing can be applied for certifying it. With the improved self-testing formalism, developed in a collaboration with Nicolas Sangouard’s group at the University of Basel [47], it is possible to show the first fully device-independent certification of a quantum link. Moreover, this is the first fully device-independent demonstration of the self-testing protocol [27].

For future developments, an even higher quality of the entangled atom-atom state is desirable. In order to achieve this, the processes involved in the atom-atom state generation, which is based on entanglement swapping from atom-photon entanglement, are thoroughly investigated. First the excitation process, which creates the atom-photon entanglement, is investigated and possible effects of misalignment and the effect of the actual multilevel atom are identified. To quantify these detrimental effects the “quantum jump model” from [33] is expanded. A time dependence for different excitation processes is obtained. To describe the effect of the imperfection of the atom-photon state generation on the atom-atom state, entanglement swapping is analyzed. This also includes the two photon interference process employed for the Bell state measurement [33]. Finally, a the dependence of the atom-atom state on the detection times of both photons. To find optimal parameters for both the excitation pulse and acceptance time-window it is necessary to include additional parameters such as photon detection efficiency, detector dark counts, and the atomic state read-out process. Once all these measures and effects are included in the model, it can be used to optimize

the results of the device independent protocols as well as future experiments with entangled atoms.

The structure of this thesis is as follows: Chapter 2 describes the methods and the experimental setup used for the creation of atom-atom entanglement. The aim of this chapter is to provide the reader with the basic background information on both experimental setup and the techniques that are used for the experiments in this work. More detailed information on the development of the experimental methods and setup can be found in the preceding PhD theses [28, 30, 48, 36, 33, 37, 34, 38]. In Chapter 3 Bell's inequality is motivated and the possible experimental loopholes are identified. Subsequently, the evaluation is discussed through the use of hypothesis testing. Chapter 4 provides a description the Bell test experiment focusing on the used physical random number generators and data evaluation. Chapter 5 concludes this thesis' treaty on Bell's theorem. Here, the alternatives to setting choices by physical random number generators are addressed. In the second part of this chapter, the Munich contribution to the Big Bell Test, which is based on atom-photon entanglement, is described. Chapter 6 is focused on possible quantum networks and device-independent applications. This includes a description of the certification process required to form a quantum network link. Chapter 7 treats on the imperfections of the atom-atom state creation. With the used model presented in this work it is possible to find optimized acceptance time windows for the photonic Bell state measurement. Lastly, possible improvements for future experiments are discussed.

## 2. Long Distance Entanglement of Atomic Qubits

One of the focus points of this thesis is to create and detect entanglement between two atomic qubits that are located in two separate laboratories approximately 400 m apart (Fig. 2.1). To achieve this, it is necessary to both trap and individually control single atoms. This chapter will introduce both the main experimental methods required to trap and entangle atoms as well as the experimental setup. First, the main features of rubidium are discussed, which will be used for the experiments discussed herein. This is followed by a description of the setup used to trap single neutral atoms, along with the procedure to control and measure the atomic state. Finally, the process of creating entanglement of two single atoms in separated traps is described.

### 2.1. Qubit Encoding in Interior States of $^{87}\text{Rb}$

To realize an atomic qubit, an atom with suitable quantum states is needed. For that purpose, the element needs to fulfill the following three requirements:

1. Possibility for entanglement of the stationary atomic qubit with a “flying” qubit to distribute the entanglement over long distances. A convenient way to realize a flying qubit is to encode it in the polarization state of a single photon, which can be guided via glass fiber and measured with high fidelity.
2. The qubit should allow for a high fidelity read-out. Furthermore, especially for the Bell experiment, the read-out needs to be very fast to enable space-like separation.
3. Since an event ready experimental scheme will be used, where the atom states are measured after the entanglement is established, the atomic coherence time must be long enough to allow for a high state fidelity after entanglement generation.

The alkali metal rubidium is chosen as the quantum states of its single valence electron are particularly well suited for this kind of experiment. Of the two naturally occurring isotopes  $^{85}\text{Rb}$  and  $^{87}\text{Rb}$ , the latter with nuclear spin of  $I = 3/2$  is used due to its better fitting hyper-fine level structure.

The qubit is encoded in the degenerate Zeeman substates  $F = 1$ ,  $m_F = \pm 1$  of the  $5^2\text{S}_{1/2}$  ground state (Fig. 2.2), satisfying all listed requirements. The spontaneous decay of the  $F' = 0$  hyper-fine level of the  $5^2\text{P}_{3/2}$  excited state to the ground state generates a photon whose polarization state is entangled with the Zeeman-state of the  $F = 1$  of the  $5^2\text{S}_{1/2}$  ground state (Sec. 2.3.1). Dipole selection rules allow to individually address the Zeeman-states with polarized light. By this method and by additionally employing particle detectors, a fast and efficient readout scheme can be implemented (Sec. 2.3.2). As a down side, the employed Zeeman-states are highly susceptible to magnetic and light fields, which need to be controlled to enable long state coherence (Sec. 2.3.3) .

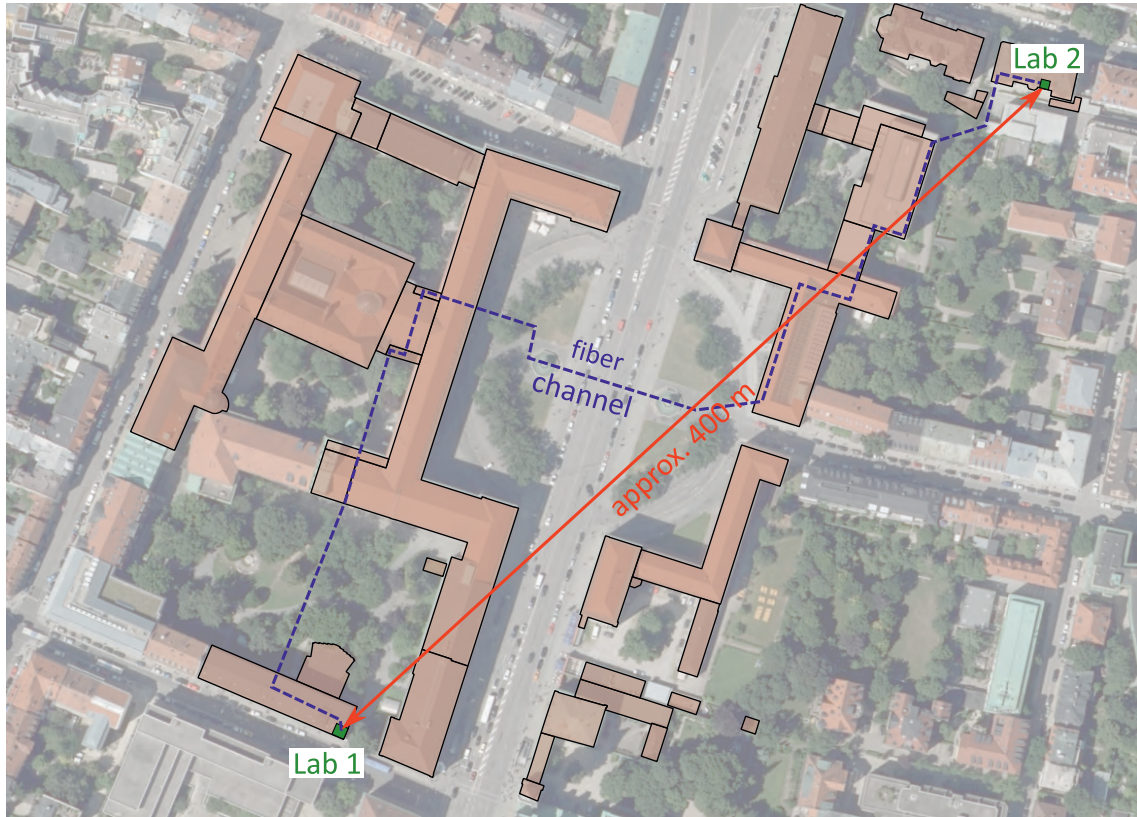


Figure 2.1.: The location of the two laboratories at the main campus of Ludwig-Maximilians-Universität in Munich. Laboratory 1 (Lab 1) is located in the basement of the faculty of physics at Schellingstraße 4. Laboratory 2 (Lab 2) is located in the basement of the department of economics at Schackstraße 4. Both labs are connected with glass fibers for communication and for guiding the fluorescence photons emitted by the atoms. Map data provided by the Bayerisches Landesamt fuer Digitalisierung, Breitband und Vermessung.

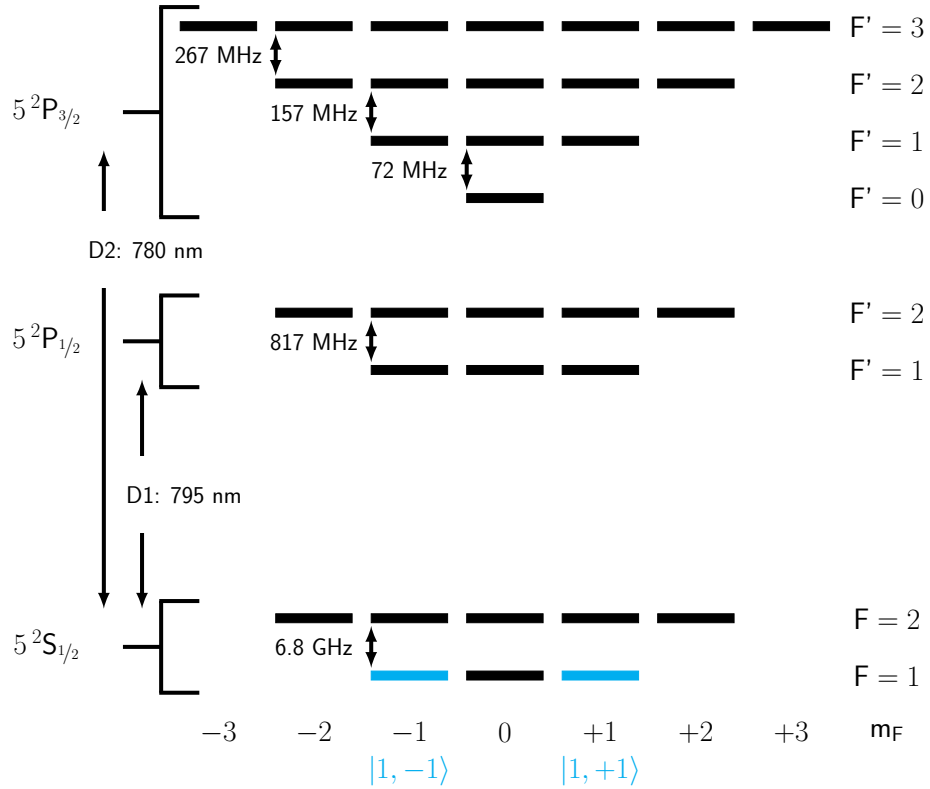


Figure 2.2.: Level scheme for the valence electron of  $^{87}\text{Rb}$  [49]: the ground state  $5^2\text{S}_{1/2}$  is split in two hyper-fine levels  $F = 1$  and  $F = 2$ . The excited state  $5^2\text{P}_{1/2}$  is split also in two hyper-fine levels  $F' = 1$  and  $F' = 2$  while the excited state  $5^2\text{P}_{3/2}$  is split into four hyper-fine levels  $F' = 0, F' = 1, F' = 2$  and  $F' = 3$ . All hyper-fine levels are split into Zeeman sublevels  $m_F$ . The transition wavelength for  $5^2\text{S}_{1/2}$  to  $5^2\text{P}_{1/2}$  ( $\text{D}_1$ ) is 795 nm and for  $5^2\text{S}_{1/2}$  to  $5^2\text{P}_{3/2}$  ( $\text{D}_2$ ) is 780 nm. The atomic qubit is encoded in the  $5^2\text{S}_{1/2}$ ,  $F = 1$ ,  $m_F = \pm 1$  ground states with  $m_F = -1 = |1, -1\rangle = |\downarrow\rangle_z$  and  $m_F = +1 = |1, +1\rangle = |\uparrow\rangle_z$  (blue).

For using single  $^{87}\text{Rb}$ -atoms as a stationary qubit, a so called quantum memory, the atoms need to be trapped and well-localized. For an optical dipole trap[50], which is the employed trapping method, it is necessary to first slow down the atoms before trapping by cooling them [51].  $^{87}\text{Rb}$  can be conveniently laser cooled via Doppler cooling [52]. Here, radiation pressure and the Doppler effect are employed to slow down atoms.

### Formal definition and nomenclature of atomic and qubit states

For convenience of the reader, the following simplified notation shall be used henceforth: the hyper fine states (F) and their associated Zeeman states ( $m_F$ ) of the  $5^2\text{S}_{1/2}$  ground state are written as  $|F, m_F\rangle$ . If not mentioned otherwise the Zeeman states are with respect to the quantization axis introduced in section 2.2 (Fig. 2.4). With this, the qubit states are defined as  $|1, -1\rangle = |\downarrow\rangle_z$  and  $|1, +1\rangle = |\uparrow\rangle_z$ . A complete definition of the atomic, qubit, and polarization states, as well as of the coordinate system used in this work, is given in Appendix B.

## 2.2. Trapping Single Atoms

The centerpieces of the experiment are the two traps for single  $^{87}\text{Rb}$ -atoms, which are set up in two laboratories 400 m apart on different sides of the campus (Fig. 2.1). One is located in the basement of the faculty of physics at Schellingstraße 4 (Lab 1) and the other in the basement of the department for economics at Schackstraße 4 (Lab 2)<sup>1</sup>.

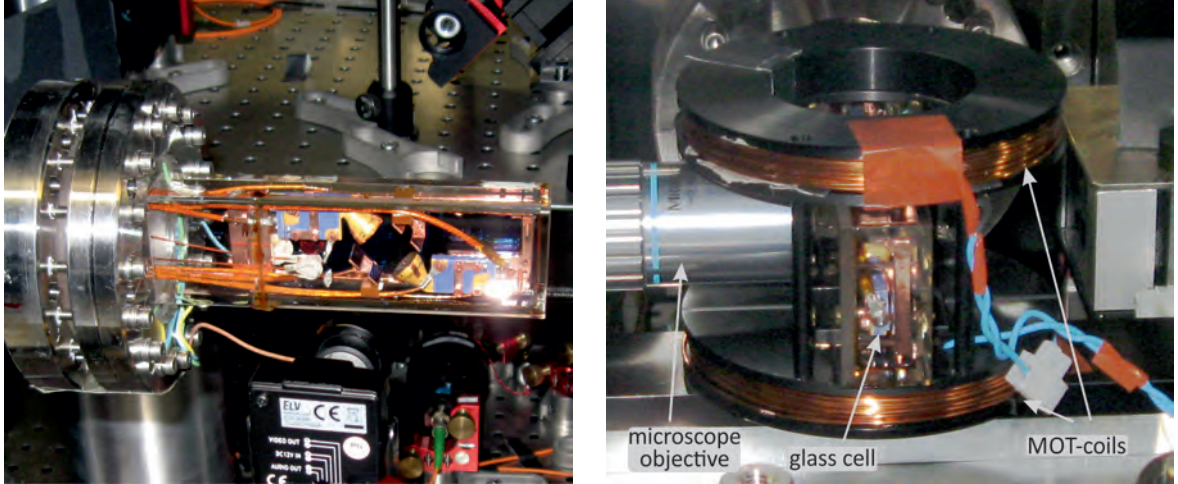
For trapping of atoms and obtaining long coherence times it is necessary to isolate them from the environment. Collisions with other atoms and molecules can only be suppressed in an ultra high vacuum environment. Therefore a core part of the trap setup is a vacuum chamber with good optical access for the required laser beams. To actually trap atoms inside the vacuum chamber, a two step scheme is implemented: first, a cloud of atoms is trapped and cooled in a magneto-optical trap (MOT) [53]. After this atoms are slow enough for the second step: to be trapped in an optical dipole trap (ODT) [50]. To verify that an atom is actually trapped the fluorescence light emitted by the atom is collected.

### Vacuum chamber and setup for the magneto-optical trap

The vacuum chamber used allows for a pressure below  $10^{-9}$  mBar. Additionally the particle detectors for the fast and efficient atomic-state measurement need to be placed (Sec. 2.3.2) inside the vacuum close to the trap position. To make this possible, the ultra high vacuum (UHV) setup incorporates a specially designed glass cell, which is attached to the main steel part. This glass cell is designed such that both particle detectors can be placed inside, without impeding optical access to the trap region (Fig. 2.3a). The main steel part of the vacuum setup houses an ion getter pump, an ion pressure gauge, and rubidium dispensers. A detailed description of the design and the construction of the vacuum setup can be found in [37, 54].

A magneto-optical trap, as the name indicates, uses a magnetic quadrupole field and laser light to trap and cool atoms [53]. The magnetic field is created by coils installed in an anti-Helmholtz configuration around the glass cell (Fig. 2.3a). Six circularly polarized laser beams,

<sup>1</sup>For clarity the trap in Lab 1 is the example for describing the core components and techniques. The minor differences of the trap in Lab 2, which are not important for the general understanding, are left for the Appendix F.



(a) The glass cell connected to the main UHV setup: The two detectors for the fast atomic state read-out (Sec. 2.3.2) are placed close to the region of the rap. (b) The glass cell inside anti-Helmholtz MOT-coils and microscope objective for the ODT and collection of fluorescence light.

Figure 2.3.: Vacuum chamber and atomic trap setup.

two counter propagating beams for each direction in space, are overlapped inside the glass cell at the center of the coils. These beams are generated by both a cooling laser, which is slightly red detuned with respect to a closed atomic transition, as well as a repump laser. By employing a quadrupole field together with circular polarized light, the atoms can not only be cooled but also confined. Thus, a cloud of cooled, trapped atoms is created. This cloud has a diameter of  $< 1$  mm and contains  $> 10^4$  atoms [30] with a temperature well below  $146 \mu\text{K}$ , which is the so-called Doppler limit for  $^{87}\text{Rb}$  [49]. The atoms are actually cooled further by a process called polarization gradient cooling [55] resulting in significantly lower temperatures of only  $30 \mu\text{K}$  to  $40 \mu\text{K}$  [38, 56].

### The optical dipole trap

To capture a single atom out of the cloud of cold atoms trapped by the MOT an optical dipole trap used [50, 57]. It relies on the interaction between an induced atomic dipole and a light field. The latter is far detuned from any transition such that other potential effects, such as optical excitation and photon scattering can be neglected. An off-resonant light field affects the energy level structure of an atom due to the AC-Stark shift. This acts like a conservative potential, depending on the detuning and local intensity of the light field. In the case of  $^{87}\text{Rb}$ , a focused red detuned laser forms a 3-dimensional potential well where atoms are attracted to the position with the highest intensity at the focal point. This potential well is typically shallow (energy equivalent of a few mK) and allows only the trapping of very slow atoms. For a linearly polarized light field, the potential takes the form

$$U(r, z) = \frac{\pi c^2 \Gamma}{2\omega_0^3} \left( \frac{2}{\Delta_{2,F}} + \frac{1}{\Delta_{1,F}} \right) \cdot I(r, z) \quad (2.1)$$

with the spontaneous decay rate of the excited state  $\Gamma$ , transition frequency of the D-line  $\omega_0$ , and the detuning of the laser with respect to the transition of the  $D_1$  and  $D_2$  line  $\Delta_{1,F}$  and

$\Delta_{2,F}$ . The spatially dependent intensity  $I(r, z)$  is defined by the Gaussian mode of the laser beam and has the form

$$I(r, z) = I_0 \left( \frac{w_0}{w(z)} \right)^2 e^{-\frac{2r^2}{w(z)^2}} \quad (2.2)$$

with  $w(z) = w_0 \sqrt{1 + \left(\frac{z}{z_R}\right)^2}$  the beam waist at a position  $z$ ,  $z_R = \frac{\pi w_0^2}{\lambda}$  the Rayleigh length,  $\lambda$  the wavelength of the laser,  $z = 0$  the focus position,  $w_0$  the waist at the focus, and  $I_0$  the intensity at the center of the focus. The potential of the trapped cold atoms can be approximated as harmonic [28, 38], with the trap frequencies

$$\omega_T = \sqrt{\frac{4U_{ODT}}{mw_0^2}} \quad (2.3)$$

$$\omega_L = \sqrt{\frac{2U_{ODT}}{mz_R^2}} \quad (2.4)$$

where  $\omega_T$  is the transversal and  $\omega_L$  is the longitudinal trap frequency,  $U_{ODT} = U(0, 0)$  is the potential depth at the focal spot of the laser light, and  $m$  is the mass of  $^{87}\text{Rb}$  (Tab.: A.2).

To implement the ODT, a laser with a wavelength of 852 nm is focused at the position of the cloud of cold  $^{87}\text{Rb}$ -atoms trapped by the MOT. The focal waist of the laser is  $w_0 = 1.92 \mu\text{m}$  with a Rayleigh length of  $z_R = 13.6 \mu\text{m}$  [37] thereby only one single atom can be trapped due to collisional blockade effects [58, 28]. This waist size together with an optical power of 60 mW of the laser results in a trapping potential  $U_{ODT} = k_B \cdot 3.2 \text{mK}$ . The trap frequencies are  $\omega_T = 2\pi \cdot 92 \text{kHz}$  and  $\omega_L = 2\pi \cdot 13 \text{kHz}$  [38].

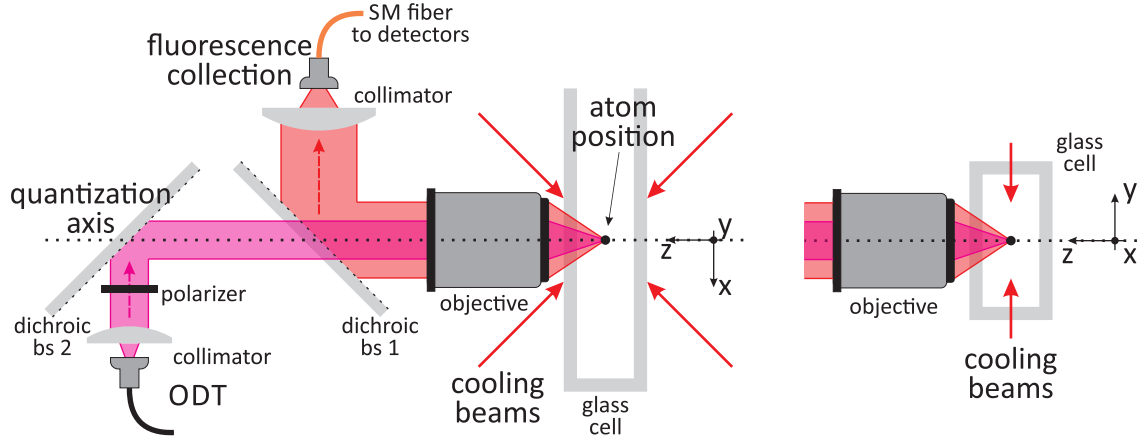
### Confocal setup for the ODT and fluorescence collection

To enable the atom being used as qubit, it is not only necessary to trap a single atom, but also to be able to collect and detect light emitted by it. Here a confocal configuration with a single high numerical aperture (NA) microscope objective<sup>2</sup> will be used to focus the ODT laser and to collect the fluorescence light (Fig. 2.4). The microscope objective is designed for both wave lengths 852 nm and 780 nm and it allows to focus light through 3.5 mm glass with a large working distance. This allows the objective to be mounted outside the vacuum setup and to collect the fluorescence light from inside the vacuum glass cell. The effective numerical aperture used for the collection of the fluorescence is  $\text{NA} = 0.267$  [37]. A dichroic beam splitter separates the light emitted by the atom with a wavelength of 780 nm from the 852 nm laser used for the ODT. The fluorescence light is then coupled into a single mode optical fiber and guided to the single photon detection setup (Fig. C.1, Fig. 2.15). The combined collection and detection efficiency of the fluorescence light,  $\eta_{\text{col}}$ , is ca 2.15%. This low efficiency is due to the small fraction of light that can be coupled into the optical fiber by the microscope objective, which is limited by the collection and aberration effects. The transmission losses in the fiber  $\tau_{\text{fib}}$ <sup>3</sup>, of the objective, and the other optical elements as well as the detector efficiencies<sup>4</sup> reduce

<sup>2</sup>Mitutoyo, G Plan Apo 50, NA = 0.5 corrected for a 3.5 mm glass plate, working distance 13.89 mm, wavelength range 435-655 nm, reduced performance in the near infrared.

<sup>3</sup> $\tau_{\text{fib}} = 0.9954$  for 5 m fiber with 4.0 dB/km at 780 nm (Thorlabs' 780-HP) and  $\tau_{\text{fib}} = 0.5249$  for 700 m fiber.

<sup>4</sup>The detection efficiency of the detectors (Laser Components Count-10C) is in a range between 0.45 and 0.65. With four detectors used simultaneously the best average detector efficiency is ca 0.60. Due to frequent detector failures detectors the efficiency changed during measurements done in this work.



(a) Top view ( $z$ - $x$  plane): The collected fluorescence light is separated from the ODT laser with a dichroic beam splitter and coupled into a single mode fiber guiding it to the single photon detection setup (Fig. C.1). Cooling beams (red arrows) in the horizontal plane. (b) Front view ( $z$ - $y$  plane) with vertical cooling beams (red arrows)

Figure 2.4.: Confocal ODT and fluorescence collection setup: The linearly polarized ODT laser (magenta) is focused with a microscope objective at the position of the atom cloud trapped by the MOT (red arrows: cooling beams) inside the vacuum glass cell. A single atom is trapped at the point of highest intensity (focus) of the ODT laser (black dot: position of the trapped single atom). The fluorescence light emitted by the trapped single atom (red) is collected with the same objective. The collection of the fluorescence light via the microscope objective into the single mode fiber defines the quantization axis of the system. It corresponds to the axis of the microscope objective.

the efficiency even further [37].

The direction of the fluorescence collection defines the quantization axis of the system. The coordinate system of the experiment is defined so that the  $z$ -axis coincides with the quantization axis (Fig. 2.4).

### Trapping sequence

The procedure to trap a single atom is the following: first the cooling beams, the current in the quadrupole coils, and the dipole trap laser are switched on. By this a cloud of cold atoms is trapped. One of these cold atoms eventually enters the dipole trap potential and is trapped providing it scatters light inside the potential. The ongoing scattering of cooling light from this atom leads to a rapid increase in the photon detection rate. If the photon detection rate is above a certain threshold, the current in the quadrupole coils is turned off. This leads the cloud of cold atoms to dissipate, while the single atom in the ODT remains trapped. This trapped single atom is now ready for experiments. If the atom is lost after some time the photon detection rate drops back to the background level. As soon as the photon detection rate is below a certain threshold, typically set lower than the first one (Fig. 2.5), the current in the quadrupole coils is turned on to trap another atom. This process is fully automated

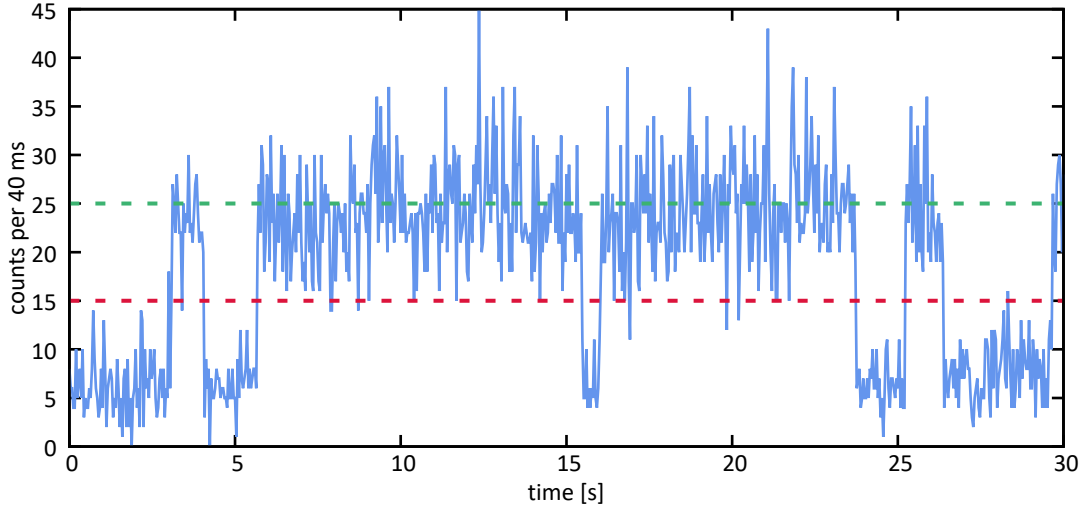


Figure 2.5.: Trace of photon counts: the photon count rate integrated for 40 ms (blue). The background count level is caused by the cooling beams and has an average of 6.75 counts. If an atom is trapped the average counts rise to 24.75. The threshold above which an atom can be considered trapped is 25 counts (green). If fewer than 15 counts (red) are recorded, the atom is considered lost. This hysteresis is needed to identify if an atom is trapped or lost correctly.

and controlled by a computer.

## 2.3. State Preparation, Control, and Measurement of Single Atoms

After trapping the single atoms, they are ready to be used as atomic qubits. For this it is necessary to prepare, control, and measure atomic states with high fidelity. For the creation and detection of long distance entanglement via entanglement swapping it is necessary to entangle the atomic qubit with a photon, perform measurements of the qubit state, and control the coherence of these states.

### 2.3.1. Creation of atom-photon entanglement

Spontaneous emission of an excited atom generally leads to entanglement of the emitted photon state with the atomic state after the decay. This can be used to entangle the atomic qubit with a photon. To achieve this, the transition of the excited  $5^2P_{3/2}$ ,  $F' = 0$  state to the ground state can be used. From this state the atom only decays to the  $5^2S_{1/2}$ ,  $F = 1$  ground state. There are three possible decay channels (Fig. 2.6c) to  $m_F = +1$  while emitting a  $\sigma^-$  (left hand circular) polarized photon, to  $m_F = 0$  while emitting a  $\pi$  (parallel to the quantization axis) polarized photon, and to  $m_F = -1$  while emitting a  $\sigma^+$  (right hand circular) polarized photon. These processes have equal Clebsch-Gordan coefficients (Fig. A.1a) [49] and thus a probability of  $1/3$ . Considering quantization along the  $z$ -axis, which is defined by the collection

optics of the experiment (Fig. 2.4), the entangled atom-photon state has the form

$$|\Psi\rangle_{AP} = \frac{1}{\sqrt{3}} (|\sigma^+\rangle |1, -1\rangle + |\pi\rangle |1, 0\rangle + |\sigma^-\rangle |1, +1\rangle)$$

The  $\pi$ -light interferes destructively when coupled into the single mode fiber leading to the photon detectors (Fig. 2.2). Filtering out  $\pi$  polarized light leaves only two decay channels to  $m_F = \pm 1$  for the collected photons, resulting in the atom-photon state

$$\begin{aligned} |\Psi\rangle_{AP} &= \frac{1}{\sqrt{2}} (|\sigma^+\rangle |1, -1\rangle + |\sigma^-\rangle |1, +1\rangle) \\ &= \frac{1}{\sqrt{2}} (|L\rangle |1, -1\rangle + |R\rangle |1, +1\rangle). \end{aligned} \quad (2.5)$$

Following the definition from Appendix B for the polarization states of the photon ( $|L\rangle \equiv |\sigma^+\rangle$ ,  $|R\rangle \equiv |\sigma^-\rangle$ )  $|L\rangle$  and  $|R\rangle$  represent the circular polarization states of the photon in the reference frame of the laboratory. This quantum state (2.5) is the  $\Psi^+$ -state, one of the four maximally entangled Bell-states. Considering the atomic qubit (Sec. 2.1), the entangled state can also be written as

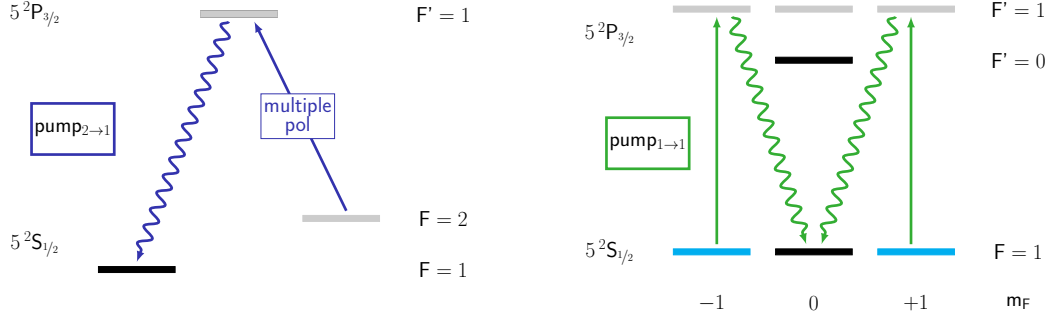
$$|\Psi\rangle_{AP} = \frac{1}{\sqrt{2}} (|L\rangle |\downarrow\rangle_z + |R\rangle |\uparrow\rangle_z) \quad (2.6)$$

A complete definition of the qubit states for all three orthogonal axes x,y, and z can be found in the Appendix B.

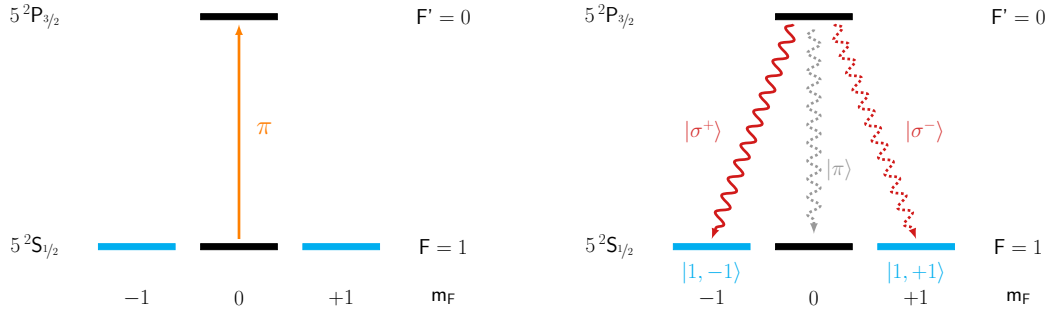
### Optical Pumping process

To employ entanglement generation via spontaneous emission, the atom is first prepared in the  $5^2S_{1/2}$ ,  $F = 1$ ,  $m_F = 0$  state and then excited to the  $5^2P_{3/2}$ ,  $F' = 0$  state via a short laser pulse. The preparation of  $5^2S_{1/2}$ ,  $F = 1$ ,  $m_F = 0$  is performed via optical pumping. After trapping and cooling, the single atom is with a high likelihood in the  $5^2S_{1/2}$ ,  $F = 2$  ground state. To transfer the population to the  $5^2S_{1/2}$ ,  $F = 1$  ground state, the atom is excited with a laser (pump<sub>2→1</sub>, Fig. 2.6a) resonant to  $5^2P_{3/2}$ ,  $F' = 1$ . From these it can decay to the  $5^2S_{1/2}$ ,  $F = 1$  ground state or back to the  $F = 2$  ground state. After several excitation-decay cycles the atom is with a very high probability in the  $5^2S_{1/2}$ ,  $F = 1$  ground state. To avoid residual population of the  $5^2S_{1/2}$ ,  $F = 2$  ground state, multiple directions and polarizations for the pump<sub>2→1</sub> laser are used, thereby addressing all Zeeman sub-levels (Fig. 2.6a and Fig. 2.7b).

The population in the  $5^2S_{1/2}$ ,  $F = 1$ ,  $m_F \neq 0$  Zeeman-states is excited with pump<sub>1→1</sub> laser to the  $5^2P_{3/2}$ ,  $F' = 1$  state from where it decays to the  $m_F = 0, \pm 1$  (Fig. 2.6b and Fig. 2.7a). The employed laser pulse is  $\pi$  polarized, where the polarization is parallel to the quantization axis and since the transition from  $5^2S_{1/2}$ ,  $F = 1$ ,  $m_F = 0$  to  $5^2S_{1/2}$ ,  $F' = 1$ ,  $m_F = 0$  is dipole forbidden, the  $5^2S_{1/2}$ ,  $F = 1$ ,  $m_F = 0$  state is not excited by the pump<sub>1→1</sub> laser. For this the incidence direction needs to be orthogonal to this axis (Fig. 2.7a). To avoid populating the  $5^2S_{1/2}$ ,  $F = 2$  ground state the pump<sub>2→1</sub> and pump<sub>1→1</sub> laser are applied simultaneously. This pumping procedure takes less than 4  $\mu$ s and has an efficiency of  $\eta_p \approx 80\%$ . A more detailed description can be found in [38].



- (a) The  $\text{pump}_{2 \rightarrow 1}$  laser transfers the population from  $F = 2$  to  $F = 1$ .  
 (b) The  $\text{pump}_{1 \rightarrow 1}$  laser transfers the  $m_F = \pm 1$  Zeeman-states to the  $m_F = 0$  Zeeman-state of the  $F = 1$  ground state.



- (c) Excitation to the  $5^2P_{3/2}$ ,  $F = 0$ ,  $m_F = 0$  state: The  $\pi$ -polarized excitation pulse (orange) excites the atom from prepared the  $5^2S_{1/2}$ ,  $F = 1$ ,  $m_F = 0$  to the excited state.  
 (d) Decay of the  $5^2P_{3/2}$ ,  $F' = 0$ ,  $m_F = 0$  excited state: the population in the excited state decays with equal probability to each of the three Zeeman levels of the  $5^2S_{1/2}$ ,  $F = 1$ . Only photons with  $\sigma^\pm$  polarization (red) emitted by the decay to the  $m_F = \pm 1$  Zeeman-ground states can be collected into the single mode fiber. The photons with  $\pi$  polarization (gray) originating in the decay to  $m_F = 0$  are not collected. This results in the entangled atom-photon state  $|\Psi_{AP}\rangle = \frac{1}{\sqrt{2}} (|\sigma^+\rangle|1, -1\rangle + |\sigma^-\rangle|1, +1\rangle)$ .

Figure 2.6.: The pumping and excitation process: preparation the  $5^2S_{1/2}$ ,  $F = 1$ ,  $m_F = 0$  ground state (a, b) and creation of atom-photon entanglement via excitation of the  $5^2P_{3/2}$ ,  $F = 0$ ,  $m_F = 0$  state (c, d).

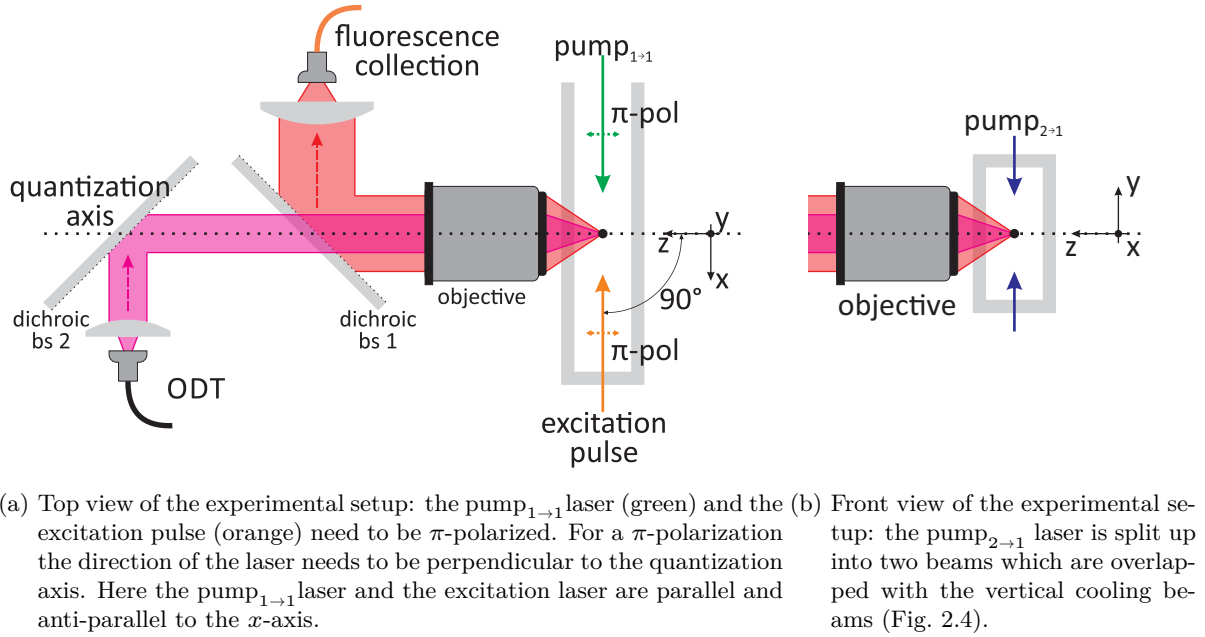


Figure 2.7.: Setup for the pump and excitation process

### Excitation process

Next, the atom, prepared  $5^2S_{1/2}$ ,  $F = 1$ ,  $m_F = 0$  ground state, is excited with a short laser pulse that is  $\pi$  polarized to the  $5^2P_{3/2}$ ,  $F' = 0$ ,  $m_F = 0$  state (Fig. 2.6c). The excited state decays with a short life time of 26.24 ns [49]. The emitted photons are subsequently collected with the confocal microscope setup, filtering out the  $\pi$  polarized photons. The remaining photons are then guided to the photon detection setup.

The fidelity of the atom-photon state (2.5) is limited by imperfections of the pumping and excitation process, leading to unwanted effects, such as off-resonant excitation resulting in two photon emission during one excitation process. These effects strongly depend on the polarization, temporal shape, and intensity of the excitation pulse. For optimizing these parameters it is necessary to consider the photon collection efficiency, the photon detection efficiency as well as the detector dark counts<sup>5</sup>. Additionally, an excitation efficiency as high as possible is required in order to achieve a reasonable event rate for executing experiments. Especially since the atom-atom entanglement rate is proportional to the square of the single-atom excitation and photon detection probability. A rigorous analysis based on [33] can be found in Chapter 6.

Considering all these parameters an approximately Gaussian shaped excitation pulse with a full width at half maximum duration (FWHM) of 20.35 ns (Fig. 2.8) and with an intensity yielding approximately 80% of the maximal excitation efficiency is chosen [33]. Together with an acceptance time window of 208 ns this results in a total photon detection probability of  $\eta = 1.7\%$  per excitation pulse.

This low detection probability makes a fast repetition of the pumping and excitation process necessary to achieve a reasonable event rate. For this the heating of the atom by repeated

<sup>5</sup>4×Laser components Count-10C with total dark counts of 40 1/s

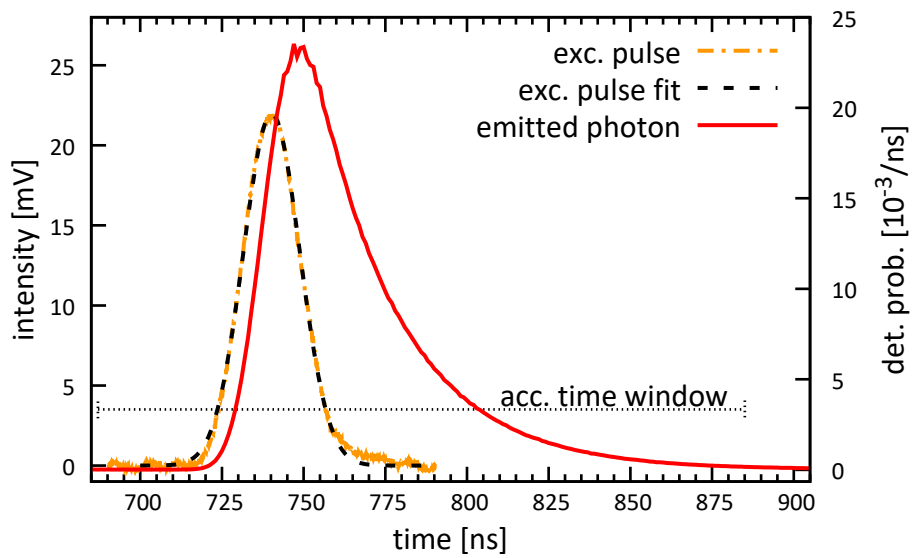


Figure 2.8.: Temporal shape of the excitation pulse and of the emitted photon: intensity of the excitation pulse measured with a fast photo-diode (orange) and Gaussian fit of the excitation pulse (black, dashed)  $I = I_0 e^{-\frac{1}{2}(\frac{t-t_0}{2T})^2}$  with  $T = 8.64$  ns,  $t_0 = 740.20$  ns, and  $I_0 = 21.98$  mV. The FWHM pulse duration is 20.35 ns. The time-dependent detection probability of the photon (red), normalized on the total photon detection events inside acceptance time window (black, finely dashed), reflects the temporal shape of the photon.

pumping and excitation has to be considered. The heating does not only lead to a possible loss of the trapped atom, but also to decoherence of the atomic state caused by stronger motion of the trapped atom (Sec. 2.3.3). A scheme in which 40 repetitions of pumping and excitation are followed by 350  $\mu\text{s}$  of cooling enables for fast repetition, without heating the atom significantly [38].

### 2.3.2. Measurement of the atomic state

In order to read-out a physical qubit, it is necessary to perform a projection measurement on the qubit with a freely chosen measurement direction. To perform such a measurement on the qubit encoded in the Zeeman states, a state selective ionization scheme is used. It is composed from two steps: first, a selected superposition of Zeeman states is excited from the  $5^2\text{S}_{1/2}$ ,  $F = 1$  ground state to the  $5^2\text{P}_{1/2}$ ,  $F' = 1$  excited state. Then the excited atoms are ionized. The ionized atoms are no longer trapped, and the cooling light and detection of fluorescence photons can be used to measure if an atom is still trapped or not.

To close one of the most significant loopholes in Bell experiments, the so called locality or communication loophole (Sec.3.3), a very fast state measurement with a high fidelity is mandatory. While the state-selective ionization process is very fast and has a high fidelity, the detection of fluorescence light in this setup has also a high fidelity but needs long measurement times of more than 30 ms. To enable a faster decision, particle detectors that can confirm the ionization are employed, which detect the  $^{87}\text{Rb}^+$ -ion and the electron directly.

#### Zeeman-level selective ionization scheme

To excite only a specific superposition of the Zeeman-levels for the  $F = 1$ ,  $m_f = \pm 1$  laser light (read-out laser) resonant to the  $5^2\text{S}_{1/2}$ ,  $F = 1$  to  $F' = 1$  transition (D1 line) is used (Fig. 2.9a). The incidence direction of the read-out laser coincides with the quantization axis, counter propagating to the dipole trap (Fig. 2.10a). Selection rules and transition dipole moments of the atom (Fig. A.1b) determine which polarization of the read-out laser  $\chi_{ro}$  (2.7) excites which superposition of the Zeeman-levels. The superposition transferred  $|\text{B}\rangle_{\chi_{ro}}$  will be called bright state (2.8) and the orthogonal superposition which is not transferred  $|\text{D}\rangle_{\chi_{ro}}$  dark state (2.9). The polarization of the read out laser is set via a quarter and a half wave plate, thus any measurement direction can be chosen.

$$\chi_{ro} = \cos(\alpha) \cdot V + e^{-i\phi} \sin(\alpha) \cdot H \quad (2.7)$$

$$|\text{B}\rangle_{\chi_{ro}} = \cos(\alpha) \frac{-1}{\sqrt{2}} (|1, -1\rangle - |1, +1\rangle) + \sin(\alpha) e^{i\phi} \frac{i}{\sqrt{2}} (|1, -1\rangle + |1, +1\rangle) \quad (2.8)$$

$$|\text{D}\rangle_{\chi_{ro}} = \sin(\alpha) \frac{1}{\sqrt{2}} (|1, -1\rangle - |1, +1\rangle) + \cos(\alpha) e^{i\phi} \frac{i}{\sqrt{2}} (|1, -1\rangle + |1, +1\rangle) \quad (2.9)$$

The ionization threshold for the excited  $5^2\text{P}_{1/2}$ ,  $F' = 1$  state is 473.67 nm and the ionization threshold for the ground state  $5^2\text{S}_{1/2}$ ,  $F = 1$  is 296.82 nm [59]. To ionize only the excited atoms a laser with a wavelength below 473 nm (Appendix F) is used, which is focused on the atom with the same microscope objective used for fluorescence collection and for focusing the dipole trap (Fig. 2.10a). Ionized atoms are immediately lost from the trap. By integrating the fluorescence counts measured at the detectors it is possible to determine whether the atom was ionized or not. It is important to note that the  $5^2\text{S}_{1/2}$ ,  $F = 1$ ,  $m_F = 0$  state is excited by any polarization. The probability to observe the bright state, meaning the atom is

ionized, for a given atomic state  $\rho$  is  $Pr_B = \langle B | \rho | B \rangle + \langle 1, 0 | \rho | 1, 0 \rangle$  while the probability to observe the dark state, in this case the atom is still trapped, is  $Pr_D = \langle D | \rho | D \rangle$  (disregarding imperfections).

The fidelity of this measurement is limited by the life-time of the excited state and by off-resonant excitation of the dark state to the state  $5^2P_{1/2}$ ,  $F' = 2$ . The short life time of 27.7 ns [49] leads to spontaneous decay to the ground states before the excited atom is ionized (Fig. 2.9b). With a probability of  $5/6$  the excited state decays to the  $F = 2$  ground state. This can be overcome by exciting this state with a laser to the  $5^2P_{3/2}$ ,  $F' = 3$  state, allowing for the ionization of the atom (Fig. 2.9c). With a probability of  $1/6$  the excited state decays to the  $F = 1$  ground state and in equal parts to bright state  $|B\rangle_{ro}$  and to dark state  $|D\rangle_{ro}$ . While the part in  $|B\rangle_{ro}$  can be excited again, the decay into  $|D\rangle_{ro}$  leads to a reduction of ionization probability of the initial bright state. The  $5^2P_{1/2}$ ,  $F' = 2$  state is separated from the  $5^2P_{1/2}$ ,  $F' = 1$  state by 816.7 MHz (Fig. 2.2) with a natural line width (FWHM) of only 5.746 MHz [49]. However, the fast ionization of the excited atom, which is caused by the high intensity (ca  $P_{ion} = 200$  mW focused with  $w_0 = 1 \mu\text{m}$  at the atom) of the ionization laser, leads to an increase of the line width, leads to significant off-resonant excitation [34, 37].

For an optimal distinction of bright and dark state, the contrast

$$C_{ro} = Pr_{ionized}(|B\rangle_{\chi_{ro}}) - Pr_{ionized}(|D\rangle_{\chi_{ro}})$$

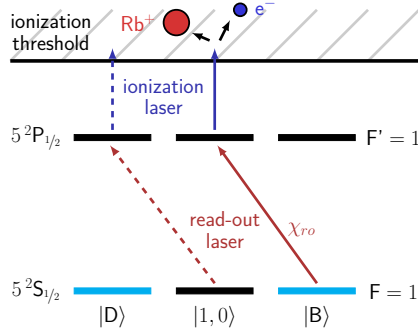
as the difference between the ionization probability of an atom prepared in  $|B\rangle_{\chi_{ro}}$  and the ionization probability of an atom prepared in  $|D\rangle_{\chi_{ro}}$  needs to be maximized. This is achieved by selecting an optimal pulse duration and power of the read-out pulse. With a pulse length of 140 ns and optical power of 1.24  $\mu\text{W}$ , ionization probabilities of  $Pr_{ionized}(|B\rangle_{\chi_{ro}}) \simeq 0.98$  and  $Pr_{ionized}(|D\rangle_{\chi_{ro}}) \simeq 0.04$  can be obtained, resulting in a contrast of  $C_{ro} \simeq 0.94$  [37]. The duration of this read-out process is less than 400 ns. A detailed analysis of the read-out scheme can be found in [37, 34].

### Detection of the ionization fragments

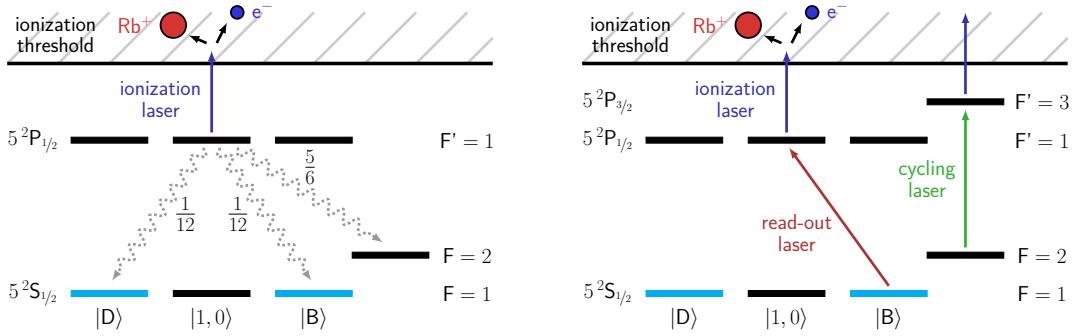
In order to close the locality loophole of a Bell-experiment, it is necessary to obtain the result of the ionization faster than with fluorescence detection. This can be achieved by a direct detection of the ionization fragments. Channel-electron-multipliers<sup>6</sup> (CEMs) are used to detect both the electron and the  $\text{Rb}^+$ -ion created during a successful ionization process. The setup consists of two CEMs (Fig.2.10c) that are set to different electrical potentials. Hence, one attracts and detects electrons and the other one  $\text{Rb}^+$ -ions. Tuning the electrical field with copper apertures on the detectors, compensation electrodes and an electrical conducting coating (ITO) enables detection efficiencies above 0.9 for each detector. This results in a probability of 0.99 to detect at least one of the fragments of an ionization process. The dark count rate of this setup is with  $< 10$  kHz for the electron and  $< 10$  Hz for the ion detector very low [35, 36, 37, 54].

The time needed for the detection of the ionization fragments is determined by the time of flight to the detectors and the response time of the detectors of ca 25 ns. The time of flight depends on the mass of the fragments and the electrical potential difference  $\Delta U_{acc}$  between

<sup>6</sup>Channel electron multiplier KBL10RS Dr. Sjuts Optotechnik GmbH. These can detect particles like ions and electrons, but also photons with a wavelength below 150 nm.

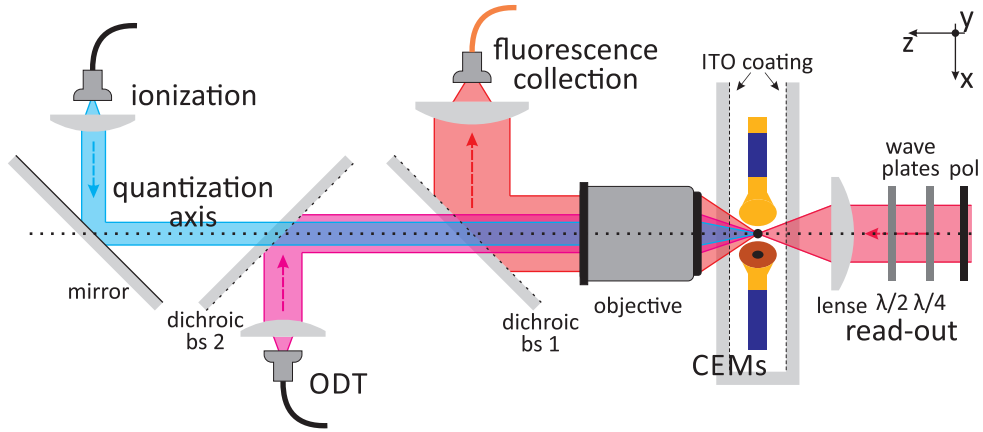


- (a) Zeeman-state selective ionization: the polarization  $\chi_{ro}$  (2.7) of the read-out laser (red) selects which superposition of the  $|1, \pm 1\rangle$  Zeeman-states, called bright state  $|B\rangle$  (2.8), is excited to the  $5^2P_{1/2}, F' = 1$  state, while the orthogonal superimposed dark state  $|D\rangle$  is not affected by the read-out laser and stays in the ground state. The third Zeeman-state  $|1, 0\rangle$  can be excited by any polarization  $\chi_{ro}$  of the read-out laser (dashed red). The excited atoms are ionized by the ionization laser (blue).

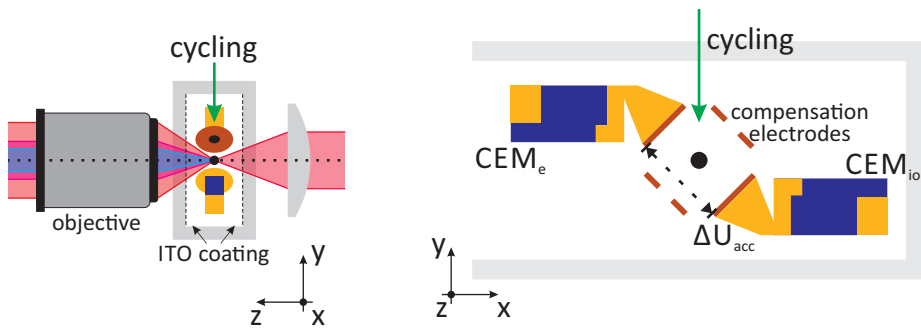


- (b) Possible decay routes from the excited state: the population in the excited  $5^2P_{1/2}, F' = 1$  state can decay before it is ionized. This decay is with probability  $5/6$  to the  $F = 2$  ground state, with probability of  $1/12$  back to bright state  $|B\rangle$ , and with the same probability to the dark state  $|D\rangle$ .
- (c) Second excitation after decay: To overcome the detrimental effect of the decay to  $F = 2$  ground state, this state is excited by the additional cycling laser (green) to the  $5^2P_{3/2}, F'=3$  excited state. Additionally, atoms that decay back to the bright state  $|B\rangle$  are re-excited by the read out laser (red).

Figure 2.9.: Fast read-out scheme based on Zeeman-state selective ionization.



- (a) Top view: The read out laser (dark red) propagating in positive  $z$ -direction (counter propagating to the ODT laser) is focused on the atom (black dot). A linear polarizer followed a  $\lambda/2$  and a  $\lambda/4$  wave plate allow to set any desired polarization  $\chi_{ro}$ . The ionization laser (blue) is overlapped with the ODT laser by a dichroic beam splitter and focused with the objective on the atom. Two channel electron multipliers (CEMs) are located near the atom inside the vacuum glass cell. The two inner surfaces of the glass cell are coated with transparent and conducting indium tin oxide (ITO) allowing for applying of electric fields.



- (b) Front view: The additional cycling (c) laser is propagating downwards in  $y$ -direction.
- (c) View from the side of the objective (scale  $2\times$ ): A high voltage  $U_{acc}$  is applied between the two CEMs to accelerate the ionization fragments to the detectors. One detector registers the  $^{87}\text{Rb}$ -ions ( $\text{CEM}_{ion}$ ) and the other one detects electrons ( $\text{CEM}_e$ ). The compensation electrodes and the ITO coated sides of the glass cell (a, b) are used to tune the electric field inside the vacuum for optimal fragment detection efficiency.

Figure 2.10.: Experimental setup for the fast and efficient state read-out.

the detectors. With a potential difference of  $\Delta U_{acc} = 4.2 \text{ kV}$ , the time of flight of an electron is  $< 2.5 \text{ ns}$ . the time of flight of a  $^{87}\text{Rb}$ -ion, having  $1.63 \cdot 10^5$  times more mass than an electron; is  $< 380 \text{ ns}$  [37]. For each detector a short acceptance time window is defined. if one particle gets detected within the given time windows, a successful ionization can be assumed. When considering the CEM detection efficiency and the acceptance time window lengths of  $240 \text{ ns}$  the probability to not detect one of the fragments when the atom is actually ionized is ca  $1\%$ . Further considering and the dark count rates, the probability to detect a background count during time windows is below  $2.4 \cdot 10^{-3}$ .

### Duration and performance of the state measurement

The fidelity of the atomic state measurement depends on the performance of the state selective ionization and the subsequent measurement, whether the atom was ionized. Using fluorescence detection to confirm the ionization the overall the measurement takes  $> 30 \text{ ns}$  and the measurement fidelity is ca  $0.97$ . However, using the particle detectors the end of the acceptance time window, which defines the end of the measurement, for ions is only  $570 \pm 3 \text{ ns}$  after the start of the read-out laser pulse [38, 60]. Still the measurement fidelity with ca  $0.965$  [37] is very high and allows for a not only fast but also efficient atomic state read-out.

### 2.3.3. Coherence of the atomic states

In the experiments presented in this thesis the atomic state is only measured if the signal heralding atom-atom entanglement is received. This is called an event-ready scheme. For the experiments to be successful the initially prepared state needs to be maintained until the state is measured after receiving the heralding signal. A long temporal coherence of the atomic state is thus necessary. In this setup the heralding signal is sent back to the trap setup after the photon detection. Thus, the time from excitation to receiving the signal is the time needed for the photon to travel to the detectors, the time needed by the detection electronics, and the time the signal needs to travel back to the setup. Considering the  $700 \text{ m}$  long fiber channel this time is about  $7 \mu\text{s}$ .

The atomic qubit is encoded in the  $|1, \pm 1\rangle$  Zeeman states of the  $S_{1/2}$  ground state. Population of these states cannot decay to a different atomic state, but can be changed by external influences. For single atoms trapped inside ultra high vacuum, these external influences are limited to laser light of the setup and the external magnetic field.

### Interaction with a magnetic field

The interaction between the atomic spin and a magnetic field  $\vec{B}$  is described by the interaction Hamiltonian  $\hat{H}_B$ . For a quantization axis in  $z$ -direction and the basis vectors  $\vec{e}_1 = |1, +1\rangle_Z$ ,  $\vec{e}_2 = |1, 0\rangle_Z$ , and  $\vec{e}_3 = |1, -1\rangle_Z$  and a magnetic field

$$\vec{B} = \begin{pmatrix} B_x \\ B_y \\ B_z \end{pmatrix}$$

the Hamiltonian is

$$\hat{H}_B = \frac{\mu_B g_F}{\hbar} \vec{B} \vec{F} \quad (2.10)$$

$$= \hbar \omega_L \begin{pmatrix} b_z & \frac{1}{\sqrt{2}}(b_x - ib_y) & 0 \\ \frac{1}{\sqrt{2}}(b_x + ib_y) & 0 & \frac{1}{\sqrt{2}}(b_x - ib_y) \\ 0 & \frac{1}{\sqrt{2}}(b_x + ib_y) & -b_z \end{pmatrix} \quad (2.11)$$

with the vector of the angular momentum operators for a spin 1 system  $\vec{F}$  ((B.1) in Appendix B), the Larmor frequency  $\omega_L = \frac{1}{\hbar} g_F \mu_B \|\vec{B}\|$ , the Bohr magneton  $\mu_B$ , the Landé factor  $g_F$  for the hyperfine state, and  $b_x = \frac{B_x}{\|\vec{B}\|}$ ,  $b_y = \frac{B_y}{\|\vec{B}\|}$ ,  $b_z = \frac{B_z}{\|\vec{B}\|}$  [38]. For cylindrical coordinates  $b_x = \sqrt{1-b_z^2} \cos(\phi)$  and  $b_y = \sqrt{1-b_z^2} \sin(\phi)$  the eigenvalues  $\lambda_i$  of  $\hat{H}_B$  are  $\lambda_1 = +\hbar\omega_L$ ,  $\lambda_0 = 0$ , and  $\lambda_{-1} = -\hbar\omega_L$  with the corresponding eigenvectors  $|\Phi_{+1}\rangle$ ,  $|\Phi_0\rangle$ , and  $|\Phi_{-1}\rangle$ .

$$\begin{aligned} |\Phi_{+1}\rangle &= \begin{pmatrix} -\frac{1}{2}(b_z+1)e^{-i\phi} \\ -\sqrt{\frac{1-b_z^2}{2}} \\ \frac{1}{2}(b_z-1)e^{i\phi} \end{pmatrix} & |\Phi_0\rangle &= \begin{pmatrix} -\sqrt{\frac{1-b_z^2}{2}}e^{-i\phi} \\ b_z \\ \sqrt{\frac{1-b_z^2}{2}}e^{i\phi} \end{pmatrix}, \\ |\Phi_{-1}\rangle &= \begin{pmatrix} -\frac{1}{2}(b_z-1)e^{-i\phi} \\ -\sqrt{\frac{1-b_z^2}{2}} \\ \frac{1}{2}(b_z+1)e^{i\phi} \end{pmatrix} \end{aligned} \quad (2.12)$$

These eigenvectors form an orthonormal basis and the time dependence for any state can be written in the form

$$|\Psi(t)\rangle = c_0 |\Phi_0\rangle + c_{-1} |\Phi_{-1}\rangle e^{i\omega_L t} + c_{+1} |\Phi_{+1}\rangle e^{-i\omega_L t} \quad (2.13)$$

with  $c_0, c_{\pm 1} \in \mathbb{C}$  and  $\sqrt{\|c_{-1}\|^2 + \|c_0\|^2 + \|c_{+1}\|^2} = 1$ .

### Interaction with the ODT light

During the time between excitation and state read-out the only laser interacting with the atom is the ODT laser. Since the ODT laser is far red off-resonant, scattering of photons is very rare and can be neglected and only the ac-stark shift needs to be considered for state evolution. The energy shift of the atomic  $5^2S_{1/2}$  ground states induced by the ODT laser light field is

$$\Delta E = -\frac{\pi c^2 \Gamma}{2\omega_0^3} \left( \frac{2 + g_F m_F P}{\Delta_{2,F}} + \frac{1 - g_F m_F P}{\Delta_{1,F}} \right) \cdot I. \quad (2.14)$$

It depends on the intensity  $I$  of the ODT laser, the decay rate and transition frequency of the central D-line  $\Gamma$  and  $\omega_0$ , the detuning  $\Delta_{1,F}$  and  $\Delta_{2,F}$  with respect to the transition of the  $D_1$  and  $D_2$  line, and  $g_F$  is the Landé factor of the considered hyperfine state.  $P$  is a

measure of the circular polarization of the electric field of the ODT laser  $\begin{pmatrix} E_x \\ E_y e^{i\delta} \\ 0 \end{pmatrix}$ , with

the relative phase shift  $\delta$ . This measure is defined as

$$P = \text{sign}(\delta) \frac{2\|A\|\|B\|}{\|A\|^2 + \|B\|^2} \quad (2.15)$$

with the semi-axes of the polarization ellipse  $A$  and  $B$  (Appendix D). Therefore,  $P = \pm 1$  corresponds to perfect circular polarization while  $P = 0$  corresponds to perfect linear polarization [61]. This energy shift  $\Delta E$  can be split up in two terms: one  $\Delta E_{lin}$  which depends only on the intensity  $I$  and detuning  $\Delta_{1,F}$ ,  $\Delta_{2,F}$  of the ODT laser and a second term  $\Delta E_{m_F}$ , with an additional dependence on the polarization  $P$  of the ODT laser and on the Zeeman level  $m_F$  of the atom.

$$\Delta E_{lin} = -\frac{\pi c^2 \Gamma}{2\omega_0^3} \left( \frac{2}{\Delta_{2,F}} + \frac{1}{\Delta_{1,F}} \right) I \quad (2.16)$$

$$\Delta E_{m_F} = \frac{\pi c^2 \Gamma}{2\omega_0^3} \left( \frac{1}{\Delta_{1,F}} - \frac{1}{\Delta_{2,F}} \right) \cdot g_F m_F P \cdot I \quad (2.17)$$

Time evolution of the qubit state can only be caused by an energy shift between the Zeeman states  $m_F$ , only the second term  $\Delta E_{m_F}$  needs to be considered. It is equivalent to an energy shift  $\Delta E_{bz} = g_F \mu_B m_F \|\vec{B}\|$  (2.10) caused by a magnetic field in  $z$ -direction ( $b_x = b_y = 0$ ,  $b_z = 1$ ). Therefore, one can define an effective magnetic field

$$\vec{B}_{eff}(\vec{x}) = \vec{B} + \begin{pmatrix} 0 \\ 0 \\ 1 \end{pmatrix} \frac{1}{\mu_B} u \cdot P_{ODT} \cdot I(\vec{x}) \quad (2.18)$$

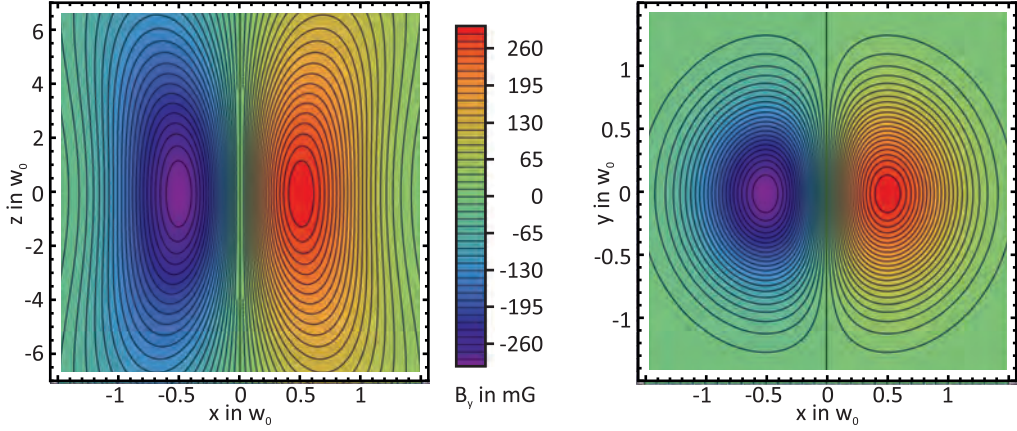
composed of the external magnetic field  $\vec{B}$  and the effect of circular polarization  $P_{ODT}$  of the ODT laser with  $u = \frac{\pi c^2 \Gamma}{2\omega_0^3} \left( \frac{1}{\Delta_{2,F}} - \frac{1}{\Delta_{1,F}} \right)$ . Furthermore, since the laser beam has the TEM<sub>00</sub>Gaussian mode, the position-dependent intensity distribution is of the form

$$I(\vec{x}) = I(r, z) = I_0 \left( \frac{w_0}{w(z)} \right)^2 e^{-\frac{2r^2}{w(z)^2}}$$

where  $w(z) = w_0 \sqrt{1 + \left( \frac{z}{z_R} \right)^2}$  is the beam waist at position  $z$ ,  $z_R = \frac{\pi w_0^2}{\lambda}$  is the Rayleigh length, and  $z = 0$  is the focal spot. The other parameters of the dipole trap are the wave length  $\lambda = 852 \text{ nm}$ , the waist at the focus  $w_0 = 1.92 \mu\text{m}$ , and intensity at the focus  $I_0$ . Thus the effective magnetic field depends not only on the ellipticity but also on the position of the atom in the trapping potential.

For a linearly polarized light field with  $P = 0$  the energy shift  $\Delta E_{m_F}$  vanishes. Thus, no state evaluation occurs when using a linearly polarized ODT laser and no magnetic field is present. Focusing a linearly polarized Gaussian beam, the emergence of longitudinal polarization near the focus has to be considered [48, 62]. In [48] the polarization of the ODT laser in the trapping region is calculated applying the formalism from [63, 64] for focusing a Gaussian beam. The position dependent amplitude of the electric field near the focus in each direction ( $E_x$ ,  $E_y$ ,  $E_z$ ) can be approximated in cylindrical coordinates ( $r$ ,  $\phi$ ,  $z$  with  $r$  in the  $x$ - $y$  plane and  $z = z$ ) as

$$\begin{pmatrix} E_x(\vec{x}) \\ E_y(\vec{x}) \\ E_z(\vec{x}) \end{pmatrix} \approx E_0 F_0(0, 0) \begin{pmatrix} \frac{1}{\sqrt{1+z^2/z_R^2}} + \frac{r^2 \cdot \cos(2\phi)}{4 \cdot z_R^2 (1+z^2/z_R^2)^{\frac{3}{2}}} \\ \frac{r^2 \cdot \sin(2\phi)}{4 \cdot z_R^2 (1+z^2/z_R^2)^{\frac{3}{2}}} \\ \frac{i 2 \cdot r \cdot \cos(\phi)}{2 \cdot z_R \cdot (1+z^2/z_R^2)} \end{pmatrix} e^{-\frac{r^2}{w(z)^2}} \quad (2.19)$$



(a)  $B_{long}(\vec{x})$  in the  $x$ - $z$  plane at  $y = 0$ ,  $P_{long}(\vec{x})$  according to Appendix D with sign change of the phase shift  $\delta$  between  $E_x$  and  $E_z$  at  $x = 0$  (solid line) (b)  $B_{long}(\vec{x})$  in the  $x$ - $y$  plane at  $z = 0$  (color scale as in (a)),  $P_{long}(z = 0) = \text{sign}(\delta) \frac{2\|E_x\| \|E_z\|}{\|E_x\|^2 + \|E_z\|^2}$  with phase  $-\pi/2$  for  $x < 0$  and  $\pi/2$  for  $x > 0$ .

Figure 2.11.: Effective magnetic field in  $y$  caused by the longitudinal polarization components  $E_z$  that arise near the focus polarization:  $B_{long}(\vec{x})$  (2.20) in the  $x$ - $z$  plane at  $y = 0$  and in the  $x$ - $y$  plane at  $z = 0$ .

for a beam propagating along the  $z$ -axis with an original polarization of the Gaussian beam in  $x$ -direction corresponding to  $\phi = 0$  direction in the cylindrical coordinates. The beam waist  $w(z)$  and the Rayleigh length  $z_R$  are defined as before.  $E_0$  is a scaling constant and  $F(0,0) = \int_0^\alpha e^{-\frac{f^2 \tan^2(\theta)^2}{w_{odt}^2}} \sqrt{\cos(\theta)} (1 + \cos(\theta)) \sin(\theta) d\theta$  with the waist of the ODT laser  $w_{odt}$  before the microscope objective ( $w_0 = \frac{\lambda \cdot f}{\pi w_{odt}}$ ), and the focal length of the objective  $f$ . The arising field component in  $z$ -direction has a phase shift of  $\delta \neq 0$  to the transverse components, resulting in an elliptical polarization. This phase is  $\delta = \arctan(z/z_r) + \pi/2$  for positive  $x$  positions and  $\delta = -\arctan(z/z_r) - \pi/2$  for negative, changing sign by crossing the  $y$ - $z$  plane ( $\phi = \pi/2, 3\pi/2 \Leftrightarrow x = 0$ ) (Appendix D). This leads to different rotation directions for the elliptical polarization on each side of this plane. Since this elliptical polarization is composed from  $E_x$  and  $E_z$ , it can be considered as elliptical polarization of a light field propagating in  $y$ -direction with the polarization  $P_{long}(\vec{x})$ , which depends on the relative amplitude and phase of the transverse and longitudinal components of the ODT light, see Appendix D. Analogous to equation (2.18), this elliptical polarization causes a state dependent AC-Stark shift, which can be considered as an effective magnetic field in  $y$ -direction

$$B_{long}(\vec{x}) = \frac{1}{\mu_B} u \cdot P_{long}(\vec{x}) \cdot I(\vec{x}) \quad (2.20)$$

$$\vec{B}_{eff}(\vec{x}) = \vec{B} + \frac{1}{\mu_B} u \cdot \begin{pmatrix} 0 \\ P_{long}(\vec{x}) \\ P_{ODT} \end{pmatrix} \cdot I(\vec{x}) \quad (2.21)$$

with  $u$  as defined above (Fig. 2.19). The direction of the shift caused by the longitudinal polarization is proportional to  $P_{long}(\vec{x})$ . The latter is position dependent and has different

sign for different sides of the  $y$ - $z$  plane, contrary to the constant  $P_{ODT}$  for the transverse circular polarization.

### Control of the magnetic field

The evolution of the atomic states is affected by the external magnetic field (2.13). The magnetic field can originate from multiple sources with a broad variety of strengths and temporal behavior. There are sources outside the laboratories, e.g., the earth magnetic field which is ca 480 mG [65] in Munich varies only very slowly. A second contribution is from the Munich U-Bahn, located only 60 m from the trap position. The current for powering the trains results in a magnetic field, which changes its amplitude on a time scale of below 1 min. Furthermore, there are sources inside the lab, e.g., the ion getter pump of the Vacuum setup, which has a large permanent magnet leading to a static field up to 1000 mG at the position of the atom. Multiple power supplies and other electronics contribute to the magnetic field with time scales below 1 s.

To control the magnetic field at the position of the atom, three pairs of coils are centered around the vacuum glass cell (Fig. 2.12a). Each pair generates a field along one direction in space ( $x$ ,  $y$ , and  $z$ -axis). These coils and their current supply are designed to compensate the magnetic field present at the position of the atom, allowing to create any desired magnetic field strength and direction in the range of  $\pm 5000$  mG.

An active feedback loop controls the current in each coil pair to stabilize the magnetic field to the set value. For this a 3D magnetic field sensor<sup>7</sup> is placed less than 2 cm from the atom (Fig 2.12b). The feedback loop has a bandwidth up to 200 Hz and the resulting residual noise of the magnetic field at the position of the atom is below 0.5 mG(rms). [38, 48? ]. Through the precise setting of the magnetic field the evolution of the atomic state can be controlled. This enables for two ways of achieving long coherence times of the atomic state: First, employing a magnetic guiding field for a controlled oscillation between the Zeeman states allows to suppress the external field fluctuations, or second setting the magnetic field to zero with no state evolution at all.

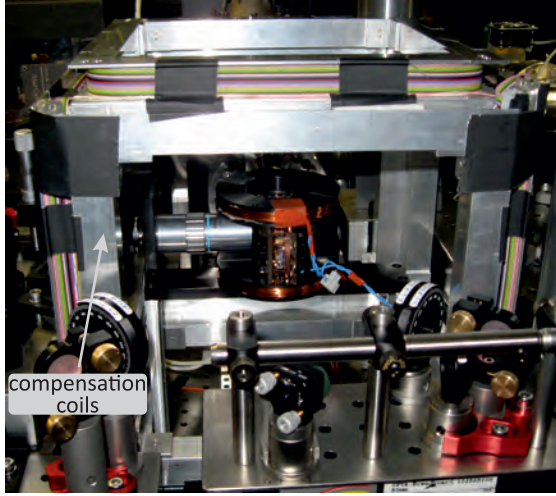
### Decoherence caused by polarization depending AC-Stark shift and motion of the atom

The circular polarization components of the ODT laser influence the atomic state evolution similarly to a magnetic field (2.21). But in contrast to the magnetic field, which is homogeneous over the trapping region  $< 1 \mu\text{m}^3$ , the effect of the ODT laser is strongly depending on the position of the atom.

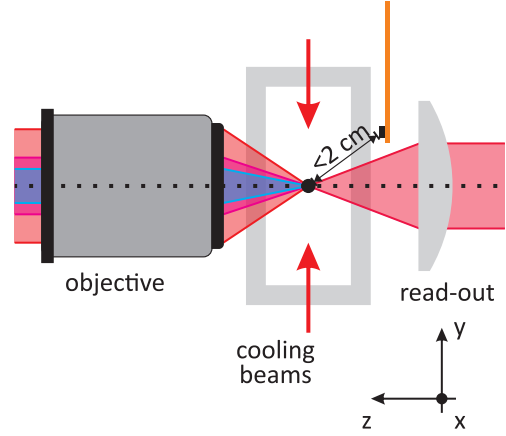
For an hypothetical case in which the atom is not moving, it is possible to compensate all effects of the ODT on the atomic state evolution perfectly. Yet in practice, the trapped atom is only cooled to a temperature of about 40  $\mu\text{K}$  and oscillates in the trap. For the trap parameters, see Section 2.2, the transverse trap oscillation periods ( $x$  and  $y$  direction) are  $T_{ODT,t} = 10.9 \mu\text{s}$  and the longitudinal is  $T_{ODT,l} = 108.9 \mu\text{s}$  [38]. The ODT potential can be approximated as an harmonic potential for low temperatures. The oscillation periods are independent of the actual energy of the atom and how it is distributed in its three degrees of freedom. The evolution of the Zeeman states however depends on the actual trajectory of the atom during the time between excitation and state measurement. This trajectory is different

---

<sup>7</sup>Honeywell, HMC1053, with a range of  $\pm 6000$  mG.



(a) The three pairs of rectangular Helmholtz coils, which are used to compensate the magnetic field, enclose the vacuum chamber with the trapped atom. (the magnetic field sensor is not on the picture)



(b) Position of the 3D magnetic field sensor (scale  $1.5\times$ ): The sensor is placed as close as possible to the atomic position outside the vacuum in such a way that it does not interfere with laser beams and fluorescence collection. This position is  $x \approx 0$  cm,  $y \approx 1$  cm, and  $z \approx 1.3$  cm.

Figure 2.12.: Setup for the control of the magnetic field: the compensation coils around the glass cell (a) and magnetic field sensor placed near the glass cell (b)

for each trial, and averaging over multiple trials of the experiment yields the average over all those trajectories. This results in decoherence of the atomic state [48].

The effect of the circular polarization of the ODT  $P_{ODT}$  can be reduced by optimizing the linear polarization. Values of  $\frac{1}{\mu_B} u \cdot P_{ODT} \cdot I(\vec{x} = 0) < 1$  mG can be achieved, resulting in a decoherence lower than the effect of the magnetic noise.

The effect of the longitudinal polarization near the focus cannot be overcome by optimizing the beam parameters; a linearly polarized strongly focused laser field will always show this behavior. Fortunately, the phase change of  $\pi$  at the  $y$ - $z$  plane also changes the sign of the state evolution. After one transverse oscillation period the state evolution on both sides of the plane cancels out, leaving the atom in the starting state. This effect is independent of the actual starting position of transverse motion of the atom in the trapping light field. This “rephasing” of the different trajectories is slightly reduced by two effects: first, the actual 3D oscillation does not allow for perfect rephasing after one period. Second, the Gaussian shaped potential of the ODT is not exactly harmonic, thus the trap frequencies for atoms with different energies are slightly different. This leads to a temperature dependence of the rephasing; the colder the atoms the better the coherence. A detailed analysis and discussion of this effect can be found in [38].

### Time resolved measurements of the atomic state evolution

To observe the temporal evolution of the atomic state, the resulting state is measured at different times after the excitation and photon detection. The entanglement between the atom and the photon allows to prepare arbitrary atomic states by a projection measurement on the photon (Appendix C).

For this measurement the atom is prepared in the state  $|\Psi_H\rangle = \frac{i}{\sqrt{2}}(|1, -1\rangle - |1, +1\rangle)$  by projecting the photon polarization on  $|H\rangle$  and  $|\Psi_V\rangle = \frac{1}{\sqrt{2}}(|1, -1\rangle + |1, +1\rangle)$  by projection on  $|V\rangle$ . These two states have favorable properties: while  $|\Psi_V\rangle$  is an eigenstate to a magnetic field in  $y$ -direction,  $|\Psi_H\rangle$  is an eigenstate to one in  $x$ -direction (2.12) [38]. The effects of a magnetic field in  $x$  or  $y$ -direction can therefore be observed individually.

While the  $m_F = 0$  Zeeman state  $|\Psi_0\rangle = |1, 0\rangle$  is not involved in the entanglement scheme (Sec. 2.3.1), it needs to be considered in the temporal evolution of the atomic states. This state is an eigenstate for a magnetic field in  $z$ -direction, but not for fields in  $x$  or  $y$ -direction. Therefore, magnetic field components in  $x$  or  $y$ -direction will lead to a population of this state. Since  $|\Psi_H\rangle$ ,  $|\Psi_V\rangle$ , and  $|\Psi_0\rangle$  are orthogonal, they form a complete basis for the spin-1 system of  $5^2S_{1/2}$ ,  $F = 1$  ground state.

Using (2.13) the evolution of these states for a given magnetic field can be calculated. For a magnetic field  $\vec{B} = \begin{pmatrix} 0 \\ 0 \\ \pm B \end{pmatrix}$ , the temporal evolution of the states is

$$\begin{aligned} |\Psi_H(t)\rangle &= |\Psi_H(0)\rangle \cos(\omega_L t) \pm |\Psi_V(0)\rangle \sin(\omega_L t) \\ |\Psi_V(t)\rangle &= |\Psi_V(0)\rangle \cos(\omega_L t) \mp |\Psi_H(0)\rangle \sin(\omega_L t). \end{aligned} \quad (2.22)$$

Likewise, for a magnetic field  $\vec{B} = \begin{pmatrix} \pm B \\ 0 \\ 0 \end{pmatrix}$ , the temporal evolution is

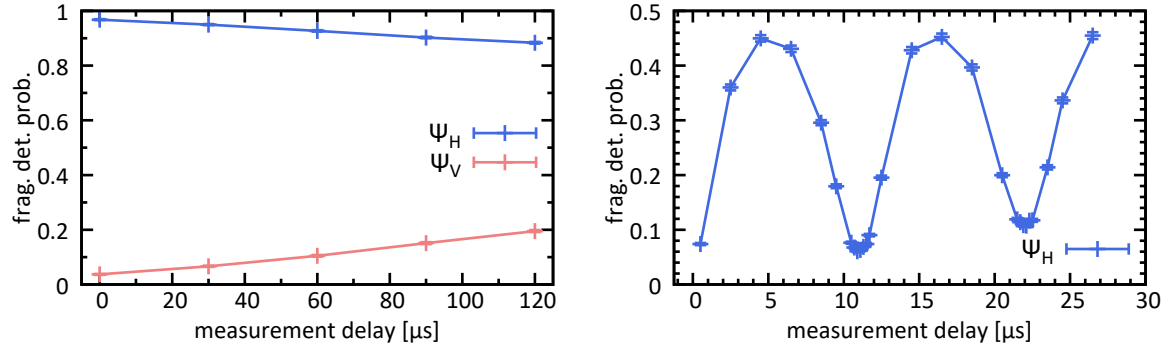
$$\begin{aligned} |\Psi_H(t)\rangle &= |\Psi_H(0)\rangle \\ |\Psi_V(t)\rangle &= |\Psi_V(0)\rangle \cos(\omega_L t) \pm i|\Psi_0\rangle \sin(\omega_L t). \end{aligned} \quad (2.23)$$

For a magnetic field  $\vec{B} = \begin{pmatrix} 0 \\ \pm B \\ 0 \end{pmatrix}$ , the temporal evolution is

$$\begin{aligned} |\Psi_H(t)\rangle &= |\Psi_H(0)\rangle \cos(\omega_L t) \mp |\Psi_0\rangle \sin(\omega_L t) \\ |\Psi_V(t)\rangle &= |\Psi_V(0)\rangle. \end{aligned} \quad (2.24)$$

By setting the overall magnetic field, including the residual effect of  $P_{ODT}$ , to zero, temporal evolution can only be caused by magnetic noise and the effect of the longitudinal polarization of the ODT near the focus. Since the longitudinal polarization  $P_{long}(x)$  (2.20) causes an effective magnetic field in  $y$ -direction, its effect is only visible in the time evolution of  $|\Psi_H\rangle$  (2.24). The latter statement holds only if the other field components are small.

To perform a projection measurement on the prepared states, the polarization of the read-out pulse is set to  $\chi_{ro} = V$  (2.7) with the dark state  $|D\rangle_V = \frac{i}{\sqrt{2}}(|1, +1\rangle - |1, -1\rangle) = |\Psi_V\rangle$  (2.9) and the bright state  $|B\rangle_V = \frac{1}{\sqrt{2}}(|1, +1\rangle + |1, -1\rangle) = |\Psi_H\rangle$  (2.8). The measurement (Fig. 2.13a) shows slow decoherence of the prepared  $|\Psi_V\rangle$  state: for a measurement with a delay of 120  $\mu\text{s}$  after the excitation the probability to find an atom in  $|\Psi_V\rangle$  is  $> 0.8$ . for a delay between 5  $\mu\text{s}$  and 15  $\mu\text{s}$  the probability is only 0.02 lower than for no delay. The decoherence of  $|\Psi_H\rangle$  appears to be even slower. However, since  $|\Psi_0\rangle$  is also a bright state independent of the polarization of the read-out pulse (Sec. 2.3.2), the projection on the bright state is insensitive



(a) Read-out polarization  $\chi_{ro} = V$ : atoms prepared in  $|\Psi(0)\rangle = |\Psi_V\rangle = \frac{1}{\sqrt{2}}(|1, +1\rangle + |1, -1\rangle)$  (red) show slow decoherence. The decoherence of atoms prepared in the  $|\Psi(0)\rangle = |\Psi_H\rangle = \frac{i}{\sqrt{2}}(|1, +1\rangle - |1, -1\rangle)$  state (blue) appears to be even slower, but this is only a feature of the read-out scheme; it does not distinguish between  $|B\rangle$  and  $|\Psi_0\rangle$ . Therefore, the time evolution of  $|\Psi_H\rangle$  can only be measured directly with  $\chi_{ro} = H$ .

(b) Read-out polarization  $\chi_{ro} = H$ : evolution of atoms from the prepared state  $|\Psi(0)\rangle = |\Psi_H\rangle = \frac{i}{\sqrt{2}}(|1, +1\rangle - |1, -1\rangle)$  (blue) to  $|\Psi_0\rangle$  is visible. The evolution is due to longitudinal polarization near the focus of the ODT (2.20). Rephasing occurs after one transverse oscillation of the atom in the trap (10.9 μs). Note the first measurement point at 0.5 μs is already influenced by the effect of the longitudinal polarization.

Figure 2.13.: Measurement of the time evolution of atoms prepared in the states  $|\Psi(0)\rangle = |\Psi_V\rangle$  and  $|\Psi(0)\rangle = |\Psi_H\rangle$ . The ionization fragment detection probability on the  $y$ -axis shows the probability to ionize the atom.

to the evolution into  $|\Psi_0\rangle$ . To measure the evolution of  $|\Psi_H\rangle$ , a second measurement has to be performed with a read-out polarization set to  $\chi_{ro} = H$  with  $|D\rangle_H = |\Psi_H\rangle$  (Fig. 2.13b).

The measurement with  $\chi_{ro} = H$  reveals a different behavior of the  $|\Psi_H\rangle$  state: the state decoheres quickly due to the longitudinal components of the ODT light introducing an effective magnetic field in  $y$ -direction. But as predicted, it is found to rephase, after one transverse oscillation period of 10.9 μs. This point in time is called a rephasing point. Through tuning of the power of the ODT laser the depth of the trapping potential can be changed. This allows to change the trap frequencies and thus, the rephasing point to a desired point in time.

These measurements show that the atomic qubit can be read-out with a very high fidelity, more than 10 μs after its preparation. Yet, one has to consider the rephasing and pick a fitting rephasing point before the experiment.

## 2.4. Creation of long Distance Atom-Atom Entanglement

Once a high level of control of the trapped atoms and a high fidelity state read-out is obtained the experiment is ready for the next step: creation of entanglement between two single atoms trapped in independent setups separated by 398 m. Here, the two atoms are entangled via the entanglement swapping process [31, 66]. This enables the transfer of entanglement of two atom-photon pairs to the atoms by performing a joint measurement on the photons [32, 33]. In order to achieve a high fidelity of the photon measurement the photons emitted by independent atoms need to fulfill specific requirements. Especially their temporal shape is of great importance. To fulfill these requirements, synchronization of the processes in both trap setups is necessary.

### 2.4.1. Heralded entanglement via entanglement swapping

For the entanglement swapping, two entangled pairs need to be considered. Here, each pair consists of an atom and a photon. The entangled atom-photon pairs initially are in the states

$$|\Psi_1\rangle = \frac{1}{\sqrt{2}} \left( |\uparrow\rangle_{A,1} |\downarrow\rangle_{P,1} + |\downarrow\rangle_{A,1} |\uparrow\rangle_{P,1} \right)$$

and

$$|\Psi_2\rangle = \frac{1}{\sqrt{2}} \left( |\uparrow\rangle_{A,2} |\downarrow\rangle_{P,2} + |\downarrow\rangle_{A,2} |\uparrow\rangle_{P,2} \right),$$

with the subscripts indicating the particle  $A$  and  $P$  for atom or photon, 1 or 2 for the pair, and the atomic states  $|\downarrow\rangle_A, |\uparrow\rangle_A$  and the photonic states  $|\downarrow\rangle_P, |\uparrow\rangle_P$ . The states are pairs of orthogonal qubit states (Appendix B). The four particle state can be written as

$$\begin{aligned} |\Psi_{all}\rangle &= |\Psi_1\rangle \otimes |\Psi_2\rangle & (2.25) \\ &= \frac{1}{\sqrt{2}} \left( |\uparrow\rangle_{A,1} |\downarrow\rangle_{P,1} + |\downarrow\rangle_{A,1} |\uparrow\rangle_{P,1} \right) \otimes \frac{1}{\sqrt{2}} \left( |\uparrow\rangle_{A,2} |\downarrow\rangle_{P,2} + |\downarrow\rangle_{A,2} |\uparrow\rangle_{P,2} \right) \\ &= \frac{1}{2} \left( |\uparrow\rangle_{A,1} |\downarrow\rangle_{P,1} |\uparrow\rangle_{A,2} |\downarrow\rangle_{P,2} + |\uparrow\rangle_{A,1} |\downarrow\rangle_{P,1} |\downarrow\rangle_{A,2} |\uparrow\rangle_{P,2} \right) \\ &\quad + \frac{1}{2} \left( |\downarrow\rangle_{A,1} |\uparrow\rangle_{P,1} |\uparrow\rangle_{A,2} |\downarrow\rangle_{P,2} + |\downarrow\rangle_{A,1} |\uparrow\rangle_{P,1} |\downarrow\rangle_{A,2} |\uparrow\rangle_{P,2} \right). \end{aligned}$$

A projection  $\langle \Psi_{Bell,P} | \Psi_{all} \rangle$  of the two photons on one of the four entangled Bell-states

$$\begin{aligned} |\Psi_{Bell}\rangle &\in \{ |\Psi^-\rangle, |\Psi^+\rangle, |\Phi^-\rangle, |\Phi^+\rangle \} \\ |\Psi^\pm\rangle &= \frac{1}{\sqrt{2}} \left( |\uparrow\rangle |\downarrow\rangle \pm |\downarrow\rangle |\uparrow\rangle \right) \\ |\Phi^\pm\rangle &= \frac{1}{\sqrt{2}} \left( |\uparrow\rangle |\uparrow\rangle \pm |\downarrow\rangle |\downarrow\rangle \right) \end{aligned}$$

results in an entangled atom-atom states of the same type. Thus a measurement of the photonic Bell state will transfer the entanglement to the atoms. The outcome of this measurement will herald which entangled atom-atom state is prepared.

#### Photonic Bell-state measurement via two photon interference

A Bell-state measurement on two photons can be implemented by employing two-photon interference on a beam splitter [66, 67]. The interference behavior of single photons at a beam splitter is described by the Hong-Ou-Mandel effect [68]: two indistinguishable photons, meaning that they overlap in every degree of freedom, entering a beam splitter in different input ports, will only be detected bunched together in one output port of the beam splitter and never one photon in each output. It is important to state that, in this experiment the photonic qubits are encoded in the polarization degree of freedom, which has to be considered in the calculation of the two photon interference.

A beam splitter with two input and two output ports (Fig. 2.14) can be described via four pairs of creation  $\hat{a}_1^\dagger$  and  $\hat{a}_2^\dagger$  for the inputs and  $\hat{b}_1^\dagger$  and  $\hat{b}_2^\dagger$  for the outputs. In general, these operators are different for photons with different properties. The operators commute

for photons in orthogonal states  $[a_\alpha^\dagger, a_\beta^\dagger] = 0$ , with  $\alpha$  and  $\beta$  being orthogonal states. For orthogonal polarizations, the creation operators are independent. For a polarization  $P$  the relation between the input and the output is given by

$$\begin{pmatrix} \hat{b}_{1,P}^\dagger \\ \hat{b}_{2,P}^\dagger \end{pmatrix} = \hat{B}_P \begin{pmatrix} \hat{a}_{1,P}^\dagger \\ \hat{a}_{2,P}^\dagger \end{pmatrix} \quad \Leftrightarrow \quad \begin{pmatrix} \hat{a}_{1,P}^\dagger \\ \hat{a}_{2,P}^\dagger \end{pmatrix} = \hat{B}_P^{-1} \begin{pmatrix} \hat{b}_{1,P}^\dagger \\ \hat{b}_{2,P}^\dagger \end{pmatrix} \quad (2.26)$$

with the matrix of the beam splitter

$$\hat{B}_P = \begin{pmatrix} \cos(\Theta_P) & \sin(\Theta_P) e^{i\delta_P} \\ -\sin(\Theta_P) e^{-i\delta_P} & \cos(\Theta_P) \end{pmatrix} \quad (2.27)$$

where  $\Theta_P$  is the angle representing the splitting ratio and  $\delta_P$  is the phase difference between transmitted and reflected part [32, 69]. When using the  $H$  and  $V$  polarization basis  $P \in \{H, V\}$ , two independent sets of creation operators are obtained.

The two photons emitted by independent single atoms, while being entangled with the emitting atom, are in a completely mixed polarization state. Since the four Bell-states form a complete orthonormal basis for this two photon space, it is possible to describe the two photon interference for any two photon polarization state by looking at the interference of the four Bell-states. Furthermore, the incidence of photons on the beam splitter can be written as a Fock state. For the four polarization Bell-states these Fock states are

$$|\Phi^\pm\rangle_{in} = \frac{1}{\sqrt{2}} (\hat{a}_{1,H}^\dagger \hat{a}_{2,H}^\dagger \pm \hat{a}_{1,V}^\dagger \hat{a}_{2,V}^\dagger) |0, 0\rangle_{in}$$

and

$$|\Psi^\pm\rangle_{in} = \frac{1}{\sqrt{2}} (\hat{a}_{1,H}^\dagger \hat{a}_{2,V}^\dagger \pm \hat{a}_{1,V}^\dagger \hat{a}_{2,H}^\dagger) |0, 0\rangle_{in}$$

with  $|0, 0\rangle_{in}$  being the zero photon (vacuum) state of the two input ports. Considering the case of a perfect, polarization independent 50/50 beam splitter ( $\Theta_H = \Theta_V = \frac{\pi}{4}$  and  $\delta_H = \delta_V = 0$ ) and two indistinguishable photons the corresponding output states are

$$|\Phi^\pm\rangle \rightarrow \frac{1}{\sqrt{2}} (\hat{b}_{1,H}^\dagger \hat{b}_{1,H}^\dagger \pm \hat{b}_{1,V}^\dagger \hat{b}_{1,V}^\dagger - \hat{b}_{2,H}^\dagger \hat{b}_{2,H}^\dagger \mp \hat{b}_{2,V}^\dagger \hat{b}_{2,V}^\dagger) |0, 0\rangle_{out}, \quad (2.28)$$

$$|\Psi^+\rangle \rightarrow \frac{1}{\sqrt{2}} (\hat{b}_{1,H}^\dagger \hat{b}_{1,V}^\dagger - \hat{b}_{2,H}^\dagger \hat{b}_{2,V}^\dagger) |0, 0\rangle_{out}, \quad (2.29)$$

$$|\Psi^-\rangle \rightarrow \frac{1}{\sqrt{2}} (\hat{b}_{1,H}^\dagger \hat{b}_{2,V}^\dagger - \hat{b}_{2,H}^\dagger \hat{b}_{1,V}^\dagger) |0, 0\rangle_{out}. \quad (2.30)$$

A detailed derivation also considering different beam splitter properties and imperfections can be found in the Appendix E and in [32].

The different output states for the Bell-states (2.28, 2.29, and 2.30) allow to deduce the input states from a measurement of the photons in the output ports of the beam splitter. For this measurement a polarizing beam splitter (PBS), separating  $H$  and  $V$  polarization, is placed at each output port of the beam splitter and single photon detectors are placed at each output port of the two PBSs (Fig. 2.14). The possible two photon detection events can be put into four different categories:

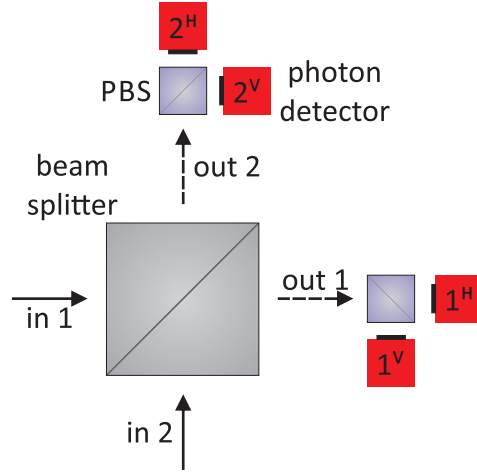


Figure 2.14.: Photonic Bell-state measurement scheme: Two photons are overlapped on a beam splitter (gray). Behind each output port of the beam splitter a polarizing beam splitter (PBS) (purple) guides  $H$  and  $V$  photons to different single photon detectors (red). The number and superscript of the detector labeling indicate the output port of the beam splitter and the polarization output of the PBS.

category 1: one photon detected in each output port of the beam splitter with detectors for different polarization. A detection in the  $1^H$  and  $2^V$  photon detectors or in the  $1^V$  and  $2^H$  photon detectors (Fig. 2.14) projects the two photon state on  $|\Psi^-\rangle$  (2.30).

category 2: both photons are detected in one output port of the beam splitter with detectors for different polarization. A detection in  $1^H$  and  $1^V$  or in  $2^V$  and  $2^H$  result projects the two photon state on  $|\Psi^+\rangle$  (2.29).

category 3: both photons are detected with the the same detector. This results corresponds to both  $|\Phi^\pm\rangle$  photon states (2.28) but a distinction between them is not possible. Since the employed detectors are not photon number resolving, this outcome is not registered in the experiments presented here.

category 4: one photon detected in each output port of the beam splitter and with detectors for the same polarization. Detection on  $1^H$  and  $2^H$  or on  $1^V$  and  $2^V$ . This result does not correspond to any of the input Bell states and does only occur due to experimental imperfections.

Thereby, it is possible to detect two out of the four Bell states and by this to prepare two entangled atom-atom states. The photonic measurement result will herald which atom-atom state is prepared.

The prepared atom-atom states depends on the chosen photon polarization basis, here  $H$

and  $V$ . In this basis the entangled atom-photon state (2.5) can be written as (C.2)

$$|\Psi\rangle_{AP} = \frac{1}{\sqrt{2}} (|H\rangle |\downarrow\rangle_x + |V\rangle |\uparrow\rangle_x)$$

and the four particle state (2.25) has the form

$$|\Psi\rangle_{All} = \frac{1}{\sqrt{2}} (|H\rangle |\downarrow\rangle_x + |V\rangle |\uparrow\rangle_x) \otimes \frac{1}{\sqrt{2}} (|H\rangle |\downarrow\rangle_x + |V\rangle |\uparrow\rangle_x).$$

A measurement result from category 1 projects the photons on

$$|\Psi^-\rangle_{PP} = \frac{1}{\sqrt{2}} (|H\rangle |V\rangle - |V\rangle |H\rangle)$$

preparing and heralding the atomic state

$$|\Psi^-\rangle_{AA} = \frac{1}{\sqrt{2}} (|\downarrow\rangle_x |\uparrow\rangle_x - |\uparrow\rangle_x |\downarrow\rangle_x). \quad (2.31)$$

A measurement result from category 2 projects the photons on

$$|\Psi^+\rangle_{PP} = \frac{1}{\sqrt{2}} (|H\rangle |V\rangle + |V\rangle |H\rangle)$$

preparing and heralding the atomic state

$$|\Psi^+\rangle_{AA} = \frac{1}{\sqrt{2}} (|\downarrow\rangle_x |\uparrow\rangle_x + |\uparrow\rangle_x |\downarrow\rangle_x). \quad (2.32)$$

### Experimental setup for a fiber based Bell state measurement

For a Bell-state measurement setup employing such a scheme one has to consider two important points. First, the beam splitter should be as close to a polarization-independent  $50/50$  beam splitter as possible. A imperfect beam splitter, e.g, partially polarizing beam splitter or a not  $50/50$  beam splitter will lead to errors in the measurement of the Bell state measurement. Depending on the type of imperfections they will allow for two photons in the  $|\Psi^+\rangle_{in}$  state also to be detected in different output port of the beam splitter (category 1) and for photons in the  $|\Psi^-\rangle_{in}$  state to be detected in the same output port (category 2) (App. E) [32]. The mixing of these states reduces the photonic Bell state fidelity and by this the fidelity of the prepared entangled atom-atom state. Second, the photons need to be indistinguishable in every degree of freedom including spectral, temporal, and spatial properties. Spectral and temporal properties are defined by the excitation and emission process (Sec. 2.3.1). However, the spatial degree of freedom needs to be considered in the Bell state measurement setup.

A perfect overlap of the spatial modes of the two photons can be ensured by using a beam splitter based on single-mode optical fibers (Fig. 2.15). The used fiber beam splitter has only a very small polarization dependence and the splitting ratio is very close to  $50/50$  [67]. Furthermore, this beam splitter allows to set the phase difference for both polarizations to zero  $\delta_H = \delta_V = 0$  (2.27), by properly compensating for the birefringence inside the optical glass fibers. The polarization analysis behind the fiber beam splitter is performed with free space optics. The light from the beam splitter is coupled out of the glass fibers, collimated and guided directly on two polarizing beam splitter cubes, these send each polarization component on a single photon counting module<sup>8</sup> (SCPM) for detection (Fig. 2.15).

<sup>8</sup>Laser Components Count-10C, with detection efficiency 0.45 to 0.65 and dark counts  $< 10^1/s$

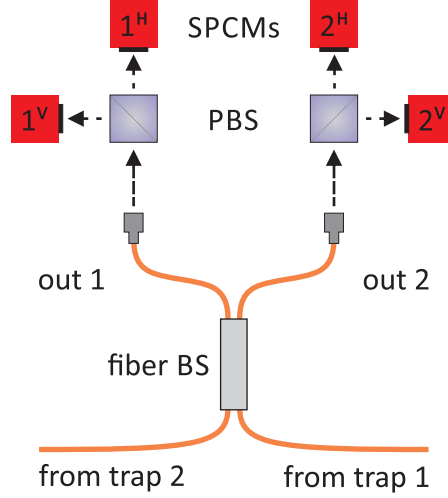


Figure 2.15.: Bell state measurement setup with a fiber beam splitter. The fiber beam splitter (gray and orange) allows for perfect spatial overlap. The subsequent polarization analysis is done free space with polarizing beam splitters (PBS, purple) and single photon detectors (SPCMs, red) yielding a high fidelity of the polarization measurement.

## 2.4.2. Operation of the two-trap setup

To create entanglement between two atoms in independent and separated traps, the fibers guiding the fluorescence photons (Fig. 2.4) are connected to the BSM setup located in lab 1 (Fig. 2.16). For trap 1, this is done with a 5 m long fiber, while trap 2 is connected via a 700 m fiber. The polarization encoding of the photon state makes compensation of the birefringence in the fibers necessary. The birefringence in the shorter fiber to trap 1 and in the fiber beam splitter, which are both inside Lab 1, drifts only very slowly and manual compensated every couple of days is sufficient. Yet, the drifts in the 700 m fiber are on a time scale below one hour and a automatized compensation of the polarization is employed [70].

Furthermore, the excitation process needs to be synchronized in a way that the emitted photons overlap temporally inside the BSM setup. This means, that while both trap setups are able to work completely independently from each other, still the systems need to communicate and to be very precisely synchronized.

## Communication between the laboratories

For communication and synchronization both labs are connected with a fiber channel (Fig. 2.1), which contains not only the glass fiber for the fluorescence photons from lab 2, but also additional fibers for fast and reliable communication<sup>9</sup>. The different signals, which need to be

<sup>9</sup>The fiber channel (Leoni AT-VQ(ZN)H(ZN)B2Y 4SM780+4G50+12E9 2,5) contains in total 20 fibers. 4 × SM780 single mode fiber (attenuation < 4 dB/km at 780 nm), 12 × E9/125 single mode fiber (attenuation between 0.154 dB/km and 0.236 dB/km at 1550 nm), and 4 × G50/125 multi mode fiber (attenuation < 0.6 dB/km at 1350 nm)



transmitted, have different requirements so the communication system between the laboratories consists of different subsystems:

- fiber based Ethernet connection between the two computers controlling the atom traps making the communication independent of the university network.
- 4 analog communication channels for the transmission of time critical signals.
- 6 asynchronous digital communication channels for time critical signals.
- 16 synchronous digital communication channels for not time critical signals.

### Control and synchronization

Figure 2.16 shows an overview of the two-trap setup. Each trap is operated via a local computer that sets most experimental parameters and controls the atom loading procedure. In the two trap experiment the computer in lab 1 serves as master that controls the experiment. It sends commands via the fiber based Ethernet connection to the computer in lab 2 serving as slave. The master monitors the trapping procedure and when two atoms are trapped it sends a command to the slave that triggers a synchronized start control unit. Upon receiving the start signal the control units take over. They execute the experimental sequence until one of the atoms is lost and the loading procedure starts again.

The timing critical parts as the control units, start control, the FPGA monitoring the photon detectors for a heralding signals, and a time to digital converter unit need to be synchronized to a common clock. For this the signal from a 100 MHz clock, located in lab 2, is distributed to all synchronized components. The signal is sent via an analog optical communication channel to lab 1 and in each lab the clock signal is distributed with a clock distribution board <sup>10</sup>. This allows for an overall synchronization of the control units with a jitter below 150 ps rms [38].

### Experimental scheme

Creation and verification of the atom-atom entanglement is divided in three steps. The first step is trapping a single atom in each of the setups. After this both trapped atoms are excited and each emits a photon entangled with the emitting atom. These photons are collected and guided to the Bell-state measurement setup, where the measurement on both photons swaps the entanglement onto the atoms. The measurement outcome heralds the entanglement and a signal is sent back to the trap setup triggering the last step, the measurement of the atomic states (Sec. 2.3.2).

**Trapping two atoms** The trapping procedure for one trap is described in section 2.2. Specific to the procedure of loading of two traps is that the fluorescence photons from both traps are guided to the same photon detectors in the BSM setup. To distinguish between atoms in the different traps the master computer switches the cooling light of the traps in turns, while monitoring the fluorescence counts on the detectors. When an atom is trapped in each trap the computer sends the command to start the excitation process.

---

<sup>10</sup>Analog Devices, AD9523-1 Evaluation Board

**Synchronized excitation process** As mentioned in section 2.4.1 it is crucial for the two photon interference employed in the BSM that photons originating from the two traps are indistinguishable in every degree of freedom. To fulfill this requirement the excitation pulses in both traps need to have the same temporal shape and intensity (Sec. 2.3.1). Additionally, they need to be timed such that the temporal shapes of the emitted photons overlap at the fiber beam splitter. For the precise timing of the pulses a synchronized start of the excitation process in both traps is necessary. The slave computer triggers the start control in lab 2 that sends synchronized signals to both control units starting the excitation process (Fig. 2.16). The start signal for lab 1 is transmitted via an asynchronous digital communication channel to preserve the precise timing on a timescale  $\ll 1$  ns.

After receiving the start signal, the control units switch to the excitation mode, in which atoms are excited and an FPGA monitors the SPCMs for two photon coincidences in a 208 ns acceptance time window (Fig. 2.17). Once a two photon coincidence heralds entanglement, the FPGA sends a signal to the control units to switch to the measurement mode. Due to the very low combined photon collection and detection probabilities of  $\eta_1 \approx 1.7\%$  for trap 1 and  $\eta_2 \approx 0.85\%$ <sup>11</sup> for trap 2, the probability for a two photon coincidence heralding atom-atom entanglement is only  $Pr_{AA} = \frac{1}{2}\eta_1\eta_2 \approx 7 \cdot 10^{-7}$  [38]. Such a low success probability makes a high repetition rate necessary. For this one has to consider the time needed from the beginning of the excitation scheme, including state preparation, to the time a potential heralding signal would have arrived. Only after waiting for this time the next excitation attempt can take place. Otherwise, one would destroy the prepared atom-atom state before it can be used. This time is the sum of the time needed for state preparation and excitation, the time for photon transmission to the BSM, and the time needed for sending the heralding signal (including photon detection and state analysis in the FPGA). Due to the asymmetric location of the BSM in lab 1 next to trap 1 this time is much larger for trap 2 than for trap 1. Altogether, this time is 10.36  $\mu$ s. Combining 40 repetitions of pumping an excitation followed by 350  $\mu$ s of cooling (Sec. 2.3.1) an excitation repetition rate of  $52.2 \cdot 10^3 \frac{1}{s}$  is achieved [38].

**Event ready state read-out** The two-photon coincidence signal from the BSM heralds the presence of an entangled state and “readiness” of the system. Only upon receiving the heralding signal the control units switch to the measurement mode. This is called an “event ready” state read-out. Due to the effects of the tightly focused ODT an atomic state measurement with high fidelity is only possible after one transversal oscillation period of the atom in the trap (Sec.: 2.3.3) starting with the photon emission. To overcome this an additional waiting time determined by the intensity of the ODT laser is introduced in the measurement mode, before the actual state read-out is performed (Sec. 2.3.2).

---

<sup>11</sup>including the loss in the 700 m fiber with an attenuation of 4 dB/km

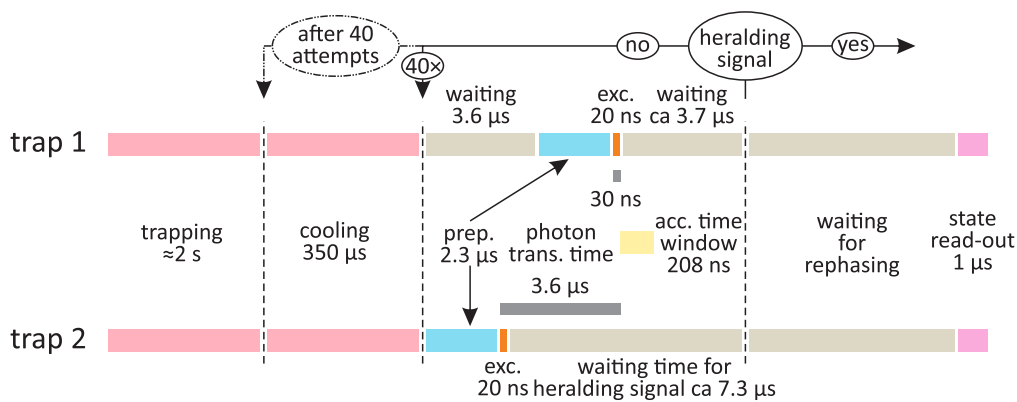


Figure 2.17.: Timing scheme for creation of atom-atom entanglement: After trapping of an atom in each trap (red) the synchronized excitation process starts. Preparation (blue) and excitation (orange) processes in both traps are timed taking into account the photon transmission times in the optical fibers (gray) such that the two photons overlap in time at the fiber beam splitter and then are detected within the acceptance time window (yellow). In the case of a two photon coincidence detection heralding entanglement the atomic state read-out process (magenta) is triggered, otherwise the preparation and excitation process is repeated. After 40 unsuccessful attempts the repetition is interrupted with an additional cooling period (red) for both atoms to assure a low atom temperature before the scheme continues until a valid coincidence detection or one of the atoms is lost.

## 3. Bell's theorem: Testing Local-Realism

Bell's theorem allows to test local-realism: while all theories which strictly obey local-realism predict results complying with Bell's inequality, quantum mechanics predicts a violation of the inequality for certain measurements on an entangled pair of two qubits. Thereby, the theorem allows, by means of experiment, to decide the dispute whether quantum mechanics is a complete description of nature or whether it might to be extended to a local-realistic theory. This chapter starts with introducing this dispute and a possible extension to quantum mechanics, the so called local-hidden variables. Then, Bell's theorem is derived in the experimenter-friendly CHSH formulation of the inequality, the scenario for an experiment is set and a bound for local-realism is found. The last part focuses on experiments testing the theorem. First, possible shortcomings in experiments, which result in loopholes for local-realist description, are pointed out. Then the requirements to close such loopholes are defined. Finally the historical development of Bell test experiments is summarized.

### 3.1. Local-Realism and Quantum Mechanics

In their famous paper “Can Quantum-Mechanical Description of Physical Reality Be Considered Complete?” [1] published in 1935, Albert Einstein, Boris Podolsky, and Nathan Rosen (EPR) challenged the completeness of quantum mechanics. For a theory to be complete they demand that “every element of the physical reality must have a counterpart in the physical theory.” They defined an element of physical reality by the possibility of certainly predicting (with probability of unity) the value of its corresponding physical quantity “without in any way disturbing the system.” Further, they pointed out that in the case of not commuting measurement operators quantum mechanics does not comply to this demand. Using the example of momentum and position they conclude “when the momentum of a particle is known, its coordinate has no physical reality”. To expand this they considered a two particle system in which two particles interact with each other at a time  $t_1$  but have no interaction later on. After  $t = t_1$  particles are described by the common wave function  $\Psi_{12}(x_1, x_2) = \sum_{n=1}^{\infty} \psi_n(x_2) u_n(x_1)$  with  $x_1, x_2$  describing the two particles (and not a variable in space). In this case of non-commuting measurements the properties of both particles cannot be real at the same time. Moreover, the physical quantities of one particle depend on measurements performed on the other even though they are separated in space and the interaction between the particles has ended before. From the lack of reality for physical quantities in certain cases and from the dependence of one particle's properties on the measurement result of a separated other one, EPR concluded that the quantum mechanical wave function “does not provide a complete description of the physical reality”. They emphasize the possibility of an extension to quantum mechanics which includes parts of physical reality, yet do not offer a concrete proposal.

Opposing the claim of incompleteness, Nils Bohr pointed out in a reply that their definition of reality demanded a prediction “without in any way disturbing the system.” He argued that for phenomena described by quantum mechanics such a not disturbing measurement

of physical quantities is in principle not possible, due to a necessary interaction between measured particle and measurement apparatus. He concluded, “it is only the mutual exclusion of experimental procedures, permitting the unambiguous definition of complimentary physical quantities, which provides room for new physical laws, the coexistence of which at first sight appear irreconcilable with the basic principles of science” [6]. As a response, Albert Einstein specified the incompleteness argument by stating that quantum mechanics is the description of the statistical properties of an ensemble of states, while the wave function lacks the ability to actually describe a single particle’s physical state [7]. Later on he extended the concept of realism by stating that in a complete theory the physical reality cannot be influenced by actions in a remote part of the space [8]. This connection of locality and reality lead to the demand for local-realism as a mandatory requirement for all physical theories.

This philosophical, precisely metaphysical, dispute about the interpretation of the quantum theory was brought to a more solid ground by discussing possible extensions for quantum mechanics and their implications. A possible extension of quantum mechanics is the introduction of “hidden variables” that allow to define values of a physical quantity independent of a possible measurement fulfilling EPRs demand on reality. This concept was already named and investigated by John von Neumann [71] in 1932. He claimed such hidden parameters cannot reproduce predictions of quantum mechanics. Nevertheless, in 1952 David Bohm presented a quantum theory with hidden variables [72, 73], which is now called Bohmian mechanics. He claimed the assumptions von Neumann used for his proof were too restrictive to be general, which lead to a long going discussion see, e.g., [74, 75].

This discussion was settled by John Bell by demonstrating that von Neumann’s rejection is based on a false requirement on the hidden variables [76]. Additionally, he pointed out that Bohm’s hidden variable theory fulfills EPRs reality demand [1], but not Einstein’s local-realism demand [8], which would imply a “local-hidden variable” (LHV) theory. Bell further investigated the possibility of such a theory reproducing the predictions of quantum mechanics in his famous paper “On the Einstein Podolskiy Rosen Paradox” [2] published in 1964. He showed that all possible local-hidden variable theories cannot reproduce certain predictions of quantum mechanics. His theorem is formulated as an inequality. The novelty of Bell’s approach was that it pointed towards an experiment to test all possible local-hidden variable theories, and by this Einstein’s concept of local-realism.

### 3.2. CHSH Inequality

Bell’s first formulation of his inequality is not directly applicable to experiments since it demanded pairs of perfectly correlated parameters. Therefore, in this work the reformulation of Bell’s inequality by Clauser, Horne, Shimony, and Holt [9], short CHSH, is used. CHSH consider a scenario (Fig. 3.1) in which a source emits pairs of particles that are sent to separated measurement devices. These devices have two possible settings determined by a binary input and give one of two possible results as output. For better understanding, here one measurement device is called Alice and the other Bob. The input of Alice is abbreviated as  $A$  and Bob’s  $B$ , which both can take values of 0 or 1. Analogously the measurement result of Alice is called  $X$  and of Bob  $Y$ . Both take values of  $-1$  or  $+1$ . The emission and measurement of one pair is called event and the experiment contains many events.

For the evaluation of the experiment one considers the CHSH value  $S$ . It is defined as

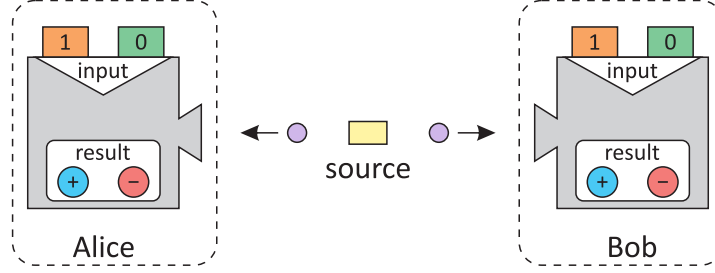


Figure 3.1.: Scenario for a CHSH experiment: A source (yellow) sends two particles (purple) to two measurement devices (gray) one called Alice the other one Bob. Each device performs a measurement on the particles depending on the input 1 (orange) or 0 (green) and give either the result “+” (blue) or “-” (red).

$$S := |E_{11} + E_{10}| + |E_{01} - E_{00}| \quad (3.1)$$

where

$$E_{a,b} := \frac{N_{a,b}^{X=Y} - N_{a,b}^{X \neq Y}}{N_{a,b}^{X=Y} + N_{a,b}^{X \neq Y}} \quad (3.2)$$

are so called correlators. Here  $N_{a,b}^{X=Y}$  and  $N_{a,b}^{X \neq Y}$  are the number of events with correlated respective anti-correlated result  $X, Y$  for the inputs  $A = a$  and  $B = b$ ,  $a, b \in \{0, 1\}$ .

To estimate the experimental outcome one considers the expectation values  $Ev \left( \frac{N_{a,b}^{X=Y}}{N_{a,b}^{X=Y} + N_{a,b}^{X \neq Y}} \right)$  and  $Ev \left( \frac{N_{a,b}^{X \neq Y}}{N_{a,b}^{X=Y} + N_{a,b}^{X \neq Y}} \right)$  in the theoretical case of infinite number of events. Without extra assumptions about the experiments one can write these expectation values also as probabilities. Thus,  $E_{ab}$  takes the form of

$$E_{ab} = Pr(X = Y | A = a, B = b) - Pr(X \neq Y | A = a, B = b) \quad (3.3)$$

with

$$Pr(X = Y | A = a, B = b)$$

being the probability for correlated measurement results of Alice and Bob for certain inputs and

$$Pr(X \neq Y | A = a, B = b)$$

the probability for anti-correlated results. They have the trivial properties

$$0 \leq Pr(X = Y | A = a, B = b) \leq 1$$

and

$$Pr(X = Y|A = a, B = b) + Pr(X \neq Y|A = a, B = b) = 1.$$

So the correlators are bounded by  $-1 \leq E_{a,b} \leq 1$  and it follows an algebraic bound of  $S \leq 4$  for 3.1.

### 3.2.1. Bound for LHV theories

To find the expectations for a possible local-realistic theory, local-hidden variables are considered with the following assumptions:

**Local measurements:** the measurement process of Alice on her particle has no influence on Bob's measurement process and vice versa.

**Independent measurements:** Alice's measurement result is independent of Bob's input and vice versa.

**Independent inputs:** the input for Alice and the input for Bob are chosen independently of each other, of the particle pair and of the local-hidden variables describing the experiment.

**Unpredictable inputs:** The input choices are random and thus the local-hidden variables and the experimental setup are independent of the input choices.

With these assumptions the probability to measure the outcomes  $X = x$  and  $Y = y$  for the inputs  $A = a$  and  $B = b$  is

$$Pr(X = x, Y = y|A = a, B = b) = \int_{\Gamma} Pr(X = x|A = a, \lambda) Pr(Y = y|B = b, \lambda) \rho(\lambda) d\lambda. \quad (3.4)$$

Here  $\lambda$  stands for a certain realization of the local-hidden variables,  $\Gamma$  is the space of all possible realizations of the LHVs, and  $\rho(\lambda)$  is their normalized probability distribution. Inserting this in (3.3) leads to

$$\begin{aligned} E_{a,b} &= \int_{\Gamma} Pr(X = 1|A = a, \lambda) Pr(Y = 1|B = b, \lambda) \rho(\lambda) d\lambda \\ &\quad - \int_{\Gamma} Pr(X = 1|A = a, \lambda) Pr(Y = 0|B = b, \lambda) \rho(\lambda) d\lambda \\ &\quad - \int_{\Gamma} Pr(X = 0|A = a, \lambda) Pr(Y = 1|B = b, \lambda) \rho(\lambda) d\lambda \\ &\quad + \int_{\Gamma} Pr(X = 0|A = a, \lambda) Pr(Y = 0|B = b, \lambda) \rho(\lambda) d\lambda \\ &= \int_{\Gamma} (2 \cdot Pr(X = 1|A = a, \lambda) - 1) Pr(Y = 1|B = b, \lambda) d\lambda \\ &\quad + \int_{\Gamma} (2 \cdot Pr(X = 1|A = a, \lambda) - 1) Pr(Y = 0|B = b, \lambda) d\lambda \\ &= \int_{\Gamma} (2 \cdot Pr(X = 1|A = a, \lambda) - 1) (2 \cdot Pr(Y = 1|B = b, \lambda)) \end{aligned}$$

For the CHSH value  $S$  (3.1) follows

$$\begin{aligned}
S &= |E_{11} + E_{10}| + |E_{01} - E_{00}| \\
&= \left| \int_{\Gamma} \left[ [2 \cdot Pr(X = 1|A = 1, \lambda) - 1] [2 \cdot Pr(Y = 1|B = 1, \lambda) - 1] \right. \right. \\
&\quad \left. \left. + [2 \cdot Pr(X = 1|A = 1, \lambda) - 1] [2 \cdot Pr(Y = 1|B = 0, \lambda) - 1] \right] \rho(\lambda) d\lambda \right| \\
&+ \left| \int_{\Gamma} \left[ [2 \cdot Pr(X = 1|A = 0, \lambda) - 1] [2 \cdot Pr(Y = 1|B = 1, \lambda) - 1] \right. \right. \\
&\quad \left. \left. - [2 \cdot Pr(X = 1|A = 0, \lambda) - 1] [2 \cdot Pr(Y = 1|B = 0, \lambda) - 1] \right] \rho(\lambda) d\lambda \right| \\
&= \left| \int_{\Gamma} [2 \cdot Pr(X = 1|A = 1, \lambda) - 1] \right. \\
&\quad \left. \cdot 2 [Pr(Y = 1|B = 1, \lambda) + Pr(Y = 1|B = 0, \lambda) - 1] \rho(\lambda) d\lambda \right| \\
&+ \left| \int_{\Gamma} [2 \cdot Pr(X = 1, A = 0, \lambda) - 1] \right. \\
&\quad \left. \cdot 2 [Pr(Y = 1, B = 1, \lambda) - Pr(Y = 1, B = 0, \lambda)] \rho(\lambda) d\lambda \right|
\end{aligned}$$

allowing for an estimation of the upper bound of

$$\begin{aligned}
S &\leq \int_{\Gamma} \left[ |[2 \cdot Pr(X = 1|A = 1, \lambda) - 1] \cdot 2 [Pr(Y = 1|B = 1, \lambda) + Pr(Y = 1|B = 0, \lambda) - 1]| \right. \\
&\quad \left. + |[2 \cdot Pr(X = 1, A = 0, \lambda) - 1] \cdot 2 [Pr(Y = 1, B = 1, \lambda) - Pr(Y = 1, B = 0, \lambda)]| \right] \rho(\lambda) d\lambda \\
&= \int_{\Gamma} I(\lambda) \rho(\lambda) d\lambda.
\end{aligned}$$

The integrand  $I(\lambda)$  can be limited from above using Lemma 1 (G.1) from Appendix G

$$\begin{aligned}
I(\lambda) &\leq 2 \left[ |[Pr(Y = 1, B = 1, \lambda) + Pr(Y = 1, B = 0, \lambda) - 1]| \right. \\
&\quad \left. + |[Pr(Y = 1, B = 1, \lambda) - Pr(Y = 1, B = 0, \lambda)]| \right] \leq 2
\end{aligned}$$

and it follows the local-realistic bound for the CHSH value

$$S \leq \int_{\Gamma} 2\rho(\lambda) d\lambda = 2. \quad (3.5)$$

This so called CHSH inequality (3.5) provides a bound that is valid for all LHV theories complying to the assumptions above, independent of the actual theory.

### 3.2.2. Bound for Quantum Mechanics

For the predictions of quantum mechanics two particles with a spin of  $1/2$  in the entangled state

$$|\Psi^-\rangle = \frac{1}{\sqrt{2}} \left( \left| \begin{matrix} 1 \\ 0 \end{matrix} \right\rangle_{Alice} \left| \begin{matrix} 0 \\ 1 \end{matrix} \right\rangle_{Bob} - \left| \begin{matrix} 0 \\ 1 \end{matrix} \right\rangle_{Alice} \left| \begin{matrix} 1 \\ 0 \end{matrix} \right\rangle_{Bob} \right) \quad (3.6)$$

Input	operator	eigenstates with eigenvalue	
		+1	-1
$A = 1$	$\hat{A}_1 = \sigma_z$	$ \vec{A}_1^{+1}\rangle = \begin{vmatrix} 1 \\ 0 \end{vmatrix}$	$\vec{A}_1^{-1} = \begin{vmatrix} 0 \\ 1 \end{vmatrix}$
$A = 0$	$\hat{A}_0 = \sigma_x$	$ \vec{A}_0^{+1}\rangle = \frac{1}{\sqrt{2}} \begin{vmatrix} 1 \\ 1 \end{vmatrix}$	$\vec{A}_0^{-1} = \frac{1}{\sqrt{2}} \begin{vmatrix} 1 \\ -1 \end{vmatrix}$
$B = 1$	$\hat{B}_1 = \frac{1}{\sqrt{2}} (\sigma_z + \sigma_x)$	$ \vec{B}_1^{+1}\rangle = \frac{1}{2\sqrt{1+\frac{1}{\sqrt{2}}}} \begin{vmatrix} 1 + \sqrt{2} \\ 1 \end{vmatrix}$	$ \vec{B}_1^{-1}\rangle = \frac{1}{2\sqrt{1+\frac{1}{\sqrt{2}}}} \begin{vmatrix} -1 \\ 1 + \sqrt{2} \end{vmatrix}$
$B = 0$	$\hat{B}_0 = \frac{1}{\sqrt{2}} (\sigma_z - \sigma_x)$	$ \vec{B}_0^{+1}\rangle = \frac{1}{2\sqrt{1+\frac{1}{\sqrt{2}}}} \begin{vmatrix} -1 - \sqrt{2} \\ 1 \end{vmatrix}$	$ \vec{B}_0^{-1}\rangle = \frac{1}{2\sqrt{1+\frac{1}{\sqrt{2}}}} \begin{vmatrix} 1 \\ 1 + \sqrt{2} \end{vmatrix}$

Table 3.1.: Quantum mechanical measurement operators for the CHSH scenario with corresponding eigenstates.

are considered. Further, the measurements performed by Alice are described by the operator  $\hat{A}_1 = \sigma_z$  for  $A = 1$  and  $\hat{A}_0 = \sigma_x$  for  $A = 0$  while the measurements performed by Bob are  $\hat{B}_1 = \frac{1}{\sqrt{2}} (\sigma_z + \sigma_x)$  for  $B = 1$  and  $\hat{B}_0 = \frac{1}{\sqrt{2}} (\sigma_z - \sigma_x)$  for  $B = 0$ . The results of the measurements are defined as  $\pm 1$  depending on the eigenvalue of the projected eigenstate of the measurement operators (Tab.: 3.1).

The probability to measure an outcome  $X = x$  and  $Y = y$  for inputs  $A = a$  and  $B = b$  is

$$Pr(X = x, Y = y | A = a, B = b) = \left| \langle \vec{A}_a^x | \langle \vec{B}_b^y | \Psi^- \rangle \right|^2$$

Inserting this in (3.3) leads to

$$\begin{aligned} E_{ab} &= \left| \langle \vec{A}_a^{+1} | \langle \vec{B}_b^{+1} | \Psi^- \rangle \right|^2 + \left| \langle \vec{A}_a^{-1} | \langle \vec{B}_b^{-1} | \Psi^- \rangle \right|^2 \\ &\quad - \left| \langle \vec{A}_a^{+1} | \langle \vec{B}_b^{-1} | \Psi^- \rangle \right|^2 - \left| \langle \vec{A}_a^{-1} | \langle \vec{B}_b^{+1} | \Psi^- \rangle \right|^2 \\ &= \langle \hat{A}_a \hat{B}_b \rangle \end{aligned} \quad (3.7)$$

the expectation value of the correlation measurement operators  $\hat{A}_a \hat{B}_b$ . This inserted in (3.1) results in

$$S = \left\| \langle \hat{A}_1 \hat{B}_1 \rangle + \langle \hat{A}_1 \hat{B}_0 \rangle \right\| + \left\| \langle \hat{A}_0 \hat{B}_1 \rangle - \langle \hat{A}_0 \hat{B}_0 \rangle \right\|. \quad (3.8)$$

A straight forward calculation, which can be found in Appendix G, shows that for  $|\Psi^- \rangle$  (3.6) (3.8) takes the value of

$$S = 2\sqrt{2}. \quad (3.9)$$

This result shows that quantum mechanics predicts for certain states and measurement operations a violation of the CHSH inequality (3.5). Boris Tsirelson<sup>1</sup> proved that

$$S \leq 2\sqrt{2}. \quad (3.10)$$

<sup>1</sup>Tsirelson or Cirel'son depending on the transcription

is indeed the upper limit for any quantum mechanical state and measurement operation [77].

The other states that allow for the maximal value of  $S$  are

$$|\Psi^+\rangle = \frac{1}{\sqrt{2}} \left( \begin{array}{c} |1\rangle \\ |0\rangle \end{array} \Big|_{Alice} \begin{array}{c} |0\rangle \\ |1\rangle \end{array} \Big|_{Bob} + \begin{array}{c} |0\rangle \\ |1\rangle \end{array} \Big|_{Alice} \begin{array}{c} |1\rangle \\ |0\rangle \end{array} \Big|_{Bob} \right), \quad (3.11)$$

$$|\Phi^-\rangle = \frac{1}{\sqrt{2}} \left( \begin{array}{c} |1\rangle \\ |0\rangle \end{array} \Big|_{Alice} \begin{array}{c} |1\rangle \\ |0\rangle \end{array} \Big|_{Bob} - \begin{array}{c} |0\rangle \\ |1\rangle \end{array} \Big|_{Alice} \begin{array}{c} |0\rangle \\ |1\rangle \end{array} \Big|_{Bob} \right), \quad (3.12)$$

$$|\Phi^+\rangle = \frac{1}{\sqrt{2}} \left( \begin{array}{c} |1\rangle \\ |0\rangle \end{array} \Big|_{Alice} \begin{array}{c} |1\rangle \\ |0\rangle \end{array} \Big|_{Bob} + \begin{array}{c} |0\rangle \\ |1\rangle \end{array} \Big|_{Alice} \begin{array}{c} |0\rangle \\ |1\rangle \end{array} \Big|_{Bob} \right) \quad (3.13)$$

(each with a different arrangement of the  $\hat{A}_1, \hat{A}_0, \hat{B}_1, \hat{B}_0$ ). This set of four states ((3.6), (3.11), (3.12) and (3.13)) are called Bell states. The Bell state represents a class of states as local rotations and basis transformations preserve the entanglement and a maximal violation of Bell's inequality is only a question of choosing the right combination of measurement operators.

With (3.5) being the absolute limit for local-realistic theories and the prediction of quantum mechanics violating it (3.9), the CHSH inequality enables for a direct experimental testing of local-realistic theories that satisfy the previous assumptions. A significant experimental violation of (3.5) would show that the experiment cannot be described by these theories and that local-realistic descriptions of the world have to be rejected. However, it would not prove quantum mechanics being ultimately the correct description of the world. There could be a different non local-realistic theory for which quantum mechanics is only an incomplete approximation, as classical mechanics is only an approximation of general relativity for special conditions. Thus, an experimental test of Bell's theorem is a test of local realism and is generally called a "Bell test" or "Bell experiment".

### 3.3. Bell experiments and "Loopholes" for local-realism

In an experiment testing local-realistic theories, a Bell experiment, one prepares and measures particles in such a way that quantum mechanics predicts a violation of Bell's inequality. For an experiment testing the CHSH inequality a pair of particles is prepared in one of the four Bell states (a perfect Bell-state fidelity is not necessary). Each particle is sent to an analysis device, which performs a measurement according to the settings for the predicted maximum of  $S$ . This procedure has to be performed numerous times. In this work the creation and measurement on one pair is called event and an experiment with numerous events is called run. For the evaluation all results are combined to calculate the  $S$  value (3.1).

Before one draws a conclusion from the experimental result, e.g., to reject local-realism, the limitations of the experiment have to be considered. These possible limitation can be specific to the experimental implementation and procedure or apply to the method of the experiment itself. One limitation that applies to every experiment is finite statistics. For a Bell test experiment this leads to the problem that the bound of  $S \leq 2$  is only strict for an infinite amount of events. A finite amount of events leads to a non zero probability for any algebraic possible value of the outcome ( $0 \leq S \leq 4$ ). To be able to draw meaningful conclusions from experiments with finite statistics the proper use of statistical analysis methods is necessary.

### 3.3.1. “Loopholes” in experiments

In section 3.2.1 four assumptions on local hidden variable theories are made to derive the probability for measurement outcomes (3.4) and the bound (3.5) is only valid for theories obeying them. For an experiment the assumptions are requirements meaning that the experimental design must be such that the assumptions are experimentally guaranteed. Moreover, each assumption which needs to be made about the experiment opens a so called loophole for local-realism. This means there exists a local-realistic theory that does not obey the assumption. Such a theory can violate (3.5) and thus is capable of explaining every possible experimental result. Such loopholes invalidate a Bell test and must be avoided.

#### Local and independent measurements and the locality loophole

The first assumption made to derive the local-realistic bound of the CHSH inequality is, that each measurement process is local and not influenced by the other measurement process. The second is, that each measurement process depends only on the local input and is independent from the other input. Without the measurements and inputs being separated the probability to get a certain result  $X = x$  and  $Y = y$  for a certain combination of the inputs  $A = a$  and  $B = b$  cannot be written as in (3.4), but has the form

$$Pr(X = x, Y = y|A = a, B = b) = \int_{\Gamma} Pr(X = x, Y = y|A = a, B = b, \lambda) \rho(\lambda) d\lambda \quad (3.14)$$

and the limit for the  $S$  value becomes 4. This is called the locality loophole.

To guarantee local measurements in an experiment, it is necessary to separate them such that no communication between Alice and Bob is possible during the time needed for the input choice and measurement process. Since no specifics of the local-hidden variable theories are assumed, the only possibility to close this loophole is to enforce space-like separation of the measurement processes including the setting choice. With each measurement process outside the past light cone of the other, influence between them is excluded for any local-realistic theories.

#### Independent and unpredictable setting choice and the freedom of choice loophole

The third and fourth assumption made to derive the local-realistic bound concern the input choices. These inputs need to be chosen freely, independently for each other, and unpredictable.

If each input is not chosen freely but does depend on the local-hidden variables this has to be considered for (3.4) and it takes the form of

$$\begin{aligned} Pr(X = x, Y = y|A = a, B = b) \\ = \int_{\Gamma} Pr(X = x|A = a, \lambda) Pr(Y = y|B = b, \lambda) \rho_{a,b}(\lambda) d\lambda \end{aligned} \quad (3.15)$$

with  $\rho_{a,b}(\lambda) = \frac{\rho(\lambda)Pr(A=a|\lambda)Pr(B=b|\lambda)}{\int_{\Gamma} \rho(\lambda)Pr(A=a|\lambda)Pr(B=b|\lambda)d\lambda}$  being a renormalized probability density for  $\lambda$  depending on the probability for the inputs  $Pr(A = a|\lambda)$  and  $Pr(B = b|\lambda)$ . Since  $\rho_{a,b}(\lambda)$  can be different for each of the four combinations of  $a$  and  $b$ ,  $S$  can take every value up to 4. If the inputs are not chosen independently of each other (3.4) they have a common source and space like separation of the input choices is not possible, which opens the locality loophole.

Furthermore, if the inputs are predictable this can have influence on the realization of the local-hidden variables and (3.4) takes the form

$$\begin{aligned} & Pr(X = x, Y = y|A = a, B = b) \\ &= \int_{\Gamma} Pr(X = x|A = a, \lambda) Pr(Y = y|B = b, \lambda) \rho(\lambda|A = a, B = b) d\lambda \end{aligned} \quad (3.16)$$

with  $\rho(\lambda|A = a, B = b)$  being the probability density adapted for the case  $A = a$  and  $B = b$ . In this case the bound of  $S$  for local realism is 4. This problem of input choice is referred to as the freedom of choice loophole.

In an experiment this loophole is usually addressed by employing two physical random number generators one for Alice's and one for Bob's setting choice. Still, random number generators suffer from the fundamental problem that randomness of their outputs cannot be proven without additional assumptions. These assumptions need to be stated and will limit the excluded theories to the ones obeying the assumptions. Furthermore, to exclude a possible influence of the pair generation onto the inputs, space like separation of the random number generation and pair creation can be used. A more detailed discussion of possibilities for closing this loophole can be found in Chapter 5.

### Fair sampling and the detection loophole

Additionally to the four explicit assumptions stated in section 3.2.1 to derive the CHSH inequality, further implicit assumptions were made. An important one is that every pair which is created is also measured and two results are produced. Already in the original CHSH paper [9] it was pointed out that this is hardly possible for experiments depending on single photon detection for their measurements. To address this, they added the assumption that the detected pairs are a fair sample of all created pairs. This assumption opens the so called detection loophole for LHV theories that exploit input-dependent detection efficiencies [78] to change the probabilities in (3.4). The form of the new probabilities also depends on the design of the conducted experiment.

If the particle pairs are created at random points in time and are identified by coincidences of detection event in Alice and Bob, which is the case in a continuously driven pair source, (3.4) takes the form

$$\begin{aligned} & Pr(X = x, Y = y|A = a, B = b) \\ &= \frac{1}{\eta_{total(a,b)}} \int_{\Gamma} Pr(X = x|A = a, \lambda) \eta_A(a, \lambda) Pr(Y = y|B = b, \lambda) \eta_B(b, \lambda) \rho(\lambda) d\lambda. \end{aligned} \quad (3.17)$$

The overall detection efficiency  $\eta_{total}(a, b) = \int_{\Gamma} \eta_A(a, \lambda) \eta_B(b, \lambda) \rho(\lambda) d\lambda$  for inputs  $a$  and  $b$  depends on the detection efficiencies  $\eta_A(a, \lambda)$  and  $\eta_B(b, \lambda)$ , which depend the LHV realization  $\lambda$ . This allows the LHV to change the detection efficiency depending on the local input choice for each pair. The bound for  $S$  can be derived by considering deterministic LHV models. In such models the local outcomes depend directly on the local inputs.

Here, the case of equal detection efficiencies for Alice and Bob  $\eta_{A,total} = \eta_{B,total} = \eta$  with  $\eta_{A,total} = \sum_{a=0}^1 \int_{\Gamma} \eta_A(a, \lambda) \rho(\lambda) d\lambda$  and  $\eta_{B,total} = \sum_{b=0}^1 \int_{\Gamma} \eta_B(b, \lambda) \rho(\lambda) d\lambda$  is examined. As an example an LHV model that chooses randomly one of the four output combinations and

$\lambda$	$A = 1$	$A = 0$	$B = 1$	$B = 0$
1	$X = 1$	$X = 1$	$X = 1$	$X = 1$
	$\eta_A = 1$	$\eta_A = \eta_d$	$\eta_B = 1$	$\eta_B = 1$
2	$X = 1$	$X = 1$	$X = 1$	$X = 1$
	$\eta_A = 1$	$\eta_A = 1$	$\eta_B = 1$	$\eta_B = \eta_d$
3	$X = 1$	$X = -1$	$X = -1$	$X = 1$
	$\eta_A = \eta_d$	$\eta_A = 1$	$\eta_B = 1$	$\eta_B = 1$
4	$X = 1$	$X = -1$	$X = -1$	$X = 1$
	$\eta_A = 1$	$\eta_A = 1$	$\eta_B = \eta_d$	$\eta_B = 1$

Table 3.2.: Example for deterministic LHV model utilizing the detection loophole by using four combinations of local outputs and detection efficiencies for local inputs. The detection efficiency for “unwanted” measurement results  $0 \leq \eta_d \leq 1$  allows for  $S \geq 2$ .

detection efficiencies from Table 3.2 for each pair is considered. The resulting  $S$  value is

$$\begin{aligned}
S &= \left\| \frac{1+1-\eta_d-\eta_d}{1+1+\eta_d+\eta_d} + \frac{1+\eta_d+\eta_d+1}{1+\eta_d+\eta_d+1} \right\| + \left\| \frac{\eta_d+1+1+\eta_d}{\eta_d+1+1+\eta_d} - \frac{+\eta_d+\eta_d-1-1}{\eta_d+\eta_d+1+1} \right\| \\
&= 2 + 2 \frac{1-\eta_d}{1+\eta_d}
\end{aligned} \tag{3.18}$$

where  $1 \geq \eta_d \geq 0$  is the a model parameter describing the reduced detection efficiency for local measurement that potentially can result in a reduced  $S$  value, while the detection efficiency for all other local measurement is 1.

Reducing  $\eta_d$  from 1 to 0 in (3.18) leads to an increase of the  $S$  value from 2 to 4 . Since the bound of  $S \leq 2\sqrt{2}$  (3.10) for quantum mechanics is not influenced by the detection efficiency in such type of experiments a test of local realism is not only possible if

$$2 \frac{1-\eta_d}{1+\eta_d} + 2 \geq 2\sqrt{2}. \tag{3.19}$$

Inserting the total detection efficiency for Alice or Bob

$$\begin{aligned}
\eta &= \sum_{\lambda} \sum_A \eta_A \frac{1}{8} \\
&= \sum_{\lambda} \sum_B \eta_B \frac{1}{8} \\
&= \frac{3+\eta_d}{4}
\end{aligned} \tag{3.20}$$

in (3.19) leads to a lower bound of

$$\eta > \frac{2+\sqrt{2}}{4} \approx 0.854.$$

The LHV model (Tab. 3.2) is a simple example to demonstrate the possibility of exploiting the detection loophole and it would lead to a very specific combination of results in an

experiment. However, the model can easily be expanded by using more combinations of outputs and detection efficiencies to a model that will produce experimental results that cannot be distinguished from the predictions of quantum mechanics. Furthermore, the not perfect detection efficiency allows for LHV theories to additionally exploit the pair finding based on time differences between single detection events. This is called the coincidence time-loophole and leads to a lower bound of  $\eta > 0.879$  for the detection efficiency [79].

In experiments with a well defined pair creation, where one can identify each created pair, e.g., with heralded entanglement creation, it is possible to assign an value to the output even in the case of no detection. This prohibits LHV models to utilize a input dependent detection efficiency and the bound of  $S < 2$  holds for local realistic theories. However, assigning an output in the case of no detection means that this output is not based on a measurement of the particle. Thus, the detection inefficiency is now a problem of measurement fidelity and decreases the predicted bound for quantum mechanics.

This can also be shown by a concrete example: one assigns the output  $X = +1$  for no detection at Alice and  $Y = +1$  for no detection at Bob and one assumes a perfectly prepared Bell state and perfect measurements. Now, it is possible to make three different categories of events in the experiment: first, only pairs with no detection on both sides, which yield  $S = 2$ ; second, with no detection on one side and a detection on the other yielding  $S = 0$ ; and the third with detection on both sides yielding  $S = 2\sqrt{2}$ . These three categories together yield the modified bound of

$$S \leq 2 + \eta_{A,total}\eta_{B,total} (2\sqrt{2} + 2) - 2(\eta_{A,total} + \eta_{B,total})$$

depending on the detection efficiencies of Alice and Bob. To still allow for a violation of the classical bound of  $S = 2$  the efficiencies of the detectors need to be above

$$\eta_{A,total}, \eta_{B,total} > 2\sqrt{2} - 2 \approx 0.829$$

[80, 81]. Using an equivalent formulation of Bell's inequality, which was derived by Clauser and Horne [82], Philippe Eberhard showed that for non-maximally entangled states, e.g.,

$$\Psi_E = \frac{1}{\sqrt{1+r^2}} \left( \left| \begin{array}{c} 1 \\ 0 \end{array} \right\rangle_{Alice} \left| \begin{array}{c} 0 \\ 1 \end{array} \right\rangle_{Bob} - r \left| \begin{array}{c} 0 \\ 1 \end{array} \right\rangle_{Alice} \left| \begin{array}{c} 1 \\ 0 \end{array} \right\rangle_{Bob} \right)$$

with  $0 \leq r$ , the lower bound for the detection efficiency can be reduced to  $\eta_{A,total}, \eta_{B,total} > 2/3$  [83].

### Finite statistics and the memory loophole

All above mentioned loopholes arise from assumptions specific to the actual implementation of the experiment and are closed by employing a fitting experimental design. But there is an additional source for assumptions: the analysis of the experiment. For an experiment testing local realism the analysis has to consider if the experimental result can be explained by local realistic theories. For this the analysis method must incorporate the finite statistic of experiments. The most frequently used methods for statistical analysis of experimental data make the assumption that the repeated experiment produces independent and identically distributed (i.i.d.) results. For many experiments this can be a fair assumption, even though experimental setups might change over time and thus the results are not independent and identically distributed.

#	$X A=1$	$X A=0$	$Y B=1$	$Y B=0$
1	+1	+1	+1	+1
2	+1	+1	+1	-1
3	+1	+1	-1	+1
4	+1	+1	-1	-1
5	+1	-1	+1	+1
6	+1	-1	+1	-1
7	+1	-1	-1	+1
8	+1	-1	-1	-1
9	-1	+1	+1	+1
10	-1	+1	+1	-1
11	-1	+1	-1	+1
12	-1	+1	-1	-1
13	-1	-1	+1	+1
14	-1	-1	+1	-1
15	-1	-1	-1	+1
16	-1	-1	-1	-1

Table 3.3.: The 16 possible input and measurement outcomes combinations for deterministic LHV strategies. The blue marked combinations are used in the example exploiting the memory loophole.

If one applies this assumption for the evaluation of a Bell experiment the so called memory loophole for theories in which the probabilities for the measurement outcomes depend on the results and inputs of previous events opens [15]. For such theories the probability for certain result for each event can differ from the previous events and might even depend on them. The probability for the event  $i$  resulting in  $X_i = x$  and  $Y_i = y$  for inputs  $A_i = a$  and  $B_i = b$  is

$$\begin{aligned}
& Pr(X_i = x, Y_i = y | A_i = a, B_i = b) \\
&= \int_{\Gamma} Pr(X_i = x | A_i = a, \lambda, h_i) Pr(Y_i = y | B_i = b, \lambda, h_i) \rho_i(\lambda, h_i) d\lambda \quad (3.21)
\end{aligned}$$

with

$$h_i = \{A_1, A_2, \dots, A_{n-1}, X_1, \dots, X_{n-1}, B_1, \dots, B_{n-1}, Y_1, \dots, Y_{n-1}, \rho_1, \dots, \rho_{n-1}\}$$

being the history (or memory) of the previous events and  $\rho_i(\lambda, h_i)$  the history dependent probability density of the LHVs  $\lambda$ . Again if the number of events  $n$  approaching infinity this does not affect the bound of  $S \leq 2$  (3.5), yet, for finite statistics the probability for an experiment with outcome  $S > 2$  increases dramatically.

The possible effect can be illustrated with an example of a very simple deterministic LHV model (close to an example in [15]), which employs a direct dependence on the history of both input choices. As mentioned already before in a deterministic LHV model the local outcomes depend directly on the local inputs. This means that for each created pair one of the 16 possible output combinations from Table 3.3 is chosen. In this model the history of the experiment, meaning the inputs and outputs from previous events, is known and used to update the strategy of the LHVs. Yet, the inputs for the next measurements are unknown

#	$A = 1, B = 1$	$A = 1, B = 0$	$A = 0, B = 1$	$A = 0, B = 0$
1	+	+	+	-
2	+	-	+	+
5	+	+	-	+
7	-	+	+	+
10	-	+	+	+
12	+	+	-	+
15	+	-	+	+
16	+	+	+	-

Table 3.4.: The change of  $S_i \rightarrow S_{i+1}$  depending on the input combination of Alice and Bob for the 8 output combinations used in the LHV model exploiting the memory loophole. + represents  $S_{i+1} \geq S_i$  and -  $S_{i+1} \leq S_i$ .

and no communication is possible after the measurement starts. In this model only the 8 blue marked combinations (1,2,5,7,10,12,15,16) from Table 3.3) are used.

Considering an ideal experiment with unbiased inputs and infinite statistic, an LHV model that fairly samples from these 8 combinations for the created pairs yields the correlators (3.2)  $E_{11} = 0.5$ ,  $E_{10} = 0.5$ ,  $E_{01} = 0.5$ , and  $E_{00} = -0.5$  and thus  $S = 2$ . But for an experiment with finite statistics and a strategy exploiting knowledge of the inputs from the previous events this is not the case. To derive such a strategy one can use a common feature of the 8 combinations:

For an experiment with  $i$  events already measured resulting in a potential  $S$  value  $S_i$  the measurement on the next pair ( $i + 1$ ) will result in an  $S_{i+1} \geq S_i$  for 3 out of 4 input combinations. Yet the 4th input combination will result in  $S_{i+1} \leq S_i$ . The inputs leading to a higher or lower  $S$  for the output combinations can be deduced from (3.1) and (3.2) and are summarized in Table 3.4. Now, the strategy is the following:

1. For the first pair 1 of the 8 combinations is chosen randomly and then the measurement with random inputs is performed.
2. From the history of the experiment the number of events for each input combination  $N_{1,1}$ ,  $N_{1,0}$ ,  $N_{0,1}$ , and  $N_{0,0}$  are determined.
3. For the next round only the combination which will lead to  $S_{i+1} \leq S_i$  for the most frequent input combination  $N_{max}$  are considered:
  - a)  $N_{max} = N_{1,1} \Rightarrow$  combinations 7 or 10.
  - b)  $N_{max} = N_{1,0} \Rightarrow$  combinations 2 or 15.
  - c)  $N_{max} = N_{0,1} \Rightarrow$  combinations 5 or 12.
  - d)  $N_{max} = N_{0,0} \Rightarrow$  combinations 1 or 16.
  - e) if there is a tie for the smallest number one of the smallest is randomly chosen to determine the strategy
4. The next measurement is performed and the strategy starts again repeating step 2. to 4. until the experiment is finished.

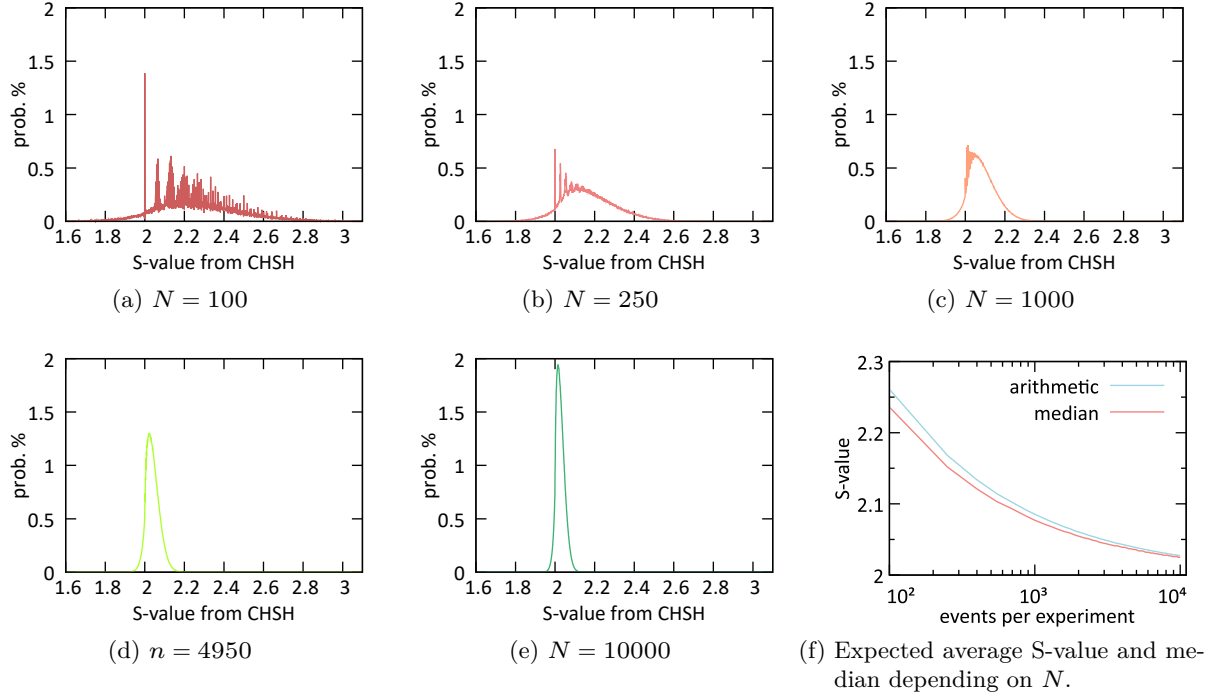


Figure 3.2.: Example for exploiting the memory loophole: S-value distribution for experiments with different number of events  $N$  using a strategy exploiting the distribution of past inputs (a,b,c,d,e) and expected average and median S-value depending on  $N$  (f). The distributions are extracted from simulating  $10^7$  experiments for each  $N$ .

In an experiment with random and unbiased input selection choosing the most frequent input combination of the previous events can lead to a positive expectation value for the change of  $S$  from event  $i$  to event  $i + 1$ . This arises from the definition of the correlators  $E_{a,b} := \frac{N_{a,b}^{X=Y} - N_{a,b}^{X \neq Y}}{N_{a,b}}$ , where the effect of a single event is smaller if the total amount of events is higher. Thus, this LHV model with a strategy based on the history of the experiment leads in the case of a small total number of events  $N$  to an expectation value for  $S$  well above 2. However, for experiments with more events the effect decreases, vanishing when approaching infinite number of events. This effect is quantified with a Monte Carlo experiment of the model with  $10^7$  experimental runs for each total events from 100 to 10000 in steps of 150 ( $S$  value distributions for selected  $n$  in Figure 3.2). The simulation shows, that for experiments with only a few hundred events the median of the resulting  $S$  value is above 2.1 and decreases for larger  $N$  to 2.025 for 10000 (Fig. 3.2) events, while a LHV model fulfilling the i.i.d. assumption would give a median of 2 independent of the events per experiment.

To address this loophole it is necessary to use an analysis method without the i.i.d. assumption. In [15] it is recommended to use a modified definition of (3.2)

$$E_{a,b} := \frac{N_{a,b}^{X=Y} - N_{a,b}^{X \neq Y}}{1/4N}$$

with the total number of events  $N$ . This modification of the correlators is allowed for experi-

ments with large  $N$  and unbiased inputs, which does not lead to any extra assumptions and is desirable for an experimental Bell test since biased inputs will lead to a residual predictability of the inputs. In this formulation the CHSH inequality is immune to this kind of history dependence. It is used, for example, in the formalism by Gill [16] modeling the experiment with a martingale process. There are also other methods that address this loophole by employing a game formalism [84, 17].

### 3.3.2. Statistical analysis of a Bell experiment

In order to draw meaningful conclusions from the experiment, it is necessary to employ an analysis method yielding a statement whether local realism can explain the outcome. The most common evaluation of a measured parameter, here  $S$ , is to consider the measured value and calculate its standard deviation. Based on this it is possible to quantify the confidence that a certain interval around a measured  $S$  includes the unknown actual  $S$ . If this interval includes only  $S$  values that violate Bell's inequality ( $S > 2$ ) one can infer that it is likely that the underlying  $S$  also violates Bell's inequality thus, local-realism can be rejected. However, this is an indirect way of answering the question whether local realism can explain the experimental results. Therefore, a different well-established method is introduced to draw meaningful conclusions with respect to local-realism from the outcome of the experiment.

#### Statistical hypothesis testing

For this situation the concept of hypotheses testing is well suited. It allows deciding between a null hypothesis  $H_0$  and an alternative hypothesis  $H_a$  based on recorded data. These hypotheses are defined in the following way: the null hypothesis  $H_0$  is an exactly defined hypothesis which is actually tested, while the alternative hypothesis  $H_a$  is defined as the complementary to the null hypothesis  $H_a = \neg H_0$ .

For performing the test, the so called  $p$  value, i.e. the probability to observe the recorded or a more extreme outcome, conditioned on the null hypotheses is true, is calculated.

$$Pr(\text{outcome and more extreme} | H_0 \text{ is true}) = p \quad (3.22)$$

If this probability is smaller than a predefined  $0 \leq \alpha \leq 1$ , giving a confidence level  $cl = 1 - \alpha$ ,  $H_0$  is rejected and  $H_a$  is accepted. Otherwise,  $H_0$  is not rejected, without any conclusion on  $H_a$ .

Since this is a statistical analysis the inference (rejection or no rejection) might be not true. There are two types of false inference: the type I error is the case when the null hypothesis is rejected although it is true and the type II error is the case where the null hypothesis is not rejected although it is false. The type I error is easy to quantify since its probability corresponds to the  $p$  value, which is indeed the probability to observe the recorded data (and more extreme) under the condition  $H_0$  is true. The type II error is more delicate to address. As it concerns the case of  $H_0$  being false  $H_a$  is then true and

$$Pr(\text{outcome and more extreme} | H_a \text{ is true}) \quad (3.23)$$

is the probability to observe the recorded or a more extreme outcome, conditioned  $H_a$  is true. This probability depends on  $H_a$  and might be 1 for every possible case of recorded data even if (3.22) yields also 1. The consideration of the two possible errors show that in general the

null hypotheses can be disproven according to the respective confidence level, but it cannot be proven<sup>2</sup> [85].

It is important to note, that these probabilities are conditioned on either  $H_0$  or  $H_a$  to be true and by this are not absolute probabilities for the occurrence of such an error. The absolute probabilities depend on the the actual scenario of the test. There is a difference between a scenario in which both hypotheses can be true, e.g., a test if individuals of a group have an infection, or a scenario in which only one hypothesis can be true, e.g., a test of physical principles. In the first example the absolute probabilities for the error of type I depends on how big the tested group is and which fraction is actually infected. However, in the second example the probability for an error of type I is either equal to  $p$  when the null hypothesis is correct, or zero if the null hypothesis is wrong. Therefore, a  $p$  value from a possible Bell test with the null hypothesis that local-realism explains the experiment is always an upper bound for the probability of an error type I. Nevertheless, the definition of  $H_0$  needs to be as exact as possible. This includes its intended meaning and its formulation in mathematical terms since conclusions made from the experiment and their significance depend on it [86].

### Requirements for a conclusive hypothesis test

When using hypothesis testing one has to be aware that there are certain requirements on the experimental and analysis procedures, which, if not followed, can obliterate the whole result. First, the analysis method should be independent of the result of the experiment. The simplest way to account for this is by fixing the way the  $p$  value is calculated before the experiment [87].

Second, the data should not be filtered to minimize the  $p$  value, for example by changing acceptance time windows or similar parameters after the experiment since this will obliterate the mathematical process to calculate  $p$  and by this the significance of  $p$ . Events may be excluded, but only on objective criteria independent from the results and defined before the experiment. This can be, for example, malfunction of experimental equipment.

Third, the experiment needs a predefined end. If the experiment is stopped when reaching a desired result, e.g., at a certain  $p$  value threshold, the  $p$  value will not correspond to the probability of a type I error and the validity of the result is diminished. One must either define a fixed duration in time or a fixed event number after which the experiment is finished.

Finally, in the case of multiple repetitions of an experiment this has to be carefully taken into account for drawing conclusions of significance. For example for an  $\alpha = 0.05$  the probability for a type I error is 5% if the experiment is performed once, but if the experiment is performed multiple times without adjusting the testing procedure this error probability dramatically increases. For 14 repetitions the probability to have at least 1 type I error is already  $> 50\%$ . The same problem arises if one tests multiple independent hypotheses with the same recorded data. This can be avoided by accounting for the multiple experimental runs within the mathematical model or combining multiple experiments with their  $p$  values using an appropriate method [88, 89]. In general it is necessary to minimize the effect of a possible bias introduced by the experimenter and the procedure [14].

---

<sup>2</sup>For special cases the probability (3.23 can be quantified and then corresponds to a new hypothesis test with  $H_0^{new} = H_a$  and  $H_a^{new} = H_0$ .

### Applying hypothesis testing to a Bell test

The concept of hypothesis testing does fit very well to a Bell test. Since a Bell experiment allows only falsify local-realism and not prove quantum mechanics (Sec. 3.2.2), the limitations of hypothesis testing do not limit the possible conclusion of the experiment.

For the analysis the null hypothesis  $H_0$  and the alternative hypothesis  $H_a$  are defined as follows:

- $H_0$ : the experiment can be described by local-realistic theories obeying stated assumptions
- $H_a = \neg H_0$ , i.e. the experiment can only be described by theories not obeying local-realism or local-realistic theories not obeying stated assumptions

Calculating the probability for all possible results for the experiment depending on the number of events is a delicate matter, because it must include all possible local-realistic theories without any additional knowledge and assumptions on their potential physical working. Moreover, the standard methods of hypothesis testing, e.g., the z-test or the t-test assume i.i.d. events disqualifying them for the full analysis of a Bell test. Still, it is possible to estimate an upper bound for  $p$  (3.22) that is sufficient for a hypothesis test. This problem has been addressed (including considerations of the memory loophole) for example in [16, 17, 90, 91].

Bounding  $p$  from above leads to an overestimation of the probability for a type I error increasing the requirements on the experiment in terms of event number and fidelity, but leading to no fundamental problems in the possibility to disprove local-realism (under the used assumptions). Since  $H_0$  and  $H_a$  do not include anything about the experiment itself, the probability for a type II error is unity not allowing to make any statement if the null hypothesis of local-realism is not rejected. Second, disproving local-realism does not prove anything else about physical theories, especially it does neither prove the correctness nor the completeness of quantum mechanics.

### Alternatives to hypothesis testing

There are also other methods using the Bayesian inference to analyze Bell test experiments[92]. In such an analysis there are the two hypotheses to decide between i.e., for a Bell test these are either local-realistic theories or quantum mechanics describe the experiment(with a very specific model of the experiment). It shows that the experiments can be explained by quantum mechanics with a much higher probability than with local-realism. Furthermore, the analysis tests whether the experiment was well characterized by quantum mechanics and performed in the expected way than if local-realism is valid or not. But the analysis does not prove whether quantum mechanics is correct or complete since neither the experiment nor the analysis tests conventional quantum mechanics against other theories that also do not obey local-realism.

### 3.3.3. Requirements for a robust Bell experiment

To make a Bell test most conclusive, it is necessary to minimize assumptions leading to loopholes (Sec. 3.3.1) as this maximizes the amount of tested local realistic theories. This is a challenging technical task, since while fulfilling the assumptions experimentally, still a sufficiently high fidelity of the entanglement creation and the readout is necessary. Otherwise,

a significant violation of the classical bound cannot be achieved. Nevertheless, it is not possible to drop all assumptions, especially those on the choice of inputs. The remaining assumptions have to be stated to specify which local realistic-theories are not tested with the experiment. Furthermore, to draw any inference on the validity of local-realism from the data, a suited analysis method needs to be chosen and applied carefully.

The requirements for a robust Bell test experiment can be summarized:

1. Space-like separation of the local measurements of Alice and Bob including random inputs choice for each event.
2. High detection efficiency of employed detectors or heralded pair creation with a high fidelity measurement.
3. Fast and random generation of the inputs for Alice and Bob, independent from each other and from the rest of the setup, as well as independent from the previous inputs.
4. Duration of the experiment defined prior to the experiment with fixed total number of events  $n$  or fixed end time.
5. Choice of an analysis method without i.i.d. assumption before the measurement.
6. No post selection of events. Excluding events is only allowed based on predefined independent objective criteria that do not allow a LHV model to violate Bell's inequality.

### 3.3.4. A short history of Bell experiments

After the introduction of Bell's theorem and proposal of an experiment in 1964 it took some time to develop a solid framework applicable for experiments like the CHSH inequality and then to actually perform such experiments.

#### First experiments

The first experiment was performed by Freedman and Clauser [10] in 1972. They used photon pairs emitted in a cascade transition of calcium and measured the polarization of the photons. The experiment showed a violation of the bound for local-realism with a significance of 5 standard deviations, but with a detection efficiency of only  $\eta \approx 10^{-3}$  and with a measurement of each of the four input choice combinations run for several minutes it did not close any loophole from section 3.3.1. Still it was a first indicator towards the rejection of local-realism.

A conceptual progress in the experiments was reported by Aspect, Dalibard, and Roger in 1982 by implementing fast switching of the measurement direction [11]. They also used photons from a calcium cascade transition and measured the polarization of the photons, but the measurement direction was quickly switched using acousto-optic deflectors every 10 ns, while the measurement devices were separated by 12 m allowing for space-like separation of the measurement process, yet, due to the periodic switching without including the input choice. The switching of the measurement was done by two independent modulations at  $\sim 50$  MHz for each side. The detection efficiency was  $\eta \approx 10^{-3}$  as in previous experiments [12]. The experimental results violated the predictions of local-realism with 5 standard deviations. It has to be pointed at, that this experiment did not close the locality loophole, because the input choice was done periodically and deterministically and not random. Still, the fast

and independent input selection removed many doubts concerning the results of the previous experiments with measurements with fixed analysis settings.

### Closing loopholes

Further steps towards a conclusive Bell test experiment took more than a decade. The first experiment closing the locality loophole was published by Weihs et al. in 1998 [93]. In this experiment entangled photon pairs created by spontaneous parametric down-conversion were sent to two devices for measuring the polarization, which were separated by 355 m. The measurement direction was set by fast switching EOMs according to inputs from a quantum random number generator based on the detection of photons in either output port of a beam splitter. The time needed the generation of the random input until the photon detection was less than 100 ns thus clearly space-like separated from the other measurement. A violation of more than 36 standard deviations was observed, yet with a detection efficiency of only  $\eta = 0.05$ .

In 2001 the first experiment without the need for the fair sampling assumption was performed by Rowe et al. using deterministic entanglement between two ions in one trap [94]. The efficiency in this experiment was unity  $\eta = 1$ , since for every measurement a result was obtained and a violation of the local-realistic bound by 8 standard deviations could be shown. Yet, with a separation of the two ions of only 3  $\mu\text{m}$  the locality loophole was left open.

An analysis method for a Bell test using hypothesis testing and closing the memory loophole was presented by Gill in 2003 [16]. Applied to the data from Weihs et al [93] with  $S = 2.73 \pm 0.02$  and  $n \approx 14700$  events the method yields  $p \leq 10^{-32}$ .

The next steps towards experiments closing locality and detection loopholes in one experiment were taken in 2012 and 2013. On one hand techniques to create heralded entanglement between widely separated quantum memories, like neutral atoms [32] (LMU Munich, Germany) and vacancy centers in diamonds [95] (TU Delft, Netherlands), were demonstrated. These paved the way for space-like separation of measurements with a detection efficiency of unity. On the other hand experiments closing the detection loophole with entangled photons [96, 97] (University Vienna, Austria and NIST Boulder, Colorado USA), which employed superconducting photon detectors with very high efficiency [98], were developed. Each of the four demonstrations finally lead to an experiment closing all major loopholes.

### Recent loophole free experiments

50 years after the publication of Bell's paper [2] the first experiments without loopholes were conducted. In August 2015 Hensen et al. (Delft) reported a Bell test experiment that used heralded entanglement between two nitrogen vacancy centers in diamond separated by 1.3 km [18]. The heralded scheme allowed for a detection efficiency of unity and a measurement readout duration of 3.7  $\mu\text{s}$ . With an additional 0.480  $\mu\text{s}$  for the random input selection employing quantum random number generators [99] enabled to close the detection and locality loophole. The experiment yielded  $S = 2.42 \pm 0.2$  with  $n = 245$  events during 220 h of measurement in 18 days. With a hypothesis test using the game formalism from Elkouss and Wehner [17] local-realism could be rejected with a  $p = 0.039$ . Even though the experiment is a very impressive test of Bell's inequality and demonstration of quantum technology the probability of nearly 4% for an experiment following local-realism to achieve the same result (error type I

in section 3.3.2) is quite high for such a fundamental decision<sup>3</sup>.

Shortly afterwards, in October 2015 two groups Giustina et al. (Vienna) [19] and Shalm et al. (Boulder) [20] performed both a violation of Bell's inequality in the Eberhard-CH formulation using pairs of entangled photons created by pulsed spontaneous parametric down conversion. Giustina et al. had detector efficiencies, including all losses between source and detector, of  $\eta_A = 0.786$  for Alice and  $\eta_B = 0.762$  for Bob thus closing the detection loophole. With Alice and Bob separated by 60 m and a measurement time of 140 ns and additional 26 ns for the random input selection the locality loophole was closed. Shalm et al. had efficiencies of  $\eta_A = 0.747$  and  $\eta_B = 0.756$  and a separation of 184.9 m with a maximum measurement time of 578 ns <sup>4</sup> including random input choice also closing both loopholes. Both report a very significant violation of Bell's inequality and with  $p = 3.74 \cdot 10^{-31}$  (Giustina et al.) and  $p = 2.3 \cdot 10^{-7}$  (Shalm et al) show a high confidence for the rejection of the null hypothesis. Both experiments used the same type of quantum random number generators as used in Hensen et al. [99].

In this thesis a Bell experiment conducted from November 2015 to June 2016 is described. Employing heralded atom-atom entanglement over 398 m, a fast and efficient read-out, and a QRNG based on photon counting [39], this experiment allowed for closing the locality and detection loophole in one experiment [60, 38]. A detailed description of the experiment follows in the next chapter.

---

<sup>3</sup>A second run of the experiment was done in 2016 with  $n = 300$  events and combining results from both run leads to a  $p = 8 \cdot 10^{-3}$  [100].

<sup>4</sup>In the experiment an input sets the measurement direction for the next 200 ns, during this time multiple laser pulses of the pump laser (12.6 ns pulse-to-pulse separation) are generating photon pairs leading to multiple acceptance time windows for the same input choice. The measurement time and  $p$  stated here are for the case of summing over events in 5 acceptance time windows.

## 4. Violation of Bell's Inequality with Entangled Atoms

As outlined in the previous chapter an experimental test of local-realism is possible by performing measurements on an entangled pair of qubits using Bell's inequality. The topic of this chapter is such an experimental Bell test, which is based on the entanglement of two rubidium atoms (Chap. 2). The chapter starts with a short description of the design and setup of the experiment and how this allows to close the detection and locality loophole (Sec 3.3.1) [38]. This is followed by a characterization of the random number generators employed for the setting choices. Then the procedures for conducting and evaluating the experiment are defined. Finally, the data collected in multiple experimental runs between November 2015 and June 2016 are presented. This includes the two main runs with 10000 events of which one was public, meaning the result for each event was available on a live feed on a publicly accessible website.

### 4.1. Design of the experiment

For a Bell experiment using the CHSH inequality (3.1), two qubits are prepared in one of the four maximally entangled Bell-states and then measurements on the qubits are performed independently. The measurement directions are chosen to allow for a maximal violation of the inequality. In this experiment the two qubits are encoded in the two independently trapped rubidium atoms (Sec 2.1). They are prepared in the  $\Psi^+ = \frac{1}{\sqrt{2}}(|\uparrow_x\rangle|\downarrow_x\rangle + |\downarrow_x\rangle|\uparrow_x\rangle)$  or the  $\Psi^- = \frac{1}{\sqrt{2}}(|\uparrow_x\rangle|\downarrow_x\rangle - |\downarrow_x\rangle|\uparrow_x\rangle)$  depending on the result of the Bell state measurement for entanglement swapping (Sec 2.4). The measurement operations on the qubits are defined in Table 4.1.

These operations are implemented via the atomic state read-out (Sec 2.3.2) with the corresponding read-out polarization  $\chi_{ro}$ . The result of a measurement is defined by the detection of ionization fragments with the CEMs. For this purpose, acceptance time windows for the de-

Setting	measurement operator	readout polarization $\chi_{ro}$	$\alpha$ and $\phi$ in (2.7)
$A = 0$	$\hat{A}_0 = \sigma_x$	$\chi_{A,0} = V$	$\alpha = 0, \phi = 0$
$A = 1$	$\hat{A}_1 = \sigma_y$	$\chi_{A,1} = \cos(\pi/4)V + \sin(\pi/4)H$	$\alpha = 45^\circ, \phi = 0$
$B = 0$	$\hat{B}_1 = \frac{1}{\sqrt{2}}(\sigma_x - \sigma_y)$	$\chi_{B,1} = \cos(\pi/8)V - \sin(\pi/8)H$	$\alpha = -22.5^\circ, \phi = 0$
$B = 1$	$\hat{B}_0 = \frac{1}{\sqrt{2}}(\sigma_x + \sigma_y)$	$\chi_{B,0} = \cos(\pi/8)V + \sin(\pi/8)H$	$\alpha = 22.5^\circ, \phi = 0$

Table 4.1.: Settings for the Bell test experiment:  $\hat{A}_0, \hat{A}_1$  are the measurement operations in Lab 1 and  $\hat{B}_0, \hat{B}_1$  in Lab 2.

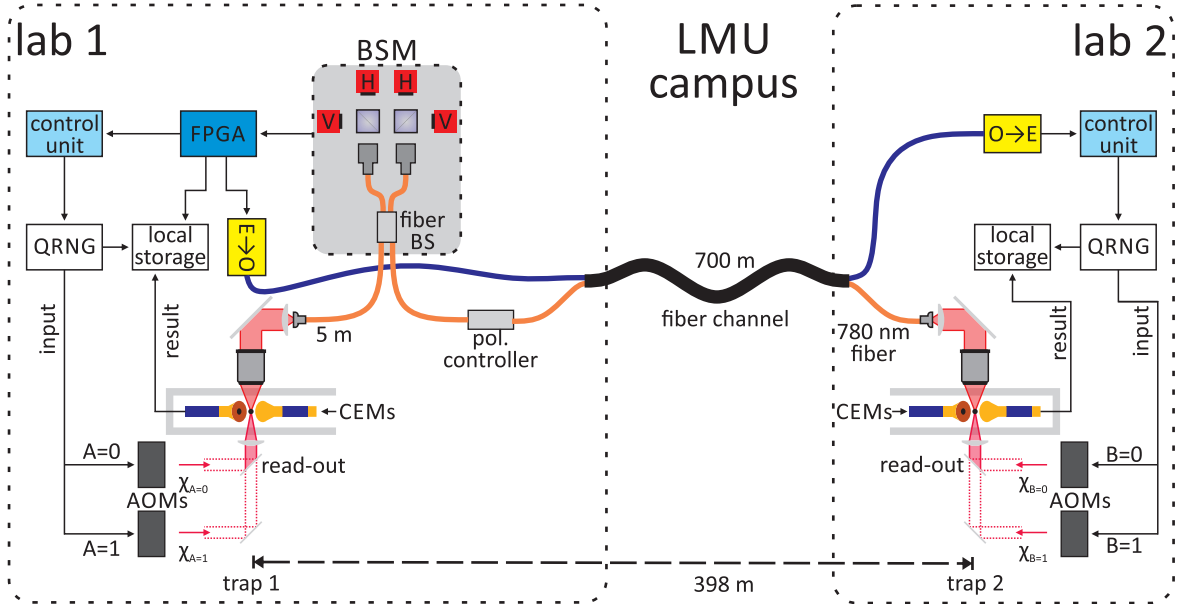


Figure 4.1.: Overview of the Bell test setup: The two trap setup for heralded entanglement as described in Section 2.4.2 and Figure 2.16. For the Bell test experiment the setting of the atomic state read-out is chosen by a random bit from the QRNG. After receiving a heralding signal the control unit in each laboratory requests a random bit from the QRNGs and depending on the bit one of two AOMs creates a read-out pulse with a polarization  $\chi_{ro}$  according to Table 4.1. The result of the measurements is determined by the detection or not detection of ionization fragments by the CEMs. The random bit and the results are recorded locally in each laboratory. The heralding signal is recorded in the local storage of Lab 1.

tection of electrons and  $^{87}\text{Rb}^+$ -ions are predefined with a fixed timing relative to the read-out laser pulse. The measurement outcome is defined as “+1” if there was at least one detector click inside the respective time window while no detection yields a “-1” outcome.

The experimental scheme is the following: two atoms are trapped and synchronously excited. A two photon coincidence detected in the Bell state measurement setup heralding atom-atom entanglement is communicated and triggers the measurement process in both laboratories. The input values that determine the measurement setting are generated by local quantum random number generators (QRNG) (Sec 4.1.2). In each laboratory the local input and output combination is recorded by a local storage unit. Additionally, the heralding signal from the Bell state measurement is recorded in the storage unit of Lab 1. After the measurement the experimental scheme starts again and the procedure is repeated until the experiment is finished.

#### 4.1.1. Closing the detection and the locality loophole

The locality and the detection loopholes (Sec 3.3.1) are of most concern for the actual design since closing them requires well performing measurement devices and a large distance between them.

The detection loophole is opened by the fair sampling assumption that is needed in the

case of insufficient detector efficiencies. Since this experiment applies entanglement swapping, the entanglement creation is heralded by the Bell state measurement result (Sec 2.4). This enables to identify and to obtain measurement results for every entangled pair. Hence, the fair sampling assumption is not needed and the loophole is closed. Inefficiencies of the measurement process, especially of the particle detectors, results in wrong answers and thus will not open the detection loophole but will reduce the resulting  $S$  value.

To close the locality loophole it is necessary to have space-like separation of the measurement processes. The measurement process starts with the random selection of the input and ends with announcing the outcome. Thus, end of the process, i.e., the announcement of the outcome on one side must be outside the forward light cone of the begin of the process, i.e., the random input selection, on the other side. In this experiment the result is announced by a hard wired logic device monitoring the CEMs signals and the latest possible announcement is defined by the end of the acceptance time window for the detection of  $^{87}\text{Rb}^+$ -ions [38], which is the later of time windows for the detection of ionization fragments (Sec 2.3.2).

### Space-like separation of the measurements

The distance between the QRNG in Lab 1 and the comparator devices in Lab 2 is 402.7 m and the distance between the QRNG in Lab 2 and the comparator devices in Lab 1 is 398.0 m (Fig. 4.2). The distances were determined by measuring the distances in each laboratory in combination with data provided by the Bayerisches Landesamt fuer Digitalisierung, Breitband und Vermessung (Bavarian Agency for Digitisation, High-Speed Internet and Surveying, short LDBV) allowing an accuracy of less than 1 m for distances. Thus, the time budget for a space like separation is  $\frac{398.0\text{m}-1\text{m}}{c} > 1324.2$  ns in Lab 1 and  $\frac{401.7\text{m}-1\text{m}}{c} > 1339.9$  ns in Lab 2 [38, 60].

Effectively, the measurement starts with the request of a random bit from the QRNG. Within the next 10 ns the QRNG returns a bit generated less than 60 ns before. To account for possible next neighbor correlations of the QRNG [39, 60] the creation of the previous random bit 20 ns before is set as the starting point of the forward light cone of the the random bit creation. Based on the random bit, one of two beam paths with different polarization  $\chi_{ro}$  (Fig. 4.1) is selected for creating a read-out laser pulse with an acousto-optic modulator (AOM)<sup>1</sup>. A beam waist of 12.5  $\mu\text{m}$  in the AOM and an acoustic frequency of 408 MHz [37] enables to create a pulse that reaches the atom in less than 220 ns after the input is received. For the fast read-out scheme the duration of state selective ionization and subsequent detection of the ionization fragments, depends mainly on the acceleration voltage  $U_{acc}$  between the CEMs. With  $U_{acc} = 4250$  V the duration of the read-out in Lab 1 is  $570 \pm 3$  ns, while in Lab 2 only a  $U_{acc} = 2400$  V is possible (Appendix F) resulting in a duration of  $725 \pm 3$  ns. Finally, the signals from CEMs are converted by comparator electronics to logic signals defining the result of the measurement, which takes another 80 ns. The total time needed for the measurement process, from the generation of the random bit for the input until the end of the ion detection time window, is  $947 \pm 1$  ns in Lab 1 and  $1093 \pm 1$  ns in Lab 2<sup>2</sup> [38, 60]. This is more than 200 ns shorter than the maximal time budget for space-like separation (Fig 4.3).

Additionally to the short duration of the measurement process, it is necessary to preci-

<sup>1</sup>AA Opto-Electronic MT350-A0, 12-800 (Lab 1), Gooch & Housego AOMO 3350-199 (Lab 2)

<sup>2</sup>The much smaller uncertainty of the the total measurement time is due to the fact that it is defined by the request of the random input and the end of the acceptance time window for the ions which both are defined by highly precise signals from the control units.

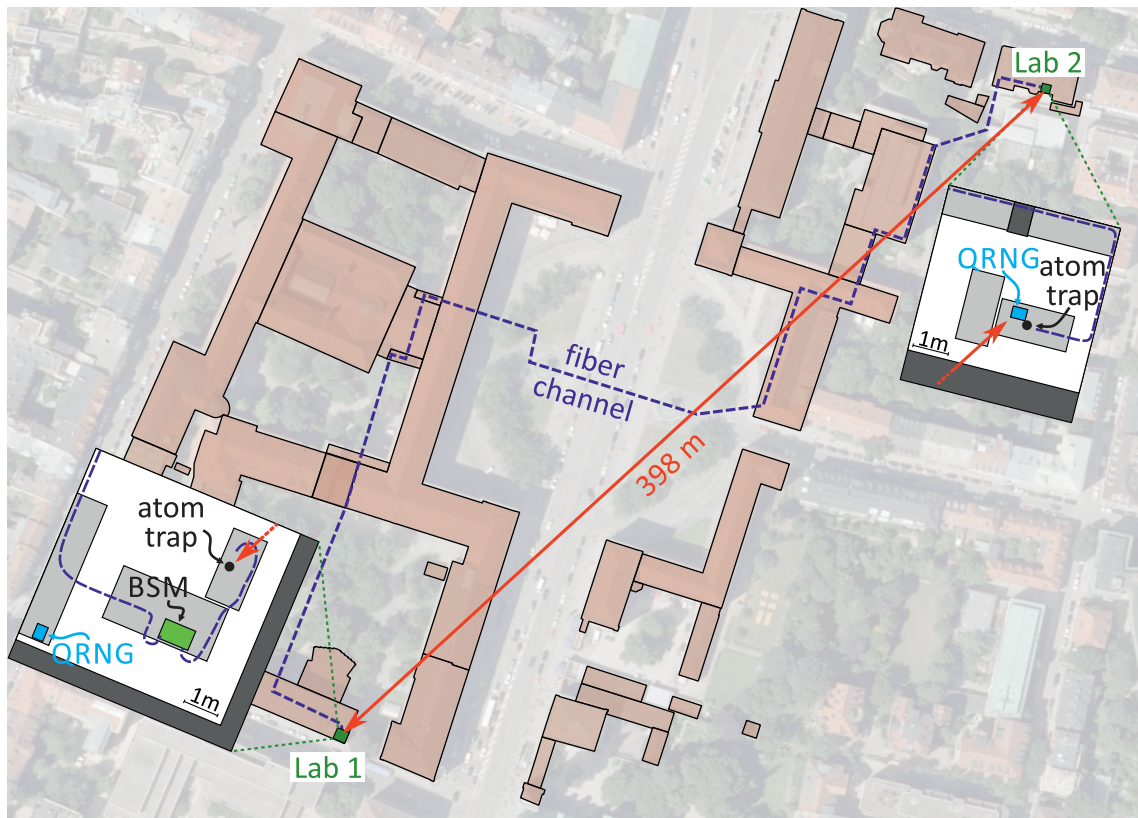


Figure 4.2.: Detailed map of the Bell experiment setup: The location of the two laboratories and the exact position of each device within. The distance of 398 m between trap 1 and the QRNG in Lab 2 (red arrow) is the shortest distances considered for the space like separation of the two measurements. Map data provided by the LDBV.

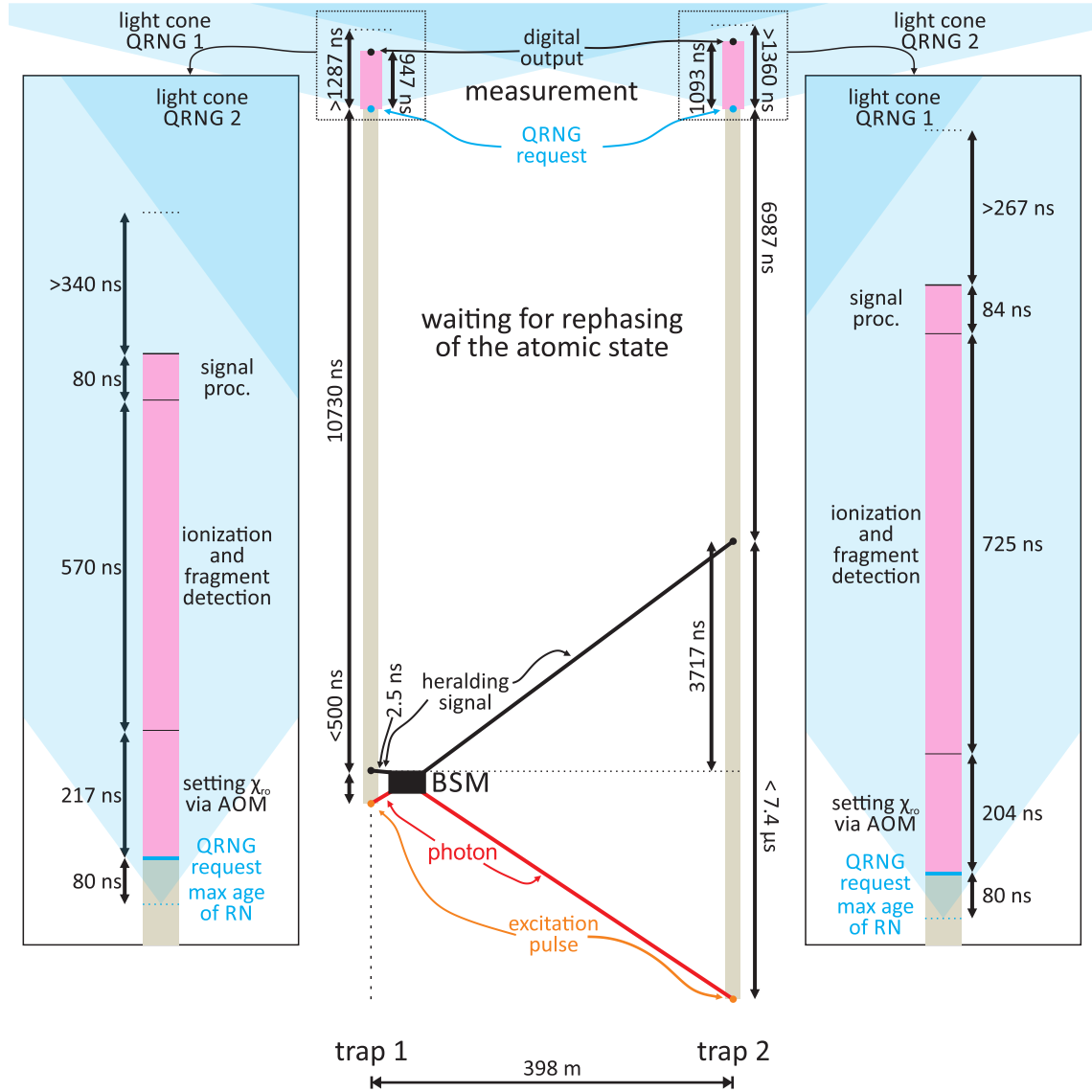


Figure 4.3.: Timing and Space-time diagram of an event during the Bell test experiment [38, 60]: First synchronized excitation (orange), which considered the different photon travel times for photons from each trap, is used to create atom-atom entanglement employing a photonic BSM. In case of a successful atom-atom state creation the heralding signal is send to the trap setups. Then at each trap a fitting waiting time is introduced to allow for space-like separated measurement. Both measurements are composed of input generation, generation of a read-out laser pulse with input depended polarization, state selective ionization with subsequent fragment detection with the CEMs, and signal processing of the CEM pulses.

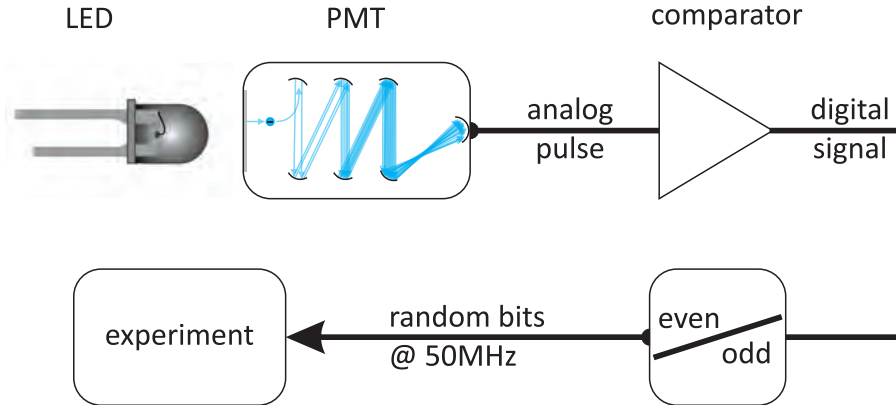


Figure 4.4.: Schematics of the quantum random number generator [39]: The photons emitted by the LED are detected by the PMT and converted to an analog pulse. A comparator converts these into digital signals that are counted within 20 ns intervals, even counts yield “0” while odd yield “1”. This allows for output of random bits with a rate of 50 MHz.

sely time both state measurements to guarantee space-like separation. Since a local state measurement is triggered by the heralding signal, the transmission of this signal is time critical. Inside Lab 1 it is transmitted via a 0.5 m coaxial cable with a transmission time of  $2.5 \pm 0.2$  ns. The transmission to Lab 2 is via an asynchronous optical communication channel and takes  $3717 \pm 7$  ns.<sup>3</sup> Considering the effects of the atoms oscillating in the tightly focused ODT (Sec. 2.3.3), the intensity of the trap lasers is set to values allowing for synchronized rephasing. This requires an additional waiting time that depends on the intensity of the ODT laser beam. For the actual parameters this results in 10730 ns in Lab 1 and 6987 ns in Lab 2 before the actual measurement process can start. Thus in total the measurement in Lab 2 starts 28.5 ns before the measurement in Lab 1. This results for a total measurement duration of  $947 \pm 1$  ns in Lab 1 in a margin of 340 ns for space-like separation and for a total measurement duration of  $1093 \pm 1$  ns in Lab 2 in a margin of 267 ns (Fig 4.3). A more detailed description of the closing of the locality loophole can be found in [38, 60].

#### 4.1.2. Generation of random inputs

To generate independent and unpredictable inputs for the Bell test two quantum random number generators that are based on photon counting are employed [39]. The light emitted by an LED is strongly attenuated and then detected by a photo-multiplier tube (PMT). The analogue electrical pulses from the PMT are converted by a comparator to digital signals. The signals are counted over a period of  $t_s = 20$  ns by an FPGA (Fig. 4.4) and the parity of these counts yields the random bit output. In particular, an even number of counts within the interval is interpreted as “0” and odd as “1”. This allows an output of random bits at a rate of 50 MHz.

<sup>3</sup>The error margin here is only to an uncertainty of cable or glass fiber length and should not to be confused with a jitter of the signal

### Physical model of the QRNG

The randomness of the output bit arises from photon detection theory: In the case of a light source with constant intensity, the number of photon detection events  $n$  in a time period with length  $t_s$ , which is longer than the coherence time  $\tau_c$  of the light source, are uncorrelated. This leads to a Poisson distribution [101, 102]

$$Pr(n, \mu) = \frac{\mu^n}{n!} e^{-\mu}$$

for the probability to detect  $n$  clicks for a mean of  $\mu$  clicks per time period. The LED is a broad band light source with a coherence time of  $\tau_c \leq \frac{1}{\Delta\omega}$ . For a typical spectral width of  $\Delta\omega > 5 \cdot 10^{13}$  the coherence time is below  $t_c < 20$  fs [102]. This means the number of detections in each time interval is independent from any event inside the backward light cone and by this random.

To allow for a constant LED output, it is stabilized by a digital feedback loop leading to Poisson distributed counts of the PMT. The comparator only registers pulses exceeding a preset threshold voltage, which introduces an extendable dead time  $t_d$  for counting photons. This deadtime depends on the threshold voltage  $U_t$  and the pulse shape of the PMT signal. It effects counts inside the time window and leads to a modified Poisson distribution (equation (2) in [39])

$$Pr(n, \mu_r, t_d, t_s) = \frac{\mu_r^n}{n!} e^{-\mu_r} \sum_{k=0}^{K-n} \frac{(-\mu_r)^k}{k!} e^{\mu_r} \left( \left( 1 - (k+n-1) \frac{t_d}{t_s} \right) \right)^{n+k} \quad (4.1)$$

with the actual mean of registered detections

$$\mu_r = \mu \cdot e^{-\mu \frac{t_d}{t_s}} \quad (4.2)$$

and the maximum of possible registered detection events in one time interval  $K \leq \left\lceil \frac{t_s}{t_d} \right\rceil$ . By summing up (4.1) for different  $n$  the probabilities for the two possible outputs "0" and "1" follow.

$$Pr("0") = \sum_{n=0,2,\dots}^{\infty} Pr(n, \mu_r, t_d, t_s) \quad (4.3)$$

$$Pr("1") = \sum_{n=1,3,\dots}^{\infty} Pr(n, \mu_r, t_d, t_s) \quad (4.4)$$

For certain values of  $\mu_r$ ,  $t_s$ , and  $t_d$  both probabilities are equal  $Pr("0") = Pr("1") = 1/2$  and unbiased random bits can be obtained [39].

### Estimation the predictability based on technical imperfections

Even though the physical model of the QRNG principally allows for perfectly unbiased random outputs, a real world implementation has imperfections that potentially can introduce a predictability of the output bits. Especially critical are photon count rate and the comparator

threshold voltage  $U_t$ , which defines the dead time  $t_d$ , since both have a direct effect on the output probabilities (4.3) and (4.4). To estimate a possible predictability the bias

$$\begin{aligned} B(\mu_r, U_t) &= Pr("1") - \frac{1}{2} \\ &= \sum_{n=1,3,\dots}^{\infty} Pr(n, \mu_r, t_d(U_t), t_s) - \frac{1}{2} \end{aligned} \quad (4.5)$$

depending on the imperfections of  $U_t$  and  $\mu_r$  is investigated. For operation of the QRNG the time periode  $t_s = 20$  ns is fixed by the clock of the FPGA with a negligible jitter.

**Photon count rate** Knowledge of the photon count rate and its fluctuation can result in a possible predictability. The mean number of registered counts per time period  $\mu_r$  (4.2) depends on the mean number of photon counts  $\mu(I_{LED}, T_{LED})$  and the extendable dead time  $t_d(U_t)$ . The count rate depends on the LED current  $I_{LED}$  and temperature  $T_{LED}$ , while the extendable dead time depends on the comparator threshold voltage  $U_t$ :

$$\mu_r(I_{LED}, T_{LED}, U_t, t_s) = \mu(I_{LED}, T_{LED}) \cdot e^{\left(-\mu(I_{LED}, T_{LED}) \frac{t_d(U_t)}{t_s}\right)}. \quad (4.6)$$

Considering a fixed  $U_t$  and  $t_s = 20$  ns the bias (4.5) becomes a function of only  $I_{LED}$  and  $T_{LED}$ . To obtain a constant photon count rate during the operation of the QRNG the temperature is stabilized and current is controlled by a digital feedback set on fixed registered photon count rate  $\mu_{r,set}$  [39]. With this the count rate shows only the expected statistical fluctuations around the set value  $\mu_{r,set}$ . The value of  $\mu_{r,set}$  resulting in minimal bias of the random bits has to be determined after each start of the QRNG. To find this value the QRNG is operated with a different digital feedback mode that controls the current with a feedback stabilizing on zero bias. After some time the system sets and the registered photon count rate  $\mu_r$  becomes constant while the bias of the input bits is very close to zero. This value of  $\mu_r$  is then used to set point  $\mu_{r,set}$  of the digital feedback for a fixed photon count rate, which enables for an operation of the QRNG with a residual bias of  $\|B\| < 1.04 \cdot 10^{-5}$  (Supplementary material of [60]).

**Threshold level of the comparator** The threshold voltage of the comparator  $U_t$  is set by a digital to analog converter (DAC). Any fluctuations of this voltage or noise on the analog signal from the PMT will lead to a change of the bias and thus of the predictability. To characterize the influence of fluctuations and noise of the threshold level and the PMT signal, the dependence of the bias  $B$  for a fixed LED current  $I_{LED}$  on the threshold voltage  $U_t$  around the working point  $U_{set} = -8.847$  mV with nearly zero bias is measured (Fig 4.5). A fit of the measured data to a second order polynomial yields

$$B(U_t) = 142.008 \frac{1}{V^2} U_t^2 + 1.957 \frac{1}{V} U_t + 0.0062, \quad (4.7)$$

which can be used to estimate the bias for a given change of the threshold  $U_f$ , e.g. introduced by noise or drift of the DAC, of using  $B(U_{set} + U_f)$ .

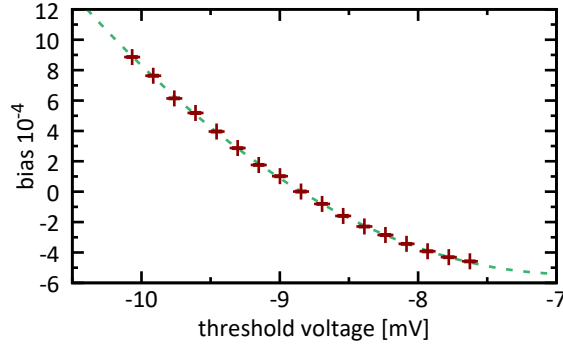


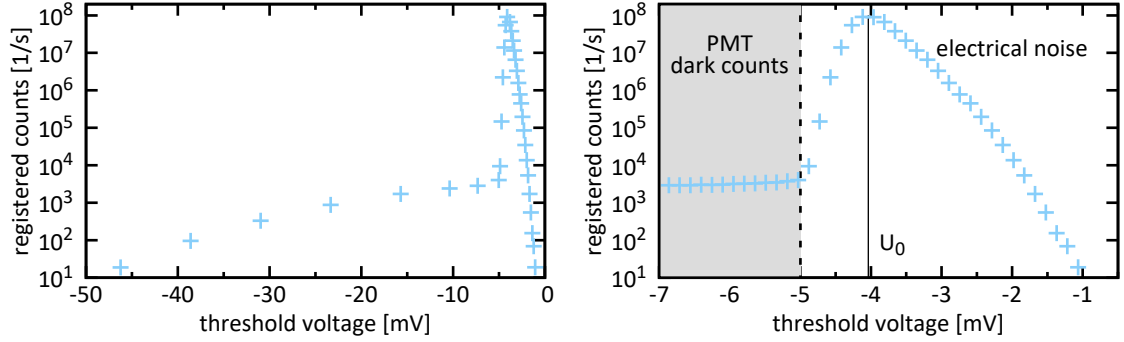
Figure 4.5.: Bias of the QRNG for fixed  $I_{LED}$  depending on the threshold voltage  $U_t$  of the comparator: measured data (red cross) and fit of a quadratic polynomial (4.7) (green, dashed line).

**Characterization of electrical noise** Since the noise of the PMT signal and of the threshold voltage both influence the comparator counts in the same manner, and if known their effect on the bias can be calculated via (4.7). However, it is hard to measure the noise of both channels of the comparator individually during operation of the QRNG without influencing them. Nevertheless, it is possible to estimate the parameters of the noise based on a measurement of the count rate of the comparator while the LED is off. A scanning the threshold voltage  $U_t$  yields an dark count rate depending on the threshold voltage (Fig. 4.6). This measurement (Fig. 4.6) shows two different regions of comparator dark counts: for large negative  $U_t < -5$  mV the counts are caused by dark counts of the PMT showing a typical behavior of random pulses with Gaussian distribution in pulse height with a rate of ca  $5 \cdot 10^3$  1/s. For threshold voltages  $-5$  mV  $\leq U_t \leq 0$  mV electrical noise is the dominant cause of counts. It leads to a peak in the count rate at  $U_t = 4.04$  mV of  $9 \cdot 10^7$  1/s (Fig. 4.6b). This is the zero level  $U_0$  for the PMT signal and the effect of the noise is the highest close to  $U_0$  even small fluctuations will trigger the comparator. Moving further away from  $U_0$  only larger and larger fluctuations, i.e. larger amplitudes in the noise, will trigger the comparator. Therefore, it is possible to estimate the amplitude distribution of the combined electrical noise from the dark count measurement. To characterize the amplitude distribution of the noise, assuming a Gaussian distribution, to each side of the peak at  $U_0$  an error function of the form

$$C^\pm(A, \mu, \sigma, U_t) = A \cdot \left( 1 \pm \operatorname{erf} \left( \frac{U_t - \mu}{\sqrt{2}\sigma} \right) \right) \quad (4.8)$$

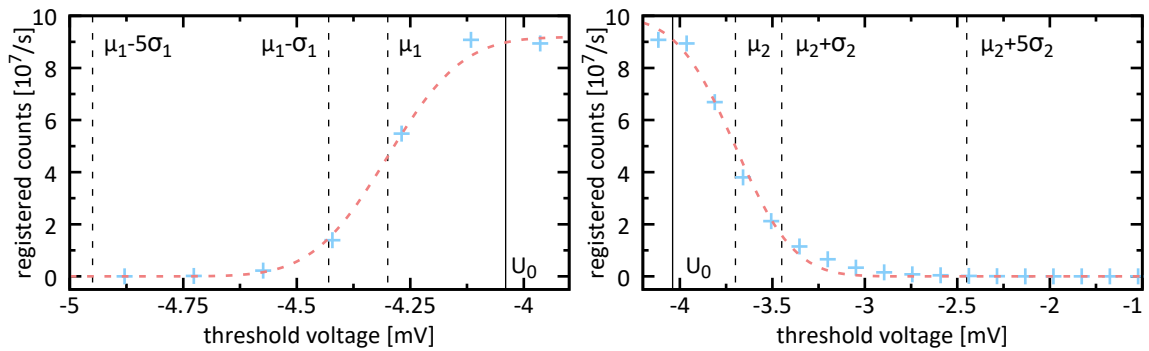
is fitted. A fit of the rising slope to  $U_t \leq U_0$   $C^+$  results in  $\mu_1 = -4.30$  mV and  $\sigma_1 = 0.13$  mV and a fit of the falling slope to  $U_t \geq U_0$   $C^-$  results in  $\mu_2 = -3.70$  mV and  $\sigma_2 = 0.25$  mV (Fig. 4.7).

**Temperature fluctuation** To avoid drifts of the important parameters caused by temperature fluctuations, critical parts of the QRNG like LED, PMT, and the comparator are actively stabilized with a precision better than  $\pm 0.15$  °C. This residual fluctuation can influence the threshold voltage  $U_t$  of the comparator. The digital to analog converter (DAC) providing the threshold voltage and the comparator are both specified to less than  $10^{-5}$  V/°C leading to a maximal drift of  $\pm 0.003$  mV.



- (a) Comparator counts depending on the threshold voltage  $U_t$ . Measured with LED current off. The lower count rates  $< 10^4$  for  $U_t < -5$  mV are caused by PMT dark counts while the peaking count rate for  $-5 \text{ mV} \leq U_t \leq 0$  mV is caused by electrical noise. (The detailed view of the threshold values between  $-7 \text{ mV} \leq U_t \leq 0$  mV in (b) includes additional measurement points)
- (b) Detailed view of (a) for threshold values for  $-7 \text{ mV} \leq U_t \leq 0$  mV with additional measurement points. The count rate for threshold voltage of  $U_t > -5$  mV allows to characterize the electrical noise. The fluctuations are centered around the zero level  $U_0 = 4.04$  mV.

Figure 4.6.: Noise of PMT signal and comparator threshold voltage  $U_t$ .



- (a) Range  $U_t \leq U_d$ : fitting  $C^+(A, \mu_1, \sigma_1, U_t)$  (4.8) results in  $A = 4.59408 \cdot 10^7$ ,  $\mu_1 = -4.30$  mV, and  $\sigma_1 = 0.13$  mV
- (b) Range  $U_t \geq U_d$ : fitting  $C^-(A, \mu_2, \sigma_2, U_t)$  (4.8) results in  $A = -4.98186 \cdot 10^7$ ,  $\mu_2 = -3.70$  mV, and  $\sigma_2 = 0.25$  mV

Figure 4.7.: Fit of the error function (4.8) to the measured count rate.

**“Reasonable” bound for the predictability** The analysis of the imperfections of the QRNG including setting of the photon count rate, electrical noise, and temperature drifts allows to derive an upper bound for the predictability

$$\tau \geq \left\| Pr("1") - \frac{1}{2} \right\|$$

of the QRNG output. Since, e.g., the electrical noise has high frequency components the actual probability  $Pr("1")$  can be different for each output but  $\tau$  is a bound for every output. Additionally one has to consider the possible information about the QRNG of a possible “adversary” that defines the LHV or the measurement results. A reasonable model allows the “adversary” to know only parameters of the QRNG which are accessible from the outside. These also include information about the current photon count rate and the current temperature inside the QRNG because both are stabilized and the information is externally available. This yields a predictability of  $\tau = 1.04 \cdot 10^{-5}$  determined by analyzing the output of the QRNG and bounding its bias (Supplementary material of [60]). This already includes the relatively small predictability stemming from the temperature drift which is  $\max(\|B(U_{set} - 0.003)\|, \|B(U_{set} + 0.003)\|) \leq 1.67 \cdot 10^{-7}$  (4.7).

**“Paranoid” bound for the predictability** For the Bell test experiment it is necessary to minimize assumptions to prevent loopholes. Hence, a more “paranoid” model of the information of the “adversary” is preferable. In this model the full information on the actual internal parameters, which include photon count rate, electrical noise on the PMT signal as well as threshold voltage, and temperature, is known to an “adversary” (Supplementary material of [60]). Since a predictability stemming from the electrical noise cannot be bounded by analyzing the output data of the QRNG, it is necessary to use a model for the noise for this task. For this the measured noise distribution (Fig 4.6b) is added to the set threshold voltage  $U_{set}$  (Fig. 4.8). Now it is possible to bound the resulting predictability using the fit of the noise from Figure 4.7 and a two sided  $5\sigma$  interval (Fig. 4.8). Additionally, the effect of the temperature has to be considered and is added to both  $5\sigma$  intervals. This results in a predictability of

$$\max\left(\|B(U_{set} - 0.26 \text{ mV} - 5 \cdot 0.13 \text{ mV} - 0.003 \text{ mV})\|, \|B(U_{set} + 0.34 \text{ mV} + 5 \cdot 0.25 \text{ mV} + 0.003 \text{ mV})\|\right) \leq 6.2 \cdot 10^{-4}.$$

Together with the effect of the predictability arising from the setting of the photon count rate of  $1.04 \cdot 10^{-5}$ , the bound for the total predictability of  $\tau \leq 6.3 \cdot 10^{-4}$  is found (Supplementary material of [60]).

#### 4.1.3. Residual assumptions made for the Bell test

As discussed in Chapter 3, assumptions made for a Bell test limit the tested LHV theories and by this need to be known to make correct statements. The design of this experiment, especially, the heralded entanglement generation, and the event ready and space-like separated measurements, allows for minimizing the assumptions made on the LHV theories. However, it is not possible to abandon all assumptions. The residual assumptions needed for this experiment belong into two categories. The first category are assumptions based on well established physical theories:

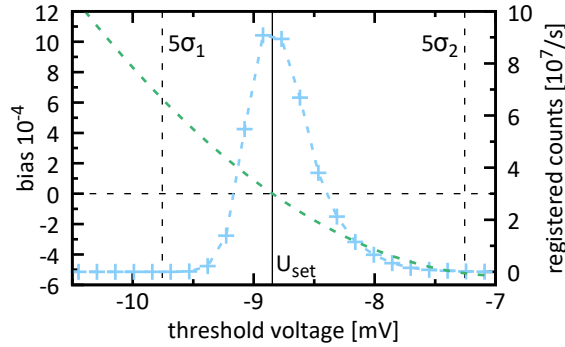


Figure 4.8.: Comparator counts caused by electrical noise (blue) of PMT signal and threshold voltage centered at the set threshold level  $U_{set} = U_0 = -8.847$  mV. Fit of the bias dependence on the threshold voltage (4.7) (green). The horizontal dashed line indicates zero bias and the two vertical dashed lines indicate the  $5\sigma$  interval of the electrical noise based on the fit from Figure 4.7.

**no faster than light communication** To allow for space-like separation of measurements of Alice and Bob it is assumed that information transmission is limited to  $c$  the speed of light in vacuum.

**physical model of the QRNGs** Each of the two QRNGs based on photon counting (physical model in Sec. 4.1.2), provides random outputs that are only predictable up to the specified level of  $\tau \leq 6.3 \cdot 10^{-4}$ .

These two assumptions limit the LHV theories tested in this experiment. The first assumption that communication is limited by the speed of light is intrinsic to local-realism, but the assumption that the QRNGs produce a random output based on photon counting restricts the test to theories in which this process of photon counting is indeed an independent process and thus allows for the creation of unpredictable inputs.

The second category concerns the correctness of time and distance measurement as well as a proper functioning data recording:

**distance measurements** The distances provided by the LDBV and the distance measurements inside the laboratories are correct within the error margins given.

**clock and timing** The time synchronization of the experiment, which is provided by the 100 Mhz clock and distributed to all time critical devices, is stable and correct as well as the timing of the measurements.

**data recording** The classical signal and data recording devices are trustworthy and reliable.

Listing these assumptions might seem meticulous and such assumptions are actually implicitly made for all experiments. Moreover, it is hard to formulate a serious local-realistic theory that would exploit them. But since the statement of a Bell test experiment is very fundamental all assumptions, even the seemingly obvious ones, should be stated to avoid confusion about the results.

## 4.2. Evaluation with Hypothesis Testing

In order to draw conclusions after a Bell experiment was conducted, a robust analysis of the whole data collected during the experiment is necessary. As described in Section 3.3.2 hypothesis testing allows for such an analysis. The decision on the null hypothesis is based on the  $p$  value that is calculated from the result of the experiment. For this Bell experiment two different ways of calculating an upper bound of the  $p$  value (3.22) are employed. The first bound, which is based on martingales and concentration inequalities follows [16], and is a relatively simple formula especially well suited for experiments with a small absolute violation of Bell's inequality but many events. The second bound from [17] based on a non-local game is tighter than the first but needs a lot more computational effort. Calculating both bounds allows for a better comparison with experiments using only one of the methods.

### Definition of the null hypothesis

The first step for the hypothesis test is to formulate the null hypothesis, i.e. that “the recorded data can be explained with local-realistic theories”, in a mathematical formulation that allows to calculate  $p$  (3.22). For this it is necessary to formulate (3.1) according to the experimental design: the experiment has two measurement devices, Alice in Lab 1 and Bob in Lab 2. For each event both devices receive an input from the QRNGs, which is triggered by the heralding signal  $H_i \in \{-1, +1\}$ , and produce an output. For the  $i$ -th event Alice's input is called  $A_i \in \{0, 1\}$  and her output is called  $X_i \in \{-1, +1\}$ . The analog definition for Bob is  $B_i \in \{0, 1\}$  and  $Y_i \in \{-1, +1\}$ . The heralding signal  $H_i$  takes the value  $-1$  if the state  $\Psi^-$  and  $+1$  if the state  $\Psi^+$  is prepared. The functions  $g^\pm(A, B)$  are defined as

$$\begin{aligned} g^+(A, B) &= -1 \vee (A, B) \neq (1, 1) \\ g^+(A, B) &= +1 \quad (A, B) = (1, 1) \end{aligned} \quad (4.9)$$

for events with the heralding signal  $H_i = +1$  and

$$\begin{aligned} g^-(A, B) &= -1 \vee (A, B) \neq (1, 0) \\ g^-(A, B) &= +1 \quad (A, B) = (1, 0) \end{aligned} \quad (4.10)$$

for  $H_i = -1$ . These allow to write  $S$ , (3.1), in the form

$$S^\pm = \sum_{A, B \in \{0, 1\}} g^\pm(A, B) \frac{\pm N_{A, B}^{X=Y} - \pm N_{A, B}^{X \neq Y}}{\pm N_{A, B}^{X=Y} + \pm N_{A, B}^{X \neq Y}} \leq 2 \quad (4.11)$$

for the two states  $\Psi^\pm$ . The  $g^\pm(A, B)$  are chosen that the expected  $S$  value for the experiment is  $S \geq 2$ , based on the entangled state and measurement directions (Tab 4.1). The formulation of  $S^+$  for  $\Psi^+$  might seem different from (3.1) but renaming the inputs or outputs would restore the old form and thus the bounds for local-realism (3.5) and quantum mechanics (3.10) are still the same.

Considering the memory loophole (Sec. 3.3.1) one can modify (4.11) making it immune to exploiting finite statistics by approximating  $\pm N_{A, B}^{X=Y} + \pm N_{A, B}^{X \neq Y}$  with  $\pm N/4$ . Note, that this is allowed for only relatively large number of total events  $N$  and unbiased inputs. This leads to the used formulation of the null hypothesis

$$S^\pm = \frac{1}{\pm N} \sum_{i=1}^{\pm N} 4 \cdot g^\pm(A_i, B_i) X_i Y_i \leq 2. \quad (4.12)$$

Furthermore, this style of writing the CHSH inequality allows to formulate a CHSH inequality combining both states  $\Psi^+$  and  $\Psi^-$

$$S_{comb} = \frac{1}{N} \sum_{i=1}^N 4 \cdot \left( \frac{1+H_i}{2} g^+(A_i, B_i) X_i Y_i + \frac{1-H_i}{2} g^-(A_i, B_i) X_i Y_i \right) \leq 2. \quad (4.13)$$

It is important to note here, that this definition unlike (3.1) does not use absolute values, thus (4.12) and (4.13) are strictly speaking bounded from two sides for LHV theories  $-2 \leq S^\pm \leq 2$ . However, permuting outcomes for  $g^\pm(A, B)$  allows to formulate an inequality with  $S^\pm \leq 2$  for every experimental realization. This one sided bound is preferable for finding an upper bound of the  $p$  value, but one has to consider, that for a hypothesis test the  $g^\pm(A, B)$  should be fixed before the experiment. Therefore, in this experiment (4.9) and (4.10) are fixed beforehand and (4.12) and (4.13) with  $S^\pm, S_{comb} \leq 2$  are tested.

#### 4.2.1. Bound based on martingales and concentration inequalities

This method is inspired by a work of Richard Gill [16] published in 2003. He showed that Hoeffding's inequality [103] or other concentration inequalities, e.g., Azuma's inequality [104], can be used to calculate a bound for the probability of an experiment following LHV theories resulting in a certain  $S > 2$  or higher. For this he modeled a Bell test experiment as a supermartingale without using the assumption of independent and identically distributed (i.i.d.) events closing the memory loophole (Sec. 3.3.1). So his method can be used to calculate  $p$  via

$$p = Pr(S \geq S_m) \leq e^{\left(\frac{-(S_m-2)^2 N}{64}\right)} \quad (4.14)$$

depending on the measured  $S$  value  $S_m$  and the total number of events  $N$ .

Here a method is derived that yields a tighter bound on the  $p$  value using an inequality shown by McDiarmid [105]. This inequality bounds processes concerning martingale difference sequences (MDS).

#### Bounding a martingale by its difference sequences

In [105] Colin McDiarmid presented an inequality ((6.1) on page 165) bounding the probability of the sum of a martingale difference sequence, which is a martingale, reaching a certain value or higher. There he considers a martingale difference sequence (MDS)  $M_1, \dots, M_n$  with  $-a_k \leq M_k \leq 1 - a_k$  for each  $k$  in  $n$ . Further, he defines  $a$  and  $\bar{a}$  as  $a = \frac{1}{n} \sum_{k=1}^n a_k$  and  $\bar{a} = 1 - a$ . With this he shows

$$P\left(\sum_{k=1}^n M_k \geq nt\right) \leq \left(\left(\frac{a}{a+t}\right)^{a+t} \left(\frac{\bar{a}}{\bar{a}-t}\right)^{\bar{a}-t}\right)^n \quad (4.15)$$

for all  $t > 0$ .

#### From the CHSH inequality to a martingale difference sequence

To use this to bound the probability to measure a certain  $S$  or higher in an experiment, it is necessary to derive a fitting MDS based on the CHSH inequality. Starting with (4.12) one

can define a violation of the inequality as

$$\begin{aligned}
\delta^\pm &= S^\pm - 2 \\
&= \frac{1}{\pm N} \sum_{i=1}^{\pm N} 4 \cdot g^\pm(A_i, B_i) X_i Y_i - 2 \\
&= \frac{1}{\pm N} \sum_{i=1}^{\pm N} 4 \cdot g^\pm(A_i, B_i) X_i Y_i - \frac{1}{\pm N} \sum_{i=1}^{\pm N} 2.
\end{aligned} \tag{4.16}$$

For the case of  $\pm N \rightarrow \infty$  the CHSH inequality limits  $\delta^\pm$  to

$$\delta^\pm = \frac{1}{\pm N} \sum_{i=1}^{\pm N} (4 \cdot g^\pm(A_i, B_i) X_i Y_i - 2) \leq 0. \tag{4.17}$$

By multiplying this by  $N^\pm$  results in the supermartingale

$$N^\pm \delta^\pm = \sum_{i=1}^{\pm N} (4 \cdot g^\pm(A_i, B_i) X_i Y_i - 2) \leq 0 \tag{4.18}$$

that can be bounded from above by the martingale

$$N^\pm \delta^\pm = \sum_{i=1}^{\pm N} (4 \cdot g^\pm(A_i, B_i) X_i Y_i - 2) = 0. \tag{4.19}$$

The individual terms of this martingale form a MDS with a maximum range of

$$-6 \leq 4 \cdot g^\pm(A_i, B_i) X_i Y_i - 2 \leq 2.$$

By normalizing the range to 1

$$-\frac{3}{4} \leq \frac{4 \cdot g^\pm(A_i, B_i) X_i Y_i - 2}{8} \leq \frac{1}{4} \tag{4.20}$$

one can define a new MDS

$$Z_i^\pm = \frac{4 \cdot g^\pm(A_i, B_i) X_i Y_i - 2}{8} \tag{4.21}$$

that fulfills the demands of (4.15) with  $a_k = 3/4$  for all  $k$ . From this follows  $a = 3/4$  and  $\bar{a} = 1/4$  and it is possible to bound the probability of  $\sum_{i=1}^{\pm N} Z_i^\pm \geq tN^\pm$  by

$$P\left(\sum_{i=1}^{N^\pm} Z_i \geq tN^\pm\right) \leq \left(\left(\frac{3/4}{3/4+t}\right)^{3/4+t} \left(\frac{1/4}{1/4-t}\right)^{1/4-t}\right)^{N^\pm}. \tag{4.22}$$

**Bounding the probability for  $S \geq S_m$**

Using  $Z_i^\pm$  in (4.12) yields

$$\begin{aligned}
\frac{1}{\pm N} \sum_{i=1}^{\pm N} Z_i^\pm &= \frac{1}{\pm N} \sum_{i=1}^{\pm N} \frac{4 \cdot g^\pm(A_i, B_i) X_i Y_i - 2}{8} \\
&= \frac{S^\pm - 2}{8}
\end{aligned}$$

setting  $t = \frac{S_m - 2}{8}$ , with  $S_m$  being the measured  $S$  value, allows to bound the probability for a certain  $S_m$  or a higher by

$$\begin{aligned} Pr(S \geq S_m) &= \left( \left( \frac{3/4}{3/4 + \frac{S_m - 2}{8}} \right)^{3/4 + \frac{S_m - 2}{8}} \cdot \left( \frac{1/4}{1/4 - \frac{S_m - 2}{8}} \right)^{1/4 - \frac{S_m - 2}{8}} \right)^N \\ &= \left( \frac{1}{\left(1 + \frac{\delta_m}{6}\right)^{\frac{6 + \delta_m}{8}} \cdot \left(1 - \frac{\delta}{2}\right)^{\frac{2 - \delta_m}{8}}} \right)^N \end{aligned} \quad (4.23)$$

with  $\delta_m = S_m - 2$ . This bound for  $p$  is derived without making additional assumptions, e.g., assuming i.i.d. events or assumptions on a possible history dependence in the LHV theories, and thus it does not open possible loopholes. (4.23) can be derived in the same manner for  $S_{comb}$ .

### Effect of partially predictable inputs

For deriving the CHSH inequality (3.5) independent and unpredictable inputs are assumed (Sec. 3.2.1). In an actual experiment one is always left with partially predictable inputs (Sec 4.1.2). This changes the bound of  $S \leq 2$  for LHV theories: for an LHV model the estimate of (4.12) is

$$\begin{aligned} E(S) &= \frac{4}{\pm N} \sum_{i=1}^{\pm N} \left[ \sum_{A, B \in \{0,1\}} \left( g^\pm(A, B) \cdot Pr(A_i = A) \cdot Pr(B_i = B) \right. \right. \\ &\quad \left. \left. \sum_{X, Y \in \{0,1\}} (X \cdot Y \cdot Pr(X_i = X|A, H_i, \lambda, G_{A,i}) \cdot Pr(Y_i = Y|B, H_i, \lambda, G_{B,i})) \right) \right]. \end{aligned} \quad (4.24)$$

$Pr(X_i = X|A, H_i, \lambda, G_{A,i})$  and  $Pr(Y_i = Y|B, H_i, \lambda, G_{B,i})$  may depend on the heralding signal  $H_i$  and the previous history of the experiment  $G_{A,i}, G_{B,i}$ <sup>4</sup>. The partial predictability of the inputs  $A_i, B_i$  can be written as

$$\frac{1}{2} - \tau_A \leq Pr(A_i = 1) \leq \frac{1}{2} + \tau_A, \quad (4.25)$$

$$\frac{1}{2} - \tau_B \leq Pr(B_i = 1) \leq \frac{1}{2} + \tau_B \quad (4.26)$$

with  $\tau_A, \tau_B \in [-1/2, +1/2]$ .

Considering an example for the  $\Psi^+$  state with  $\tau = \max(\tau_A, \tau_B)$ ,  $Pr(A_i = 0) = 1/2 + \tau$  and  $Pr(B_i = 0) = 1/2 + \tau$  a deterministic LHV strategy producing always anti-correlated

<sup>4</sup> $G_{A,i}, G_{B,i}$  can include the hole backwards light cone of the announcement of the measurement outcome on their side.

measurement outcomes will produce an expectation value of

$$\begin{aligned}
E(S) &\leq 4 \left[ (-1)(-1) \left(\frac{1}{2} + \tau\right)^2 + (-1)(-1) \left(\frac{1}{2} + \tau\right) \left(\frac{1}{2} - \tau\right) \right. \\
&\quad \left. + (-1)(-1) \left(\frac{1}{2} - \tau\right) \left(\frac{1}{2} + \tau\right) + (+1)(-1) \left(\frac{1}{2} - \tau\right)^2 \right] \\
&= 4 \left[ \left(\frac{1}{4} + \tau + \tau^2\right) + \left(\frac{1}{4} - \tau^2\right) + \left(\frac{1}{4} - \tau^2\right) - \left(\frac{1}{4} - \tau + \tau^2\right) \right] \\
&= 4 \left(\frac{1}{2} + 2\tau - 2\tau^2\right) = 2 + 8(\tau - \tau^2).
\end{aligned}$$

It is easy to verify that this is the maximum for all 16 deterministic LHV strategies (Tab. 3.3). It is possible to find such strategies for all combinations of state and input probabilities. Considering now many events and a predictability bounded by (4.25) and (4.26) for all events it is possible to bound the CHSH value by

$$S \leq 2 + 8(\tau - \tau^2) \quad (4.27)$$

with  $\tau = \max(\tau_A, \tau_B)$ .

Here it is important to state, that this bound is independent of the actual reason for the predictability. It can be due to electrical noise and other technical imperfections as assumed in this experiment (Sec. 4.1.2), due to history dependence, e.g., next neighbor correlations. In and case the LHV theories allowing for a prediction of the physical process in the random number generators would utilize it for the generation of output values, yet, would be always bound by (4.27).

### Calculation of the $p$ value with partially predictable inputs

With this updated bound a new MDS can be derived from (4.21)

$$\tilde{Z}_{i,\pm} = \frac{4 \cdot g^\pm(A_i, B_i) X_i Y_i - (2 + 8(\tau - \tau^2))}{8}$$

with  $a = 3/4 + \tau - \tau^2$  and  $\bar{a} = 1/4 - \tau + \tau^2$ . Setting  $t = \delta_m - \tau + \tau^2$  leads than to a new bound for a certain  $S_m$  or a higher one

$$Pr(S \geq S_m) \leq p_m = \left( \left( \frac{3/4 + \tau - \tau^2}{3/4 + \frac{\delta_m}{8}} \right)^{3/4 + \frac{\delta_m}{8}} \left( \frac{1/4 - \tau + \tau^2}{1/4 - \frac{\delta_m}{8}} \right)^{1/4 - \frac{\delta_m}{8}} \right)^N \quad (4.28)$$

This is an upper bound of the  $p$  value of the hypothesis test.

### 4.2.2. Bound derived from a non-local game

For this approach the Bell test is formulated as a game. Alice and Bob have to generate correlated or anticorrelated outputs based on the inputs given. They win a round if they produce the right correlation for the given inputs. The challenge of the game is that each party only knows its local input in each round [84]. To design a game for the CHSH inequality

(3.1) one defines the winning correlations as the ones that would lead to  $S_{i-1} \leq S_i$  for the  $i$ -th event in a Bell test. Using (4.9) and (4.10) one can define a winning function

$$w_i^\pm = \frac{g^\pm(A_i, B_i) X_i Y_i + 1}{2}$$

for  $H_i = \pm 1$  and a winning function for both  $H_i$  combined

$$w_i^{combo} = \frac{1 + H_i}{2} \frac{g^+(A_i, B_i) X_i Y_i + 1}{2} + \frac{1 - H_i}{2} \frac{g^-(A_i, B_i) X_i Y_i + 1}{2}$$

$w_i^{\pm, combo}$  is 1 if the game is won and otherwise 0.

$$W^\pm = \sum_{i=1}^N \frac{1 \pm H_i}{2} w_i^\pm$$

and

$$W_{combo} = \sum_{i=1}^N w_i^{combo}$$

count the rounds won by Alice and Bob. For local-realistic theories the winning probabilities in each round  $Pr(w_i^\pm = 1)$  and  $Pr(w_i^{combo} = 1)$  is bounded by

$$Pr(w_i^\pm = 1), Pr(w_i^{combo} = 1) \leq 3/4 \quad (4.29)$$

yielding the null hypothesis [17]. For example  $Pr(w_i^\pm = 3/4)$  is true for deterministic LHV models as presented in (Tab 3.4): in three out of four cases  $w_i^\pm = 1$ . Considering partially predictable inputs as in (4.25) and (4.26) the probability of winning in each round is

$$Pr(w_i^\pm = 1), Pr(w_i^{combo} = 1) \leq 3/4 + (\tau - \tau^2) = \xi \quad (4.30)$$

with  $\tau = \max(\tau_A, \tau_B)$ . With this it is possible to bound the probability of winning at least  $W$  times in  $N$  rounds

$$P(W, N) \leq p_g = \sum_{j=W}^N \binom{N}{j} \xi^j (1 - \xi)^{N-j}. \quad (4.31)$$

This is an upper bound for the  $p$  value of the hypothesis test.

The total number of is are connected to the  $S$  value (4.12) via

$$\begin{aligned} \frac{S^\pm + 4}{8} &= \frac{1}{\pm N} \sum_{i=1}^{\pm N} \frac{4 \cdot g^\pm(A_i, B_i) X_i Y_i + 4}{8} \\ &= \frac{1}{\pm N} \sum_{i=1}^{\pm N} \frac{g^\pm(A_i, B_i) X_i Y_i + 1}{2} \\ &= \frac{W^\pm}{\pm N}. \end{aligned} \quad (4.32)$$

For fixed  $N$  (4.32) is a bijective and strictly monotonically increasing function thus an upper bound for  $Pr(S \geq S_m)$  is also a bound for  $Pr(W \geq W_i)$  and vice versa.

### 4.2.3. Applying the hypothesis test

This evaluation method is designed for an experiment using CHSH's scenario (Fig. 3.1) with a relatively unbiased and unpredictable input selection. The maximal allowed bias is  $\frac{1-\sqrt{2\sqrt{2}}}{2} \approx 0.117$ . A higher bias, i.e., predictability  $\tau$ , would allow local-realistic theories to violate the Tsirelson Bound 3.10 for the modified CHSH inequality (4.12) as well as to surpass the correspondent winning probability for the non-local game (4.30). Therefore, in case of such a high bias (4.28) and (4.31) yield a  $p$  close or equal to 1 even for an experiment employing a perfectly entangled Bell-state and perfect measurements. This susceptibility to bias is a specific problem of the presented methods to estimate  $p$ . The unmodified CHSH inequality (4.11) is actually robust against biased input choices if the bias is constant and a method to estimate  $p$  in cases of high, but constant bias can be found in the supplemental materials of [41, 42].

In the presented experiment the bias and predictability of the employed QRNGs are far below the critical value of 0.117 (Sec 4.1.2), thus the presented methods to estimate  $p$  can be used. Both bounds (4.31) and (4.28) are a bound of the same underlying  $p$  value and thus one can freely choose between them. Even after the experiment it is possible since the underlying  $p$  is not changed by the choice of the bound. (4.31) is a tighter bound for  $p$  but for many events (large  $N$ ) the computation can become very time-consuming, so the choice depends on how much computational power and time are available. In this work both bounds are calculated to compare to other experiments employing different methods of bounding  $p$ . Since  $p_g$  is the more accurate bound, the null hypothesis is judged on it.

## 4.3. Avoiding expectation bias

A scientific experiment consists of both empiric data collection and inference based on these data. Each part should be done as impartially as possible in order to allow for meaningful results. This might seem obvious, but it can happen very easily that an experimenter unintentionally biases an experiment towards his or hers expectation, e.g., by stopping an experiment when the expected result occurs, or when an experiment is optimized and repeated several times and finally, just one measurement run with the expected result is taken into account. A collection of experiments in which such problems occurred can be found in [14].

To avoid such an expectation bias, rules for conducting the Bell test in this work are set:

- The number of events to be collected is fixed before an experimental run
- The measurement procedure, including all acceptance time windows, is defined beforehand.
- The analysis method is chosen before the experiment.
- The maintenance for the setup is performed once every 24 hours (morning). It is limited to:
  - adjustment of the laser system (optical powers and frequency stabilization)
  - check of the compensation of the magnetic field
  - minimizing the polarization rotation in the fiber components guiding the single photons and checking the automatized polarization compensation procedure of the 700 m long fiber connecting trap 2 to the BSM.

$N$	$P_m$	$p_g$	$T_D$
500	$\approx 0.45$	$\approx 0.12$	$\approx 4.1$ h
1000	$\approx 0.20$	$\approx 0.04$	$\approx 8.2$ h
2500	$\approx 0.02$	$\approx 2.5 \cdot 10^{-3}$	$\approx 21$ h
5000	$\approx 3 \cdot 10^{-4}$	$\approx 3 \cdot 10^{-5}$	$\approx 44$ h
10000	$\approx 9 \cdot 10^{-8}$	$\approx 6.6 \cdot 10^{-9}$	$\approx 89$ h
20000	$\approx 8 \cdot 10^{-15}$	$\approx 4.2 \cdot 10^{-16}$	$\approx 181$ h

Table 4.2.: Expected duration  $T_D$  and  $p$  depending on the total number of events  $n$  for  $S = 2.2$ .

- UV-cleaning the CEM setup in trap 2 (Appendix F)
- Events are only excluded from the evaluation in three cases:
  1. Malfunction of the CEMs: The voltage supplies of the CEMs shut down in the case of over-current, e.g., during of a sparkover.
  2. Jump of the frequency of one of the stabilized lasers.
  3. During maintenance no events are counted and all data is excluded.

The CEM voltage supplies and the laser frequencies are monitored during the experiment with cameras. They enable to register the exact timing of a shut down or a frequency jump and inform the experimenter of the malfunction. This allows to exclude the data collected until the problem is solved manually.

#### 4.4. Experimental violation of Bell's inequality

Before conducting an experiment under the rules set in Section 4.3 the total number of events  $N$  for a run has to be fixed. Considering an expected  $S \approx 2.20$  as in previous experiments [32], a run that can yield a  $p$  with a comparable confidence to a  $5\sigma \approx 5.75 \cdot 10^{-5}$  confidence level needs a total number of events  $N$  of ca 5000 (Fig .4.9 and Tab. 4.2). For this experiment  $\pm N = 5000$  for each of the two Bell states  $\Psi^+$  and  $\Psi^-$  is chosen leading to a total number of  $N = 10000$  events. With an expected average rate of 120 events per minute this will lead to a measurement duration of  $T_D \approx 89$  h  $\approx 4$  days already including daily maintenance of 2 h. This is only a rough estimate,  $T_D$  depends not only on the loading rate and life time of atoms in each trap, but also possible detector or laser malfunctions might increase it.

##### First runs

Since a full run with 10000 events has a duration of several days a highly stable performance of the experiment is necessary to execute such a run. The first runs in November 2015 where considering only the first events gave a clear violation of Bell's inequality yet, the stability of the system over a longer time was not yet possible. Temperature fluctuations in the laboratories as well as a changing MOT coil temperature between the trap calibration measurement and atom-atom entanglement creation lead to polarization and magnetic field drifts. Nevertheless, the first sign of a violation of the CHSH inequality could be shown on November 27th 2015 after 300 events with an  $S = 2.415 \pm 0.185$  calculated via (3.1) and (3.2) (Supplement material of [60]).

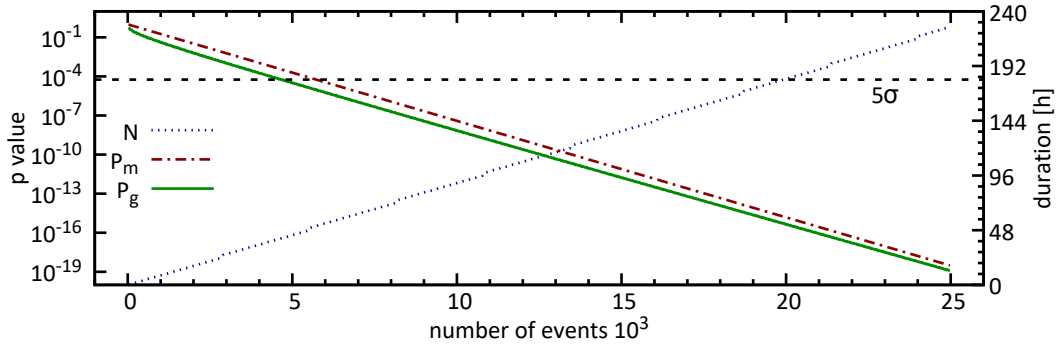


Figure 4.9.: Expected duration  $T_D$  (blue) and  $p_m$  (4.28) (red)  $p_g$ (4.31) (green) depending on the total number of events  $N$  for  $S = 2.2$ . The dashed black line is the  $5\sigma$  confidence level for the  $p$  value.

#### 4.4.1. Runs with 10000 events

After improving the overall temperature stability in the trap setups [37], introducing a magnetic field offset between single trap calibration measurements and two trap operation, and better cooling of the single atom in the trap [38], the required long term stability and performance was possible to measure a complete run.

##### First complete run with 10000 events

The first full run that strictly followed all rules defined in Section 4.3 was started on April 15th 2016. Over a period of 90 h  $\pm N = 5000$  events for both states  $\Psi^\pm$  were collected. It showed a violation of the CHSH inequality with  $S = 2.204 \pm 0.047$  for  $\Psi^+$ ,  $S = 2.240 \pm 0.047$  for  $\Psi^-$ , and  $S = 2.221 \pm 0.033$  for both combined (Tab. 4.3). The hypothesis test yields a  $p^+ \leq 2.643 \cdot 10^{-5}$  for  $\Psi^+$ ,  $p^- \leq 7.397 \cdot 10^{-7}$  for  $\Psi^-$ , and  $p \leq 1.739 \cdot 10^{-10}$  (game formalism (4.31)) for both combined leading to a rejection of local-realism under the few residual assumptions stated in Section 4.1.3.

##### “Live” run with 10000 events

To confirm and strengthen these results, a second full run was started on June 14th 2016. This run did not only follow the rules defined in Section 4.3 but was additionally publicly announced via twitter and on a conference. Everyone could follow the experiment online. In this run, the event rate was lower and the 10000 events were collected over a time period of 10 days. The reason for the lower event rate was a lower loading rate and shorter trapping time of the atoms. The run resulted in  $S = 2.057 \pm 0.048$  for  $\Psi^+$ ,  $S = 2.134 \pm 0.048$  for  $\Psi^-$ , and  $S = 2.096 \pm 0.034$  for both combined (Tab. 4.4). The hypothesis test yields a  $p^+ \leq 0.13$  for  $\Psi^+$ ,  $p^- \leq 2.752 \cdot 10^{-3}$  for  $\Psi^-$ , and  $p \leq 2.818 \cdot 10^{-3}$  for both combined. These results violate Bell’s inequality but not as significantly as the run from April 15th. The main reasons for the lower  $S$  are higher fluctuations of the temperature during the run, which lead to stronger drifts over the longer measurement duration. Still, the hypothesis test for the combined value leads to a rejection of local-realism.

Input	++	+-	-+	--	$N_{X=Y}$	$N_{X\neq Y}$	$N_{total}$	$E_{a,b}$
$A = 1, B = 1$	489	160	182	443	932	342	1274	$0.463 \pm 0.025$
$A = 1, B = 0$	134	499	513	117	251	1012	1263	$-0.603 \pm 0.022$
$A = 0, B = 1$	135	471	507	107	242	978	1220	$-0.603 \pm 0.023$
$A = 0, B = 0$	154	483	471	135	289	954	1243	$-0.535 \pm 0.024$
						total	5000	$S = 2.204 \pm 0.047$

(a) Data for the  $\Psi^+$  state

Input	++	+-	-+	--	$N_{X=Y}$	$N_{X\neq Y}$	$N_{total}$	$E_{a,b}$
$A = 1, B = 1$	172	439	483	130	302	922	1244	$-0.507 \pm 0.025$
$A = 1, B = 0$	535	115	128	461	996	243	1239	$0.608 \pm 0.023$
$A = 0, B = 1$	122	492	510	117	239	1002	1241	$-0.615 \pm 0.022$
$A = 0, B = 0$	168	443	536	149	317	979	1296	$-0.511 \pm 0.024$
						total	5000	$S = 2.240 \pm 0.047$

(b) Data for the  $\Psi^-$  state

state	$S_m$	$p_m$	$W$	$p_g$
$\Psi^+$	2.2016	$\leq 2.611 \cdot 10^{-4}$	3876	$\leq 2.643 \cdot 10^{-5}$
$\Psi^-$	2.2384	$\leq 8.444 \cdot 10^{-6}$	3899	$\leq 7.397 \cdot 10^{-7}$
$\Psi^+ \& \Psi^-$	2.22	$\leq 2.569 \cdot 10^{-9}$	7775	$\leq 1.739 \cdot 10^{-10}$

(c) Result of the hypothesis test

Table 4.3.: Experimental data of the run started at April 15th 2016

Input	++	+-	-+	--	$N_{X=Y}$	$N_{X\neq Y}$	$N_{total}$	$E_{a,b}$
$A = 1, B = 1$	506	158	127	489	995	285	1280	$0.555 \pm 0.025$
$A = 1, B = 0$	161	441	427	173	334	868	1202	$-0.478 \pm 0.022$
$A = 0, B = 1$	144	482	450	185	329	932	1261	$-0.444 \pm 0.023$
$A = 0, B = 0$	118	483	510	146	264	993	1257	$-0.555 \pm 0.024$
						total	5000	$S = 2.057 \pm 0.048$

(a) Data for the  $\Psi^+$  state

Input	++	+-	-+	--	$N_{X=Y}$	$N_{X\neq Y}$	$N_{total}$	$E_{a,b}$
$A = 1, B = 1$	104	523	484	132	236	1007	1243	$-0.620 \pm 0.022$
$A = 1, B = 0$	431	159	160	454	885	319	1204	$0.470 \pm 0.026$
$A = 0, B = 1$	162	466	410	207	369	876	1245	$-0.407 \pm 0.026$
$A = 0, B = 0$	133	533	537	105	238	1070	1308	$-0.636 \pm 0.021$
						total	5000	$S = 2.134 \pm 0.048$

(b) Data for the  $\Psi^-$  state

state	$S_m$	$p_m$	$W$	$p_g$
$\Psi^+$	2.0608	$\leq 0.52$	3788	$\leq 0.13$
$\Psi^-$	2.1408	$\leq 0.02$	3838	$\leq 2.752 \cdot 10^{-3}$
$\Psi^+ \& \Psi^-$	2.1008	$\leq 0.021$	7626	$\leq 2.818 \cdot 10^{-3}$

(c) Result of the hypothesis test

Table 4.4.: Experimental data of the run started at June 14th 2016

Input	++	+-	-+	--	$N_{X=Y}$	$N_{X\neq Y}$	$N_{total}$	$E_{a,b}$
$A = 1, B = 1$	2696	966	902	2453	1868	5149	7017	$0.486 \pm 0.011$
$A = 1, B = 0$	873	2686	2644	730	1603	5330	6933	$-0.538 \pm 0.010$
$A = 0, B = 1$	809	2629	2708	816	1625	5337	6962	$-0.533 \pm 0.010$
$A = 0, B = 0$	778	2621	2770	804	1582	5391	6973	$-0.546 \pm 0.010$
						total	27885	$S = 2.085 \pm 0.020$

(a) Data for the  $\Psi^+$  state

Input	++	+-	-+	--	$N_{X=Y}$	$N_{X\neq Y}$	$N_{total}$	$E_{a,b}$
$A = 1, B = 1$	865	2620	2640	791	1656	5260	6916	$-0.521 \pm 0.010$
$A = 1, B = 0$	2783	787	840	2503	5286	1627	6913	$0.529 \pm 0.010$
$A = 0, B = 1$	696	2570	2788	772	1468	5358	6826	$-0.570 \pm 0.010$
$A = 0, B = 0$	817	2596	2873	742	1559	5469	7028	$-0.556 \pm 0.010$
						total	27683	$S = 2.177 \pm 0.020$

(b) Data for the  $\Psi^-$  state

state	$S_m$	$p_m$	$W$	$p_g$
$\Psi^+$	2.0841	$\leq 6.448 \cdot 10^{-4}$	21207	$\leq 6.538 \cdot 10^{-5}$
$\Psi^-$	2.1765	$\leq 8.932 \cdot 10^{-16}$	21373	$\leq 4.527 \cdot 10^{-17}$
$\Psi^+ \& \Psi^-$	2.1301	$\leq 1.014 \cdot 10^{-16}$	42580	$\leq 4.891 \cdot 10^{-18}$

(c) Result of the hypothesis test

Table 4.5.: Experimental data from all runs between November 27th 2015 and June 24th 2016

#### 4.4.2. Evaluation of all collected events and further analysis

In the 7 month between November 27th 2015 and June 24th 2016 a total 55568 valid events were collected. Events were only discarded in case of an objective criteria from Section 4.3 or other clear experimenter mistake, e.g., read-out beam path blocked. These combined runs showed a violation of  $S = 2.085 \pm 0.020$  for  $\Psi^+$ ,  $S = 2.177 \pm 0.020$  for  $\Psi^-$ , and  $S = 2.130 \pm 0.014$  for both combined (Tab. 4.5). Since the events were only discarded based on objective criteria a hypothesis test is possible yielding  $p \leq 4.891 \cdot 10^{-18}$  for both states combined leading to a very strong rejection of local-realism.

#### Test for correlation between remote inputs and signaling

The independence of the measurements in Lab 1 and Lab 2 are ensured by space-like separation and random input choices. To test if there are still possible signs of correlation between the random inputs or signaling from one side (Alice) of the experiment to the other (Bob) during the measurement, which would make the test of local-realism void [106, 107], a possible correlation between the inputs generated by the QRNGs as well as possible dependence of the local measurement outcomes on the remote inputs are investigated.

**Independence of inputs** Averaged over all 55568 events the probabilities for  $B_i = 0$  conditioned on  $A_i$  are  $Pr(B_i = 0|A_i = 0) = 0.5038 \pm 0.0030$  and  $Pr(B_i = 0|A_i = 1) = 0.4984 \pm 0.0030$ . These shows no significant derivation from the expected  $Pr(B = 0) = 0.5$ . The same is true

if  $A_i$  is conditioned on  $B_i$ .

For a test of a possible time dependent correlation of  $A_i$  and  $B_i$  the 55568 events are split in interval of 500 events<sup>5</sup> and the frequency of  $B_i = 0$  for  $A_i = 0$  and  $A_i = 1$  are compared in a chi-squared test. The test statistic has the form

$$\chi^2 = \sum_{k=1}^{112} \frac{(n_{k,0} - E(n_{k,0}))^2}{E(n_{k,0})} + \sum_{k=1}^{112} \frac{(n_{k,1} - E(n_{k,1}))^2}{E(n_{k,1})}$$

where  $k$  is the number of the interval,

$$n_{k,0} = \sum_{i \in \text{interval}} \delta(A_i) \delta(B_i),$$

is the sum of the inputs  $B_i = 0$  in the interval conditioned on  $A = 0$  and

$$n_{k,1} = \sum_{i \in \text{interval}} \delta(1 - A_i) \delta(B_i)$$

is the sum conditioned on  $A = 1$ .

$$E(n_{k,0}) = \sum_{i \in \text{interval}} \delta(A_i) \cdot \frac{1}{2}$$

and

$$E(n_{k,1}) = \sum_{i \in \text{interval}} \delta(1 - A_i) \cdot \frac{1}{2}$$

are the theoretically expected values for independent and nearly perfect QRNGs .

For 112 intervals the test yields a  $\chi^2 = 100.8$  representing a  $p > 0.695$  for 111 degrees of freedom. This does not allow to reject the null hypothesis that the inputs are independent from each other. Thus there is no reason to suspect any dependence of  $A_i$  on  $B_i$  or vice versa.

**No signaling** The space-like separation of the measurements including the random input choice is used to enforce independent local measurements. To test, if this no signaling assumption one can test the independence of the results in one device  $X_i$  respectively  $Y_i$  from the the inputs at the other device  $B_i$  respectively  $A_i$ . For this task a chi-squared test is employed in a similar manner as for the test of independent inputs above. For this test one has to consider that the ionization probabilities might be different for the two states as well as for the two different measurement settings. To exclude an interference of such effects the 55568 events are first split into the two prepared states  $\Psi^+$  and  $\Psi^-$  and the two measurement settings. Since there are two possible dependencies  $X_i$  on  $B_i$  and  $Y_i$  on  $A_i$ , each event is used in two independent tests (Tab. 4.6). These test show no sign of signaling and the  $p$  values are far from a possible rejection of the no signaling hypothesis. Also further tests with 500 event intervals show no sign of a no signaling violation.

The analysis of independent random numbers and no signaling shows no anomalies. Therefore, there is no reason to doubt the space-like separation of the measurements or the independence of the QRNGs. A comparable analysis with the same result based on slightly different statistical tests can be found in the supplement of [60]. There each of the experimental runs is individually tested for independent random numbers as well as signs of signaling. These tests show also no significant deviation from the null-hypothesis of independent random numbers and no-signaling.

---

<sup>5</sup>The last 68 interval has only 68 events

		$X = -1$	$X = +1$	total	$\chi^2$	$p$
$A = 0$	$B = 0$	3574	3399	6973	0.07	0.79
	$B = 1$	3524	3438	6962		
	total	7098	6837	13935		
$A = 1$	$B = 0$	3374	3559	6933	0.13	0.72
	$B = 1$	3355	3662	6962		
	total	6729	7221	13950		

(a) Test for  $X_i$  depending on  $B_i$  for  $\Psi^+$

		$X = -1$	$X = +1$	total	$\chi^2$	$p$
$A = 0$	$B = 0$	3615	3413	7028	0.09	0.76
	$B = 1$	3560	3266	6826		
	total	7175	6679	13854		
$A = 1$	$B = 0$	3343	3570	6913	0.28	0.60
	$B = 1$	3431	3485	6916		
	total	6774	7055	13829		

(b) Test for  $X_i$  depending on  $B_i$  for  $\Psi^-$

		$Y = -1$	$Y = +1$	total	$\chi^2$	$p$
$B = 0$	$A = 0$	3425	3548	6973	0.01	0.92
	$A = 1$	3416	3517	6933		
	total	6841	7065	13906		
$B = 1$	$A = 0$	3445	3517	6962	0.10	0.75
	$A = 1$	3419	3598	7017		
	total	6864	7115	13979		

(c) Test for  $Y_i$  depending on  $A_i$  for  $\Psi^+$

		$Y = -1$	$Y = +1$	total	$\chi^2$	$p$
$B = 0$	$A = 0$	3338	3690	7028	$10^{-3}$	0.97
	$A = 1$	3290	3623	6913		
	total	6628	7313	13941		
$B = 1$	$A = 0$	3342	3484	6826	0.02	0.89
	$A = 1$	3411	3505	6916		
	total	6753	6989	13742		

(d) Test for  $Y_i$  depending on  $A_i$  for  $\Psi^-$

Table 4.6.: No signaling test: categories and results for all 55568 events.

## 5. Addressing Assumptions for the Choice of Random Inputs

Two out of the four assumptions made to derive the local-realistic bound for the CHSH inequality (Sec. 3.2.1), consider the independence and unpredictability of the inputs. In an experiment without such inputs the freedom of choice loophole (Sec. 3.3.1) is open. To account for this in the experiment presented in Chapter 4 two physical random number generators (QRNG) (Sec. 4.1.2) are used. In the other Bell test experiments [18, 19, 20] also quantum random number generators [99] are employed for that task.

The use of the physical QRNGs replaces the two assumptions from Section 3.2.1 with the assumption that the QRNG creates independent and unpredictable random bits. This assumption is based on a physical model of the QRNG and thus it ultimately rests on a physical theory. For the QRNGs used for the experiment in Chapter 4 this is photon counting theory [39, 101], while the ones used for [18, 19, 20] are based on phase differences between independent laser pulses [108]. Furthermore, to estimate a predictability technical imperfection, e.g., electrical noise, are used.

Even though, the physical theories that allow for the random bit generation are well established, one can think of a underlying local-realistic theory in which a set of LHVs  $\lambda_i$  determines both the outputs of the RNGs  $A_i(\lambda_i)$  and  $B_i(\lambda_i)$  and the measurement results  $X_i(A_i, \lambda_i)$ ,  $Y_i(B_i, \lambda_i)$  on the particle pairs depending on the input. Also theories in which the the outputs of the QRNGs  $A_i(h_i)$ ,  $B_i(h_i)$  and the LHVs  $\lambda_i(h_i)$  depend on a common past  $h_i$  are possible. Therefore, these theories cannot be tested by an experiment using random number generators.

### 5.1. Separating input generation from the experiment

One way to increase the amount of tested LHVs theories, while additionally reducing the plausibility of the not tested theories, one can spatially separate the input generation from the rest of the experiment. Of special concern here is separation of the QRNGs from the generation of the entangled particle pairs. In experiments using photon pairs the pair source was set up at least 29 m [19] respectively 126.2 m [20] from the measurement devices and the random number generators. This allowed for a space-like separation of the photon pair creation and the random input generation. Thus, theories in which the LHVs  $\lambda_i$  determining the measurement results  $X_i(A_i, \lambda_i)$ ,  $Y_i(B_i, \lambda_i)$  are fixed when the particle pair can be tested. Moreover, placing the QRNGs in a completely different room at another end of a more than 100 m long building as done in [20] reduces the plausibility for a theory connecting the devices.

For experiments using stationary particles and entanglement swapping, defining a single point in space-time of the entanglement creation, is hardly possible. The LHVs at the stationary particles determining the measurement results  $X_i(A_i, \lambda_i)$ ,  $Y_i(B_i, \lambda_i)$  must be set before the entanglement swapping. To space-like separate the random number generation and pair creation one has to place the RNGs at a different place as Alice respectively Bob (Fig. 5.1).

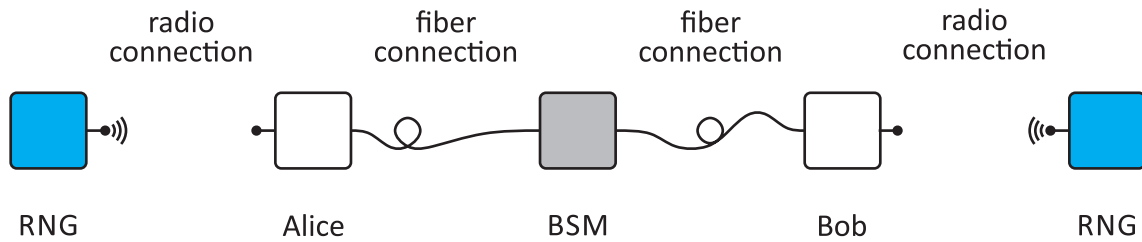


Figure 5.1.: Possible setup for a Bell test experiment using stationary qubits and entanglement swapping with space-like separated random input generation: Alice and Bob hold each a stationary qubit and are connected via glass fibers to the Bell state measurement (BSM) setup. They create entanglement between their stationary qubits and photons which are then send via the fiber link to the (BSM) for entanglement swapping. The inputs for Alice and Bob are generated in the two remote RNGs and are send via a radio connection to the measurement devices.

Depending on the actual experimental scheme it might be necessary to implement a free space connection, e.g., via radio between the QRNGs and the measurement devices to allow for space-like separation.

### “Cosmic” Bell test experiments

The space-like separation of the pair generation and input generation limits the possible form of the underlying local realistic-theory. However, theories in which the LHVs determining the the measurement outcomes are set before the pair generation are still possible. The same is true for theories allowing for a common history dependence of random inputs and LHVs. Increasing the distance between the input generation and the measurement devices reduces the possibilities for such theories. To maximize this distance, it was proposed to utilize photons stemming from distant stars for the random input selection [40]. The first Bell test experiment closing the locality loophole while using photons from stars, which are roughly 600 ly away from the sun, was performed in Vienna in 2016 [41]. Yet, this experiment did not close the detection loophole. To further expand the distance, a similar experiment was conducted on La Palma in 2018. It utilized the William Herschel Telescope and the Telescopio Nazionale Galileo for collecting photons from quasars, which emitted the light  $7.78 \cdot 10^9$  yr respectively  $12.21 \cdot 10^9$  yr ago [42]. In this experiment a history influencing the input choices would need to reach  $13.15 \cdot 10^9$  yr into the past. Furthermore, in 2018 an Bell text experiment, which additionally to the locality loophole also closed the detection loophole, while using photons from stars at a distance of at least 11.4ly was performed in Shanghai [43].

These experiments limit the possible LHV theories to those allowing for a common history dependence. In in the loophole free case the common history needs to include more than a decade, while in the case of the detection loophole open the common history must start close to the beginning of the Universe. One can consider performing a loophole free experiment using inputs stemming from quasars for an otherwise loophole free Bell test experiment. This will maximize the time constraint on for all LHV theories.

## 5.2. Human free will as sources for randomness: “The Big Bell Test”

The random number generators and also the randomness from photons emitted by stars are a technical approach to create random inputs. At the end there is always a physical theory used to verify the claim of random inputs. These physical theories are well established and trusted, but ultimately they cannot be proven. To address this one can try to take a completely different approach to provide independent and unpredictable inputs : the human free will [44].

Free will is a metaphysical concept as such it cannot be proven, either. Using input choice made by humans allow to test LHV theories that allow for humans to decide between "0" and "1" independently from any experiment. This excludes only LHV theories that do not allow for an independent human decision. To test such theories, which restrict the human free will, is anyhow hardly possible for a human.

The work presented in this section was done in collaboration with many experimenters from around the world in the “BIG Bell Test Collaboration” (<https://thebigbelltest.org>) [45]. This collaboration was initiated and managed by the group of Morgan W. Mitchell from ICFO, Barcelona. The goal was to perform multiple independent Bell experiments simultaneously, while their settings are chosen by human participants around the world via a browser game. The BIG Bell Test was conducted on November 30th 2016 and in total 13 experiments in 12 different laboratories on five continents were conducted, while the participants generated 97347490 random bits. These bits were collected at the ICFO and rerouted to the single experiments on request during that time. A description on how the human made bits were collected and the results of the experiments can be found in [45]. A detailed description of every experiment is presented in its supplementary information.

### 5.2.1. The Munich contribution

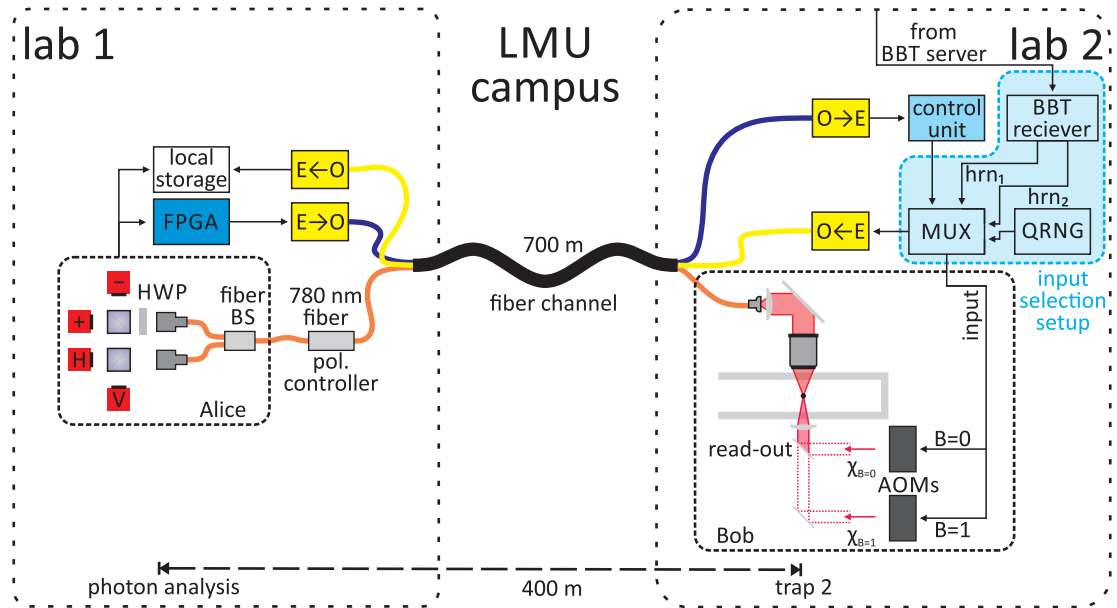
The Munich contribution to the the Big Bell Test is a Bell test based on atom-photon entanglement. The goal of the experiment is to test local-realistic theories using human made input and inputs originated from a random number generator in one measurement run.

#### Bell test with entangled atom-photon pairs

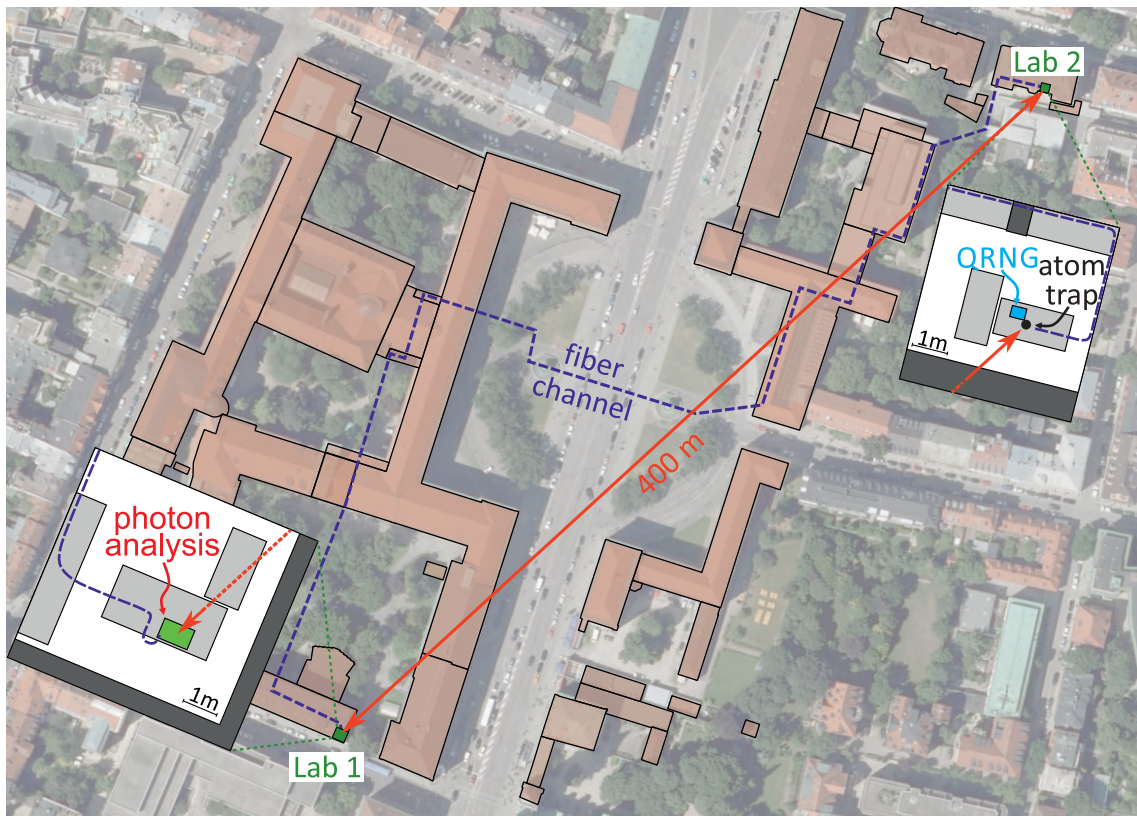
The experiment is based on entanglement between a single atom in trap 2 and a photon emitted by it (Sec 2.3.1). The atom-photon state can be written in the atomic qubit bases as shown in Appendix C (C.2) as

$$\begin{aligned} |\Psi\rangle_{AP} &= \frac{1}{\sqrt{2}} (|H\rangle|\downarrow\rangle_x + |V\rangle|\uparrow\rangle_x) \\ &= \frac{1}{\sqrt{2}} (|+\rangle|\downarrow\rangle_y + |-\rangle|\uparrow\rangle_y) \end{aligned} \quad (5.1)$$

The experimental scheme is as follows: after trapping and cooling one atom in trap 2 (Bob) the atom is prepared and then excited to emit a single photon. This photon is guided via the 700 m long optical fiber to the photon analysis setup (Alice) in Lab 1 (Fig. 5.2). Due to the low probability of  $\eta \approx 0.8\%$  to detect a single photon after an excitation attempt, the preparation and excitation is repeated rapidly and interrupted by a cooling period every 40 excitation attempts. The detection of a single photon emitted by the atom in trap 2 interrupts the excitation process and triggers the state read-out of the atom (Fig. 5.3).



(a) Setup for Bell test with atom-photon entanglement: The single atom is trapped in trap 2 (Bob) and its emitted photon is guided via the 700 m long fiber to the photon analysis (Alice) in Lab 1. The input choice is done by a fiber beam splitter with different polarization analysis at each output port. A detection of a single photon is registered by an FPGA that triggers the atomic state read out. The atomic input choice is determined by a human random bit ( $hrn_1$ ) that chooses via a multiplexer (MUX) between another human random bit ( $hrn_2$ ) or a bit from the QRNG. Depending on this input one of two AOMs creates a read-out pulse with a polarization  $\chi_0$  or  $\chi_1$ . The input choices and measurement outcomes are stored in an local storage in Lab 1.



(b) Location of Lab 1 with the photon analysis, Lab 2 with the atom trap, and the connecting fiber channel. Map data provided by the Bayerisches Landesamt fuer Digitalisierung, Breitband und Vermessung.

Figure 5.2.: Atom-photon Bell test setup and Map for The BIG Bell Test.

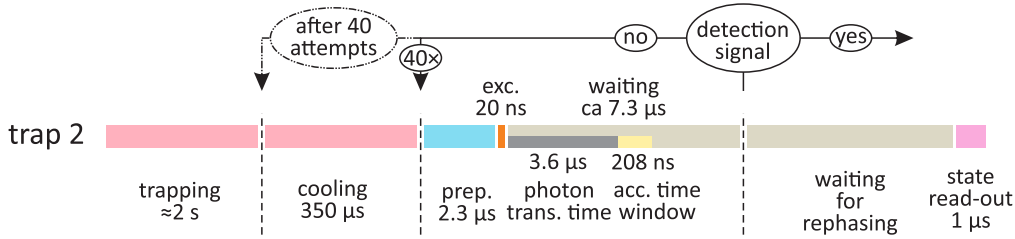


Figure 5.3.: Experimental Sequence for the atom-photon Bell test experiment: After trapping a single atom in trap 2 the preparation and excitation sequence is started. It is repeated until a photon detection in the 208 ns long acceptance time window (yellow) after an excitation (orange) occurred. Since the photons are detected in the photon analysis setup in lab 1 a total waiting time for the detection signal of  $7.3 \mu\text{s}$  is necessary after each excitation pulse. After 40 excitation tries  $350 \mu\text{s}$  cooling is performed before continuing with the sequence. In the case of a photon detection the atomic state measurement is performed after an extra waiting time for the atomic state rephasing (Fig. 2.13b).

**Measurement of the photon** The photon analysis setup is the same setup used for BSM (Fig. 2.15). When used for one photon only the BSM setup is a polarization measurement with four detectors. To enable two different measurement settings (Tab 5.1a) a half-wave plate at  $22.5^\circ$  is placed between one output of the fiber beam splitter and the polarizing beam splitter in that arm (Fig. 5.2a). Therefore, the measurement choice for the photon is passive and not based on an explicit input. The inputs and results are defined by which SPCM detects the photon: the  $V$  detector yields  $A = 0$  and  $X = -1$ , the  $H$  detector yields  $A = 0$  and  $X = +1$ , the  $+$  detector yields  $A = 1$  and  $X = +1$ , and the  $-$  detector yields  $A = 1$  and  $X = -1$ .

**Measurement of the atom** The measurement of the atom is performed with the selective ionization based read-out scheme (Sec. 2.3.2). The settings from Table 5.1b are chosen using two beam paths and AOMs as described in Section 4.1.1 and the decision whether the atom was ionized is on fluorescence collection. The special part here is the input choice: to compare the input choice by humans to the one of the QRNG (Sec. 4.1.2), a human made random bit ( $\text{hrn}_1$ ) is used to decide whether a second human made random bit ( $\text{hrn}_2$ ) or random bit from the QRNG should be the input. With this one receives two randomly selected data sets that are measured in one experimental run. To implement this scheme a multiplexer (MUX) is used for a fast selection of the input source based on  $\text{hrn}_1$  as shown in the light blue box in Figure 5.2a.

## 5.2.2. Experimental Results “Humans vs QRNG”

In the time period between 14:30 November 30th 2016 and 03:50 December 1st 2016 59330 random bits made by humans were received from the BIG Bell Test server. This allowed to measure in total 39614 events (Tab. 5.2c). For 19716 events the input was chosen by human made random bits (Tab. 5.2a) and for 19898 events the input was chosen by the QRNG (Tab. 5.2b).

Setting	measurement operator	polarization analysis	result
$A = 0$	$\hat{A}_0 = \sigma_x$	$ V\rangle,  H\rangle$	$V = -1, H = +1$
$A = 1$	$\hat{A}_1 = \sigma_y$	$ +\rangle,  -\rangle$	$+ = -1, - = +1$

(a) Photonic measurement settings (Alice)

Setting	measurement operator	readout polarization $\chi_{ro}$	$\alpha$ and $\phi$ in (2.7)
$B = 0$	$\hat{B}_1 = \frac{1}{\sqrt{2}}(\sigma_x - \sigma_y)$	$\chi_1 = \cos(\pi/8)V - \sin(\pi/8)H$	$\alpha = -22.5^\circ, \phi = 0$
$B = 1$	$\hat{B}_0 = \frac{1}{\sqrt{2}}(\sigma_x + \sigma_y)$	$\chi_0 = \cos(\pi/8)V + \sin(\pi/8)H$	$\alpha = 22.5^\circ, \phi = 0$

(b) Atomic measurement settings (Bob)

Table 5.1.: Definition of measurement settings for the Bell test experiment using atom-photon entanglement.

Input	++	+-	-+	--	$N_{total}$	$E_{A,B}$
$A = 0, B = 0$	1745	297	347	2173	4562	$0.718 \pm 0.010$
$A = 0, B = 1$	1747	477	734	1963	4921	$0.508 \pm 0.012$
$A = 1, B = 0$	683	1570	1920	715	4888	$-0.428 \pm 0.013$
$A = 1, B = 1$	2247	215	391	2492	5345	$0.773 \pm 0.009$
				total	19716	$2.427 \pm 0.022$

(a) Results for human made inputs

Input	++	+-	-+	--	$N_{total}$	$E_{A,B}$
$A = 0, B = 0$	1782	321	331	2372	4761	$0.726 \pm 0.010$
$A = 0, B = 1$	1685	452	728	1916	4781	$0.506 \pm 0.013$
$A = 1, B = 0$	714	1621	2007	766	5108	$-0.421 \pm 0.013$
$A = 1, B = 1$	1782	221	417	2428	5248	$0.757 \pm 0.009$
				total	19898	$2.410 \pm 0.022$

(b) Results for inputs from the QRNG

Input	++	+-	-+	--	$N_{total}$	$E_{A,B}$
$A = 0, B = 0$	3527	618	678	4500	9323	$0.722 \pm 0.009$
$A = 0, B = 1$	3432	929	1462	3879	9702	$0.507 \pm 0.010$
$A = 1, B = 0$	1397	3191	3927	1481	9996	$-0.424 \pm 0.009$
$A = 1, B = 1$	4429	436	808	4920	10593	$0.765 \pm 0.006$
				total	39614	$2.418 \pm 0.018$

(c) Results for all events during the BIG Bell test

Table 5.2.: Result from the Munich contribution to the BIG Bell Test.

### Bias in the input choices

The data collected shows a clear bias in the photon measurement input choice as well as in the human chosen inputs. The bias in the photon input choice is observed in the whole data (Tab. 5.2c): 20589 times  $A = 1$  and only 19025  $A = 0$  and the estimate for  $P(A = 1) = 0.52$  this corresponds to a  $7.81\sigma$  deviation to an unbiased input with  $P(A = 1) = 0.5$ . It is independent from the atomic input choice as well as from the way it is chosen by humans or the QRNG. This bias stems from two sources: first the fiber beam splitter deviates slightly from a perfect  $50/50$  splitting ratio [67]. The second reason are differences in the detection efficiencies of the SPCMs<sup>1</sup>.

The inputs chosen by humans show a bias of  $P(B = 0) = 0.52$ . This is in agreement with bias found during the analysis of all human made random bits from the BIG Bell Test [45]. The analysis also showed a strong tendency towards alternation for humans generating random bits ( $P("1", "0") = P("0", "1") = 0.6406$ ). The strong bias and high next neighbor correlations of the human made random bits exceed the maximal predictability of 0.117 that is allowed for the analysis method from Section 4.2. Thus, it cannot be used for the evaluation. Instead the standard definition of  $S$  (3.1) together with error estimation is used to evaluate the data. For this method the values of the correlators  $E_{a,b}$  (3.2) are independent from the ratio of the inputs. Therefore,  $S$  is not effected by a constant bias. There are also other evaluation methods allowing to deal with high bias of the inputs (Supplemental Material from [41]), but for this not loophole free experiment with a large number of events  $N$  calculating  $S$  and its standard deviation is sufficient for drawing conclusions.

### Test of local realism

The data set with human input choices yielded  $S = 2.427 \pm 0.022$ , the data set with inputs from the QRNG yielded  $S = 2.410 \pm 0.022$ , and both combined yield  $S = 2.418 \pm 0.018$ . These results show a clear violation of the CHSH inequality (3.5) with a quite small standard deviation and thus support for a rejection of local realism. The results for human choices and for the QRNG inputs agree within the error margins. This was to be expected and also agrees with the result of the experiment conducted by Liu et al. at the IQOQI in Vienna for the BIG Bell test (experiment 4 in [45]).

All 13 experiments conducted during the BIG Bell test show results strongly supporting the rejection of local-realism in many different physical systems. Off course one has to consider that the experiments for the BIG Bell test, like this atom-photon Bell test experiment, are not loophole free, yet the results are quite clear. The experiment conducted by Shalm et al. from NIST in Boulder, Colorado<sup>2</sup> (experiment 13 in [45]) closed the detection loophole and had space-like separated measurements. But the human random bits were always generated before and thus the input choice cannot be space like separated. The earth diameter of 12756 km [109] is to small for space-like separation of human choices so closing the locality loophole completely in an experiment using human made inputs is not possible on Earth and would need a maned space mission.

---

<sup>1</sup>The detection efficiency of the detectors (Laser Components Count-10C) is in a range between 0.45 and 0.65.

<sup>2</sup>The same group performed the loophole free experiment [20].

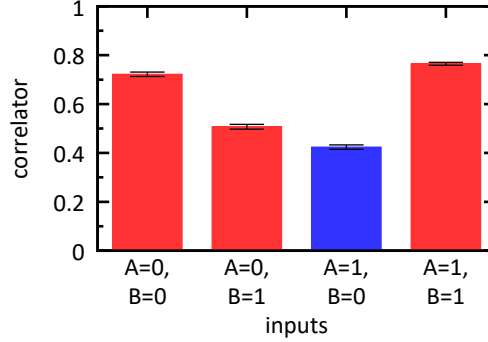


Figure 5.4.: Correlators for all events during the BIG Bell test from Table 5.2c. The red bars represent positive values and the blue bar a negative value.

photon state $ p\rangle$	$Pr( p\rangle)$	prepared atom state
$ V\rangle$	$0.264 \pm 0.003$	$\frac{1}{\sqrt{2}}( 1, -1\rangle +  1, +1\rangle) =  \uparrow\rangle_x$
$ H\rangle$	$0.216 \pm 0.003$	$\frac{i}{\sqrt{2}}( 1, -1\rangle -  1, +1\rangle) =  \downarrow\rangle_x$
$ +\rangle$	$0.281 \pm 0.003$	$\frac{1}{\sqrt{2}}e^{-i\frac{\pi}{4}}( 1, -1\rangle + i 1, +1\rangle) =  \downarrow\rangle_y$
$ -\rangle$	$0.239 \pm 0.003$	$\frac{1}{\sqrt{2}}e^{i\frac{\pi}{4}}( 1, -1\rangle - i 1, +1\rangle) =  \uparrow\rangle_y$

Table 5.3.: Probabilities for the outcome of the photon projection measurement and the prepared atomic state.

### 5.2.3. Model of the Bell test using atom-photon entanglement

The bias of the input selection is not the only noticeable feature of the collected data. There are more anomalies that should be analyzed. The most obvious is that all four correlators  $E_{a,b}$  have significantly different absolute values (Fig. 5.4) as it would be expected from the atom-photon state (5.1) and the settings (Tab. 5.1). This is not critical for a Bell test experiment and a rotation of the prepared atom-photon state as well as errors in the polarization settings for the read-out laser or the photon measurement are a possible explanation. However, in this experiment the situation is a bit more complex.

Another more critical anomaly is a correlation of the photon input choice  $A$  with the measurement outcome of the atom  $Y$ . This is quite notable since the measurement of the atoms should be independent from the measurement settings for the photon for both local-realism as well as quantum mechanics. The reason for these anomalies is a combination of experimental design and the state evolution of the atom caused by the magnetic field and the optical dipole trap (Sec. 2.3.3).

#### Imperfections in the state measurement

The photon measurement (Fig. 5.2a and Tab. 5.1a) projects the photon onto one of the four polarization states  $|V\rangle$ ,  $|H\rangle$ ,  $|+\rangle$ , or  $|-\rangle$ . For the entangled atom-photon state  $|\Psi\rangle_{AP}$  (5.1) each of four possible measurement outcomes has the same probability of  $1/4$ . But due to small imperfections in the fiber beam splitter and the different detection efficiencies the probabilities for the four measurement outcomes are different from each other (Tab. 5.3).

Each of the four outcomes prepares one atomic state (Tab. 5.3) with certain probabilities

atom state	$Pr(Y = -1 B = 0, \Psi_p)$	$Pr(Y = -1 B = 1, \Psi_p)$
$ \Psi_V\rangle =  \uparrow\rangle_x$	$0.94 \cdot \cos(-22.5^\circ)^2 + 0.02$	$0.94 \cdot \cos(22.5^\circ)^2 + 0.02$
$ \Psi_H\rangle =  \downarrow\rangle_x$	$0.94 \cdot \sin(-22.5^\circ)^2 + 0.02$	$0.94 \cdot \sin(22.5^\circ)^2 + 0.02$
$ \Psi_+\rangle =  \downarrow\rangle_y$	$0.94 \cdot \cos(22.5^\circ)^2 + 0.02$	$0.94 \cdot \cos(67.5^\circ)^2 + 0.02$
$ \Psi_-\rangle =  \uparrow\rangle_y$	$0.94 \cdot \sin(22.5^\circ)^2 + 0.02$	$0.94 \cdot \sin(67.5^\circ)^2 + 0.02$

Table 5.4.: Probability for the measurement result  $Y = -1$  depending on the prepared atomic state and the input  $B$  for perfect state preparation and state read-out.

for measuring  $Y = +1$  or  $Y = -1$  outcome for the different setting for  $B = 0$  or  $B = 1$  (5.1b). Considering a perfect preparation but an imperfect state-read out (Sec. 2.3.2) the probability to measure a projection of the prepared atomic state  $|\Psi\rangle_p$  on the read-out dark state (2.9) for  $B = b$  with  $b \in \{0, 1\}$  is

$$Pr(Y = -1|B = b, \Psi_p) = 0.96 \cdot \langle D_{\chi_b} | \Psi \rangle_p + 0.02 \left( 1 - \langle D_{\chi_b} | \Psi \rangle_p \right) \quad (5.2)$$

$$0.94 \cdot \langle D_{\chi_b} | \Psi \rangle_p + 0.02 \quad (5.3)$$

with

$$\begin{aligned} |D\rangle_{\chi_0} &= \sin(-22.5^\circ) \frac{1}{\sqrt{2}} (|1, -1\rangle - |1, +1\rangle) + \cos(-22.5^\circ) \frac{i}{\sqrt{2}} (|1, -1\rangle + |1, +1\rangle) \\ &= -i \cdot \sin(-22.5^\circ) |\downarrow\rangle_x + i \cdot \cos(-22.5^\circ) |\uparrow\rangle_x \\ &= i \cdot \cos(22.5^\circ) |\downarrow\rangle_y - \sin(22.5^\circ) |\uparrow\rangle_y \end{aligned}$$

for  $B = 0$  and

$$\begin{aligned} |D\rangle_{\chi_1} &= -i \cdot \sin(22.5^\circ) |\downarrow\rangle_x + i \cdot \cos(22.5^\circ) |\uparrow\rangle_x \\ &= i \cdot \cos(67.5^\circ) |\downarrow\rangle_y - \sin(67.5^\circ) |\uparrow\rangle_y. \end{aligned}$$

for  $B = 1$ . The values of (5.2) for the four prepared states can be found in Table 5.4. Considering the photon detection probabilities the probability to detect a certain atomic state depending on the photon setting  $A$  takes the form

$$Pr(Y = -1|A = 0) = \frac{\sum_{p \in \{V, H\}} \sum_{b \in \{0, 1\}} Pr(|p\rangle) \cdot Pr(Y = -1|B = b, \Psi_p) Pr(B = b)}{Pr(|V\rangle) + Pr(|H\rangle)} \quad (5.4)$$

and

$$Pr(Y = -1|A = 1) = \frac{\sum_{p \in \{+, -\}} \sum_{b \in \{0, 1\}} Pr(|p\rangle) \cdot Pr(Y = -1|B = b, \Psi_p) Pr(B = b)}{Pr(|+\rangle) + Pr(|-\rangle)}. \quad (5.5)$$

While for equal detection efficiencies the probabilities for  $Y = -1$  are equal and no correlation of  $Y$  on  $A$  can be seen, unequal detection probabilities give rise to a correlation between  $Y$  on  $A$ . Yet, the photon detection probabilities from Table 5.3 alone do not explain the data measured.

### Effects of atomic state evolution

There is another important factor to consider for the dependence of the atomic state measurement result  $Y$  for a give result of the measurement of the photon: the temporal evolution of the atomic state. As explained in Section 2.3.3, it is only possible to measure the atomic state with high fidelity after a full transverse oscillation of the atom in the ODT (Fig. 2.13b). In this experiment the oscillation period is  $T = 14.4 \mu\text{s}$  and so the actually measured atomic state is not the initially prepared state  $|\Psi_p\rangle$ , but the one after this time  $|\Psi_p(t = 14.4 \mu\text{s})\rangle$ . Thus, the atomic state has to be changed accordingly in (5.4) and (5.5).

Considering (2.13) each of the prepared states has a different representation in the eigenvectors of the magnetic field. Therefore they have a different temporal evolution and are susceptible to different magnetic field vectors. A simulation, employing the Monte Carlo Method and considering the distribution of different atom trajectories and magnetic field noise [38, 56], is used to estimate the evolution for different states. The simulation shows that a magnetic field on the order of several mG (Fig. 5.5c and Fig. 5.5d) would explain the measured data.

Since before the start of the experiment the magnetic field was set to zero with an accuracy below 1 mG (Fig. 5.5a and Fig. 5.5b), the drift of the active magnetic field stabilization (Sec. 2.3.3) explaining such a magnetic field would have to be quite strong. In fact it would need to be well above the expected drifts, especially for  $B_x$  and  $B_y$ . Indeed the experimental data evaluated in 3 h intervals show a drift of the resulting correlators (Fig. 5.6). However, this drift is small and slow compared the result of the simulation. Additionally, already the results of first interval have a quite strong offset to the values that are expected for a magnetic field close to zero.

### Calibration error of the automatized fiber birefringence compensation

A possible reason for that offset is a calibration error of the polarimeter [110] used in the automatized compensation of the birefringence in the 700 m long fiber. The polarimeter drifts very slowly over time and needs a calibration after several weeks. A calibration error leads to a constant extra rotation of the photon measurement angles. An error of ca  $-3^\circ$  for  $V$  and  $H$  and of  $6^\circ$  for  $+$  and  $-$ , together with a small magnetic field drift over the duration of the experiment explains the offset as well as the drift over time of the correlators.

This carefully and explicitly developed model of the experiment can explain the noticeable features of the measured data and shows that they stem from the design of the experiment or small calibration errors. For a “normal” experiment one can think of a repetition with an optimized calibration, but for an experiment conducted live and parallel to others, as during the BIG Bell test, this is not possible. Both effects, polarization rotation and atomic state evolution, can be seen as a rotation of the measurement settings and thus neither change the evaluation nor inference of a Bell test experiment.

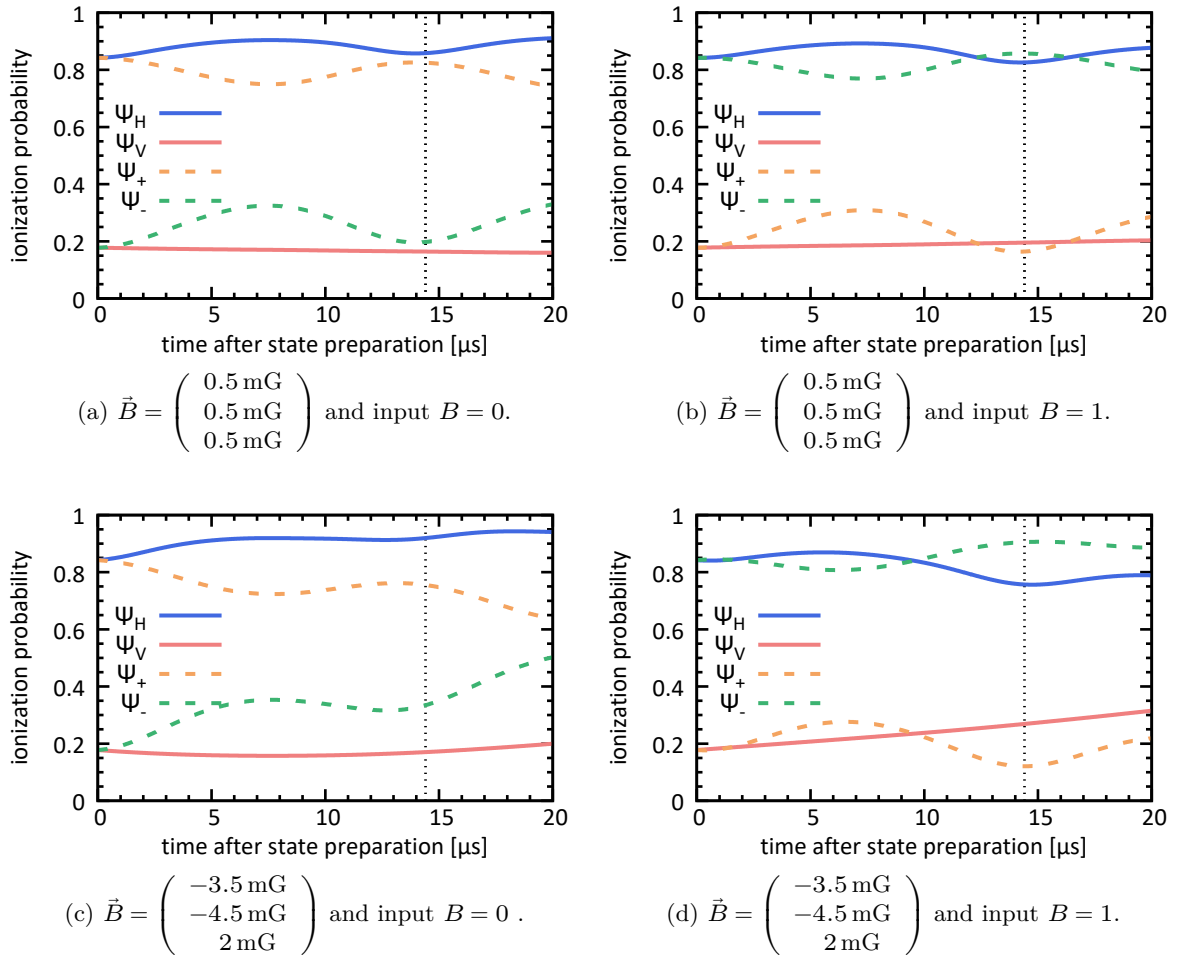
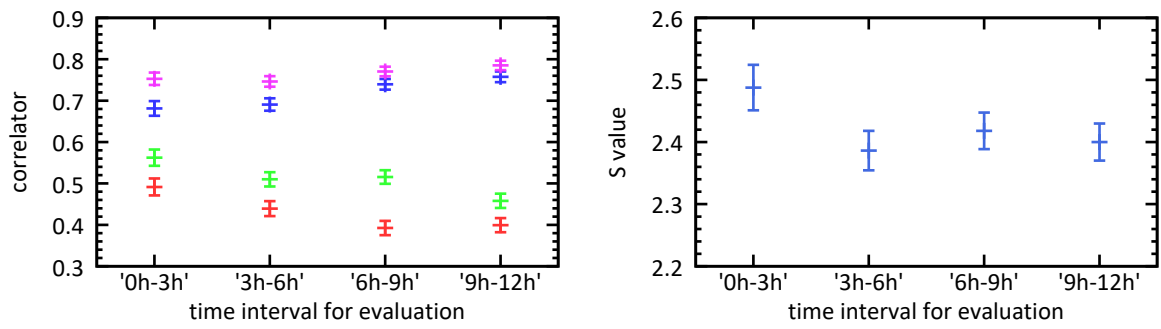


Figure 5.5.: Simulation of the atomic state evolution: ionization probability depending on time delay between state preparation and atomic state measurement. The measurement in the experiment is conducted at a delay of  $14.4 \mu\text{s}$  (dashed black line).



(a) Correlators  $E_{AB}$ :  $A = 0, B = 0$  (blue),  $A = 0, B = 1$  (green),  $A = 1, B = 0$  (red),  $A = 1, B = 1$  (pink)

(b) CHSH  $S$  value

Figure 5.6.: Data evaluation in 3 h time intervals shows a small drift of the experiment.

## 6. Towards Applications and Quantum Networks with Atom-Atom Entanglement

The entanglement between two stationary qubits, e.g., atoms, is not only useful to test the fundamentals of quantum mechanics, but also a key ingredient in quantum technology and an integral part of future quantum networks. This chapter is focused on employing long-distance entanglement of atoms for such purposes. After a general introduction into quantum networks, the possibility of networks based on quantum memories and their possible realizations are discussed. Next, the interesting possibility of device-independent applications is introduced and different examples that can be realized with atom-atom entanglement are shown. One of such applications, self-testing, allows for the test of entanglement. Here, the first application of self-testing to certify a quantum network link is demonstrated.

### 6.1. Quantum Networks

Quantum networks [111] have many different quantum communication applications, e.g., quantum key distribution (QKD) [112, 5], precise time synchronization [26], and distributed quantum computing [113]. These different applications have different demands on the network: while QKD can be realized by simpler networks based only on photon states, distributed quantum computing needs a more sophisticated network establishing entanglement between connected quantum memories.

#### QKD Networks

The first networks employing quantum technology are networks for QKD. These networks can be realized by utilizing photons guided in optical fibers [114, 115, 116, 117, 118, 119] or free space links [120, 121], which also include connections to airborne senders [122] or even in satellites [123].

However, the transmission of these networks is limited by losses due to absorption in fiber or by geometrical losses in free space. Furthermore, decoherence of the transmitted states is introduced during the transmission in the optical fiber or by atmospheric turbulence. This restricts range and secret key rate of such networks. To overcome this, as done in the 2000 km QKD link between Beijing and Shanghai [119, 124], longer distances are split up in smaller sections connected via classical relay stations. The QKD protocols are only performed in each of the sections separately. Afterwards the resulting secret keys are then used to distribute a secret key between sender and receiver. However, a big drawback from using the classical relay stations is that the security is not guaranteed by the QKD scheme. To guarantee secure communication, the relay stations need to be trusted and hence, such stations are called trusted nodes. Another example of a trusted node QKD is the satellite based intercontinental QKD link where the satellite serves as moving relay station [125, 126]. Since trusted nodes

relay only classical information, they cannot distribute entanglement from one section to the next, and thus quantum state transfer via teleportation is not possible.

### Networks connecting quantum memories

The next step is to go forward towards a universal quantum network capable of more than the standard QKD schemes, frequently called quantum internet [24]. Such a quantum network consists of nodes that can store and process quantum information in so called quantum memories. The nodes are connected with quantum channels that allow for the distribution of quantum states via photons<sup>1</sup>. The main difference to the QKD networks are the quantum nodes that allow for the relay of entanglement via entanglement swapping in so called quantum repeater schemes [25]. The quantum repeater do not breach the security of QKD schemes and allow for overcoming the problems introduced by photon loss. Such schemes also employ entanglement distillation or purification to overcome imperfections and decoherence in the quantum state distribution.

Currently, the demonstrators for this kind of networks are limited to a basic quantum link consisting of two nodes with one connection. The two atom traps form such a link over 398 m distance, respectively 700 m fiber connection (Fig. 2.16). Besides the 400 m link (700 m fiber) presented in this thesis, other realizations of such links are: atomic ensembles [127, 128, 129], single atoms [130], single ions [131, 132], impurity-vacancy centers in diamond [95, 18, 133], quantum dots [134], and superconducting qubits [135].

The next step towards an universal quantum network is to demonstrate a quantum repeater and hence entangle two nodes via an intermediate node. For the presented experiment, this demands a third atom trap with two atoms, which can be entangled with the existing traps, and which allows for a Bell state measurement to swap entanglement to the distant atoms.

## 6.2. Device-independent quantum protocols

Quantum entanglement enables many different applications, particularly interesting are the so called “device-independent” (DI) applications. The term device-independent can be understood in different ways, so a proper definition is helpful. The most common use of the term is in the sense of compatibility with different devices, as for example in computer science: device-independent data formats or applications are meant to work on different platforms independent of the hardware and operating system. Device-independent accessibility should allow for the use of programs independently of the interface hardware. Also, in physics device-independent evaluation methods exist, allowing to evaluate results for different setups in the same manner. In the field of quantum technology device-independent is understood in the sense of device-independent trust in the results. The protocols are designed to guarantee for trusted results even in the case of imperfect or not trustworthy devices.

### 6.2.1. Scenario for DI protocols

For ordinary (device-dependent) quantum protocols it is assumed that the devices deliver a certain quantum state. In contrast, device-independent protocols ensure via a Bell test that a quantum state  $\rho_{AB} \in \mathcal{H}_{AB}$  generated by the devices  $A$  and  $B$  (Fig. 6.1), has the properties

---

<sup>1</sup>For the exchange of additional information the nodes are also connected with classical channels.

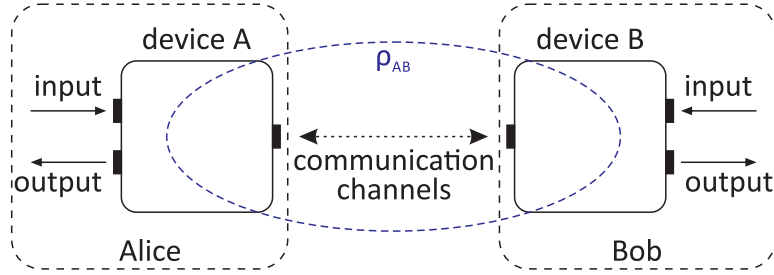


Figure 6.1.: Device-independent scenario: Alice and Bob have a “black box” device each. Both parties provide inputs for their devices and record the outputs. The quantum state  $\rho_{AB} \in \mathcal{H}_{AB}$  is not assumed but certified by a Bell test.

applicable for the protocol [21]. This allows to summarize the assumptions made to derive DI protocols [21, 23, 47] as follows:

1. Quantum mechanics describes the system.
2. The system is composed of two well defined separate devices that receive an input and respond to it with an output. The protocol is split in well defined rounds with each device receiving one input and giving one output back.
3. Device inputs are provided independently of the devices.
4. No communication between the devices between the in- and output in one round<sup>2</sup>.

These assumptions, except the first one which is an obvious assumption for quantum technology, are a slightly relaxed version of the assumptions made to derive the CHSH inequality in Section 3.2. More important, they neither concern nor limit the internal functioning of the devices. Therefore, the devices can be considered “black boxes” and no knowledge about their internal workings are used in the protocol (Fig. 6.1). This includes the communication of the devices, its specifics are not considered but it is not allowed during the time between receiving input and answering output. Especially, there are no limitations on the dimension of the Hilbert space  $\mathcal{H}_{AB} = \mathcal{H}_A \otimes \mathcal{H}_B$  of the joint quantum state  $\rho_{AB} \in \mathcal{H}_{AB}$  of the devices. Nevertheless, a certain violation of Bell’s inequality ensures two things: first, the shared quantum state of Alice and Bob has a certain amount of monogamous entanglement [136]. Second, the measurement results of the devices are not programmed in the devices beforehand, as this is equivalent to LHV theories and cannot violate Bell’s inequality. From this it is possible to infer that the results of the protocol, e.g. a secret key, are neither accessible by third party measurement devices nor already known to the manufacturer of the devices, and by this can be trusted.

### Requirements for the systems

For a real world implementation of DI protocols, the assumptions 2 to 4 turn into requirements for the system. Similarly to Bell test experiments, in which assumptions open loopholes for

<sup>2</sup>For cryptography applications the limitation of the communication between the devices is stronger: inputs and outputs must not be communicated by the devices.

local-realism (Sec. 3.3.1), assumptions that are not met by the employed system allow for potential adversaries to compromise the results of the protocol. There are diverse solutions for complying with the requirements for DI independent protocols. Some include the ones for loophole free Bell tests, but others might differ quite strongly, depending on the task of the protocol and resources available.

**Assumption 2** A system with two well defined separate devices is a straight forward requirement. The same is true for well defined rounds with one input and output for each device. The two devices should be macroscopic devices that can be identified by non experts and have clearly defined input and output mechanism.

**Assumption 3** Providing inputs independent of the devices can be implemented in many different ways. Possible solutions among others are: random number generators, both a pseudo RNG as well as a physical one, hashing of information independent of the devices, or human choices. In contrast to a loophole free Bell test experiment, DI applications can accept reasonable claims of independence and do not need “freshly” generated random inputs.

**Assumption 4** To ensure for no communication between the two devices during the time needed from first input to outputs in one round is a more delicate problem. For a loophole free Bell test, it is ensured by space-like separation of the measurements. This is also possible for some DI applications, but for other applications it is necessary that the inputs and outputs are not communicated at all. This cannot be granted based on fundamental physical theories, but it might be reasonable to use a shielded, bug proof room to control the communication capability of the devices (Supplementary information of [23]).

## 6.2.2. Examples of DI applications

Entangled quantum states that violate Bell’s inequality enable DI protocols in real world applications. Two prominent examples for this are randomness generation and secure communication.

### Randomness generation

In 2010 Pironio et al. showed that measurements on entangled particles can be used to generate random bits and this randomness can be certified by a violation of Bell’s inequality enabling DI generation of random numbers [23]. Using heralded entanglement of single  $^{171}\text{Yb}^+$  ions trapped 1 m apart (see [131]), made it possible to produce 42 new random bits with 99% confidence [23]. Yet, there were only a few small measures taken to ensure the no communication assumption (Assumption 4). The same is true for the demonstrations based on entangled photons [137, 138], which provided a random bit rate of more than  $100 \text{ bits/s}$  with confidence of  $1 - 10^{-5}$  or higher for each bit.

The realization of loophole free Bell test, as shown in Chapter 4 and in [18, 19, 20] fulfilled the no communication requirement by space-like separation. This led to the first fully DI random number generation extracting 1024 random bits [139], followed by extracting  $6.2469 \cdot 10^7$  random bits with a confidence of  $1 - 10^{-5}$  for each bit [140].

Also, the data from the Bell test experiment in Chapter 4 allows for the extraction of certified random bits. Following [23] the number of random bits that can be extracted from a Bell test experiment is

$$n_{\text{bits}} = N \cdot f(S_m - \epsilon), \quad (6.1)$$

with

$$f(I) = 1 - \log_2 \left( 1 + \sqrt{2 - \frac{I^2}{4}} \right)$$

and

$$\epsilon(N, S_m, q, \alpha) = \sqrt{2 \frac{\ln(1/\alpha) (1/q + S_m)^2}{N}}. \quad (6.2)$$

Here  $q$  is the probability for a setting combination in a Bell test experiment (Sec. 4.1) and  $1 - \alpha$  is the confidence level. Using all 55568 events from Section 4.4.2 with  $S_m = 2.1301$  and setting  $q = \frac{1}{4}$  and  $\alpha = 0.01$  it is possible to extract 1059 certified random bits.

### Secure communication

Another very interesting protocol is device-independent quantum key distribution (DIQKD), as proposed by Andrew Yao and Dominic Mayers in 1998 [21]. It addresses the problem, that for the commonly used prepare and measure QKD protocols, e.g., BB84 [112] and COW [141], the precise generation of the quantum states is necessary since otherwise possible side channels can spoil the secrecy [142]. This means that for the security proofs the dimension of the Hilbert space of the quantum system is limited to the desired ones [143]. Though Ekert's protocol from 1991 [5] points already in the direction of using Bell's inequality for QKD it needed to be modified to become a device-independent protocol [143, 144] with no assumptions about the Hilbert space (Sec 6.2.1).

The protocols for DIQKD were further investigated and improved over the last two decades [136, 145], but still the implementation, even for a prove of concept demonstration, is not yet possible. The main reason is that the protocol needs a relatively low quantum bit error rate of  $Q_{\text{ber}} \leq 7.1\%$  (equivalent to a CHSH value of  $S \geq 2.426$ ) to be able to produce a secret key [146]. Furthermore, for  $S = 2.426$  the needed total number of events  $n$  to extract the first bit of secure key is  $10^{15}$ [147]. Currently, the two experiments showing a loophole free violation of Bell's inequality employing entanglement between stationary qubits (employing nitrogen vacancy centers in diamonds [18, 100] and single atoms, as presented in Chapter 4), did neither show the needed  $S$  value nor a suitable event rate allowing for any kind of QKD. The loophole free Bell test experiment with entangled photons [19, 20] did show a much higher event rate, but they employed a scheme for the Clauser Horn inequality[82], also called Eberhard inequality [83], with a not maximally entangled state to overcome the detection loophole (Sec 3.3.1). Therefore the absolute violation of the inequality was with an equivalent of  $S \approx 2.00004$  [148] very small and the detection efficiency is by far not high enough to allow for the DIQKD schemes. Hence for a proof of concept demonstration many improvements of e.g. state fidelity and event rate are necessary.

For a demonstration based on the Bell experiment described in Chapter 4 a significant increase of the measured  $S$  value and even more critical an improvement of the event rate are

necessary. A thorough investigation of the atom-atom entanglement generation and possibilities to improve on the fidelity can be found in Chapter 7. A perfectly created atom-atom state together with improved temporal coherence of the state (Sec. 2.3.3) will allow for an of  $S \approx 2.5$  that is only reduced by the imperfections of the atomic state read-out (Sec. 2.3.2). However, this  $S$  value represents a  $Q_{ber} \approx 5.8\%$  and thus requires  $n > 10^8$  for a positive key rate [147], which is impossible to achieve with an event rate of 2 events per minute. Even with a significantly improved rate of  $\sim 1$  Hz (using the new collection optics [149]) the measurement would take years. Thus, an improvement on the read-out fidelity together with an even further improvement of the event rate will be necessary. With  $S = 2.66$  a positive key rate starts after reaching  $n = 10^7$  hence an even rate of  $> 10$  Hz would allow this within 12 days of measurement and thus, enable a proof of concept experiment [147, 148]. Additionally, new DIQKD protocols [150] using advantage distillation, based on two-way communication [151], show progress in reducing the high experimental demands on the quantum bit error rate ( $Q_{ber} \leq 9.1$  equivalent to  $S \geq 2.313$ ). However, these protocols need expansion to account for coherent attacks [136] and finite-size security [152] to enable the full device-independent trust.

### 6.3. Self-testing: A device-independent characterization of entanglement

Another device-independent application is the so called “self-testing” [22]. The purpose of this protocol is to device-independently characterize the quantum state shared by two devices and by this allowing for a device-independent certification of entanglement. Such a certification of entanglement does not have a specific purpose, e.g., the generation of random bits or QKD, but it allows to device-independently test if a connection in a quantum network distributes entanglement and by this, to confirm the usability for other quantum protocols.

To characterize a quantum state, one would perform certain measurements that allow to estimate the properties of the state, e.g., a fidelity in respect to a target state. In most cases to allow for the inference from measurements to properties of the quantum system it is necessary to exactly know the measurement settings and to have a model of the investigated physical system, especially its dimension. In contrast to this, Self-testing as a DI protocol, is based on a Bell test in the device-independent scenario only using the four assumptions from Section 6.2.1.

#### 6.3.1. Self-testing with a Bell state fidelity

In this work, the fidelity of a maximally entangled Bell-state is estimated using self-testing with the CHSH inequality. An overview of self-testing can be found in [27]. In the DI scenario (Fig. 6.1) the measurements performed by device A are defined as observables  $A_0$  and  $A_1$  that act on the Hilbert space  $\mathcal{H}_A$  and the measurements performed by device B as observables  $B_0$  and  $B_1$  act on the Hilbert space  $\mathcal{H}_B$ . Since this is done without making any assumptions about the underlying physical system, both Hilbert spaces  $\mathcal{H}_A$  and  $\mathcal{H}_B$  are of unknown dimension. The tested quantum state  $\rho_{AB}$  is element of the joint Hilbert space  $\mathcal{H}_{AB} = \mathcal{H}_A \otimes \mathcal{H}_B$ . Using local trace-preserving maps  $\Lambda_A$  from  $\mathcal{H}_A$  to  $\mathbb{C}^2$  and  $\Lambda_B$  from  $\mathcal{H}_B$  to  $\mathbb{C}^2$  it is possible to calculate the Trace of  $\rho_{AB}$  with a Bell state  $\Psi \in \{\Psi^+, \Psi^-, \Phi^+, \Phi^-\}$

$$\text{Trace}(\rho_{AB}, \Lambda_A, \Lambda_B) = \text{Tr}((\Lambda_A \otimes \Lambda_B)[\rho_{AB}], |\Psi\rangle\langle\Psi|). \quad (6.3)$$

The Fidelity of  $\rho_{AB}$  with respect to  $\Psi$  is defined as the maximum of (6.3)

$$F(\rho_{AB}) = \max_{\Lambda_A, \Lambda_B} (\text{Tr}((\Lambda_A \otimes \Lambda_B)[\rho_{AB}], |\Psi\rangle \langle \Psi|)) \quad (6.4)$$

for all possible local trace-preserving maps  $\Lambda_A$  and  $\Lambda_B$ .

To exactly determine this fidelity based on a measured CHSH  $S$  value (3.1) is not possible since neither the state  $\rho_{AB}$  nor the measurement observables  $A_0, A_1, B_0,$  and  $B_1$  are known. However, it is possible to find a lower bound  $\mathcal{F}$  for the fidelity (6.4) by finding the state with the lowest fidelity that still allows for the measured  $S$  value. Hence, one minimizes over the set  $Set_{AB,S}$  of all states  $\rho_{AB}$  and observables  $A_0, A_1, B_0,$  and  $B_1$  that allow for the measured  $S$  with

$$E_{a,b} = \text{Tr}(\rho_{AB} A_a B_b).$$

Then, the minimum fidelity can be written as

$$\mathcal{F} = \min_{Set_{AB,S}} (F(\rho_{A,B})).$$

Minimizing over the set of unknown states measured using unknown observables, which are in a Hilbert space having an unknown dimension, is not a trivial task. Currently, the best known lower bound considering the CHSH inequality is equation (10) in [153]:

$$\mathcal{F} \geq \frac{1}{2} + \frac{1}{2} \cdot \frac{S - S_{min}}{2\sqrt{2} - S_{min}} \quad (6.5)$$

with

$$S_m = \frac{16 + 14\sqrt{2}}{17} \approx 2.106 \quad (6.6)$$

being the minimum violation of the CHSH inequality that allows for a non trivial bound of  $\mathcal{F} \geq 0.5$  on the fidelity.

### Bound for finite data

The bound (6.5) is derived for an exactly known  $S$  value, however, an actual measurement will only yield an estimate of  $S$  limited by the finite number of events  $n$ . Further, real devices might have some imperfections and the prepared state  $\rho_{AB}$  might change between events. Therefore, a method for bounding the average fidelity for  $n$  events

$$\bar{\mathcal{F}} = \frac{1}{n} \sum_{i=1}^n \mathcal{F}_i$$

was derived in collaboration Jean-Daniel Bancal, Pavel Sekatski, and Nicolas Sangouard from the University of Basel [47].

For this analysis  $S_m$  is calculated via (4.12) from the measurement results. The actual formulation of (4.12) depends on the Bell state  $\Psi$  chosen for the self-testing<sup>3</sup>. To estimate the

<sup>3</sup>The definition of (4.12) is for the  $\Psi^+$  and  $\Psi^-$  state, but a modification of the  $g^\pm(h_i)$  allows to define it for all four Bell states.

average CHSH value during the measurement, it is bounded with a confidence level of  $1 - \alpha$  by

$$\hat{S}_\alpha = 8 (I_\alpha^{-1}(nt_m - 1, n(1 - t_m) + 2) - \tau - \tau^2) - 4,$$

where  $t_m = (4 + S_m)/8$ ,  $I_\alpha^{-1}(x, y)$  is the inverse incomplete Beta function, and  $\tau$  is a bound for the possible predictability of the inputs. This bound on  $S$  allows to calculate a lower bound for the average fidelity via (6.5). This results in

$$\begin{aligned} \hat{\mathcal{F}} &= \frac{1}{2} + \frac{1}{2} \cdot \frac{\hat{S}_\alpha - S_{min}}{2\sqrt{2} - S_{min}} \\ &= \frac{12 + (4 + 5\sqrt{2})(5\hat{S}_\alpha - 8)}{80} \end{aligned} \quad (6.7)$$

with a confidence level of  $1 - \alpha$ . The bound was derived without assuming that the measurement outcomes are independently and identically distributed. The prove for the bound of the average fidelity can be found in Appendix B of [47].

The average fidelity allows to device-independently characterize and certify entanglement. Therefore, it can be used to ensure the distribution of entanglement in future quantum networks.

### 6.3.2. DI certification of an elementary quantum network link

In future quantum networks, it will be necessary to test and certify the performance of the quantum links. Since the self-testing formalism is device-independent, it can be applied to all possible realizations of quantum networks. Furthermore, the results are trustworthy even if the network providers and device manufacturers are not trustworthy. So it allows for a universal certification of quantum network links, assuming the requirements from Section 6.2.1 for DI applications are fulfilled. As mentioned before, loophole free tests of Bell's inequality fulfill those requirements and thus the Bell test experiment from Chapter 4 can be used to certify a 398 m elementary quantum network link formed by the two atom traps.

#### Setup for DI certification

To implement the certification protocol based on self-testing, the experimental setup for the Bell test experiment (Fig. 4.1) is divided into two parts (Fig. 6.2):

**Quantum network link** The quantum network link consists of two nodes connected with one channel. The two atom trap setups, including laser setup and control electronics, form the nodes and the BSM and the fiber link form the communication channel.

**Certification setup** To test the quantum link a trusted input generation and data storage are necessary. For this setup these are the QRNGs and local storage units. Additionally, a common clock is necessary to allow for ensuring the space-like separation of the measurements, as well as a possibility to combine the data from both local storage units.

The quantum network link with the two nodes in different laboratories, clearly fulfills assumption 2, being a well defined system of two devices that receive inputs and answer outputs.

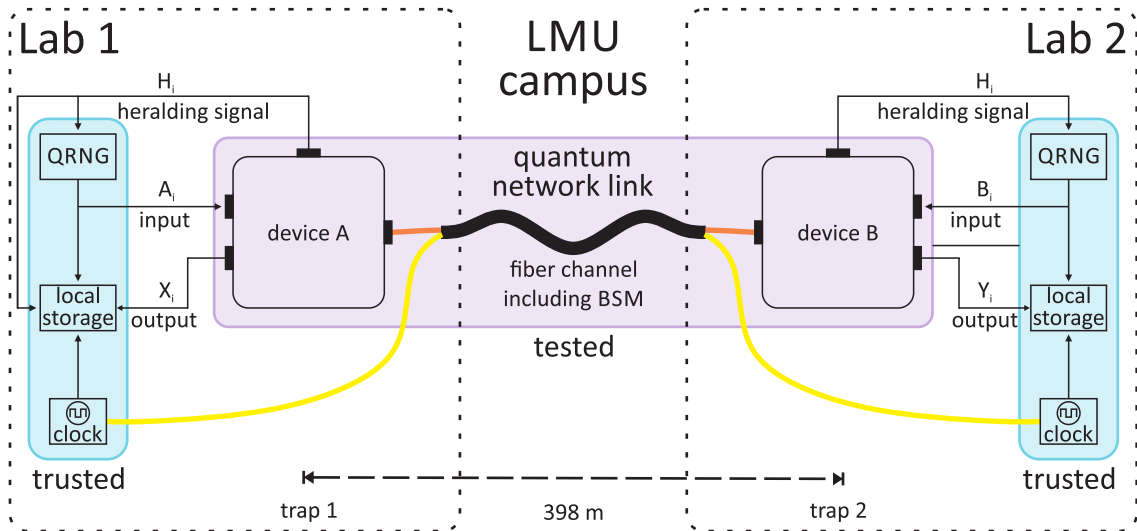


Figure 6.2.: Setup for the certification of a 398 m elementary quantum link. The quantum network link (violet) is considered to be two black box devices, one in each laboratory, that give a heralding signal ( $H_i$ ) when they are ready to receive inputs ( $A_i$ ,  $B_i$ ) and after receiving the input each device replies an output ( $X_i$ ,  $Y_i$ ) in less than  $1.2 \mu\text{s}$  (to be space-like separated). The certification setup (blue) provide inputs on request and stores the inputs and outputs in a local storage units in each laboratory. Additionally, the heralding signal is stored in Lab 1 and a common clock for both storage units allows ensure space-like separation of the measurement in the devices, as well as combing the data from both storage units. Since the clock is distributed via one of the glass fibers of the fiber link (yellow) this fiber is trusted as well.

State	$S_m$	$N$	$\hat{\mathcal{F}}, \alpha = 0.05$	$\hat{\mathcal{F}}, \alpha = 0.01$	$\hat{\mathcal{F}}, \alpha = 10^{-3}$
$\Psi^+$	2.2016	5000	0.5067	—	—
$\Psi^-$	2.2384	5000	0.5325	0.5099	—
combined	2.2200	10000	0.5365	0.5205	0.5025

Table 6.1.: Self-testing for the experimental run April 2016 (Tab 4.3)

State	$S_m$	$N$	$\hat{\mathcal{F}}, \alpha = 0.05$	$\hat{\mathcal{F}}, \alpha = 0.01$	$\hat{\mathcal{F}}, \alpha = 10^{-3}$
$\Psi^+$	2.0841	27885	—	—	—
$\Psi^-$	2.1765	27683	0.5220	0.5124	0.5016
combined	2.1301	55568	—	—	—

Table 6.2.: Self-testing for the full data of all runs combined (Tab 4.5)

The other requirements concern the certification setup. The inputs are generated by QRNGs (Sec. 4.1.2), which are independent from the network link and thus fulfilling the requirement based on assumption 3. Finally, space-like separation of input  $A_i$  from  $Y_i$  as well as  $B_i$  from  $X_i$  enforces the last assumption on no communication. The local storage units only accept outputs in a time window of  $1.2\ \mu\text{s}$  after the input. Otherwise the output is set to “−1”. By synchronization of the storage units with a common clock it is possible to verify space-like separation and by this the no communication requirement.

### Certification results

Using the data collected in the Bell experiments (Sec. 4.4), it is possible to certify the quantum network link. Applying the formalism (6.7), with a predictability of  $\tau = 6.3 \cdot 10^{-4}$  (Sec. 4.1.2), to the data from the run in April 2016 with 5000 events for each state allows to certify an average Bell state fidelity with a confidence level of 0.95 ( $\alpha = 0.05$ ) above 0.5 for both prepared states (Tab. 6.1). With a higher confidence level of 0.99 ( $\alpha = 0.01$ ) it is only possible to certify the distribution of the  $\Psi^-$  state with  $\hat{\mathcal{F}} = 0.5099$ . Even higher confidence levels demand either a higher  $S_m$  or more events. Therefore (6.7) is applied to the combined data collected in all runs of the Bell experiment (Tab. 4.5). Now, it is possible to certify the distribution of the  $\Psi^-$  state with a confidence level of 0.999. However, the  $S_m = 2.0841$  of the  $\Psi^+$  state is below the threshold for self testing (6.6) (Tab. 6.2).

Furthermore, it is possible to use the combined data for both prepared states to calculate  $\hat{\mathcal{F}}$  (6.7). One might object to the use of the data for both prepared state, as the fidelity is only defined towards one of the four Bell states. However, this can be refuted as follows: Considering an example with the exact same setup as in Figure 6.2 with the differences that the heralding signal always announces the creation of  $\Psi^+$  and inside device B in case of a preparation of  $\Psi^-$  the measurements for input  $B_i = 0$  and  $B_i = 1$  are switched. This quantum link uses the same states as the original quantum link, yet it pretends to only create  $\Psi^+$  and the result is equivalent to the original result for both states. Since for self-testing there are no assumptions made about the working of the devices, especially not about their measurement

operations, all requirements for it are met and the result can be used in the formalism. A bit more formal is the argument, that the heralding signal can be seen as an extra dimension in the Hilbert space for  $\rho_{AB}$  and the local trace preserving maps  $\Lambda_A, \Lambda_B$  are such that they map differently onto  $\Psi$  from regions with heralding signal for  $\Psi^+$  than from regions with heralding signal  $\Psi^-$ . Therefore using the data from the run in April 2016 allows to certify the distribution of entanglement even with a confidence level of 0.999 ( $\alpha = 10^{-3}$ ) (Tab. 6.1). Also, the combined data for both states from all runs can be combined. However, the relatively low  $S = 2.1301$  allows even with  $n = 55568$  a fidelity of  $\hat{\mathcal{F}} > 0.5$  only for a rather low confidence level of 90.6%.

## 7. Improving the Atom-Atom State Preparation

The certification of the elementary quantum network link demonstrates a step forward on the path towards new quantum communication applications, however, the performance of the quantum link is limited by a low event rate, imperfect atom-atom state creation, decoherence of atomic states, and the limitations of atomic state measurement. In this section possible improvements on the atom-atom entanglement creation are investigated. As described in Chapter 2, the atom-atom entanglement is generated by swapping the entanglement from two entangled atom-photon pairs onto the atoms. Therefore, the atom-atom state fidelity directly depends on the quality of the atom-photon states and a detailed modeling of the process for creation of atom-photon entanglement can be utilized to improve the atom-atom state.

### 7.1. Detailed model for photon emission from a single atom

In the experiment described in this work, atom-photon entanglement (Sec 2.3.1) generation is based on the spontaneous emission of a photon during the decay from the  $5P_{3/2}, F' = 0, m_{F'} = 0$  excited state to the  $5S_{1/2}, F = 1, m_F = 0, \pm 1$  ground states (Fig. 2.6d). Since photons originating from the decay to the  $F = 1, m_F = 0$  are not collected by the setup (Sec. 2.4) the resulting entangled atom-photon state is  $|\Psi\rangle_{AP} = \frac{1}{\sqrt{2}} (|\sigma^+\rangle |1, -1\rangle + |\sigma^-\rangle |1, +1\rangle)$  (2.5). To implement this scheme the atom is prepared in the  $F' = 1, m_{F'} = 0$  state and excited via a short laser pulse to the  $F' = 0, m_{F'} = 0$ . The emitted photons are collected with a microscope objective, coupled into a single mode fiber, and guided to the photon analysis setup.

#### 7.1.1. Deviations from the ideal excitation process

In Section 2.3.1, only a simplified excitation model is considered, using two atomic levels and a perfectly  $\pi$ -polarized excitation pulse. For a more realistic examination of the excitation process, the complete level structure of the atom has to be considered as well as limitations and imperfections in the experimental realization [33].

First, the preparation of the  $F = 1, m_F = 0$  by optical pumping (Fig. 2.6a and Fig. 2.6b) is not perfect with a success probability of  $Pr_{prep} \approx 80\%$  [33]. Since the preparation for each excitation try is independent of the others, this results in the mixed state

$$\rho_{prep} = Pr_{prep} |1, 0\rangle \langle 1, 0| + ((1 - Pr_{prep}) A |1, -1\rangle \langle 1, -1| + B |1, +1\rangle \langle 1, +1|), \quad (7.1)$$

with  $A + B = 1$  being the population ratio between  $|1, -1\rangle$  and  $|1, +1\rangle$ . In the experiment, the state preparation is optimized for the trade-off between minimal duration and maximal efficiency.  $A$  and  $B$  dependent of different properties, e.g., on the pumping laser adjustment, dipole trap properties, and magnetic field. Thus  $A$  and  $B$  are different for each trap and can change over time.

Second, the excitation process it self is more complex as described in Section 2.3.1. Considering the hyperfine structure and imperfections of the excitation pulse alignment three different excitation processes are possible:

**Resonant excitation** This is the desired excitation process by a  $\pi$ -polarized excitation pulse that is resonant to the transition from  $F = 1, m_F = 0$  to  $F' = 0, m_F = 0$ , see Figure 7.1a. The resonant excitation process is by far the most dominant.

**Off-resonant excitation** This is a possible off-resonant excitation to the  $F' = 1$  level, see Figure 7.1b. It is separated from  $F' = 0$  by 72 MHz and has a natural line width of 6.065 MHz [49]. Since the excitation from  $F = 1, m_F = 0$  to  $F' = 1, m_F = 0$  with  $\Delta F = 0$  and  $\Delta m_F = 0$  is forbidden, only the  $F = 1, m_F = \pm 1$  can be excited to  $F' = 1, m_F = \pm 1$  by  $\pi$ -polarized light.

**$\sigma_{exc}$ -polarized excitation** This is a possible excitation to  $F' = 0, m_F = 0$  caused by residual  $\sigma$ -polarization of the excitation pulse, see Figure. 7.1c. This residual  $\sigma_{exc}$  can excite a certain superposition of  $5S_{1/2}, F = 1, m_F = \pm 1$  to  $5P_{3/2}, F = 1, m_F = 0$ . The amplitude of  $\sigma_{exc}$  is due to imperfect alignment of the excitation laser pulse and normally very small and thus, off-resonant excitation by  $\sigma$ -polarized light can be neglected.

Finally, the excitation pulse (Fig. 2.8) has a finite duration of 20.35 ns (FWHM). In case of the atom emitting a photon before the excitation pulse has ended there is a possibility of a second excitation of the atom resulting in the emission of a second photon. Additionally, the short pulse leads to a spectral broadening (21.6 MHz) of the excitation light increasing the probability for off-resonant excitation.

### 7.1.2. Unconditioned Atom-photon state

These different processes lead to a complex atom-photon state  $\rho_{AP}$  that is not only partially mixed but also includes possible two photon states. To describe the total state, it is split into substates resulting from different effects. For this subsection the condition of only collecting  $\sigma^\pm$  photons, which is introduced by the collection into the single mode optical fiber (Sec. 2.3.1), not considered. The photon conditioning on possible detection will be considered afterwards.

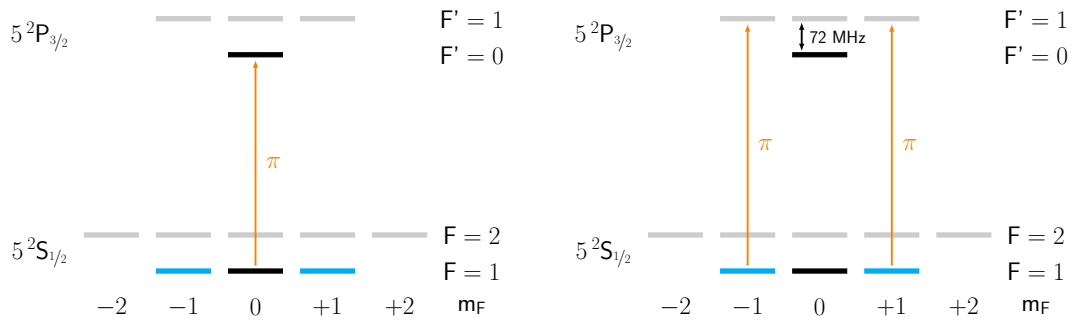
To denote the substates and excitation process, the following notation is used. The atomic states and photon polarization, considering quantization in  $z$ -direction, is  $|F, m_F\rangle$  and  $|\sigma^\pm\rangle_i$ ,  $|\pi\rangle_i$  with  $i \in \{1, 2\}$  representing the first or second emitted photon. For an excitation process  $\zeta$  and atom-photon state  $\rho$  or  $\Psi$  the superscripts indicate the excitation type, whereby  $r$ ,  $o$ , and  $\sigma$  denote resonant, off-resonant, and  $\sigma_{exc}$ -polarized excitation, respectively. For example  $\zeta^r$  denotes a resonant excitation with one emitted photon resulting in  $|\Psi^r\rangle$ , while  $\zeta^{r,o}$  denotes two resonant excitations with two emitted photons resulting in  $|\Psi^{r,o}\rangle$

#### One photon processes $\zeta^r$ , $\zeta^o$ , and $\zeta^\sigma$

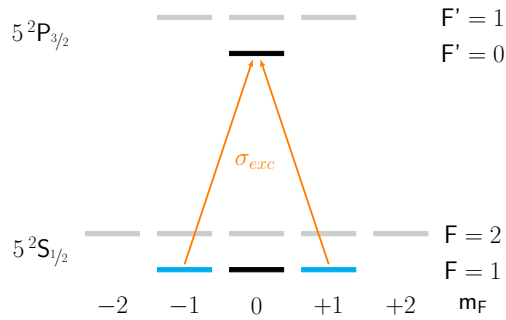
Starting from the (imperfectly) prepared state  $\rho_{prep}$  there are three processes that involve only one emitted photon:

$\zeta^r$ : Resonant excitation of the  $F = 1, m_F = 0$  (Fig. 7.1d) leads to

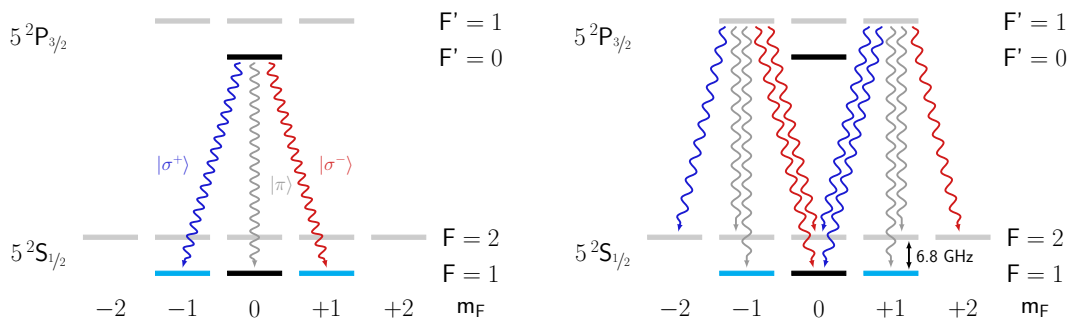
$$|\Psi^r\rangle = \frac{1}{\sqrt{3}} (|\sigma^+\rangle_1 |1, -1\rangle + |\pi\rangle_1 |1, 0\rangle + |\sigma^-\rangle_1 |1, +1\rangle). \quad (7.2)$$



- (a) Resonant excitation from  $5S_{1/2}, F = 1, m_F = 0$  to  $5P_{3/2}, F = 0, m_F = 0$  with a  $\pi$ -polarized excitation pulse (orange).  
 (b) Off-resonant excitation from  $5S_{1/2}, F = 1, m_F = \pm 1$  to  $5P_{3/2}, F = 1, m_F = \pm 1$  with a  $\pi$ -polarized excitation pulse (orange).



- (c) Resonant  $\sigma$ -excitation from  $5S_{1/2}, F = 1, m_F = \pm 1$  to  $5P_{3/2}, F = 0, m_F = 0$  with a  $\sigma_{exc}$ -polarized excitation pulse (orange).



- (d) Photon emission subsequent to a resonant excitation.  
 (e) Photon emission subsequent to off-resonant excitation. Photon polarization indicated by color  $|\sigma^+\rangle$  (blue), with polarization  $|\sigma^-\rangle$  (red), and  $|\pi\rangle$  (gray)

Figure 7.1.: Detailed excitation and emission process

This is the simplified atom-photon state considered in Section 2.3.1.

$\zeta^o$ : Off-resonant excitation to  $F' = 1, m_F = \pm 1$  states leads to a state that includes decay to the  $F = 2$  ground state (Fig. 7.1e). An off-resonant excitation of  $\rho_{prep}$  results in

$$\rho^o = A |\Phi^A\rangle \langle \Phi^A| + B |\Phi^B\rangle \langle \Phi^B| \quad (7.3)$$

with  $A, B$  from (7.1) and

$$\begin{aligned} |\Phi^A\rangle &= \sqrt{\frac{25}{60}} |\sigma^-\rangle_1 |1, 0\rangle - \sqrt{\frac{1}{60}} |\sigma^-\rangle_1 |2, 0\rangle \\ &+ \sqrt{\frac{25}{60}} |\pi\rangle_1 |1, -1\rangle - \sqrt{\frac{3}{60}} |\pi\rangle_1 |2, -1\rangle \\ &- \sqrt{\frac{6}{60}} |\sigma^+\rangle_1 |2, -2\rangle \end{aligned}$$

for the excitation from  $|1, -1\rangle$  and

$$\begin{aligned} |\Phi^B\rangle &= \sqrt{\frac{25}{60}} |\sigma^+\rangle_1 |1, 0\rangle + \sqrt{\frac{1}{60}} |\sigma^+\rangle_1 |2, 0\rangle \\ &+ \sqrt{\frac{25}{60}} |\pi\rangle_1 |1, +1\rangle + \sqrt{\frac{3}{60}} |\pi\rangle_1 |2, +1\rangle \\ &+ \sqrt{\frac{6}{60}} |\sigma^-\rangle_1 |2, +2\rangle \end{aligned}$$

from  $|1, +1\rangle$  (see Appendix A Figure A.1 for Clebsch-Gordan coefficients).

$\zeta^\sigma$ : Resonant excitation by residual  $\sigma$ -polarization of the excitation pulse (Fig. 7.1d) leads to

$$|\Psi^\sigma\rangle = \frac{1}{\sqrt{3}} (|\sigma^+\rangle_1 |1, -1\rangle + |\pi\rangle_1 |1, 0\rangle + |\sigma^-\rangle_1 |1, +1\rangle). \quad (7.4)$$

### Two photon processes $\zeta^{r,r}$ , $\zeta^{r,o}$ , and $\zeta^{r,\sigma}$

For the processes that involve multiple emitted photons only the two photon processes starting with a resonant excitation are considered. Since the probability for other two or more photon processes have only a very small probability, their contribution to the atom-photon state is neglectable. There are three such two photon processes:

$\zeta^{r,r}$ : A first decay to  $F = 1, m_F = 0$  emitting a  $\pi$ -polarized photon followed a second resonant excitation and decay (Fig. 7.1d) lead to

$$|\Psi^{r,r}\rangle = \frac{1}{\sqrt{3}} |\pi\rangle_1 (|\sigma^+\rangle_2 |1, -1\rangle + |\pi\rangle_2 |1, 0\rangle + |\sigma^-\rangle_2 |1, +1\rangle). \quad (7.5)$$

$\zeta^{r,o}$ : A first decay to  $F = 1, m_F = \pm 1$  emitting  $\sigma^\pm$ -polarized photons followed by a off-resonant excitation (Fig. 7.1e) to  $5P_{3/2}, F = 1, m_F = \pm 1$  leading to an emission

of a second photon (Fig. 7.1e). This process results in the state

$$\begin{aligned}
|\Psi^{r,o}\rangle = & \sqrt{\frac{25}{60}} \frac{1}{\sqrt{2}} (|\sigma^+\rangle_1 |\sigma^-\rangle_2 + |\sigma^-\rangle_2 |\sigma^+\rangle_1) |1, 0\rangle \\
& + \sqrt{\frac{1}{60}} \frac{1}{\sqrt{2}} (-|\sigma^+\rangle_1 |\sigma^-\rangle_2 + |\sigma^-\rangle_1 |\sigma^+\rangle_2) |2, 0\rangle \\
& + \sqrt{\frac{25}{60}} |\pi\rangle_2 (|\sigma^+\rangle_1 |1, -1\rangle + |\sigma^-\rangle_1 |1, +1\rangle) \\
& + \sqrt{\frac{3}{60}} |\pi\rangle_2 (-|\sigma^+\rangle_1 |2, -1\rangle + |\sigma^-\rangle_1 |2, +1\rangle) \\
& + \sqrt{\frac{6}{60}} \frac{1}{\sqrt{2}} (-|\sigma^+\rangle_1 |\sigma^+\rangle_2 |2, -2\rangle + |\sigma^-\rangle_1 |\sigma^-\rangle_2 |2, +2\rangle).
\end{aligned} \tag{7.6}$$

This state involves the  $F = 2$  level and includes entanglement between the first and second emitted photon.

$\zeta^{r,\sigma}$ : Two photon process with first a decay to  $F = 1, m_F = \pm 1$  emitting a photon with a polarization state  $\sigma_{exc}$  analog to the residual  $\sigma$ -polarization of the excitation pulse can be excited again to the  $F' = 1, m_F = 0$ . The emission of the second photon (Fig. 7.1d) results in the state

$$|\Psi^{r,\sigma}\rangle = \frac{1}{\sqrt{3}} |\sigma_{exc}\rangle (|\sigma^+\rangle_2 |1, -1\rangle + |\pi\rangle_2 |1, 0\rangle + |\sigma^-\rangle_2 |1, +1\rangle). \tag{7.7}$$

### Combined atom-photon state

The six substates from one and two photon processes can be combined to the following atom-photon state

$$\rho_{AP} = Pr_{prep} |\Psi\rangle_{su} \langle\Psi|_{su} + (1 - Pr_{prep}) (Pr^o \rho^o + Pr^\sigma |\Psi^\sigma\rangle \langle\Psi^\sigma|), \tag{7.8}$$

with

$$|\Psi_{su}\rangle = A^r |\Psi^r\rangle + A^{r,r} |\Psi^{r,r}\rangle + A^{r,o} |\Psi^{r,o}\rangle + A^{r,\sigma} |\Psi^{r,\sigma}\rangle.$$

The probabilities  $Pr^o$  and  $Pr^\sigma$  as well as the amplitudes  $A^r$ ,  $A^{r,r}$ ,  $A^{r,o}$ , and  $A^{r,\sigma}$  depend on the properties of the excitation pulse including temporal shape, intensity, and polarization.

### 7.1.3. Atom-photon state conditioned on photon detection

The observable atom-photon state in the experiment differs from the atom photon state (7.8) since in the experiment only  $\sigma^\pm$  photons can be collected by the employed optics. Further, the efficiency of photon collection and detection is only  $Pr_{det} \approx 2 \cdot 10^{-3}$  [37] and thus the probability to detect both photons from a two photon process is a factor of  $10^{-3}$  lower compared to detecting one of the photons. This leads to four different categories of conditioned photon detection: one photon process with a detection (subscript 1), two photon process with the detection of the first photon (subscript 1), two photon process with the detection of the second photon (subscript 2), and two photon detection (subscript 1, 2).

**One photon processes** The one photon processes conditioned on the detection of  $|\sigma^\pm\rangle$  photons result in the states:

$$\zeta_1^r \rightarrow |\Psi_1^r\rangle = \frac{1}{\sqrt{2}} (|\sigma^+\rangle_1 |1, -1\rangle + |\sigma^-\rangle_1 |1, +1\rangle), \quad (7.9)$$

$$\zeta_1^o \rightarrow \rho_1^o = A |\Phi_1^A\rangle \langle \Phi_1^A| + B |\Phi_1^B\rangle \langle \Phi_1^B| \quad (7.10)$$

with

$$|\Phi_1^A\rangle = \sqrt{\frac{25}{32}} |\sigma^-\rangle_1 |1, 0\rangle - \sqrt{\frac{1}{32}} |\sigma^-\rangle_1 |2, 0\rangle - \sqrt{\frac{6}{32}} |\sigma^+\rangle_1 |2, -2\rangle \quad (7.11)$$

and

$$|\Phi_1^B\rangle = \sqrt{\frac{25}{32}} |\sigma^+\rangle_1 |1, 0\rangle + \sqrt{\frac{1}{32}} |\sigma^+\rangle_1 |2, 0\rangle + \sqrt{\frac{6}{32}} |\sigma^-\rangle_1 |2, +2\rangle, \quad (7.12)$$

and

$$\zeta_1^\sigma \rightarrow |\Psi_1^\sigma\rangle = \frac{1}{\sqrt{2}} (|\sigma^+\rangle_1 |1, -1\rangle + |\sigma^-\rangle_1 |1, +1\rangle).$$

**Detection of the first of two photons** From the three possible two photon processes  $\zeta^{r,r}$  (7.5),  $\zeta^{r,o}$  (7.6), and  $\zeta^{r,\sigma}$  (7.7) only the two later ones involve a first photon that is detectable by the setup. Conditioning on a detection of the first photon and no detection of the second means tracing out the second photon in (7.6) and (7.7). This results in partially mixed atom-photon states

$$\begin{aligned} \zeta_1^{r,o} \rightarrow \rho_1^{r,o} &= \frac{25}{120} (|\sigma^+\rangle_1 |1, -1\rangle + |\sigma^-\rangle_1 |1, +1\rangle) (\langle \sigma^+|_1 \langle 1, -1| + \langle \sigma^-|_1 \langle 1, +1|) \\ &+ \frac{25}{120} |\sigma^+\rangle_1 |1, 0\rangle \langle \sigma^+|_1 \langle 1, 0| + \frac{25}{120} |\sigma^-\rangle_1 |1, 0\rangle \langle \sigma^-|_1 \langle 1, 0| \\ &+ \frac{1}{120} |\sigma^+\rangle_1 |2, 0\rangle \langle \sigma^+|_1 \langle 2, 0| + \frac{6}{120} |\sigma^-\rangle_1 |2, +2\rangle \langle \sigma^-|_1 \langle 2, +2| \\ &+ \frac{1}{120} |\sigma^-\rangle_1 |2, 0\rangle \langle \sigma^-|_1 \langle 2, 0| + \frac{6}{120} |\sigma^+\rangle_1 |2, -2\rangle \langle \sigma^+|_1 \langle 2, -2| \\ &+ \frac{3}{120} (-|\sigma^+\rangle_1 |2, -1\rangle + |\sigma^-\rangle_1 |2, +1\rangle) (-\langle \sigma^+|_1 \langle 2, -1| + \langle \sigma^-|_1 \langle 2, +1|), \end{aligned}$$

and

$$\begin{aligned} \zeta_1^{r,\sigma} \rightarrow \rho_1^{r,\sigma} &= \frac{1}{3} |\sigma_{exc}\rangle_1 |1, -1\rangle \langle \sigma_{exc}|_1 \langle 1, -1| \\ &+ \frac{1}{3} |\sigma_{exc}\rangle_1 |1, 0\rangle \langle \sigma_{exc}|_1 \langle 1, 0| \\ &+ \frac{1}{3} |\sigma_{exc}\rangle_1 |1, +1\rangle \langle \sigma_{exc}|_1 \langle 1, +1|. \end{aligned}$$

category	excitation process	resulting state
1	$\zeta_1^r, \zeta_1^\sigma, \zeta_2^{r,r}, \zeta_2^{r,\sigma}$	atom-photon entanglement (2.5)
2	$\zeta_1^o, \zeta_1^{r,o}, \zeta_1^{r,\sigma}, \zeta_2^{r,o}$	mixed atom-photon state
3	$\zeta_{1,2}^{r,o}, \zeta_{1,2}^{r,\sigma}$	two-photon state

Table 7.1.: Categories of the excitation processes with conditioning on the detected photon (indicated by the subscripts) on the measured atom-photon state ( $M_{pro} = \{\zeta_1^r, \zeta_1^\sigma, \zeta_2^{r,r}, \zeta_2^{r,\sigma}, \zeta_1^o, \zeta_1^{r,o}, \zeta_1^{r,\sigma}, \zeta_2^{r,o}\}$ ).

**Detection of the second of two photons** The detection of the second photon is possible for all two photon processes and tracing out the first photon and a projection on the detectable  $|\sigma^\pm\rangle_2$  second photons leads to

$$\zeta_2^{r,r} \rightarrow |\Psi_2^{r,r}\rangle = \frac{1}{\sqrt{2}} (|\sigma^+\rangle_2 |1, -1\rangle + |\sigma^-\rangle_2 |1, +1\rangle),$$

$$\zeta_2^{r,o} \rightarrow \rho_2^{r,o} = \frac{1}{2} |\Phi_2^A\rangle \langle \Phi_2^A| + \frac{1}{2} |\Phi_2^B\rangle \langle \Phi_2^B| \quad (7.13)$$

with  $|\Phi_2^A\rangle = |\Phi_1^A\rangle$  (7.11) and  $|\Phi_2^B\rangle = |\Phi_1^B\rangle$  (7.11) (with  $i = 2$  for the detected photon), and

$$\zeta_2^{r,\sigma} \rightarrow |\Psi_2^{r,\sigma}\rangle = \frac{1}{\sqrt{2}} (|\sigma^+\rangle_2 |1, -1\rangle + |\sigma^-\rangle_2 |1, +1\rangle).$$

**Two photon detection** The detection of both photons is again only possible for  $\zeta^{r,o}$  (7.6), and  $\zeta^{r,\sigma}$  (7.7) this leads to the states

$$\begin{aligned} \zeta_{1,2}^{r,o} \rightarrow |\Psi_{1,2}^{r,o}\rangle &= \sqrt{\frac{25}{32}} \frac{1}{\sqrt{2}} (|\sigma^+\rangle_1 |\sigma^-\rangle_2 + |\sigma^-\rangle_1 |\sigma^+\rangle_2 |1, 0\rangle) \\ &+ \sqrt{\frac{1}{35}} \frac{1}{\sqrt{2}} (-|\sigma^+\rangle_1 |\sigma^-\rangle_2 + |\sigma^-\rangle_1 |\sigma^+\rangle_2 |2, 0\rangle) \\ &+ \sqrt{\frac{6}{35}} \frac{1}{\sqrt{2}} (-|\sigma^+\rangle_1 |\sigma^+\rangle_2 |2, -2\rangle + |\sigma^-\rangle_1 |\sigma^-\rangle_2 |2, 2\rangle) \end{aligned} \quad (7.14)$$

and

$$\zeta_{1,2}^{r,\sigma} \rightarrow |\Psi_{1,2}^{r,\sigma}\rangle = \frac{1}{\sqrt{2}} |\sigma_{exc}\rangle_1 (|\sigma^+\rangle_2 |1, -1\rangle + |\sigma^+\rangle_2 |1, +1\rangle).$$

These 10 different substates can be sorted in three different categories based on their effect on the combined atom-photon states (Tab 7.1): The first category is formed by processes that lead to the desired atom-photon state  $|\Psi\rangle_{AP} = \frac{1}{\sqrt{2}} (|\sigma^+\rangle |1, -1\rangle + |\sigma^-\rangle |1, +1\rangle)$  (2.5) ( $\zeta_1^r, \zeta_1^\sigma, \zeta_2^r, \zeta_2^\sigma$ ). These processes involving only resonant excitation to the  $F' = 0, m_F = 0$ , regardless whether the excitation is caused by  $\pi$ -polarized light or residual  $\sigma_{exc}$ -polarization and but only consider one photon processes or the detection of the second of two photons. The second category are lead to a mixed state. In this category are two photon processes in which only

the first photon is detected ( $\zeta_1^{r,o}, \zeta_1^{r,\sigma}$ ), which are called “disturbed states” because the second excitation disturbs the entangled state between the first photon and the atom. Also in this category are processes involving off-resonant excitation ( $\zeta_1^o, \zeta_2^{r,o}$ ). The last category is formed by the two photon detection processes  $\zeta_{1,2}^{r,o}$  and  $\zeta_{1,2}^{r,\sigma}$  these two-photon-atom states can be identified and excluded from measurements. Therefore, they do not contribute to the atom-photon state.

## 7.2. Possible reduction of unwanted processes

Since only processes from the first category from Table 7.1 lead to the desired atom-photon state, while the other two categories reduce the atom-photon state fidelity, it is preferable to minimize the contribution of the unwanted processes. There are two different options of reducing the unwanted processes by minimizing the occurrence of those processes or filter out events with unwanted processes. Minimizing the occurrence is possible by finding optimal parameters of optical pumping and the excitation pulse. In order to be able to filter out events, it is necessary to discriminate between the desired and the unwanted processes by means of measurement. Then it is possible to exclude the unwanted processes from the evaluation. This is for example possible for the two photon detection events<sup>1</sup> or photons originating in a decay to  $5S_{1/2}, F = 2$  that have a 6.8 GHz (Fig. 2.2) lower frequency than the desired photons.

For both options of reducing unwanted processes a thorough quantitative analysis of the excitation process considering the level structure of  $^{87}\text{Rb}$  and the parameters of the excitation pulse is very helpful. Such an analysis was performed in [33] based on optical Liouville equations with a model called “quantum jump model”. By expanding the analysis of this model it is possible to find optimized parameters as well as possibilities to filter out the unwanted processes.

### 7.2.1. Model of the excitation process

Liouville’s equation, in quantum mechanics called von Neuman’s equation [154], allows to calculate the time evolution of a density matrix  $\rho$  for an Hamiltonian  $H$

$$i\hbar \frac{\partial \rho}{\partial t} = -[\rho, H].$$

The Hamiltonian  $H = H_0 + \frac{\hbar}{2}\Omega(exc(t)) - \hbar\Delta$  is composed of the unperturbed Hamiltonian of a single atom  $H_0$  and an interaction part including the Rabi frequencies for all transitions  $\Omega_{ij}(exc(t))$  caused by the excitation pulse  $exc(t)$  and the detuning of the light field  $\Delta_{ij}$ . To account for the spontaneous decay with decay rate  $\Gamma$  the equation is modified to

$$i\hbar \frac{\partial \rho}{\partial t} = -[\rho, H] + \frac{i\hbar}{2} \{\Gamma, \rho\},$$

with  $\{\Gamma, \rho\} = \Gamma\rho + \rho\Gamma$  [155]. For the excitation pulse a Gaussian shape

$$exc(t) = P_O e^{-\frac{1}{2}\left(\frac{t-t_0}{2T}\right)^2} \quad (7.15)$$

---

<sup>1</sup>Only possible for atom photon entanglement, for the BSM with two photon coincidences these events cannot be filtered out so easily.

excitation process	1 <sup>st</sup> photon	2 <sup>nd</sup> photon
resonant	$Pr_{e1}^r(t_1)$	$Pr_{e2}^r(t_2 t_1)$
off-resonant	$Pr_{e1}^o(t_1)$	$Pr_{e2}^o(t_2 t_1)$
$\sigma_{exc}$ -polarized	$Pr_{e1}^\sigma(t_1)$	$Pr_{e2}^\sigma(t_2 t_1)$

Table 7.2.: Photon emission probabilities for the excitation process.

process	Detection probability
$\zeta_1^r$	$Pr_1^r(t_1) = Pr_{prep} \cdot \frac{2}{3} Pr_{e1}^r(t_1) Pr_{det}^{\sigma^\pm} (1 - \int (Pr_{e1}^{or}(t_2 t_1) + Pr_{e1}^\sigma(t_2 t_1)) dt_2)$
$\zeta_1^o$	$Pr_1^o(t_1) = (1 - Pr_{prep}) \frac{32}{60} Pr_{e1}^o(t_1) Pr_{det}^{\sigma^\pm}$
$\zeta_1^\sigma$	$Pr_1^\sigma(t_1) = (1 - Pr_{prep}) \frac{2}{3} Pr_{e1}^\sigma(t_1) Pr_{det}^{\sigma^\pm}$
$\zeta_1^{r,o}$	$Pr_1^{r,o}(t_1) = Pr_{prep} \cdot \frac{2}{3} Pr_{e1}^r(t_1) Pr_{det}^{\sigma^\pm} \int Pr_{e2}^o(t_2 t_1) dt_2 (1 - Pr_{det}^{\sigma^\pm})$
$\zeta_1^{r,\sigma}$	$Pr_1^{r,\sigma}(t_1) = Pr_{prep} \cdot \frac{2}{3} Pr_{e1}^r(t_1) Pr_{det}^{\sigma^\pm} \int Pr_{e2}^\sigma(t_2 t_1) dt_2 (1 - Pr_{det}^{\sigma^\pm})$
$\zeta_2^{r,r}$	$Pr_2^{r,r}(t_2) = Pr_{prep} \cdot \int \frac{2}{3} Pr_{e2}^r(t_2 t_1) Pr_{det}^{\sigma^\pm} \frac{1}{3} Pr_{e1}^r(t_1) dt_1$
$\zeta_2^{r,o}$	$Pr_2^{r,o}(t_2) = Pr_{prep} \cdot \int \frac{32}{60} Pr_{e2}^o(t_2 t_1) Pr_{det}^{\sigma^\pm} \frac{2}{3} Pr_{e1}^r(t_1) (1 - Pr_{det}^{\sigma^\pm}) dt_1$
$\zeta_2^{r,\sigma}$	$Pr_2^{r,\sigma}(t_2) = Pr_{prep} \cdot \int \frac{2}{3} Pr_{e2}^\sigma(t_2 t_1) Pr_{det}^{\sigma^\pm} \frac{2}{3} Pr_{e1}^r(t_1) (1 - Pr_{det}^{\sigma^\pm}) dt_1$

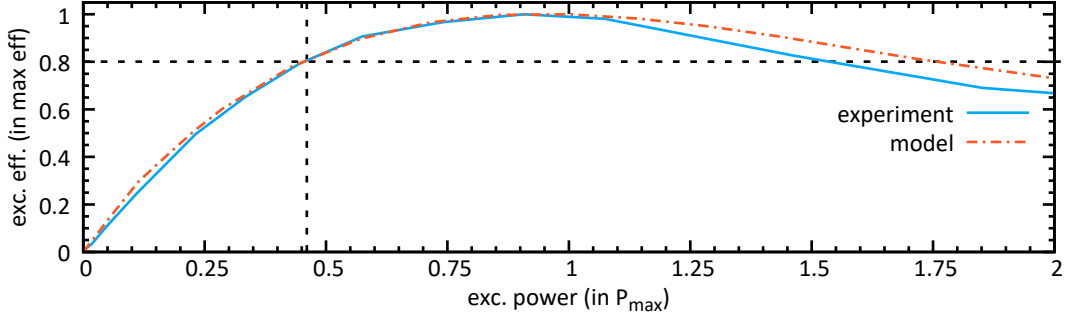
Table 7.3.: Probabilities for single photon detection for the considered processes ( $M_{pro}$ ) calculated from the result of the “quantum jump” model (Tab. 7.2).

is used, which is a very good approximation of the excitation used in the experiment (Fig. 7.3a). It has the parameters width  $T$ , absolute timing  $t_0$ , and optical power density at the atom  $P_O$ . An additional parameter is the polarization  $\chi_{exc} = \cos(\beta) |\pi\rangle + \sin(\beta) |\sigma_{exc}\rangle$  of the excitation pulse. This applied in the “quantum jump model” from [33] allows for the extraction of the time dependent photon emission probability for each of the possible excitation processes from Section 7.1.2.

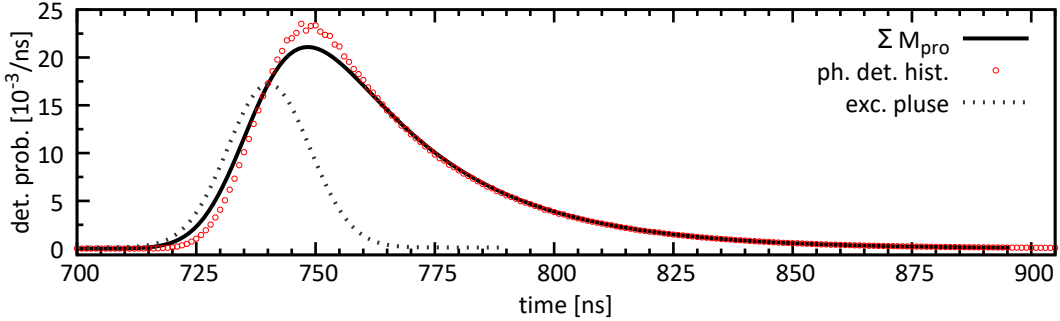
## 7.2.2. Time dependence of the excitation process

The quantum jump model yields time dependence of the photon emission probabilities for the different excitation processes (Sec. 7.1): for a first photon  $Pr_1^{pro}(t_1)$ , and for a second photon  $Pr_2^{pro}(t_2|t_1)$  conditioned on the emission of a first photon at time  $t_1$  (Tab. 7.2). This emission probabilities include emission in all possible polarizations.

To calculate the time dependent photon detection probabilities it is necessary to include further parameters: the polarization of the emitted photons, the collection of only  $\sigma^\pm$  photons, and the collection and detection efficiency. The estimated detection probability  $Pr_{det} = 2 \cdot 10^{-3}$  already includes that  $\pi$ -polarized photons are not collected and thus a modified detection probability for only  $\sigma^\pm$ -photons of  $Pr_{det}^{\sigma^\pm} = 3 \cdot 10^{-3}$  is used. Considering this, the photon detection probabilities for the one photon detection processes  $M_{pro}$  from Table 7.1 are calculated in Table 7.3.



(a) Excitation efficiency depending on the excitation pulse power experimental data (blue) and simulated data (green). The  $y$  axis is normalized on maximal excitation efficiency and the  $x$  axis is normalized on the power for maximal excitation efficiency  $P_{max}$ . For  $0.47 \cdot P_{max}$  excitation power the excitation efficiency is  $0.8 \cdot \eta_{max}$ .



(b) Measured photon detection time histogram (red dots) and simulated photon emission probability (black line) for the simulation parameters  $P_O = 0.52 \text{ mW/mm}^2$  and  $t_0 = 736 \text{ ns}$ . Photon emission of all processes combined ( $\sum_{\zeta \in M_{pro}} Pr_{\zeta}$ ) (black line) and fitted excitation pulse (gray, dashed line, a.u.).

Figure 7.2.: Estimation of the optical power of the excitation pulse  $P_O$  based on the excitation efficiency.

### Estimation of parameters

For calculating the dynamics for the experiments in this thesis, it is necessary to set the four parameters of the excitation pulse (7.15) according to the one used in the experiment. The width  $T = 8.64 \text{ ns}$  can be extracted from a fit of the measured excitation pulse (Fig. 2.8), while the other three parameters are not directly accessible.  $t_0$  needs to be exact with respect to the measured photon detection times and  $P_O$  and  $\chi_{exc}$  cannot be measured exactly at the position of the atom inside the vacuum. There are two ways to estimate  $P_O$  by combining the experimental data and the model. The first is to measure the excitation efficiency depending on the excitation laser pulse power and to compare the result to a simulation of this measurement using the model. For the atom-atom entanglement experiments the excitation power is set to a value yielding 80% of the maximal excitation efficiency  $\eta_{max}$ . The respective power is 47% of the power  $P_{max}$  needed for the maximal excitation efficiency  $\eta_{max}$  (Fig. 7.2a). The simulation yields a  $P_{max} = 1.14 \text{ mW/mm}^2$  and thus the actual optical power can be estimated to  $P_O = 0.47 \cdot 1.14 \text{ mW/mm}^2 = 0.52 \text{ mW/mm}^2$ . However, a simulation with this optical power and  $t_0 = 736 \text{ ns}$  yields a time dependent photon emission probability that does not agree with the measured photon detection histogram (Fig 7.2b). The second option to estimate the

optical power is to fit the time dependence of the simulated emission probability to a measured photon detection time histogram (Fig. 7.3a). This approach yields an optical power of the excitation pulse of  $P_O = 1.08 \text{ mW/mm}^2$ . Additionally, overlapping the photon detection histogram and the emission probability allows to estimate  $t_0 = 740 \text{ ns}$ .

The discrepancy between the values of  $P_O$  obtained with the two different model is most probably a cause of the fact that the quantum jump model from [33] still not a perfect model of the excitation. For example the different processes are simulated independently of each other. A more detailed model considering all involved atomic state levels and other potential parameters might solve might be necessary in the future. Nevertheless, the simulation fitted to the measured photon shape reproduces the temporal shape of the photon emission. Therefore it is a fair estimation of the actual process and allows for a thorough investigation of the time dependent photon emission probability for each sub process. The final parameter that has to be determined is the polarization of the excitation laser pulse  $\chi_{exc}$ . It cannot be measured directly and indirect measurements, as performed in [33]<sup>2</sup>, need a long measurement time and the value might actually change between measurements. Hence,  $\chi_{exc}$  is determined by estimating the misalignment of beam path and polarizer setting. Combining possible misalignment of the fluorescence collection (quantization axis) to the excitation beam path (Fig. 2.6), the polarizer setting and possible birefringence in the front part of the glass cell an polarization misalignment of  $5^\circ$  is estimated.

Using the fit and the estimated  $\chi_{exc}$  for the “quantum jump model” result in the normalized detection probabilities for the different excitation processes shown in Figure 7.3. The time dependent photon emission probabilities for the different processes are quite different. Especially, the unwanted processes from Table 7.1 occur preferably during the excitation pulse, while the photon having the desired atom-photon state are also emitted at later times.

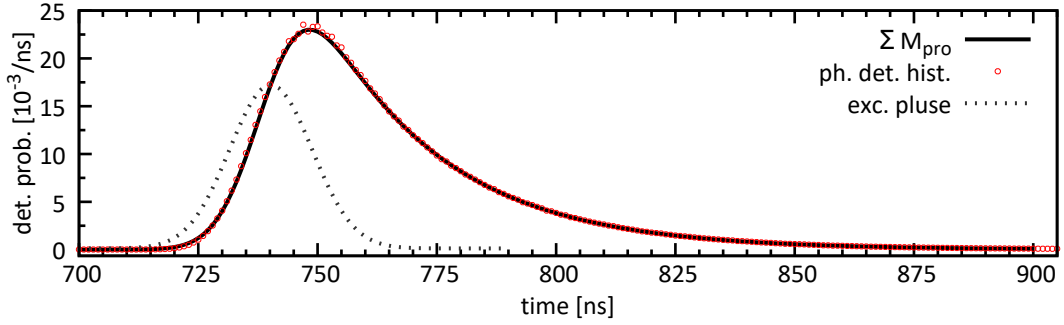
### 7.2.3. Time filtering and optimizing pulse parameters

The calculation shows that reducing the unwanted processes in the atom-photon state is possible by time filtering. For optimizing the photon detection acceptance time window it is necessary to consider background and detector dark counts. Here, a value of  $60 \text{ counts/s}$  background and dark counts is used. Using an acceptance time window for the photon detection which excludes all detection events during the duration of the excitation pulse, e.g.,  $[755 \text{ ns}, 800 \text{ ns}]$  reduces the fraction of unwanted processes from 2.72% to 0.97%, while also reducing the total photon detection probability to 0.47 of the previous value. Such a time filtering has the advantage that it can be employed for both future experiments as well as for post processing data of previous experiments. For example, it can be applied to the data of the atom-photon Bell test experiment conducted during the Big Bell Test (Sec. 5.2.1)<sup>3</sup>. This leads to an  $S = 2.477 \pm 0.022$  with  $N = 18715$ , which is slightly above the original value of  $2.418 \pm 0.018$  with  $N = 39614$ .

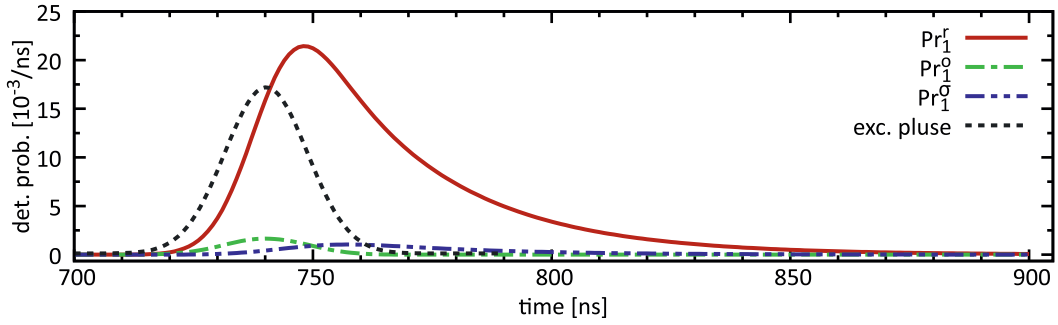
For future experiments, time filtering can also be applied using the FPGA that switches the control units to measurement mode (Fig. 5.2a). Since in atom-photon entanglement experiments, the event rate is limited by loading atoms in the trap and not by the photon

<sup>2</sup>The value from [33] was measured for a previous version of the atom trap.

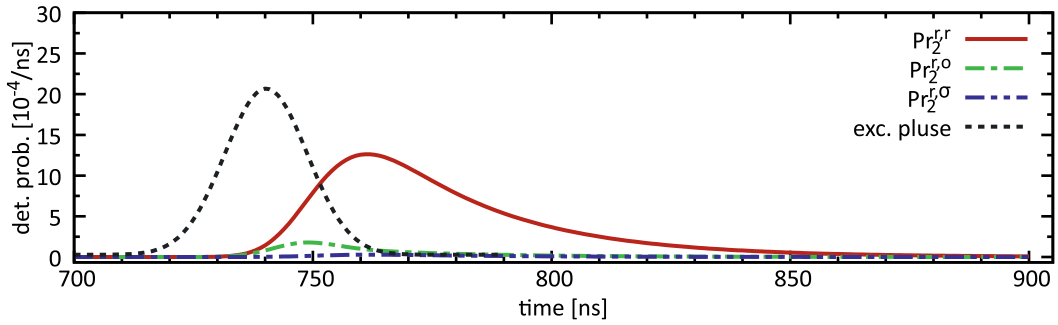
<sup>3</sup>Post selection of data recorded in a Bell test experiment is usually not permitted (Sec. 3.3.3). However, here the purpose is not to test local realism, but to show the effect of time filtering. Additionally, it is necessary to consider the time difference  $t_0$  of the model and the actual timing of the excitation pulse in the experiment of  $+8 \text{ ns}$  has to be considered,. This results in an actual time window of  $[763 \text{ ns}, 808 \text{ ns}]$ .



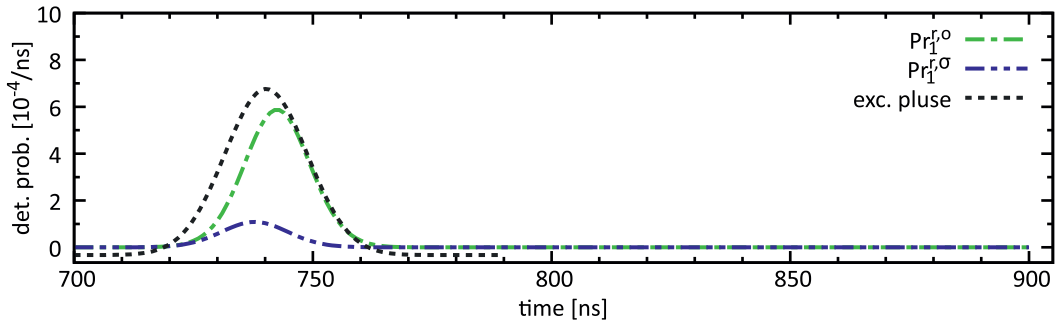
(a) Measured photon detection time histogram (red dots) and fitted simulated photon emission probability for all processes combined ( $\sum_{\zeta \in M_{pro}} Pr_{\zeta}$ ) (black line) for the fitted excitation pulse (gray, dashed line, a.u).



(b) One photon processes:  $Pr_1^r(t_1)$  (red),  $Pr_1^o(t_1) \times 10$  (green), and  $Pr_1^\sigma(t_1) \times 10$  (blue).



(c) Second photon of two photon processes:  $Pr_2^{r,r}(t_1)$  (red),  $Pr_2^{r,o}(t_1)$  (green), and  $Pr_2^{r,\sigma}(t_1)$  (blue).



(d) First photon of two photon processes (disturbed states):  $Pr_1^{r,o}(t_1)$  (green) and  $Pr_1^{r,\sigma}(t_1)$  (blue).

Figure 7.3.: Calculated time dependent photon emission probability for all processes (only detectable photons) for  $P_O = 1.08 \text{ mW/mm}^2$ ,  $t_0 = 740 \text{ ns}$ . The the excitation pulse is shown (a.u) to display the relative timing.

detection efficiency, time filtering will not influence the overall event rate. However, it is more promising to combine time filtering with additionally optimizing the excitation pulse parameters to minimize the unwanted effects. Reducing the excitation power will reduce both wanted and unwanted processes. Since the unwanted processes are reduced more, the state fidelity is higher. Here, it is necessary to find the optimal trade-off between excitation probability, background and dark counts, and the acceptance time window to optimize the state fidelity.

The model shows for an excitation power of reduced by 50% of the current value and an acceptance time window of [755 ns, 800 ns] a reduction of the unwanted processes  $< 0.5\%$ , while the total photon detection probability is reduced by a factor of 0.45. For the improved collection optics [149] the optimal time window is larger, since the better photon collection improves by a factor of 3 reduces the effect of possible dark counts. The time window of [755 ns, 840 ns] yields a fraction of unwanted processes of  $< 0.4\%$  with a total photon detection probability of  $> 0.5$  compared to the full time window of [700 ns, 900 ns]. These parameters allow for a higher state fidelity and the photon detection probability would still be increased by a factor of 1.5 with the new setup.

### 7.3. Effect of the photon emission on the two atom state fidelity

The atom-atom state fidelity is not only affected by the two photon processes resulting in mixed atom-photon states (Tab. 7.1), but also by reduced two photon interference caused by the different time dependence of the photons emitted in different processes (Fig. 7.3).

#### 7.3.1. Two photon interference

The entanglement swapping is realized by performing a Bell-state measurement based on two photon interference at a beam splitter (Sec. 2.4.1). This two photon interference requires indistinguishable photons in all degrees of freedom, including the frequency and time dependence of the photons. Hence, the interference contrast decreases when the photons become distinguishable, e.g., in case of a two photon process at one of the atoms, information carried by the other photon from that process causes the distinguishability. The reduced two photon interference results in a corrupted Bell-state measurement and the distinction between  $\Psi^+$  and  $\Psi^-$  suffers. A figure of merit for this is the temporal mode overlap  $O$  that is connected with the probability to identify a Bell state correctly by

$$Pr(\Psi^\pm \rightarrow \Psi^\pm) = \frac{1 - O^2}{2}.$$

This temporal mode overlap can be calculated using the temporal shape of the two interfering photons. It is sufficient to calculate the overlap for the case with a resonant one photon process  $\zeta_1^r$  for one of the atoms. The probability for other combinations is quite low and, additionally, in those cases the temporal mode overlap has only a minor contribution to the atom-atom state. Thus, it takes the form

$$O_\zeta^2 = \left( \int_{t_s}^{t_e} dt \sqrt{\beta_\zeta(t) \cdot \sqrt{|\alpha_{e1}^r(t)|^2}} \right)^2.$$

Here  $\zeta$  represents the excitation process of the second atom,

$$|\alpha_{e1}^r(t)|^2 = \frac{Pr_{e1}^r(t)}{\int_{t_s}^{t_e} Pr_{e1}^r(t) dt} \quad (7.16)$$

is the normalized expectation value of the temporal amplitude of the photon from  $\zeta_1^r$  process, and  $\beta_\zeta(t)$  represents the temporal amplitude of the photon emitted by the second atom [33]. For a one photon process  $\beta_\zeta$  has a form analogous to (7.16) with the respective time depending emission probabilities from Table 7.2. For photons from a two photon process the emission probabilities of the photons are connected, a second photon can only be emitted after the first one and a first one only before the second. Thus, the temporal emission probability of the second emitted photon depends on the emission time of the first with a  $\beta_\zeta(t|t_1)$  and the emission time of the second photon yields information on the first photon and thus changes the conditioned temporal amplitude  $\beta_\zeta(t|t_2)$  of the first photon. A thorough analysis of the two photon interference, considering the two photon processes and other imperfections can be found in [33]. From all excitation processes there are a single excitation process ( $\zeta_1^\sigma$ ), two two-photon processes with a second photon detected ( $\zeta_2^{r,r}$ ,  $\zeta_2^{r,\sigma}$ ), and one two-photon process with a first photon detected ( $\zeta_1^{r,o}$ ) where the temporal mode overlap has an effect on the atom-atom state fidelity. For these the parameters needed to calculate the two photon overlap are

$$|\alpha_{e1}^\sigma(t)|^2 = \frac{Pr_{e1}^\sigma(t)}{\int_{t_s}^{t_e} Pr_{e1}^\sigma(t) dt}$$

$$\beta_{\zeta_2^{r,r}}(t|t_1) = \sqrt{\frac{Pr_{e2}^{r,r}(t_2|t_1)}{\int_{t_s}^{t_e} Pr_{e2}^{r,r}(t_2|t_1) dt_2}},$$

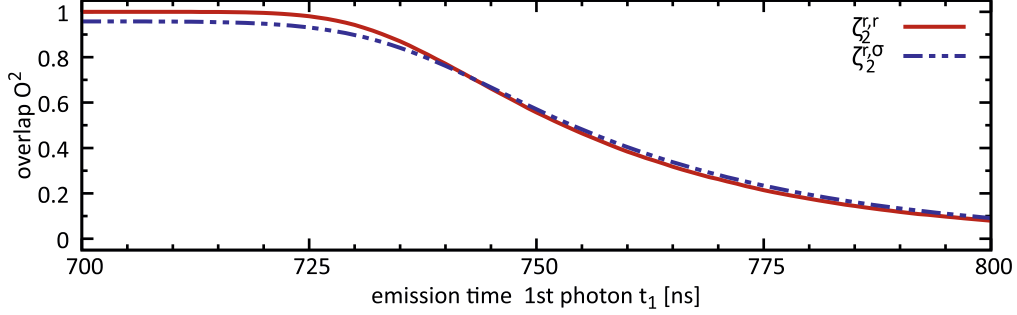
$$\beta_{\zeta_2^{r,\sigma}}(t|t_1) = \sqrt{\frac{Pr_{e2}^{r,\sigma}(t_2|t_1)}{\int_{t_s}^{t_e} Pr_{e2}^{r,\sigma}(t_2|t_1) dt_2}},$$

and

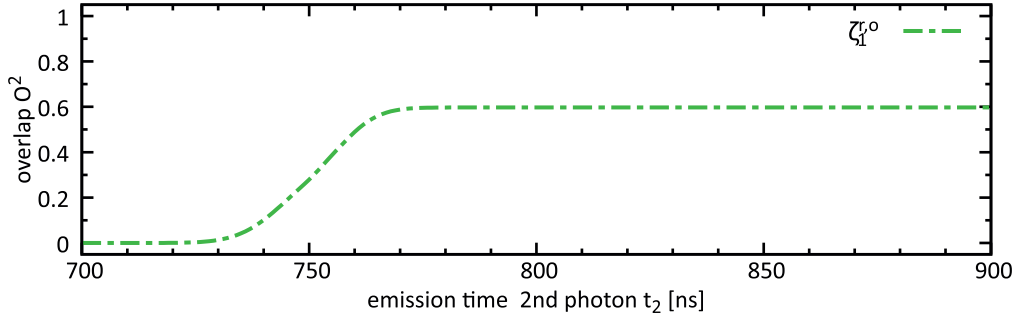
$$\beta_{\zeta_1^{r,o}}(t|t_2) = \sqrt{\frac{Pr_{e1}^r(t_1) Pr_{e2}^{r,o}(t_2|t_1)}{\int_{t_s}^{t_e} Pr_{e1}^r(t_1) Pr_{e2}^{r,o}(t_2|t_1) dt_1}}.$$

The respective  $O_{\zeta_1^\sigma}^2$ ,  $O_{\zeta_2^{r,r}}^2(t_1)$ ,  $O_{\zeta_2^{r,\sigma}}^2(t_1)$ , and  $O_{\zeta_1^{r,o}}^2(t_2)$  are displayed in Figure 7.4.

Considering the features of the interference together with the atom-photon states (Tab. 7.1) allows to categorize the excitation processes according to their effect on the Bell-state measurement and thus on the atom-atom state fidelity (Tab. 7.4). The main difference to the effects on the atom-photon entanglement is that, because of the reduced temporal mode overlap,  $\zeta_1^\sigma$ ,  $\zeta_2^{r,r}$ , and  $\zeta_2^{r,\sigma}$  reduce the atom-atom state fidelity, even though the atom-photon entanglement is perfect. Also, the detection of two photons from only one of the atoms leads to a completely mixed atom-atom state and since the BSM is based on two photon coincidence detection these events cannot be simply filtered out.



(a) Temporal mode overlap of the second emitted from atom A  $(O_{\zeta_2^{r,r}}(t_1))^2$  (red) and  $(O_{\zeta_2^{r,\sigma}}(t_1))^2$  (blue) depending on the emission time of the first photon  $t_1$  of atom A.



(b) Temporal mode overlap of the first emitted photon from atom A  $(O_{\zeta_1^{r,o}}(t_2))^2$  (green) dependent on the emission time of the second photon  $t_2$  from atom A.

Figure 7.4.: Two photon temporal mode overlap on the beam splitter for various two photon processes with  $\zeta_A \in \{\zeta_2^{r,r}, \zeta_2^{r,\sigma}, \zeta_1^{r,o}\}$  for one atom and  $\zeta_B = \zeta_1^r$  for the other atom. For the one photon processes the value for  $O_{\zeta_1^r} = O_{\zeta_2^{r,r}}(t_1 = 700) = 1$  respectively  $O_{\zeta_1^o} = O_{\zeta_2^{r,\sigma}}(t_1 = 700)$  is used. The processes  $\zeta_1^o$ ,  $\zeta_2^{r,o}$ , and  $\zeta_2^{r,\sigma}$  at atom A (not displayed here) result in a completely mixed atom-atom state and independent of the temporal overlap with the photon from atom B.

category	excitation processes	resulting state
1	$\zeta_1^r$	atom-atom entanglement
2	$\zeta_1^\sigma, \zeta_2^{r,r}, \zeta_2^{r,\sigma}$	atom-atom entanglement with reduced fidelity
3	$\zeta_1^o, \zeta_1^{r,o}, \zeta_1^{r,\sigma}, \zeta_2^{r,o}, \zeta_1^{r,o}, \zeta_1^{r,\sigma}$	mixed atom-atom state

Table 7.4.: Consequences of the different excitation processes on the atom-atom state including effects of the two photon interference.

### 7.3.2. Detection time dependent atom-atom state

To apply temporal filtering on the two photon coincidence detection of the BSM it is necessary to first calculate the detection time dependence of the atom-atom state fidelity. Possibly one could also calculate the dependence on the detection time for or another figure of merit, e.g., for the CHSH  $S$  value.

#### Two photon coincidences from two atoms

To find the time dependence for a figure of merit, the synchronized excitation of two independent single atoms is considered. This allows to calculate the probability

$$Pr_{\zeta_A, \zeta_B}(t_A, t_B) = \frac{1}{4} Pr_{\zeta_A}(t_A) Pr_{\zeta_B}(t_B)$$

for a two photon coincidence, which heralds the state  $|\Psi^\pm\rangle$ . It considers the case of the detecting one photon emitted from atom A in the excitation process  $\zeta_A$  at time  $t_A$  and on from atom B, respectively, using the time depended emission probabilities from Table 7.3. Additionally, it is possible to calculate the atom-atom state  $\rho_{\zeta_A, \zeta_B}(t_A, t_B)$  for such a coincidence using the atom-photon states and the photon overlap resulting from  $\zeta_A$  and  $\zeta_B$ .

Summing over all combinations of  $\zeta_A, \zeta_B \in M_{pro} = \{\zeta_1^r, \zeta_1^\sigma, \zeta_2^{r,r}, \zeta_2^{r,\sigma}, \zeta_1^{r,o}, \zeta_1^{\sigma,o}, \zeta_2^{r,\sigma}, \zeta_2^{r,o}\}$ , yields the time depending atom-atom state

$$\rho_{AB}(t_A, t_B) = \frac{1}{N(t_A, t_B)} \sum_{\zeta_A, \zeta_B \in M_{pro}} Pr_{\zeta_A, \zeta_B}(t_A, t_B) \rho_{\zeta_A, \zeta_B}(t_A, t_B), \quad (7.17)$$

with the normalization

$$N(t_A, t_B) = \sum_{\zeta_A, \zeta_B \in M_{pro}} Pr_{\zeta_A, \zeta_B}(t_A, t_B).$$

The time dependent states  $\rho_{\zeta_A, \zeta_B}(t_A, t_B)$  can be calculated for each combination of  $\zeta_A, \zeta_B \in M_{pro}$  leading to 64 different combinations. From this 8 examples with  $\zeta_B = \zeta_1^r$  and  $\zeta_A \in M_{pro}$  are discussed in more detail.

**One photon processes** First the three cases with  $\zeta_A$  being a one photon process are considered. For such cases  $\rho_{\zeta_A, \zeta_B}(t_A, t_B) = \rho_{\zeta_A, \zeta_B}$  is independent of the photon detection times. The processes  $\zeta_A = \zeta_1^r$  results in the desired atom-atom state

$$\rho_{\zeta_1^r, \zeta_1^r} = |\Psi^\pm\rangle \langle \Psi^\pm|.$$

For  $\zeta_A = \zeta_1^\sigma$  the emitted photon has a slightly different temporal mode that leads to a not perfect overlap ( $O_{\zeta_1^\sigma} < 1$ ) and therefore results in a not perfectly entangled atom-atom state

$$\rho_{\zeta_1^\sigma, \zeta_1^r} = |\Psi^\pm\rangle \langle \Psi^\pm| \frac{1 + O_{\zeta_1^\sigma}^2}{2} + |\Psi^\mp\rangle \langle \Psi^\mp| \frac{1 - O_{\zeta_1^\sigma}^2}{2}$$

with the correct Bell state  $|\Psi^\pm\rangle$ , wrong Bell-state  $|\Psi^\mp\rangle$ , and the overlap  $O_{\zeta_1^\sigma} = O_{\zeta_2^{r,\sigma}}(t_1 = 700)$  (Fig. 7.4).

The off-resonant process  $\zeta_A = \zeta_1^o$  results in a mixed state  $\rho_{\zeta_1^{or}, \zeta_1^r}$ . Here, atom  $A$  is in a partially mixed state similar to (7.10) which is partially entangled with atom  $B$  in a superposition state of  $|1, \pm 1\rangle$ . For this state the influence of the spectral mode overlap of the photons is reduced since the off-resonant photon includes a different frequency from decay to  $F = 2$  ( $\Delta f = 6.8$  GHz), which reduces the interference for this decay to zero [33]. Moreover, even with perfect two photon interference the atom-atom state is still mixed. Considering all possible Zeeman states of both hyperfine levels of the  $5S_{1/2}$  ground state  $\rho_{\zeta_1^r, \zeta_1^r}$  gives a  $64 \times 64$  density matrix.

**Two photon processes** The two photon process  $\zeta_A = \zeta_2^{r,r}$  leads to a photon detection time depending atom-atom state  $\rho_{\zeta_2^{r,r}, \zeta_1^r}(t_A, t_B)$ . To calculate this state one has to consider that the temporal overlap of the two detected photons depends on the emission time  $t_1$  of the first not detected photon of  $\zeta_2^{r,r}$ . This results in a  $t_1$  dependence of the atom-atom state

$$\rho_{\zeta_2^{r,r}, \zeta_1^r}(t_1) = |\Psi^\pm\rangle \langle \Psi^\pm| \frac{1 + (O_{\zeta_2^{r,r}}(t_1))^2}{2} + |\Psi^\mp\rangle \langle \Psi^\mp| \frac{1 - (O_{\zeta_2^{r,r}}(t_1))^2}{2}.$$

Hence, it is necessary to integrate this state over all possible first photon emission times  $t_1 \leq t_A$  to obtain a state depending on  $t_A$  and  $t_B$ :

$$\rho_{\zeta_2^{r,r}, \zeta_1^r}(t_A, t_B) = \frac{1}{N_{\zeta_2^{r,r}, \zeta_1^r}(t_A)} \int_{t_1 < t_A} \rho_{\zeta_2^{r,r}, \zeta_1^r}(t_1, t_A, t_B) Pr_1^r(t_1) Pr_2^r(t_1|t_A) dt_1 \quad (7.18)$$

where  $Pr_1^r(t_1)$  and  $Pr_2^r(t_1|t_A)$  are the time dependent emission probabilities for the first and the second photon from Table 7.2, and

$$N_{\zeta_2^{r,r}, \zeta_1^r}(t_A) = \frac{1}{\int_{t < t_A} Pr_1^r(t) Pr_2^r(t, t_A) dt}$$

is the normalization. For the process  $\zeta_A = \zeta_2^{r,\sigma}$  the resulting state  $\rho_{\zeta_2^{r,\sigma}, \zeta_1^r}(t_A, t_B)$  is calculated analogous to (7.18) with  $O_{\zeta_2^{r,\sigma}}(t)$  and  $Pr_2^\sigma(t|t_A)$ . The state  $\rho_{\zeta_2^{r,o}, \zeta_1^r}(t_A, t_B)$  for  $\zeta_A = \zeta_2^{r,o}$  is mixed and very similar to  $\rho_{\zeta_1^{or}, \zeta_1^r}$  but also includes a small time dependence from the two photon interference. However, this time dependence is not important for the state fidelity concerning the wanted  $|\Psi^\pm\rangle$  state.

The other possible two photon processes  $\zeta_A = \zeta_1^{r,o}$  and  $\zeta_A = \zeta_1^{r,\sigma}$  are conditioned on the detection of a first photon. Since for  $\zeta_1^{r,\sigma}$  all information on the state of atom  $A$  is in the not detected second photon, the atom-atom state mixed with atom  $A$  being in  $|1, 0\rangle$  or  $|1, \pm 1\rangle$  with an equal probability of  $1/3$  independent of atom  $B$ . The situation for the process  $\zeta_1^{r,o}$  is more complex, since, due to possible  $\pi$ -decay from  $F' = 1, m_F = \pm 1$ , the second photon does not carry all information about the atomic state. Hence, the atom-atom state

$$\rho_{\zeta_1^{r,o}, \zeta_1^r}(t_A, t_B) = \frac{5}{12} \rho_{\zeta_1^{r,o}, \zeta_1^r}^I(t_A, t_B) + \frac{7}{12} \rho_{\zeta_1^{r,o}, \zeta_1^r}^{II}$$

is a mixture of a detection time dependent partially mixed state

$$\rho_{\zeta_1^{r,o}, \zeta_1^r}^I(t_A, t_B) = \int_{t_2 > t_A} \rho_{\zeta_1^{r,o}, \zeta_1^r}^I(t_2) Pr_2^o(t_A, t_2) dt_2,$$

with the state

$$\rho_{\zeta_1^{r,o}, \zeta_1^r}^I(t_2) = |\Psi^\pm\rangle \langle \Psi^\pm| \frac{1 + (O_{\zeta_1^{r,o}}(t_2))^2}{2} + |\Psi^\mp\rangle \langle \Psi^\mp| \frac{1 - (O_{\zeta_1^{r,o}}(t_2))^2}{2}$$

depending on the emission time of the second photon  $t_2$  and normalization

$$N_{\zeta_1^{r,o}, \zeta_1^r}(t_A) = \frac{1}{\int_{t_2 > t_A} Pr_2^o(t_A, t_2) dt_2}.$$

and a constant mixed state  $\rho_{\zeta_1^{r,o}, \zeta_1^r}^{II}$  with atom  $A$  uncorrelated to atom  $B$ .

### Two photon coincidences from one atom

In addition to the two photon coincidences with photons from two atoms, there is also the possibility of two photon originating from one atom. This always leads to a completely uncorrelated atom-atom states  $\rho_{\zeta_{1,2}^{r,o}, \zeta_B}$  and  $\rho_{\zeta_{1,2}^{r,\sigma}, \zeta_B}$ .

In the case of off-resonant excitation  $\zeta_{1,2}^{r,o}$  one has to consider entanglement between the two emitted photons (7.14). For two photons resulting in the atomic state  $|1, 0\rangle$ , which are in the entangled state  $\frac{1}{\sqrt{2}}(|\sigma^+\rangle_1 |\sigma^-\rangle_2 + |\sigma^-\rangle_1 |\sigma^+\rangle_2) = \frac{1}{\sqrt{2}}(|H\rangle_1 |H\rangle_2 + |V\rangle_1 |V\rangle_2)$ , the BSM analyzing the photons in the  $H, V$  polarization basis (Sec. 2.4.1) never results in heralding of an entangled atom-atom state [33]. Thus, they do not contribute to the atom-atom state and the mixed atom-atom state  $\rho_{\zeta_{1,2}^{r,o}, \zeta_B}$  considers only the  $F = 2$  ground state in one of the atoms. The two photon detection caused by imperfect polarization  $\zeta_{2,1,2}^\sigma$  results in  $\rho_{\zeta_{1,2}^{r,\sigma}, \zeta_B}$  with only  $F = 1$  ground states. The two photon detection probabilities are

$$Pr_{\zeta_{1,2}^{r,o}, \zeta_B}(t_{A_1}, t_{A_2}) = \frac{1}{16} Pr_2^o(t_{A_1}, t_{A_2})$$

and

$$Pr_{\zeta_{1,2}^{r,\sigma}, \zeta_B}(t_{A_1}, t_{A_2}) = \frac{1}{4} Pr_2^\sigma(t_{A_1}, t_{A_2}).$$

### Combined atom-atom state

To combine all possible two photon coincidence types to the complete detection time dependence of the atom-atom state one has to consider that the BSM cannot differentiate between photons from atom  $A$  and  $B$ . So the combined atom-atom state  $\rho_{AA}^{co}$  (subscript analogous to the atom-atom state in Section 2.4) for a coincidence with detection times  $t_1$  and  $t_2$  has the form

$$\rho_{AA}^{co}(t_1, t_2) = \frac{1}{N(t_1, t_2)} \left[ Pr_{AB}(t_1, t_2) \rho_{AB}(t_1, t_2) + Pr_{AB}(t_2, t_1) \rho_{AB}(t_2, t_1) \right. \\ \left. + 2 \cdot Pr_{\zeta_{1,2}^{r,o}, \zeta_B}(t_1, t_2) \rho_{\zeta_{1,2}^{r,o}, \zeta_B} + 2 \cdot Pr_{\zeta_{1,2}^{r,\sigma}, \zeta_B}(t_1, t_2) \rho_{\zeta_{1,2}^{r,\sigma}, \zeta_B} \right], \quad (7.19)$$

with the probability for a coincidence  $Pr_{AB}(t_A, t_B)$  with a photon from atom  $A$  at time  $t_A$  and a photon from atom  $B$  at time  $t_B$  and the normalization

$$N(t_1, t_2) = (Pr_{AB}(t_1, t_2) + Pr_{AB}(t_2, t_1) + 2 \cdot Pr_{\zeta_{1,2}^{r,o}, \zeta_B}(t_1, t_2) + 2 \cdot Pr_{\zeta_{1,2}^{r,\sigma}, \zeta_B}(t_1, t_2)).$$

This allows to calculate the atom-atom state for a certain acceptance time window  $[t_s, t_e]$ , conditioned on  $t_s \leq t \leq t_e$ , via integration of the time dependent state over the time window

$$\rho_{AA}^{co}([t_s, t_e]) = \frac{1}{N_{[t_s, t_e]}} \int_{t_s}^{t_e} \int_{t_1}^{t_e} (\rho_{AA}^{co}(t_1, t_2) \cdot N(t_1, t_2)) dt_2 dt_1,$$

with normalization

$$N_{[t_s, t_e]} = \int_{t_s}^{t_e} \int_{t_1}^{t_e} N(t_1, t_2) dt_2 dt_1.$$

The fidelity to the Bell-state  $|\Psi^\pm\rangle$  can be calculated via

$$F(\rho_{AA}^{co}([t_s, t_e]), |\Psi^\pm\rangle) = \langle \Psi^\pm | \rho_{AA}^{co}([t_s, t_e]) | \Psi^\pm \rangle.$$

## 7.4. Optimizing the two photon coincidence time window

As shown in the previous section, it is possible to calculate the prepared atom-atom state using the model from [33] and based on this to optimize the acceptance conditions for the coincidence detection. However the full density matrix of  $\rho_{AA}$  has dimension  $64 \times 64$  and even if most of the 4096 entries are zero still many not vanishing entries remain. Additionally, since the atomic state read-out (Sec. 2.3.2) only discriminates a certain superposition of  $|1, \pm 1\rangle$ , the dark state (2.9), from all other states, the full density matrix is not needed to predict the results of an experiment. Strictly speaking, the read-out will lead to an ionization of  $|1, 0\rangle$  and all  $F = 2$  Zeeman states independent of the actual measurement setting. Hence, the measurement results for most states involving an off-resonant excitation process are simply  $+1$ . This allows to bypass the complex mixed state resulting from off-resonant excitation reducing the complexity of the atom-atom model.

### 7.4.1. Model for the $S$ value dependence on the detection times

Such a consideration enables to calculate an expectation value for a measured CHSH  $S$  value for every excitation process. To do so, here a model with the following considerations is used:

1.  $S$  is defined accordingly to (4.12) with the measurement settings from Table 4.1.
2. The atomic measurement process is assumed to be perfect.
3. The evolution of atomic states is not considered.
4. Imperfections of the photon collection and detection are considered, i.e, imperfect collection and detection efficiency and detector dark counts.
5. All imperfections of read-out and decoherence are implemented afterwards with a constant factor  $f_{imp}$ .

The general atom-atom state is composed from four different types of states. First, there is the desired Bell state  $|\Psi^\pm\rangle$ . Then there is a contribution from the unwanted Bell state  $|\Psi^\mp\rangle$  due imperfect two photon interference. Further, there are the mixed or partially mixed atom-atom states where one atom is in a combination of  $|1, 0\rangle$  and  $F = 2$  Zeeman states.

atom-atom state	$S^\pm$
$ \Psi^\pm\rangle$	$2\sqrt{2}$
$ \Psi^\mp\rangle$	0
one of the atoms in $ 1, 0\rangle$ and $F = 2$ states	0
both atoms in $ 1, 0\rangle$ and $F = 2$ states for both atoms	-2

Table 7.5.: Expected  $S^\pm$  for specific atom-atom states according to (4.11).

Finally, there is a very small contribution from states where both atoms are in a combination of  $|1, 0\rangle$  and  $F = 2$  Zeeman states.

When evaluating  $S^+$  (4.11), with  $|\Psi^+\rangle$  the desired state and  $|\Psi^-\rangle$  the wrong component due to bad overlap, the expectation is  $S^+ = 2\sqrt{2}$  for  $|\Psi^+\rangle$  and 0 for  $|\Psi^-\rangle$  (and vice versa for  $S^-$  with the respective superscripts). For the states where one of the atoms is in a combination of  $|1, 0\rangle$  and  $F = 2$  Zeeman states the measurement results are uncorrelated and thus, the expectation is  $S = 0$ . And for the cases where both atoms are in a combination of  $|1, 0\rangle$  and  $F = 2$  Zeeman states the measurement yields always the result +1 for both sides and thus correlated. Since in the Bell settings in the experiment from Chapter 4 (Tab. 4.1) predict for three out of the four input combinations negative correlator functions full correlation leads to an expected  $S = -2$ .

Combining these expectation values allows to calculate the expected  $S$  for all excitation process combinations. Some specific examples can be found in Table 7.6. With this the coincidence detection time time depending  $S^{co}(t_1, t_2)$

$$S^{co}(t_1, t_2) = \frac{1}{N_{(t_1, t_2)}} \left[ Pr_{AB}(t_1, t_2) S(\rho_{AB}(t_1, t_2)) + Pr_{AB}(t_2, t_1) S(\rho_{AB}(t_2, t_1)) \right. \\ \left. + \eta_{AB} \left( Pr_{\zeta_{1,2}^{r,o}, \zeta_B}(t_1, t_2) S(\rho_{\zeta_{1,2}^{r,o}, \zeta_B}) + Pr_{\zeta_{1,2}^{r,\sigma}, \zeta_B}(t_1, t_2) S(\rho_{\zeta_{1,2}^{r,\sigma}, \zeta_B}) \right) \right] \quad (7.20)$$

according to (7.19) with  $N_{(t_1, t_2)}$  from (7.19) and the reduced detection efficiency for detecting two photons from one atom

$$\eta_{AB} = \frac{\eta_A^2 + \eta_B^2}{\eta_A \cdot \eta_B}.$$

Here  $\eta_A$  is the combined collection detection and detection efficiency for Atom A and  $\eta_B$  for Atom B. The total collection and detection efficiency of the trap setup in Lab 2 is reduced by  $\sim 50\%$  in comparison to the setup in Lab 1, due to the significantly photon loss in the 700 m long fiber connection (Fig. 2.1), resulting in  $\eta_{AB} \approx 2.5$ .

To optimize the acceptance conditions for the coincidences heralding atom-atom entanglement, it is necessary to include experimental parameters such as noise introduced by detector dark counts or by a possible background in the model. Coincidences caused by at least one noise detection lead always to an uncorrelated atom-atom state and thus  $S \leq 0$  is expected, depending on the emission process of the other detected photon. The time dependent probability of a coincidence from a background count and a photon from atom A is

$$Pr_{noise,A}^{co}(t_1, t_2) = \sum_{\zeta_A \in M_{pro}} \left( Pr_{\zeta_A}(t_1) \cdot Pr_{noise} + Pr_{\zeta_A}(t_2) \cdot Pr_{noise} \right)$$

$\zeta_A$	$\zeta_B$	$S(t_A, t_B)$
$\zeta_1^r$	$\zeta_1^r$	$2\sqrt{2}$
$\zeta_{1_1}^{or}$	$\zeta_1^r$	0
$\zeta_{1_1}^o$	$\zeta_1^r$	$2\sqrt{2} \frac{1+(O_{\zeta_2^{r,\sigma}}(0))^2}{2}$
$\zeta_{2_2}^r$	$\zeta_1^r$	$\frac{2\sqrt{2}}{12} \frac{Pr_1^r(t_1)Pr_2^o(t_A,t_A)dt_1}{\int_{t < t_A} \frac{1+(O_{\zeta_2^{r,r}}(t_1))^2}{2}} Pr_1^r(t_1)Pr_2^r(t_1, t_A)dt_1$
$\zeta_{2_1}^{or}$	$\zeta_1^r$	$\frac{5}{12} \frac{2\sqrt{2}}{\int_{t > t_A} Pr_2^o(t_A, t_2)dt_2} \int_{t > t_A} \frac{1+(O_{\zeta_1^o}(t_2))^2}{2} Pr_2^o(t_A, t_2)dt_2$
$\zeta_{2_1}^o$	$\zeta_1^r$	0
$\zeta_{2_{1,2}}^{or}, \zeta_{2_{1,2}}^o$	—	0
$\zeta_2^{r,r}$	$\zeta_2^{r,r}$	$\frac{2\sqrt{2}}{\int_{t < t_A} Pr_1^r(t_1)Pr_2^o(t,t_A)dt_1} \int_{t_{1,A} < t_A} \int_{t_{1,B} < t_B} \frac{1+(O_{\zeta_2^{r,r}}( t_{1,A}-t_{1,B} ))^2}{2} Pr_1^r(t_{1,A})Pr_2^r(t_1, t_A)dt_{1,A}dt_{1,B}$
$\zeta_1^o$	$\zeta_1^o$	-2

Table 7.6.: Expectation  $S^\pm$  for different excitation process combinations at atom  $A$  and atom  $B$ . ( $S(t_A, t_B)$  for the  $\zeta_2^r, \zeta_{2_2}^r$  process is only an estimate, since the overlap of two photons from two photon processes is not calculated in the model from [33])

with the constant probability density for a noise detection

$$Pr_{noise} = R_{noise} \Delta t$$

depending on the noise rate  $R_{noise}$  and normalized for the detection time bin  $\Delta t$ . Resulting in the following noise dependent  $S$  value

$$S_{noise}^{co}(t_1, t_2) = S^{co}(t_1, t_2) \frac{N(t_1, t_2)}{N(t_1, t_2) + Pr_{noise,A}^{co}(t_1, t_2)} \quad (7.21)$$

that can be used to optimize the acceptance conditions for the coincidence detection.

### Including parameters of the experiment

To calculate an  $S$  that is actually comparable to the experiment in Chapter 4 a factor  $F_{imp}$  to account for imperfections of the experiment, e.g., imperfect read-out and decoherence, is needed. Since the experimental deficiencies only effect the processes with expected  $S > 0$ , this factor is only applied if  $S(\rho_{AA}(t_A, t_B)) > 0$  resulting in a new

$$S_{imp}^{co}(t_1, t_2) = \frac{N(t_1, t_2)}{N(t_1, t_2) + Pr_{noise,A}^{co}(t_1, t_2)} \quad (7.22)$$

$$\left[ Pr_{AB}(t_1, t_2) S_{imp}(\rho_{AB}(t_1, t_2)) + Pr_{AB}(t_2, t_1) S_{imp}(\rho_{AB}(t_2, t_1)) \right. \\ \left. + \eta_{AB} \left( Pr_{\zeta_{1,2}^{r,\sigma}, \zeta_B}(t_1, t_2) S_{imp}(\rho_{\zeta_{1,2}^{r,\sigma}, \zeta_B}) + Pr_{\zeta_{1,2}^{r,\sigma}, \zeta_B}(t_1, t_2) S_{imp}(\rho_{\zeta_{1,2}^{r,\sigma}, \zeta_B}) \right) \right]$$

with a modified expected  $S$  value

$$\begin{aligned} S_{imp}(\rho_{AA}(t_A, t_B)) &= S(\rho_{AA}(t_A, t_B)) & S(\rho_{AA}(t_A, t_B)) &\leq 0 \\ S_{imp}(\rho_{AA}(t_A, t_B)) &= S(\rho_{AA}(t_A, t_B)) \cdot F_{imp} & S(\rho_{AA}(t_A, t_B)) &> 0. \end{aligned}$$

Here, for the noise only the dark count rate of 60 counts/sis considered and  $F_{imp} = 0.83975$  is chosen to result in an expected  $S = 2.2$  for all events combined. The coincidence detection probabilities and respective  $S$  values for these parameters are illustrated in Figure 7.5).

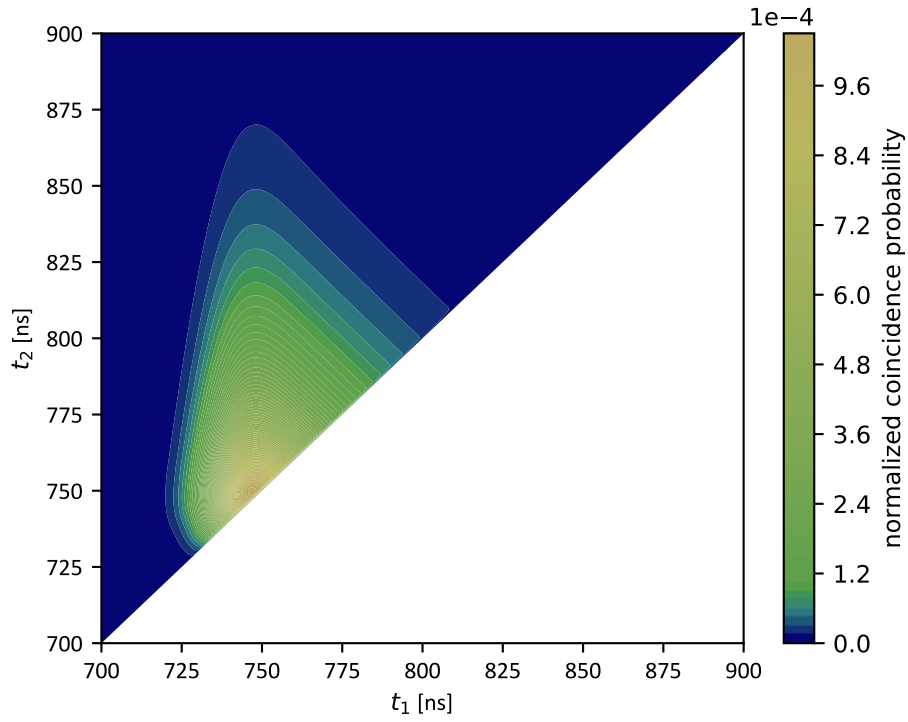
### Acceptance conditions for coincidences

There are several ways to define acceptance conditions for the coincidence detection. To find the optimal conditions two different kinds of coincidence conditions are considered. The first one is absolute acceptance time windows  $[t_s, t_e]$  for both detection times resulting in

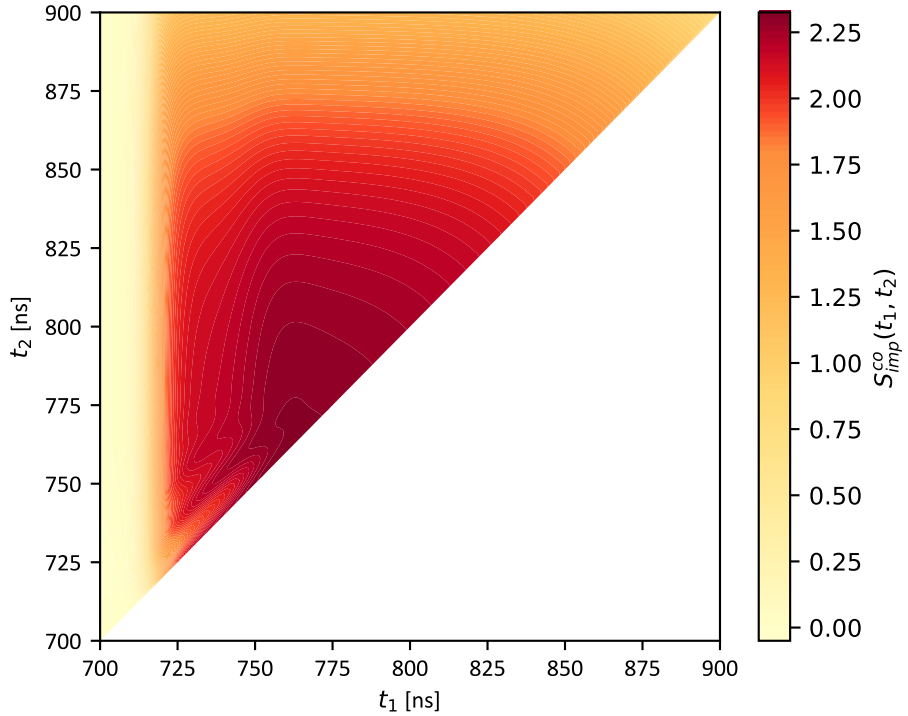
$$S_I^{co}(t_s, t_e) = \frac{1}{N_{[t_s, t_e]}} \int_{t_s}^{t_e} \int_{t_1}^{t_e} \left( S_{noise}^{co}(t_1, t_2) \cdot \left( N(t_1, t_2) + Pr_{noise,A}^{co}(t_1, t_2) \right) \right) dt_2 dt_1 \quad (7.23)$$

with normalization

$$N_{[t_s, t_e]} = \int_{t_s}^{t_e} \int_{t_1}^{t_e} \left( N(t_1, t_2) + Pr_{noise,A}^{co}(t_1, t_2) \right) dt_2 dt_1. \quad (7.24)$$



(a) Normalized probability for a coincidence at  $t_1$  and  $t_2$



(b) Expected  $S$  value  $S_{imp}^{co}(t_1, t_2)$  for a coincidence at  $t_1$  and  $t_2$

Figure 7.5.: Model for coincidence depending  $S$  value considering noise and other imperfections.

A second possibility for coincidence conditions is an absolute time window  $[t_s, t_e]$  for  $t_1$  and a relative time window  $[t_1, t_1 + \delta t]$  depending on  $t_1$  for  $t_2$ . This results in

$$S_{II}^{co}(t_s, t_e, \delta t) = \frac{1}{N_{[t_s, t_e, \delta t]}} \int_{t_s}^{t_e} \int_{t_1}^{t_1 + \delta t} \left( S_{noise}^{co}(t_1, t_2) \cdot \left( N(t_1, t_2) + Pr_{noise, A}^{co}(t_1, t_2) \right) \right) dt_2 dt_1 \quad (7.25)$$

with normalization

$$N_{[t_s, t_e, \delta t]} = \int_{t_s}^{t_e} \int_{t_1}^{t_1 + \delta t} \left( N(t_1, t_2) + Pr_{noise, A}^{co}(t_1, t_2) \right) dt_2 dt_1. \quad (7.26)$$

### Comparison with experimental data

During the experiment not only data on the measurement results and the heralding signal was collected, but also the coincidence detection times for each event. This allows to compare the results from model (Fig 7.6) to experimental data collected during the Bell experiment (Sec. 4.4.2).

By choosing the optimal time window for  $S_I$  (7.23), an improvement of the expected  $S$  value from 2.20 to  $\geq 2.29$ , with  $[t_s = 757 \text{ ns}, t_e = 800 \text{ ns}]$  is realized (Fig. 7.6a). However, tightening the time window lowers the fraction of accepted coincidences significantly. For the optimal  $S$  the fraction of accepted coincidences is only  $N_I^{co}(t_s, t_e) = 0.18$  (Fig. 7.6b). Also with the second method for time filtering (7.25), using an additional constraint  $t_2 - t_1 \leq \delta t$ , a significant improvement of the atomic state is possible (Fig. 7.6c). A short relative time window  $[t_1, t_1 + \delta t]$  allows for  $S > 2.30$ , but the fraction of accepted coincidences  $N_{II}^{co}(t_s, t_e, \delta t)$  approaches zero. For a reasonable amount of accepted coincidences (Fig. 7.6c), the second method yields results comparable to the first method, using an absolute time window.

To compare the results of the model to the actual experiment, the data collected during the Bell test experiment is filtered with the same acceptance condition as the model. This comparison is limited to the  $\Psi^-$  state, which was more robust against drifts of the setup. Additionally, only data collected after the installation of an accurate temperature control of the trap setups in December 2015 and January 2016, which made a realignment of the excitation beam path necessary and by this changed  $t_0$ , is used. The Results in a total number of events of  $N = 25189$  Comparing the expected  $S$  values from the model to the time filtered experimental data shows that the data fits to the model with error margins (Fig. 7.7). Yet, there is a tendency that the model shows less improvement of the  $S$  value compared to the experimental data. This might be due to an underestimation of the misalignment of the excitation pulse and also due to the detailed but still not perfect model of the excitation process.

### 7.4.2. Optimal acceptance time windows for different applications

Finding the optimal acceptance conditions is not only based on the optimal  $S$ , it is also necessary to consider the lower the event rate. Additionally, different experiments and application have different dependencies on both the dependence on the atom-atom state fidelity, respectively on the  $S$  value, and on the number events  $N$ . Therefore, there are different optima for different applications.

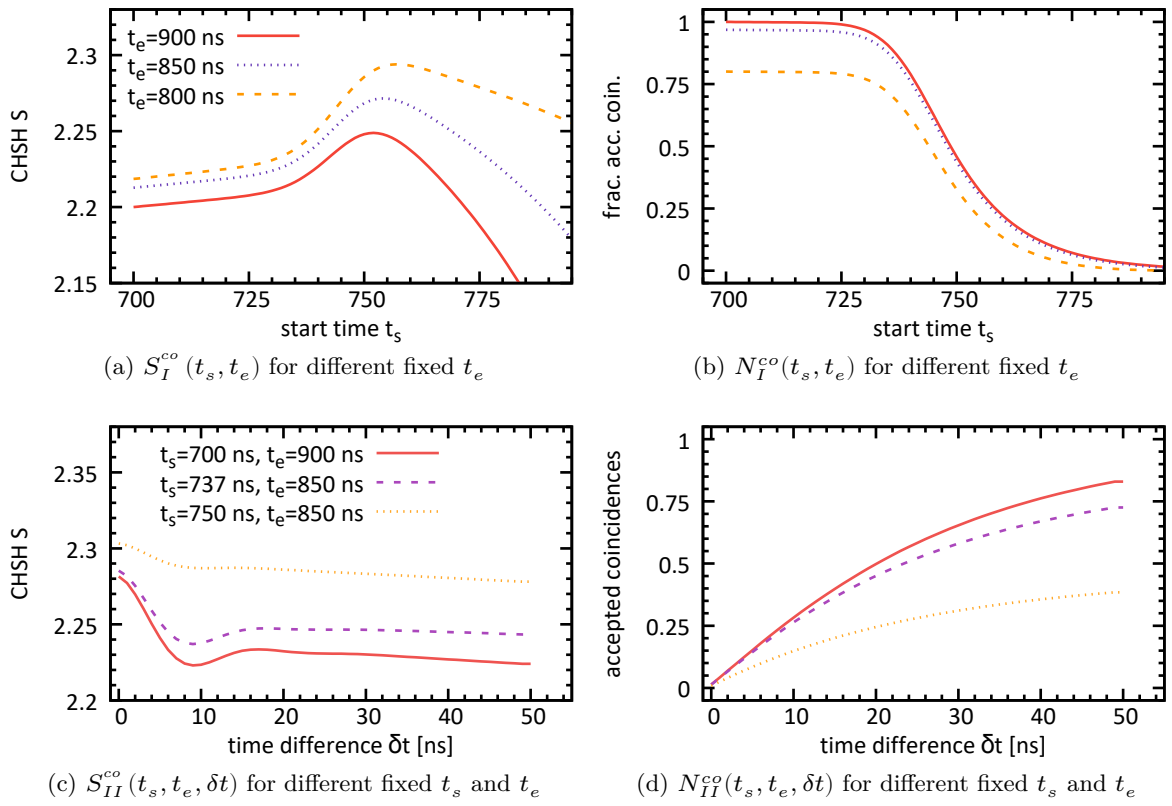


Figure 7.6.: Expected CHSH  $S$  value and fraction of accepted coincidence for both coincidence conditions (7.23) and (7.25).

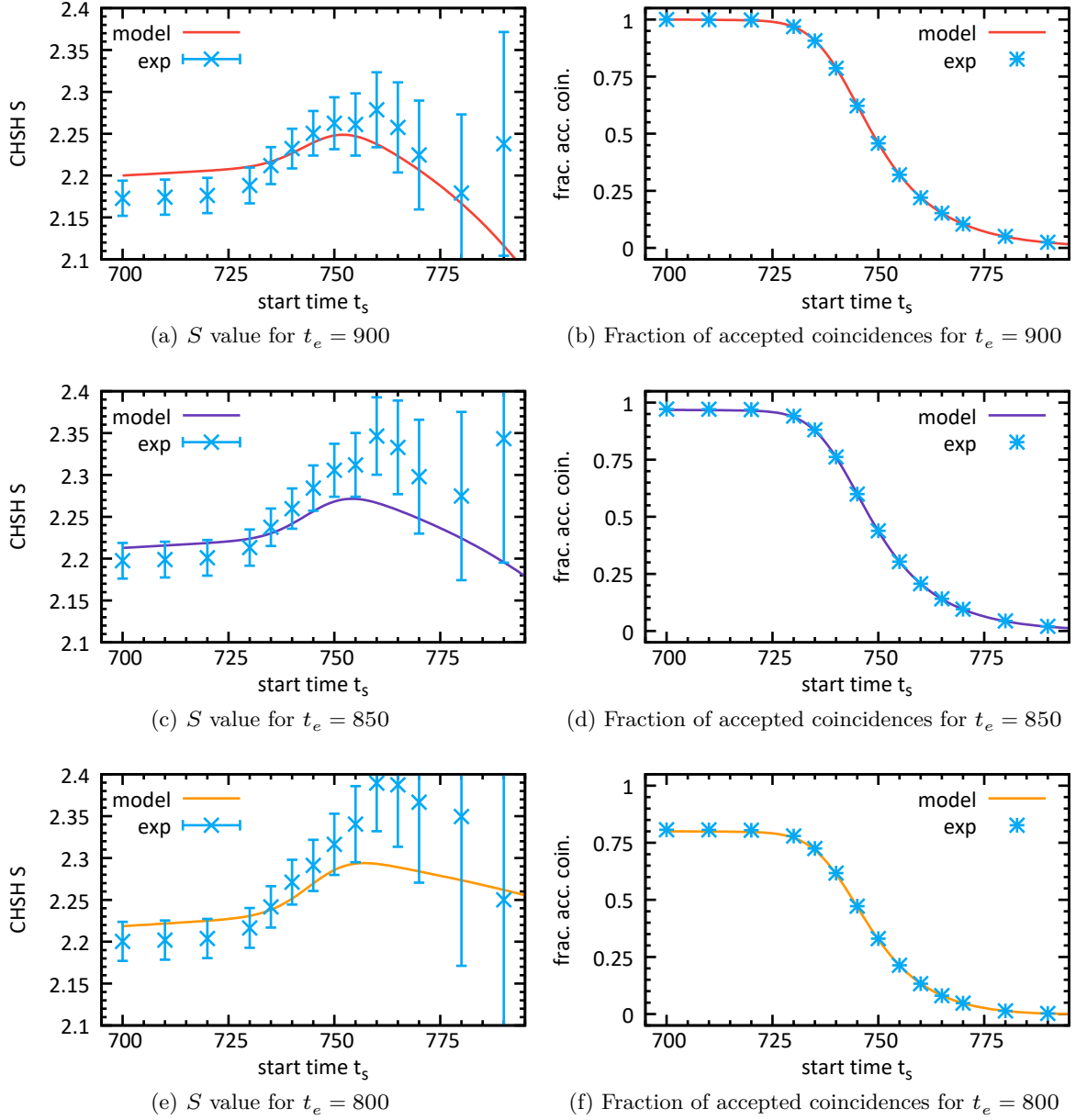


Figure 7.7.: Comparison of  $S_1^{co}(t_s, t_e)$  from the the model to the experimental data for the  $\Psi^-$  state conditioned on the same acceptance conditions.

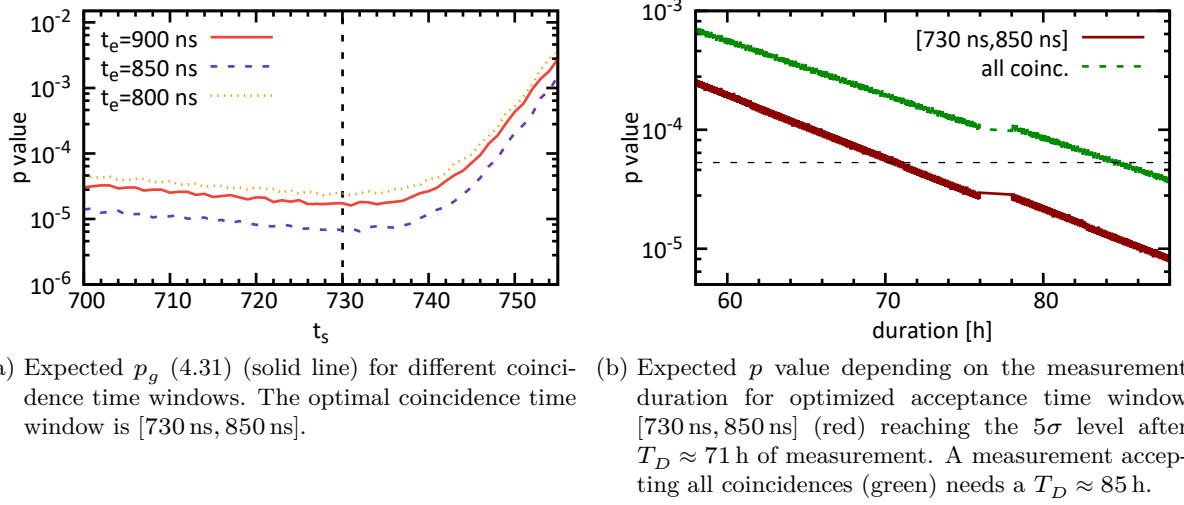


Figure 7.8.: Optimized coincidence time window for the measurement duration of a Bell experiment. The optimization is based on the experiment in Section 4.4 and the considerations in Figure 4.9.

**Bell test experiment** For the Bell experiment in Chapter 4 an  $N$  for a run was chosen to allow for an expected violation comparable to a  $5\sigma$  confidence interval for each heralded state. This resulted in a certain measurement duration  $T_D$  (Tab. 4.2, Fig 4.9). Here, the task is to find acceptance conditions that minimize the measurement duration  $T_D$  needed to reach such a confidence level. The optimal acceptance time window [730 ns, 850 ns] (Fig 7.8) leads to an expected reduction of the measurement duration by a factor of  $< 5/6$ . Using this result for a future Bell test experiment the duration of a run can be reduced by 14 h.

**DI random numbers** For the generation of random bits the generation rate  $C_{rbits} = \frac{n_{rbits}}{T_D}$  is the interesting property. Yet the rate for DI random bits is not linear in time, since the fraction of generated random bits (6.1) from  $N$  events

$$\frac{n_{rbits}}{N} = f(S_m - \epsilon(N, S_m, q, \alpha))$$

depends on  $N$  (6.2). With fixed  $q$  and  $\alpha$  and a constant event rate  $C_N$  this leads to a random bit rate

$$C_{rbits} = C_N f(S_m - \epsilon(N, S_m)),$$

depending on the total number of events  $N$  and  $S_m$ . This behavior does not allow to determine an absolute optimum for the acceptance time window, but it is possible to find optimal time windows for fixed number of total events  $N$ . Considering  $N = 25189$  from the data collected in 2016 the model yields an optimal acceptance time window of [731 ns, 850 ns] for the randomness extraction (Fig. 7.9a).

Since the used model is an ab initio model of the atom-atom state generation, which is derived independently from any measurement, the filtering with an acceptance time window is a preselection of the events and does not diminish the trust in the DI protocol. Without

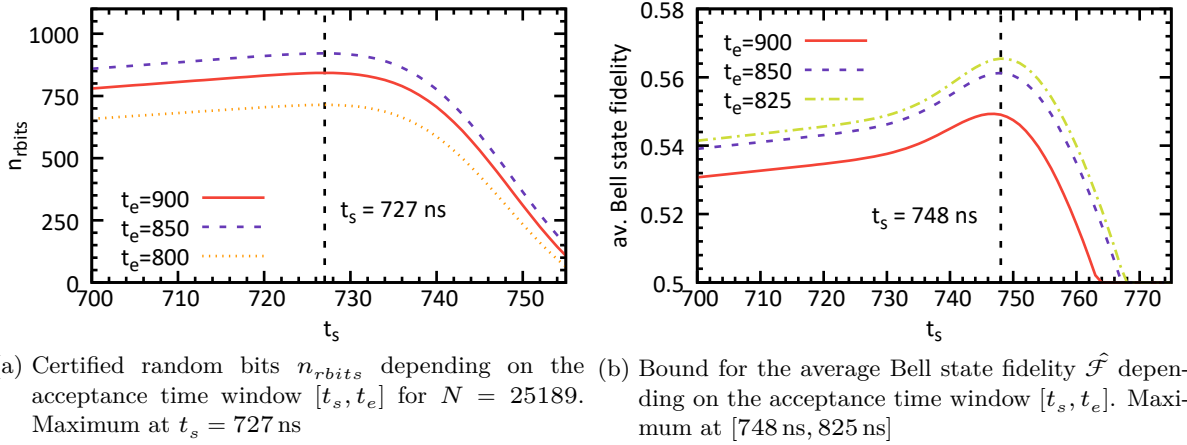


Figure 7.9.: Optimization of the acceptance time window for DI random number generation and self-testing

the preselection the  $N = 25189$  events resulting in  $S_m = 2.1729$  allow for an extraction of  $n_{\text{bits}} = 516$  random bits with a confidence level of 99%. Now applying the new acceptance time window (Fig. 7.9a) to the data leads to  $N = 24126$  accepted events with  $S_m = 2.2084$  and  $n_{\text{bits}} = 801$  certified random bits. Considering the data for both states, the time window filtering yields  $N = 48341$  events with  $S_m = 2.1593$  and  $n_{\text{bits}} = 1358$  random bits. This is a significant improvement of the randomness extraction presented in Section 6.2.2.

**Self-testing** In this thesis, the certification of a quantum network link using self-testing (Sec. 6.3) is demonstrated. Here, the figure of merit is the average Bell state fidelity  $\hat{\mathcal{F}}$ , which, like  $p$  and  $n_{\text{bits}}$ , depends on  $S_m$  as well as the number of events  $N$  (6.7). However, in contrast to the previous two examples a larger minimal  $S_m$  of 2.106 (6.6) is required. Thus, the optimization here is more towards higher  $S_m$  than larger  $N$ . As for the DI random number generation optimizing is only possible for a fixed number of total events  $N$ . Considering  $N = 25189$  events and a confidence interval of  $\alpha = 99\%$  leads to an optimal time window of  $[748$  ns,  $825$  ns] (Fig. 7.9b). With this new acceptance time window (Fig. 7.9b) the data for  $\Psi^-$  from 2016 gives  $N = 111725$  and  $S_m = 2.3038$  resulting in a certified Bell state fidelity of  $\hat{\mathcal{F}} = 0.584$  with 99% confidence. For a higher confidence level of 99.99% optimal the time window is  $[745$  ns,  $825$  ns] resulting in  $\hat{\mathcal{F}} = 0.549$ . Considering both  $\Psi^+$  and  $\Psi^-$  applying these time windows yields a  $\hat{\mathcal{F}} = 0.568$  with 99% confidence and  $\hat{\mathcal{F}} = 0.53$  with 99.99% confidence.

This is a very strong improvement to the results presented in Section 6.3. Especially, the improvement for the combined states shows that the two atom traps form an unprecedented quantum network link over the distance of 400 m. This link allows for device-independent applications and opens the possibility for future quantum networks.

## 7.5. Optimal excitation parameters for future experiments

In future experiments, an optimized time dependence and absolute power of the excitation pulse could allow for a higher atom-atom state fidelity. For this purpose, the detailed model of the excitation process can be used to find optimal parameters of such a pulse. It must be

pointed out that the optimal excitation pulse parameters are not the same for different applications and experimental goals. Additionally, it is necessary to consider improvements and changes in the experimental setup, since certain parameters of the experiment, e.g, pumping efficiency, photon detection efficiency, and background counts might change. To account for this, different scenarios are considered.

### Setup with higher photon detection efficiency

Recently, a new custom designed high NA objective was installed for fluorescence collection [149, 156]. With the new optics an increase of the collection efficiency by a factor of about 3 is expected leading to an increase of the atom-atom event rate by a factor of 9. This higher collection efficiency reduces the effect of background counts. Therefore, besides time filtering, a weaker excitation pulse, which will reduce the probability of two photon processes while still allowing for a good signal to background ratio, can be implemented.

Reducing the excitation pulse power by a factor of 0.5 from the value used for the experiments in this work leads to a strong reduction of the unwanted processes. A simulation with  $P_O = 0.5 \cdot 1.08 \text{ mW/mm}^2$  while all other parameters are the same as in Section 7.2.2 leads to an expected  $S$  value of above 2.28 without any extra time filtering. Still, reducing the excitation power by 0.5 will reduce the total photon emission probability by the factor 0.625 (Fig. 7.2a) resulting in a reduction of the two photon coincidence rate by 0.39. However, given the improved photon collection the total event rate will still rise by a factor of 3.5.

### Setup for longer distance between the atoms

The next step towards quantum networks is to increase the distance between the atom traps. To overcome the photon loss of  $4 \text{ dB/km}$  at  $780 \text{ nm}$  in the fiber wavelength conversion of the fluorescence photons to a wavelength with lower fiber losses is necessary. Conversion to  $1522 \text{ nm}$  reduces the attenuation to  $0.2 \text{ dB/km}$  [156]. To detect photons of this wavelength new highly efficient superconducting nanowire single-photon detector (SNSPD) will be used in the BSM. Therefore, the new total photon collection and detection efficiency depends on the conversion efficiency, fiber length, and the SNSPD detection efficiency. Furthermore, due to the frequency conversion additionally background counts will be introduced on the detectors and thus spectral filtering ( $27 \text{ MHz}$ ) is needed to suppress this background to an acceptable level of roughly  $1000 \text{ counts/s}$ . This high background count rate makes a short acceptance time window necessary but the spectral filtering has the additional positive effect that photons resulting from a decay to the  $5S_{1/2}, F = 2$  are filtered out.

A simulation considering the higher noise but using the same parameters as in Section 7.2.2 otherwise suggests an acceptance time window [ $735 \text{ ns}, 785 \text{ ns}$ ], which results in an expected  $S = 2.16$  while still allowing for an event rate of 0.5 of all coincidences. An even narrower acceptance time window of [ $748 \text{ ns}, 775 \text{ ns}$ ] results in  $S = 2.2$  but reduces the event rate to 0.2 of the original value.

## 8. Conclusion and Outlook

In this work, entanglement of two independent  $^{87}\text{Rb}$  atoms separated by 398 m was used for a test of local-realism with Bell's inequality, but also the first steps towards its application in quantum networks and for device-independent protocols were shown.

The Bell test with entangled atoms yielded a violation of the CHSH inequality with  $S = 2.221 \pm 0.033$ , while closing all major experimental loopholes. This results in a  $p$  value of  $1.739 \cdot 10^{-10}$  allowing for a strong rejection of local-realism. To minimize possible expectation bias the experiment was conducted following a set of strict rules. Additionally, a "Live" run of the experiment was conducted to allow for maximal transparency. The only part of the experiment that still relied on assumptions was the creation of random inputs for the setting choice. To address this, human made random numbers were used for a Bell test employing atom photon entanglement. This experiment was part of "The Big Bell Test", which included 13 parallel experiments. They were provided with random bits created by online participants around the world, which then were used as inputs in the experiment. All 13 experiments showed a clear violation of the predictions based on local-realism.

The result of the Bell test also confirms the entanglement between the two atoms. Being stationary qubits and by this quantum memories, the entangled atoms form a basic quantum network link with two nodes and a 700 m fiber connection. Such links are the building blocks of future large scale quantum networks incorporating quantum repeaters. Furthermore, the setup allowed for device-independent applications. In such protocols no assumptions on the devices used are made and they are considered black boxes. This allows for trusted results even in the case of imperfect or not trustworthy devices. The 55568 entanglement events collected within 7 months allowed for the extraction of 1059 DI certified random bits. Additionally, it was possible to demonstrate the first fully device independent certification of entanglement. Using the self-testing formalism, it was possible to obtain a device-independent Bell state fidelity of 51.24% for the  $\Psi^-$  state with a confidence of 99%, certifying the quantumness of the network link.

To further improve the performance of the quantum network link, a thorough analysis of the creation of atom-atom entanglement, which is based on entanglement swapping, was conducted. A realistic model of the excitation process creating the atom-photon entanglement used for the swapping allows for the optimization of the entanglement creation. This model allowed to find optimized acceptance conditions for the Bell-test measurement of the swapping process. Applying those conditions for the data for the device independent protocols allows for a significant improvement of those, leading to 1358 certified random bits and a Bell state fidelity of 58.4% with 99% confidence. Furthermore, the model can be used to optimize the parameters of the excitation laser pulse for higher rates and fidelity in future experiments.

The next step towards quantum networks and further quantum communication applications is to extend the distance between the entangled atoms. Due to the attenuation of  $4.0 \text{ dB/km}$  for 780 nm light in optical fibers a frequency conversion of the single photons to the telecom range with 1522 nm with an attenuation of only  $\approx 0.2 \text{ dB/km}$  is necessary [156]. Further, the event ready scheme makes it necessary that the coherence of the atomic state is improved

significantly. For this, a lower temperature of the trapped atoms is necessary. Also a possible state transfer of the qubit from the Zeeman states to the hyperfine states can help to prolong the coherence time by several orders of magnitude [157]. Additionally, to improve the entanglement generation rate, the collection of the fluorescence photons needs to be improved. For this a new custom designed collection optics will be implemented [149]. The expected improvement of the collection efficiency by a factor of 3 will lead to an improvement of the event rate by a factor of 9.

A further step can be the expansion of the experiment to a three node network, with a middle node containing two trapped atoms. By additionally implementing an atom-atom Bell state measurement at the middle node, a quantum repeater can be realized. This would be an important milestone for quantum networks and quantum communication in the future.

## A. Physical Constants and Properties of $^{87}\text{Rb}$

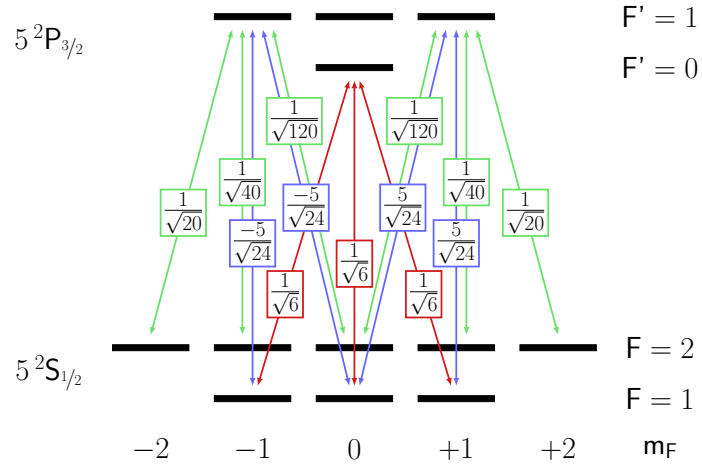
Physical constants and properties of the  $^{87}\text{Rb}$ -atoms used in the experiments are from [49] including Clebsch-Gordan coefficients for dipole transition concerning the excitation process (Sec. 2.3.1) and the read-out process (Sec. 2.3.2).

constant	description	value
$\hbar = \frac{h}{2\pi}$	reduced Planck constant	$1.054571726 \cdot 10^{-34} \text{ J} \cdot \text{s}$
$c$	speed of light in vacuum	$2.99792458 \cdot 10^8 \text{ m/s}$
$\mu_0$	permeability of free space	$1.25663770614 \cdot 10^{-6} \text{ N/A}^2$
$\epsilon_0 = \frac{1}{c^2 \mu_0}$	permittivity of free space	$8.8541878176 \cdot 10^{-12} \text{ F/m}$
$e$	elementary charge	$1.602176565 \cdot 10^{-19} \text{ C}$
$u$	atomic mass unit	$1.660538921 \cdot 10^{-27} \text{ kg}$
$k_B$	Boltzmann constant	$1.38064852 \cdot 10^{-23} \frac{\text{m}^2 \cdot \text{kg}}{\text{s}^2 \cdot \text{K}}$

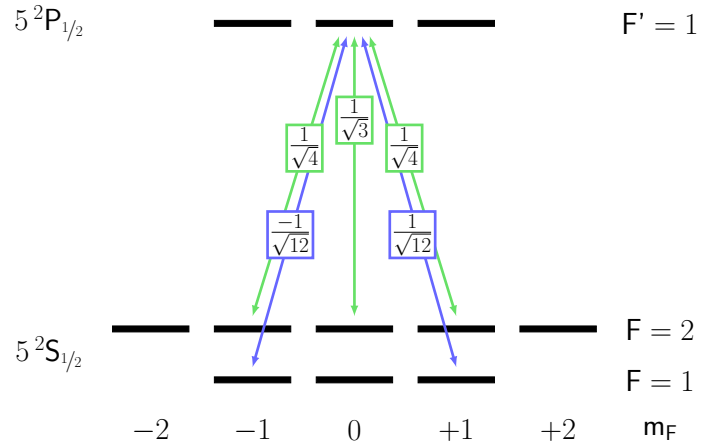
Table A.1.: Physical constants

constant	description	value
$^{87}\text{Rb}$ -atom		
$Z$	atomic number	37
$m$	mass	$86.90918020 \cdot u$
$I$	nuclear spin	$3/2$
$\tau_n$	nuclear life time	$4.88 \cdot 10^{10}$ yr
$E_0$	ground state energy	4.177127 eV
	ionization limit	296.817 nm
$D1$ transition $5^2\text{S}_{1/2} \rightarrow 5^2\text{P}_{1/2}$		
$\Gamma_{D1}$	decay rate	$2\pi \cdot 5.7500$ MHz
$\tau_{D1}$	life time of $5^2\text{P}_{1/2}$ excited state	27.70 ns
$d_{D1}$	dipole matrix element	$2.537 \cdot 10^{-29}$ C · m
$\lambda_{D1}$	transition wavelength	794.979 nm
$D2$ transition $5^2\text{S}_{1/2} \rightarrow 5^2\text{P}_{3/2}$		
$\Gamma_{D2}$	decay rate	$2\pi \cdot 6.0666$ MHz
$\tau_{D2}$	life time of the $5^2\text{P}_{3/2}$ excited state	26.24 ns
$d_{D2}$	dipole matrix element	$3.584 \cdot 10^{-29}$ C · m
$\lambda_{D2}$	transition wavelength	780.241 nm

Table A.2.: Atomic properties of  $^{87}\text{Rb}$



(a) Dipole transitions for the excitation process  $5^2S_{1/2}, F = 1, 5^2S_{1/2}, F = 2, 5^2P_{3/2}, F' = 0$ , and  $5^2P_{3/2}, F' = 1$



(b) Dipole transitions for the read-out process  $5^2S_{1/2}, F = 1$  and  $5^2P_{1/2}, F = 1$

Figure A.1.: Clebsch-Gordan coefficients for transitions between selected states

## B. Definition of the Coordinate System, Polarization, and Atomic States

For a consistent description of the performed experiment it is necessary to define a coordinate system applicable for the setups in both labs. It is important to connect the reference frame of a single atom with the one of the laboratory in a consistent way. This includes definitions of polarization for photons emitted by the atom and laser light in the setup as well as fitting definitions of the atomic states.

The older definition of [48] used also in [34, 33] and with modifications in [37, 38] fits for a previous stage of the trap setup used for the experiment published in [32] and is sometimes misleading in the current setup.

### Definition of the coordinate system

The coordinate system for both traps is defined in the following way:

1. The origin is at the focal spot of the dipole trap (position of the atom).
2. The  $z$ -axis is defined by the axis of the microscope objective pointing from the focal spot towards the objective.
3. The  $x$ -axis is defined parallel to the optical table (horizontal plane) orthogonal to the  $z$ -axis. Pointing from the focal spot towards front side of the glass cell.
4. The  $y$ -axis is defined perpendicular to the table pointing upwards.

This coordinate system has a right hand orientation. See also Figure B.1.

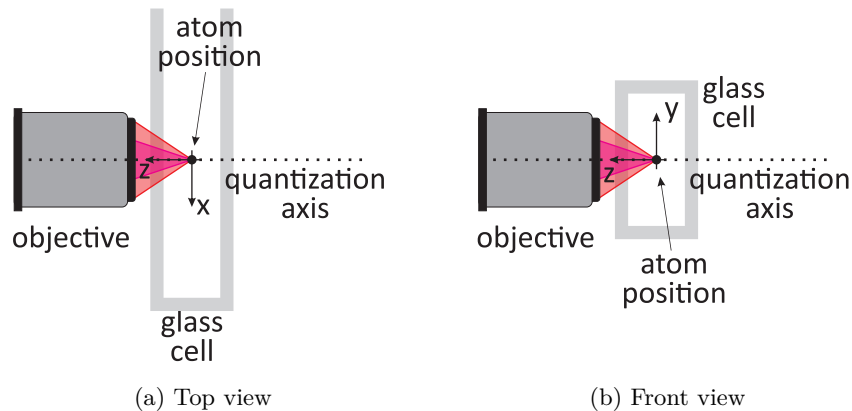


Figure B.1.: Definition of the coordinate system

## Definition polarization and photon states

### Reference frame of the atom

For the atom with a quantization axis  $\mathcal{Z}$  the polarization of the photon emitted by the atom is defined in the following way:

1.  $\sigma^+$  with a right hand rotation of the polarization in traveling direction for a change of  $\Delta m_{f,\mathcal{Z}} = -1$
2.  $\sigma^-$  with a left hand rotation of the polarization in traveling direction with a change of  $\Delta m_{f,\mathcal{Z}} = +1$
3.  $\pi$  linear polarization parallel to  $\mathcal{Z}$  for with a change of  $\Delta m_{f,\mathcal{Z}} = 0$

### Reference frame of the laboratory

In the laboratory (coordinate system from section B) the polarization of light is defined in the following way:

1.  $H$  is a linear polarization parallel to the surface of the optical table ( $x$ - $z$  plane).
2.  $V$  is a linear polarization vertical to the surface of the optical table ( $y$ -axis).
3.  $+$  is a linear polarization rotated  $45^\circ$  right hand side in traveling direction with respect to  $V$ .
4.  $-$  is a linear polarization rotated  $45^\circ$  left hand side in traveling direction with respect to  $V$ .
5.  $L$  is a circular polarization with right hand rotation in the direction of propagation (historic left hand rotation for the counter propagating direction)
6.  $R$  is a circular polarization with left hand rotation in the direction of propagation (historic right hand rotation for the counter propagating direction)

### Boundary conditions of the physical system

To connect the coordinate systems in a consistent way there are boundary conditions to be respected:

1. the axis of the microscope objective for photon collection defines the quantization axis of the atom system as the  $z$ -axis  $\mathcal{Z} = z$ .
2. a photon emitted with the linear polarization  $H$  propagating along the  $z$ -axis is a photon with  $\pi$ -polarization for the atom with quantization axis  $\mathcal{Z} = x$  ( $\Delta m_{f,x} = 0$ )
3. a photon emitted with the linear polarization  $V$  propagating along the  $z$ -axis is a photon with  $\pi$ -polarization for the atom with quantization axis  $\mathcal{Z} = y$  ( $\Delta m_{f,y} = 0$ )

### Definition of photon states

The definition of the polarization in the reference frame of the atom and the reference frame of the laboratory together with the boundary conditions lead to the definition of photon states for collected photons and the read-out laser, which have a  $k$  vector along the  $z$ -axis

$$\vec{k} = \begin{pmatrix} 0 \\ 0 \\ k \end{pmatrix}, \text{ found in Table B.1.}$$

polarization state	composition in $ R\rangle$ and $ L\rangle$	composition in $ \sigma^+\rangle$ and $ \sigma^-\rangle$	E-field for light in $z$ -direction
$ L\rangle$	$ L\rangle$	$ \sigma^+\rangle$	$\frac{1}{\sqrt{2}}\ E\  \begin{pmatrix} e^{-i\frac{\pi}{2}} \\ 1 \\ 0 \end{pmatrix} e^{i(kz-\omega t)}$
$ R\rangle$	$ R\rangle$	$ \sigma^-\rangle$	$\frac{1}{\sqrt{2}}\ E\  \begin{pmatrix} e^{i\frac{\pi}{2}} \\ 1 \\ 0 \end{pmatrix} e^{i(kz-\omega t)}$
$ H\rangle$	$\frac{i}{\sqrt{2}}( L\rangle -  R\rangle)$	$\frac{i}{\sqrt{2}}( \sigma^+\rangle -  \sigma^-\rangle)$	$\ E\  \begin{pmatrix} 1 \\ 0 \\ 0 \end{pmatrix} e^{i(kz-\omega t)}$
$ V\rangle$	$\frac{1}{\sqrt{2}}( L\rangle +  R\rangle)$	$\frac{1}{\sqrt{2}}( \sigma^+\rangle +  \sigma^-\rangle)$	$\ E\  \begin{pmatrix} 0 \\ 1 \\ 0 \end{pmatrix} e^{i(kz-\omega t)}$
$ +\rangle$	$\frac{1}{\sqrt{2}}e^{i\frac{\pi}{4}}( L\rangle - i R\rangle)$	$\frac{1}{\sqrt{2}}e^{i\frac{\pi}{4}}( \sigma^+\rangle - i \sigma^-\rangle)$	$\frac{1}{\sqrt{2}}\ E\  \begin{pmatrix} 1 \\ 1 \\ 0 \end{pmatrix} e^{i(kz-\omega t)}$
$ -\rangle$	$\frac{1}{\sqrt{2}}e^{-i\frac{\pi}{4}}( L\rangle + i R\rangle)$	$\frac{1}{\sqrt{2}}e^{-i\frac{\pi}{4}}( \sigma^+\rangle + i \sigma^-\rangle)$	$\frac{1}{\sqrt{2}}\ E\  \begin{pmatrix} -1 \\ 1 \\ 0 \end{pmatrix} e^{i(kz-\omega t)}$

Table B.1.: Definition of the polarization: states of the photon

qubit state	in qubit z states	composition in $m_{F,z}$
$ \downarrow\rangle_z$	$ \downarrow\rangle_z$	$ 1, -1\rangle$
$ \uparrow\rangle_z$	$ \uparrow\rangle_z$	$ 1, +1\rangle$
$ \downarrow\rangle_x$	$\frac{i}{\sqrt{2}} ( \downarrow\rangle_z -  \uparrow\rangle_z)$	$\frac{i}{\sqrt{2}} ( 1, -1\rangle -  1, +1\rangle)$
$ \uparrow\rangle_x$	$\frac{1}{\sqrt{2}} ( \downarrow\rangle_z +  \uparrow\rangle_z)$	$\frac{1}{\sqrt{2}} ( 1, -1\rangle +  1, +1\rangle)$
$ \downarrow\rangle_y$	$\frac{1}{\sqrt{2}} e^{-i\frac{\pi}{4}} ( \downarrow\rangle_z + i \uparrow\rangle_z)$	$\frac{1}{\sqrt{2}} e^{-i\frac{\pi}{4}} ( 1, -1\rangle + i 1, +1\rangle)$
$ \uparrow\rangle_y$	$\frac{1}{\sqrt{2}} e^{i\frac{\pi}{4}} ( \downarrow\rangle_z - i \uparrow\rangle_z)$	$\frac{1}{\sqrt{2}} e^{i\frac{\pi}{4}} ( 1, -1\rangle - i 1, +1\rangle)$

Table B.2.: Atomic-qubit state definition

## Atomic states

### The qubit: a two level quantum system

Analogue to a classical bit that has two possible values, zero and one, a qubit is a two level quantum system [158]. This system can be described via the density matrix

$$\hat{\rho} = \frac{1}{2} (\hat{1} + c_x \hat{\sigma}_x + c_y \hat{\sigma}_y + c_z \hat{\sigma}_z) = \sum_{i=0}^3 c_i \hat{\sigma}_i$$

with  $\hat{\sigma}_i \in \{\hat{1}, \hat{\sigma}_x, \hat{\sigma}_y, \hat{\sigma}_z\}$  being the identity and the three Pauli operators and the  $c_i$  are the expectation values for the respective  $c_i = \langle \hat{\sigma}_i \rangle$  with  $c_x^2 + c_y^2 + c_z^2 \leq 1$ .

### Definition of the atomic qubit

The atomic qubit is encoded in  $F = 1$ ,  $m_F = \pm 1$  of the  $5^2S_{1/2}$  ground state (Fig. 2.2) with the  $z$ -axis as quantization axis and  $|1, -1\rangle = |\downarrow\rangle_z$  and  $|1, +1\rangle = |\uparrow\rangle_z$  are defined as the eigenvectors to the Pauli matrix  $\hat{\sigma}_z$ . This allows to define the qubit also in the eigenvectors of  $\hat{\sigma}_x$  and  $\hat{\sigma}_y$  accordingly in Table B.2. Their definition is tailored to fit to the definition of the photon states in Table B.1. It is important to notice that the  $|\downarrow\rangle_x, |\uparrow\rangle_x, |\downarrow\rangle_y, |\uparrow\rangle_y$  are labeled with  $x$  and  $y$  because they are eigenvectors of the Pauli operators  $\hat{\sigma}_{x,y}$  and not because they are Zeeman states for a quantization axis in  $x, y$ -direction, labeled  $|F, m_{F,x}\rangle_x$  and  $|F, m_{F,y}\rangle_y$ . These are two different set of states and must not be confused.

### Spin-1 system: Zeeman states of the $5^2S_{1/2}$ , $F = 1$ ground state

The qubit is defined on  $F = 1$ ,  $m_F = \pm 1$  of the  $5^2S_{1/2}$  ground state (quantization axis =  $z$ -axis) (Sec. 2.1 and B), but these states themselves are part a the Spin-1 system, the  $5^2S_{1/2}$ ,  $F = 1$  ground state. For physical effects like the state evolution in a magnetic field the whole spin-1 system has to be considered.

The angular momentum operators for a spin-1 system in the basis of the  $z$  eigenvectors ( $|1, -1\rangle_z$ ,  $|1, 0\rangle_z$ , and  $|1, +1\rangle_z$ ) are

$$\hat{F}_z = \hbar \begin{pmatrix} 1 & 0 & 0 \\ 0 & 0 & 0 \\ 0 & 0 & -1 \end{pmatrix}, \quad \hat{F}_x = \frac{\hbar}{\sqrt{2}} \begin{pmatrix} 0 & 1 & 0 \\ 1 & 0 & 1 \\ 0 & 1 & 0 \end{pmatrix}, \quad \hat{F}_y = \frac{\hbar}{\sqrt{2}} \begin{pmatrix} 0 & -i & 0 \\ i & 0 & -i \\ 0 & i & 0 \end{pmatrix}. \quad (\text{B.1})$$

Their respective eigenvectors and eigenvalues are for  $\hat{F}_z$

$$\lambda_{-1} = -1 \quad \Phi_{-1} = \begin{pmatrix} 0 \\ 0 \\ 1 \end{pmatrix}, \quad \lambda_0 = 0 \quad \Phi_0 = \begin{pmatrix} 0 \\ 1 \\ 0 \end{pmatrix}, \quad \lambda_{+1} = +1 \Phi_{+1} = \begin{pmatrix} 1 \\ 0 \\ 0 \end{pmatrix},$$

for  $\hat{F}_x$

$$\lambda_{-1} = -1 \quad \Phi_{-1} = \begin{pmatrix} 1 \\ -\sqrt{2} \\ 1 \end{pmatrix}, \quad \lambda_0 = 0 \quad \Phi_0 = \begin{pmatrix} -1 \\ 0 \\ 1 \end{pmatrix}, \quad \lambda_{+1} = +1 \quad \Phi_{+1} = \begin{pmatrix} 1 \\ \sqrt{2} \\ 1 \end{pmatrix},$$

for  $\hat{F}_y$

$$\lambda_{-1} = -1 \quad \Phi_{-1} = \begin{pmatrix} -1 \\ i\sqrt{2} \\ 1 \end{pmatrix}, \quad \lambda_0 = 0 \quad \Phi_0 = \begin{pmatrix} 1 \\ 0 \\ 1 \end{pmatrix}, \quad \lambda_{+1} = +1 \quad \Phi_{+1} = \begin{pmatrix} 1 \\ -i\sqrt{2} \\ -1 \end{pmatrix}.$$

This allows to transform The Zeeman states from  $z$  as quantization axis to the Zeeman states for  $x$  or  $y$  [159].

### Read-out Polarization and corresponding $|B\rangle$ and $|D\rangle$ states

The read-out polarization  $\chi_{ro}$  follows the definition from Table B.1. The definition of  $\chi_{ro}$  (2.7) using  $H$  and  $V$  polarization allows to calculate the bright  $|B\rangle$  (2.8) and dark state  $|D\rangle$  (2.9). Transformed for  $L = \sigma^+$  and  $R = \sigma^-$  polarization they are

$$|\chi_{ro}\rangle = \frac{1}{\sqrt{2}} \left( |L\rangle \left( \cos(\alpha) + \sin(\alpha) e^{-i(\phi - \frac{\pi}{2})} \right) + |R\rangle \left( \cos(\alpha) + \sin(\alpha) e^{-i(\phi + \frac{\pi}{2})} \right) \right),$$

$$|B\rangle = \frac{-1}{\sqrt{2}} \left( \left( \cos(\alpha) + e^{i(\phi - \frac{\pi}{2})} \sin(\alpha) \right) |1, -1\rangle - \left( \cos(\alpha) + \sin(\alpha) e^{i(\phi + \frac{\pi}{2})} \right) |1, +1\rangle \right),$$

and

$$|D\rangle = \frac{1}{\sqrt{2}} \left( \left( \cos(\alpha) e^{i(\phi - \frac{\pi}{2})} + \sin(\alpha) \right) |1, -1\rangle + \left( \cos(\alpha) e^{i(\phi + \frac{\pi}{2})} + \sin(\alpha) \right) |1, +1\rangle \right).$$

This  $L$  and  $R$  dependent definition can be useful for understanding the read-out scheme in the  $^{87}\text{Rb}$  level scheme in Figure 2.2. A list of  $|D\rangle$  and  $|B\rangle$  for the six polarizations  $\chi_{ro}$  defined in Table B.1 can be found in Table B.3.

$\chi_{ro}$	$ B\rangle$	$ D\rangle$
$L$	$ 1, -1\rangle$	$ 1, +1\rangle$
$R$	$ 1, +1\rangle$	$ 1, -1\rangle$
$H$	$\frac{1}{\sqrt{2}} ( 1, -1\rangle +  1, +1\rangle)$	$\frac{i}{\sqrt{2}} ( 1, -1\rangle -  1, +1\rangle)$
$V$	$\frac{i}{\sqrt{2}} ( 1, -1\rangle -  1, +1\rangle)$	$\frac{1}{\sqrt{2}} ( 1, -1\rangle +  1, +1\rangle)$
$+$	$\frac{1}{\sqrt{2}} e^{i\frac{\pi}{4}} ( 1, -1\rangle - i 1, +1\rangle)$	$\frac{1}{\sqrt{2}} e^{-i\frac{\pi}{4}} ( 1, -1\rangle + i 1, +1\rangle)$
$-$	$\frac{1}{\sqrt{2}} e^{-i\frac{\pi}{4}} ( 1, -1\rangle + i 1, +1\rangle)$	$\frac{1}{\sqrt{2}} e^{i\frac{\pi}{4}} ( 1, -1\rangle - i 1, +1\rangle)$

Table B.3.: Polarization of the read-out pulse and resulting bright  $|B\rangle$  and dark states  $|D\rangle$

## C. On the Entangled Atom-Photon State

Some more details on the atom-photon entanglement employed for the creation of atom-atom entanglement are given in this Appendix: a complete formulation of the atom-photon state in the possible bases defined in Appendix B, a description of the photonic state measurement setup, a measurement verifying the atom-photon entanglement, and atomic state preparation with photonic projection measurements.

### Entangled Atom-Photon state

The entangled atom-photon-state (2.5) can be expressed in different bases by using the tables B.2.

1. In Zeeman states:

$$\begin{aligned}
 |\Psi\rangle_{AP} &= \frac{1}{\sqrt{2}} (|L\rangle|1, -1\rangle_z + |R\rangle|1, +1\rangle_z) \\
 &= \frac{1}{\sqrt{2}} \left( |H\rangle \frac{i}{\sqrt{2}} (|1, +1\rangle_z - |1, -1\rangle_z) + |V\rangle \frac{1}{\sqrt{2}} (|1, -1\rangle_z + |1, +1\rangle_z) \right) \\
 &= \frac{1}{\sqrt{2}} \left( |+\rangle \frac{1}{\sqrt{2}} e^{-i\frac{\pi}{4}} (|1, -1\rangle + i|1, +1\rangle) + |-\rangle \frac{1}{\sqrt{2}} e^{i\frac{\pi}{4}} (|1, -1\rangle - i|1, +1\rangle) \right)
 \end{aligned} \tag{C.1}$$

2. In qubit states:

$$\begin{aligned}
 |\Psi\rangle_{AP} &= \frac{1}{\sqrt{2}} (|L\rangle|\downarrow\rangle_z + |R\rangle|\uparrow\rangle_z) \\
 &= \frac{1}{\sqrt{2}} (|H\rangle|\downarrow\rangle_x + |V\rangle|\uparrow\rangle_x) \\
 &= \frac{1}{\sqrt{2}} (|+\rangle|\downarrow\rangle_y + |-\rangle|\uparrow\rangle_y)
 \end{aligned} \tag{C.2}$$

### Preparation of an atomic state via photon detection

A measurement of the photon projects the atom onto the state corresponding to its result (C.1). This allows to use the measurement of the single photon as a preparation of an atomic state as listed in Table C.1.

### Photonic state measurement

The single photon emitted by the atom is coupled into a fiber and guided to a setup for measurement of the photonic polarization state. This measurement setup consists of a  $\lambda/4$ -wave plate, a  $\lambda/2$ -wave plate, a polarizing beam splitter and two single photon detectors (Laser

prepared atomic state	photonic measurement result	read-out pol
$ 1, +1\rangle_x = \frac{1}{\sqrt{2}} ( 1, -1\rangle_z +  1, +1\rangle_z)$	$ V\rangle$	$ V\rangle$
$ 1, -1\rangle_x = \frac{i}{\sqrt{2}} ( 1, -1\rangle_z -  1, +1\rangle_z)$	$ H\rangle$	$ H\rangle$
$ 1, -1\rangle_y = \frac{-1}{\sqrt{2}} e^{-i\frac{\pi}{4}} ( 1, -1\rangle_z + i 1, +1\rangle_z)$	$ +\rangle$	$ +\rangle$
$ 1, +1\rangle_y = \frac{1}{\sqrt{2}} e^{i\frac{\pi}{4}} ( 1, -1\rangle_z - i 1, +1\rangle_z)$	$ -\rangle$	$ -\rangle$
$ 1, -1\rangle_z$	$ \sigma^+\rangle$	$ \sigma^-\rangle$
$ 1, +1\rangle_z$	$ \sigma^-\rangle$	$ \sigma^+\rangle$

Table C.1.: Atomic state preparation corresponding to result of the photonic measurement and the read-out polarization corresponding to that state being the dark state

Components C10) (Fig. C.1). Since the polarizing beam splitter can only separate H and V polarization the wave plates are employed to project on every combination of orthogonal polarizations. The detection of a single photon at one of the SPCMs then indicates the polarization state of that photon.

### Measurement of atom-photon entanglement

Typical measurement to confirm and characterize atom-photon entanglement: The photon is analyzed in to mutually unbiased polarization bases here  $+/-$  and  $H/V$  using the setup in Figure C.1 , while the atomic analysis angle ( $\alpha$  from (2.7)) is rotated from  $0^\circ$  to  $180^\circ$  in step of  $22.5^\circ$  using a  $\lambda/2$  wave plate (Fig. 2.10a). The result of such a measurement is shown in Figure C.2. Calculating the probability for correlated and anti-correlated measurement results of atom and photon leads to the correlation fringes shown in Figure C.2b.

To estimate the fidelity of the experimental atom-photon state to the maximally entangled one (C.2) the experimental state is assumed to be of the form

$$\hat{\rho} = V |\Psi_{AP}\rangle \langle \Psi_{AP}| + \frac{1}{4} (1 - V) \hat{1}$$

with the visibility  $V$  [48, 38]. The visibility is the average contrast between the maximum and the minimum of the correlation fringes. Fitting a sinusoidal function  $A \frac{\sin(2\cdot\alpha+\phi)+1}{2}$  to each correlation fringe enables to calculate the Visibility

$$V = \frac{1}{4} \sum |A|.$$

With this the Fidelity is

$$\begin{aligned} F &= \langle \Psi_{AP} | \hat{\rho} | \Psi_{AP} \rangle \\ &= 0.25 + 0.75 \cdot V \\ &= 0.25 + \frac{3}{16} \sum |A|. \end{aligned}$$

For the measurement in Figure C.2 the visibility is  $V = 0.902 \pm 0.009$  resulting in a fidelity of  $F = 0.9265 \pm 0.0068$ .

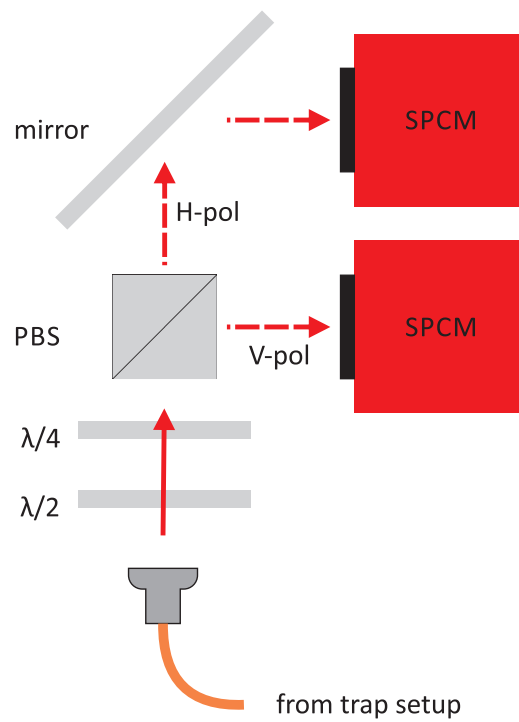
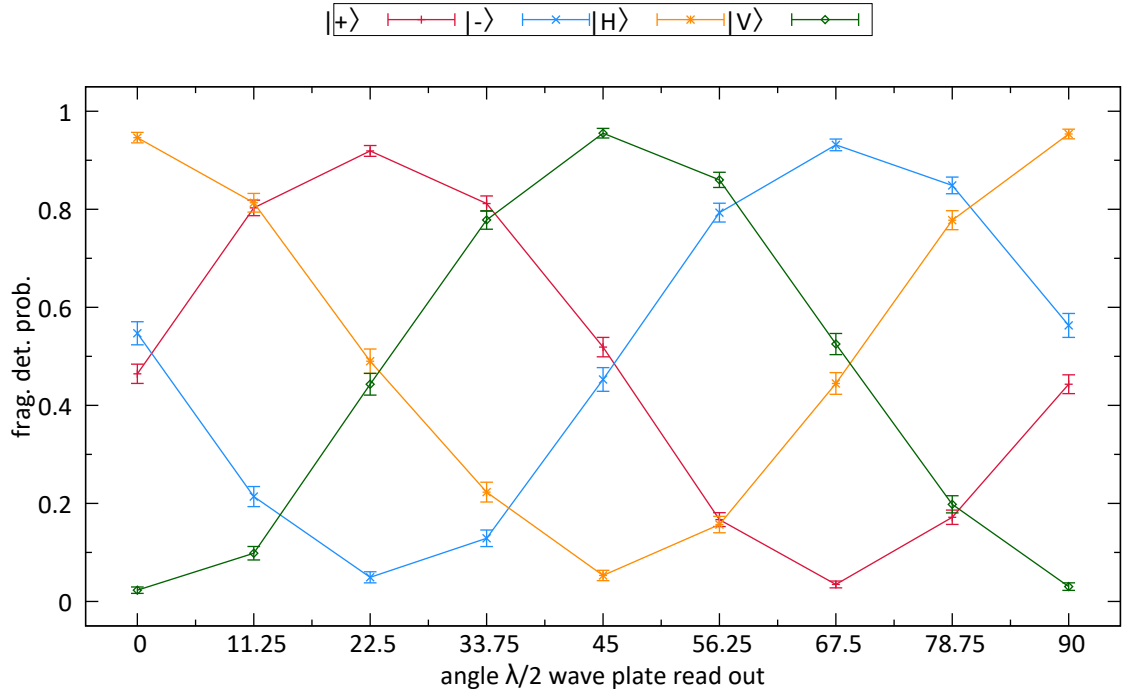
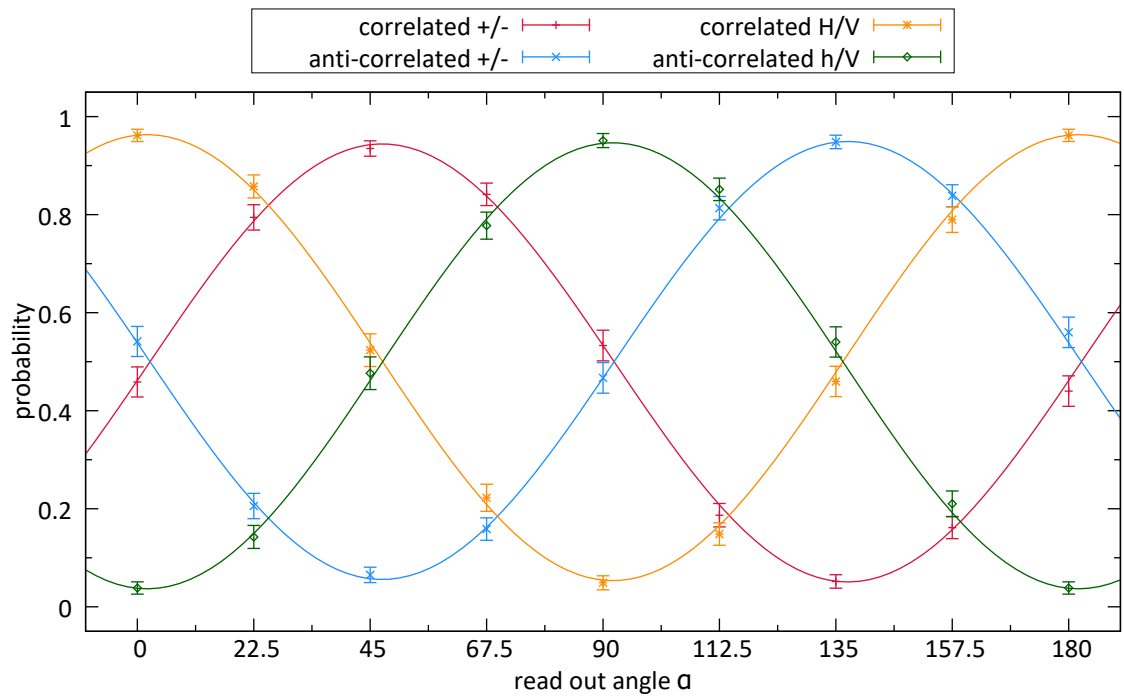


Figure C.1.: Photonic state measurement setup: The wave plates ( $\lambda/4$  and  $\lambda/2$ ) define which polarization of the single photon is projected on each output port of the polarizing beam splitter (PBS) with H or V polarization and the detected by the corresponding single photon detector (SPCM).



(a) Fragment detection probability for the for projected photon state  $|+\rangle, |-\rangle, |H\rangle$ , and  $|V\rangle$  depending on the setting of the read-out  $\lambda/2$  wave plate.



(b) Atom-photon correlations based on the measurement in (a). In the  $+/-$  basis projection on  $|+\rangle$  is considered as  $+1$  and  $|-\rangle$  as  $-1$ , in the  $H/V$   $|H\rangle$  is considered as  $+1$  and  $|V\rangle$  as  $-1$ . Additionally, a sinusoidal function  $A \frac{\sin(2\alpha + \phi) + 1}{2}$  is fitted to each correlator and anti-correlator to estimate the fidelity of the entangled atom-photon state.

Figure C.2.: Measurement for the characterization of atom photon entanglement performed on the 22.10.2015.

## D. Light field of the ODT near its focus

The trapping potential of the optical dipole trap (D.1) [37, 61, 57] is depending on the shape, intensity, and detuning of the laser used. Furthermore, it depends on the considered hyperfine state  $F$  and Zeeman state  $m_F$  of the atom.

$$U(r, z) = \frac{\pi c^2 \Gamma}{2\omega_0^3} \left( \frac{2 + g_F m_F P}{\Delta_{2,F}} + \frac{1 - g_F m_F P}{\Delta_{1,F}} \right) \cdot I(\vec{x}) \quad (\text{D.1})$$

$\Gamma$  and  $\omega_0$  are the decay rate and transition frequency of the central D-line,  $g_F$  is the Landé factor of the considered hyper fine state,  $\Delta_{1,F}$  and  $\Delta_{2,F}$  is the detuning of the laser with respect to the transition of the  $D_1$  and  $D_2$  line,  $P$  a measure of the circular polarization [61], is the polarization of the laser,  $I(\vec{x})$  the intensity of the ODT laser. This is usually estimated with a Gaussian beam  $I_0 \left( \frac{w_0}{w(z)} \right)^2 e^{-\frac{2r^2}{w(z)^2}}$  with  $z = 0$  as focus position,  $w_0 = 1.92 \mu\text{m}$  as waist at the focus, and  $I_0$  as intensity at the Focus.

However, to calculate the actual light field near the focus of the ODT laser one has to consider that the behavior of a strongly focused linearly polarized beam. Here we consider polarization along the  $x$  axis. Following the formalism developed in [60] based on [63, 64] the electric field amplitude vector takes the form

$$\begin{aligned} E_x &= E_0 (F_0(r, z) + F_2(r, z) \cdot \cos(2\phi)) \\ E_y &= E_0 F_2(r, z) \cdot \sin(2\phi) \\ E_z &= i2 \cdot E_0 F_1(r, z) \cdot \cos(\phi) \end{aligned}$$

using cylindrical coordinates to calculate the Cartesian vector of the electric field amplitude ( $z = z$ ,  $x = r \cos(\phi)$ ,  $y = r \sin(\phi)$ ). This can be approximated using

$$\begin{aligned} F_0 &\approx F_0(0, 0) \frac{1}{\sqrt{1 + \frac{z^2}{z_R^2}}} e^{-r^2 \cdot \left( w_0^2 \left( 1 + \frac{z^2}{z_R^2} \right) \right)^{-1}} \\ F_1 &\approx F_0(0, 0) \frac{r}{2z_R \left( 1 + \frac{z^2}{z_R^2} \right)} e^{-r^2 \cdot \left( w_0^2 \left( 1 + \frac{z^2}{z_R^2} \right) \right)^{-1}} \\ F_2 &\approx F_0(0, 0) \frac{r^2}{4z_R^2 \left( 1 + \frac{z^2}{z_R^2} \right)^2} e^{-r^2 \cdot \left( w_0^2 \left( 1 + \frac{z^2}{z_R^2} \right) \right)^{-1}}. \end{aligned}$$

Since  $E_y \approx 0$  only  $E_x$  and  $E_z$  are important for further considerations (Fig D.1 (a-d)).

The dynamics of the Zeeman states of the  $F = 1$  ground state, which are used to encode the atomic qubit (Tab. B.2), is influenced by a Zeeman state depending vector light shift

introduced by circular polarization of the ODT laser (Sec. 2.3.3). To characterize this  $I(\vec{x})$  and  $P(\vec{x})$  need to be estimated. The intensity

$$I(\vec{x}) = \|E_x\|^2 + \|E_y\|^2$$

follows directly from the electric field amplitude. The polarization of the beam  $P(\vec{x})$  depends additionally to the electric field amplitude also on the phase differences between the  $x$  and  $z$  component of the ODT laser. This phase difference can be approximated by approximating the  $x$  component by the TEM<sub>00</sub> mode and the  $z$  component by the TEM<sub>10</sub> mode [160]. This leads to a phase difference

$$\delta(z) = \arctan\left(\frac{z}{z_r}\right)$$

based on the difference between the Gouy phase between the two modes [161, 162]. With this it is possible to calculate  $P(\vec{x})$  based on (2.15)

$$P = \text{sign}(\delta) \frac{2\|A\|\|B\|}{\|A\|^2 + \|B\|^2}.$$

For this the time time depending electric field vector at position  $\vec{x}$  is simplified to

$$E(\vec{x}, t) = E_x(\vec{x}) \cos(\omega t) \hat{e}_x + E_z(\vec{x}) \cos(\omega t + \delta(z)) \hat{e}_z. \quad (\text{D.2})$$

Therefore the semi-major axis of the polarization ellipse is

$$A = \max_{0 \leq \omega t \leq 2\pi} \left( \sqrt{\|E_x(\vec{x})\|^2 \cos^2(\omega t) + \|E_z(\vec{x})\|^2 \cos^2(\omega t + \delta(z))} \right) \quad (\text{D.3})$$

and the respective semi-minor axis is

$$B = \min_{0 \leq \omega t \leq 2\pi} \left( \sqrt{\|E_x(\vec{x})\|^2 \cos^2(\omega t) + \|E_z(\vec{x})\|^2 \cos^2(\omega t + \delta(z))} \right). \quad (\text{D.4})$$

The resulting  $P(\vec{x})$  is displayed in Figure. D.1 e) and f).

### Finding the semi axes of the polarization ellipse

To find an analytical solution for (D.3) and (D.4) is straight forward. To find the extrema of

$$\|E(\vec{x}, t)\| = \sqrt{\|E_x(\vec{x})\|^2 \cos^2(\omega t) + \|E_z(\vec{x})\|^2 \cos^2(\omega t + \delta(z))}$$

the square root can be neglected due to its strictly monotonic behavior. Further,  $\omega$  is set to 1 to simplify the calculation. The derivative of

$$\|E(\vec{x}, t)\|^2 = \|E_x(\vec{x})\|^2 \cos^2(t) + \|E_z(\vec{x})\|^2 \cos^2(t + \delta(z))$$

is

$$\frac{d}{dt} \|E(\vec{x}, t)\|^2 = -\|E_x(\vec{x})\|^2 2 \cos(t) \sin(\omega t) - \|E_z(\vec{x})\|^2 2 \cos(t + \delta(z)) \sin(t + \delta(z)).$$

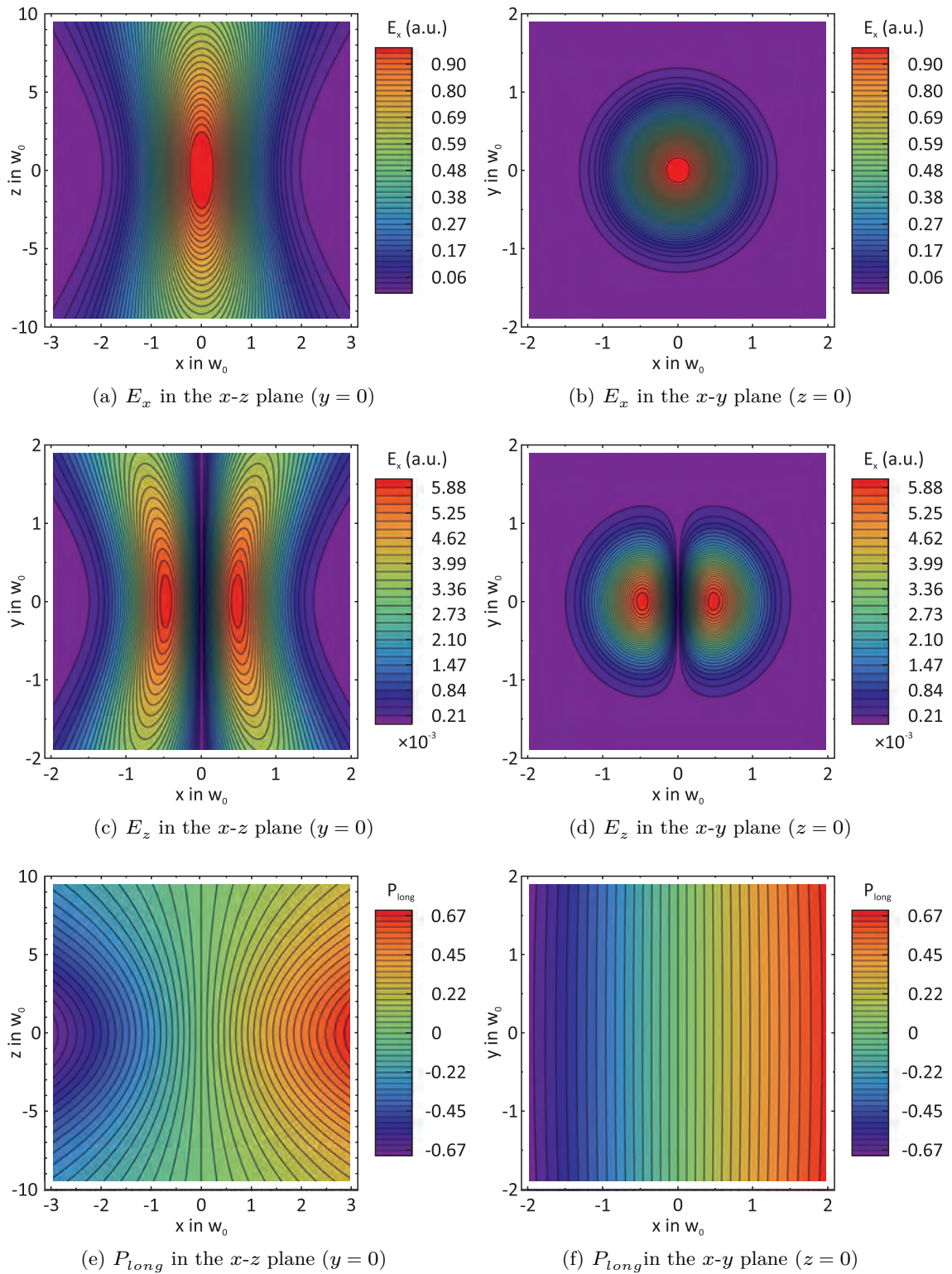


Figure D.1.: Electric field amplitude for  $E_x$  and  $E_z$  (a-d) and polarization  $P_{long}(\vec{x})$  (e, f) near the focus

Using the identities

$$\sin(2x) = 2 \sin(x) \cos(x)$$

and

$$\cos(2x) = \cos^2(x) - \sin^2(x)$$

this can be written as

$$\frac{d}{dt} \|E(\vec{x}, t)\|^2 = \left[ -\|E_x(\vec{x})\|^2 - \|E_z(\vec{x})\|^2 \cos(2\delta(z)) \right] \sin(2t) - \|E_z(\vec{x})\|^2 \sin(2\delta(z)) \cos(2t)$$

and  $\frac{d}{dt} \|E(\vec{x}, t)\|^2 := 0$  yields the extrema

$$t_{ext} = \frac{1}{2} \arctan \left( \frac{-\|E_z(\vec{x})\|^2 \sin(2\delta(z))}{\|E_x(\vec{x})\|^2 + \|E_z(\vec{x})\|^2 \cos(2\delta(z))} \right).$$

Due to the elliptic form of  $\|E(\vec{x}, t)\|$  the minima and maxima alternate with a periodicity of  $\omega t = \pi/2$ . And since (2.15) needs a pair of minimum and maximum it is possible to use the values for  $\omega t = t_{ext}$  and  $\omega t = t_{ext} + \pi/2$  in (D.2) to calculate  $P(\vec{x})$ .

## E. Hong Ou Mandel effect for unpolarized photons

In section 2.4.1 I introduced a Bell state measurement based on the Hong Ou Mandel effect [68, 66]. There the formalism for the two photon interference is only treated in a very condensed matter. For the sake of completeness in this chapter a thorough analysis is done following the considerations in [32, 69]. Here the picture of a cubic beam splitter with reflected and transmitted modes will be used, the formalism still is valid for all kinds of beam splitter, e.g., fiber or wave guide based ones. First the two photon interference without special consideration for unpolarized photons is derived. Afterwards unpolarized photons are introduced.

### Two photon interference with identical polarization

A beam splitter with two input and two output ports (Fig. E.1, can be described via four pairs of creation and annihilation operators  $\hat{a}_1, \hat{a}_1^\dagger$  and  $\hat{a}_2, \hat{a}_2^\dagger$  for the inputs and  $\hat{b}_1, \hat{b}_1^\dagger$  and  $\hat{b}_2, \hat{b}_2^\dagger$  for the outputs. In the general case these operators are different for photons with different properties. The relation between the input and the output is given

$$\begin{pmatrix} \hat{b}_1^\dagger \\ \hat{b}_2^\dagger \end{pmatrix} = \hat{B} \begin{pmatrix} \hat{a}_1^\dagger \\ \hat{a}_2^\dagger \end{pmatrix} \quad \rightarrow \quad \begin{pmatrix} \hat{a}_1^\dagger \\ \hat{a}_2^\dagger \end{pmatrix} = \hat{B}^{-1} \begin{pmatrix} \hat{b}_1^\dagger \\ \hat{b}_2^\dagger \end{pmatrix} \quad (\text{E.1})$$

while the matrix

$$\hat{B} = e^{i\phi_0} \begin{pmatrix} \cos(\Theta) e^{i\phi_\tau} & \sin(\Theta) e^{i\phi_\rho} \\ -\sin(\Theta) e^{-i\phi_\rho} & \cos(\Theta) e^{-i\phi_\tau} \end{pmatrix} \quad (\text{E.2})$$

with a general phase shift  $\phi_0$ , a phase shift  $\phi_\tau$  for the transmission mode, and a phase shift  $\phi_\rho$  for the reflection mode of the beam splitter [32, 69]. With this the input of one photon at each input port, described by the Fock state

$$|1, 1\rangle_{in} = \hat{a}_1^\dagger \hat{a}_2^\dagger |0, 0\rangle_{in} \quad (\text{E.3})$$

leads to this output state

$$e^{i\phi_0} \left( \hat{b}_1^\dagger \cos(\Theta) e^{i\phi_\tau} - \hat{b}_2^\dagger \sin(\Theta) e^{i\phi_\rho} \right) e^{i\phi_0} \left( \hat{b}_1^\dagger \sin(\Theta) e^{-i\phi_\rho} + \hat{b}_2^\dagger \cos(\Theta) e^{-i\phi_\tau} \right) |0, 0\rangle_{out}. \quad (\text{E.4})$$

This can be rearranged to identify the three different output combinations, both in output one, in each output, and both in output two:

$$\begin{aligned} & \hat{b}_1^\dagger \hat{b}_1^\dagger \cos(\Theta) \sin(\Theta) e^{i(\phi_\tau - \phi_\rho + 2\phi_0)} |0, 0\rangle_{out} \\ & - \hat{b}_1^\dagger \hat{b}_2^\dagger \cos^2(\Theta) e^{i2\phi_0} |0, 0\rangle_{out} + \hat{b}_2^\dagger \hat{b}_1^\dagger \sin^2(\Theta) e^{i2\phi_0} |0, 0\rangle_{out} \\ & - \hat{b}_2^\dagger \hat{b}_2^\dagger \sin(\Theta) \cos(\Theta) e^{i(\phi_\rho - \phi_\tau + 2\phi_0)} |0, 0\rangle_{out}. \end{aligned}$$

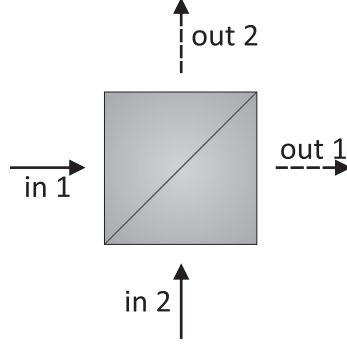


Figure E.1.: Basic scheme of a beam splitter with two input ports and two output ports. (the quibic shape is only an example)

To simplify this expression the global phase is set to zero ( $\phi_0 = 0$ ) and only the phase difference between transmission and reflection  $\delta = \phi_\tau - \phi_\rho$  is considered without limiting the generality.

Considering the case of a perfect 50/50 beam splitter ( $\Theta = \frac{\pi}{4}$ ) the output state is of the form

$$\frac{1}{2} (\hat{b}_1^\dagger \hat{b}_1^\dagger e^{i\delta} - \hat{b}_1^\dagger \hat{b}_2^\dagger + \hat{b}_2^\dagger \hat{b}_1^\dagger - \hat{b}_2^\dagger \hat{b}_2^\dagger e^{-i\delta}) |0, 0\rangle_{out}.$$

In the case of indistinguishable photons, both photons are described by identical operators and together with the commutation relations for the creation and annihilation operators for bosonic particles  $[\hat{a}_i, \hat{a}_j^\dagger] = [\hat{b}_i, \hat{b}_j^\dagger] = \delta_{i,j}$  and  $[\hat{a}_i^\dagger, \hat{a}_j^\dagger] = [\hat{b}_i^\dagger, \hat{b}_j^\dagger] = 0$  with  $i, j \in \{1, 2\}$ , the output state reduces to

$$\begin{aligned} & \frac{1}{2} \hat{b}_1^\dagger \hat{b}_1^\dagger e^{-i\delta} + \frac{1}{2} \underbrace{(-\hat{b}_1^\dagger \hat{b}_2^\dagger + \hat{b}_2^\dagger \hat{b}_1^\dagger)}_{=[\hat{b}_2^\dagger, \hat{b}_1^\dagger]=0} - \frac{1}{2} \hat{b}_2^\dagger \hat{b}_2^\dagger e^{-i\delta} |0, 0\rangle_{out} \\ & = \frac{1}{2} e^{-i\delta} (|2, 0\rangle_{out} - |0, 2\rangle_{out}). \end{aligned}$$

This shows that two indistinguishable photons, one in each input mode of the beam splitter, will always both be detected after output 1 or output 2 of the beam splitter and never one photon in each output.

## Two photon interference with unpolarized photons

In the experiment the single photons, which are interfered on the beam splitter, are entangled with the emitting atoms. In particular the polarization of the emitted photon is entangled with the Zeeman states of the emitting atom (2.5). If one only considers the photon its state

is totally mixed with the density matrix  $\rho = \frac{1}{2} |L\rangle \langle L| + \frac{1}{2} |R\rangle \langle R| = \frac{1}{2} |H\rangle \langle H| + \frac{1}{2} |V\rangle \langle V| = \frac{1}{2} |+\rangle \langle +| + \frac{1}{2} |-\rangle \langle -|$  and by this unpolarized.

To describe this photon state in the formalism described in the previous section (E) one needs to consider polarization for creation and annihilation operators. This leads to independent operators for the orthogonal polarization. Here, the  $H$  and  $V$  polarization basis is used. Analog to (E.1) the relation between the input and the output is given for both polarization independently

$$\begin{pmatrix} \hat{b}_{1,P}^\dagger \\ \hat{b}_{2,P}^\dagger \end{pmatrix} = \hat{B}_P \begin{pmatrix} \hat{a}_{1,P}^\dagger \\ \hat{a}_{2,P}^\dagger \end{pmatrix} \quad \Leftrightarrow \quad \begin{pmatrix} \hat{a}_{1,P}^\dagger \\ \hat{a}_{2,P}^\dagger \end{pmatrix} = \hat{B}_P^{-1} \begin{pmatrix} \hat{b}_{1,P}^\dagger \\ \hat{b}_{2,P}^\dagger \end{pmatrix} \quad (\text{E.5})$$

while analog to (E.2) and directly simplifying the phase shifts the matrix

$$\hat{B}_P = \begin{pmatrix} \cos(\Theta_P) & \sin(\Theta_P) e^{i\delta_P} \\ -\sin(\Theta_P) e^{-i\delta_P} & \cos(\Theta_P) \end{pmatrix} \quad (\text{E.6})$$

with  $\Theta_P$  for the splitting ratio of the beam splitter, the phase difference between transmitted and reflected part  $\delta_P$ , and  $P \in \{H, V\}$  indicating the polarization. In contrast to equation (E.3) writing the an input state for the beam splitter with two unpolarized photons is not so trivial. It is necessary to consider the basis states of the state  $\rho_1 \otimes \rho_2$  as input states, here the indices stand for the photons at different input ports. Using the four Bell states as a complete set of orthonormal basis vectors the input states are

$$\begin{aligned} |\Phi^+\rangle_{in} &= \frac{1}{\sqrt{2}} (\hat{a}_{1,H}^\dagger \hat{a}_{2H}^\dagger + \hat{a}_{1,V}^\dagger \hat{a}_{2V}^\dagger) |0, 0\rangle_{in}, \\ |\Phi^-\rangle_{in} &= \frac{1}{\sqrt{2}} (\hat{a}_{1,H}^\dagger \hat{a}_{2H}^\dagger - \hat{a}_{1,V}^\dagger \hat{a}_{2V}^\dagger) |0, 0\rangle_{in}, \\ |\Psi^+\rangle_{in} &= \frac{1}{\sqrt{2}} (\hat{a}_{1,H}^\dagger \hat{a}_{2V}^\dagger + \hat{a}_{1,V}^\dagger \hat{a}_{2H}^\dagger) |0, 0\rangle_{in}, \end{aligned}$$

and

$$|\Psi^-\rangle_{in} = \frac{1}{\sqrt{2}} (\hat{a}_{1,H}^\dagger \hat{a}_{2V}^\dagger - \hat{a}_{1,V}^\dagger \hat{a}_{2H}^\dagger) |0, 0\rangle_{in}.$$

Analog to (E.4) these states leads to the following output states:

1.  $|\Phi^+\rangle_{in} \rightarrow$

$$\begin{aligned} & \frac{1}{\sqrt{2}} \left( (\hat{b}_{1,H}^\dagger \cos(\Theta_H) - \hat{b}_{2,H}^\dagger \sin(\Theta_H) e^{i\delta_H}) (\hat{b}_{1,H}^\dagger \sin(\Theta_H) e^{-i\delta_H} + \hat{b}_{2,H}^\dagger \cos(\Theta_H)) \right. \\ & \left. + (\hat{b}_{1,V}^\dagger \cos(\Theta_V) - \hat{b}_{2,V}^\dagger \sin(\Theta_V) e^{i\delta_V}) (\hat{b}_{1,V}^\dagger \sin(\Theta_V) e^{-i\delta_V} + \hat{b}_{2,V}^\dagger \cos(\Theta_V)) \right) |0, 0\rangle_{out} \\ &= \frac{1}{\sqrt{2}} \left( \hat{b}_{1,H}^\dagger \hat{b}_{1,H}^\dagger \cos(\Theta_H) \sin(\Theta_H) e^{-i\delta_H} + \hat{b}_{1,V}^\dagger \hat{b}_{1,V}^\dagger \cos(\Theta_V) \sin(\Theta_V) e^{-i\delta_V} \right. \\ & \left. + \hat{b}_{1,H}^\dagger \hat{b}_{2,H}^\dagger \cos^2(\Theta_H) - \hat{b}_{2,H}^\dagger \hat{b}_{1,H}^\dagger \sin^2(\Theta_H) \right. \\ & \left. + \hat{b}_{1,V}^\dagger \hat{b}_{2,V}^\dagger \cos^2(\Theta_V) - \hat{b}_{2,V}^\dagger \hat{b}_{1,V}^\dagger \sin^2(\Theta_V) \right. \\ & \left. - \hat{b}_{2,H}^\dagger \hat{b}_{2,H}^\dagger \cos(\Theta_H) \sin(\Theta_H) e^{-i\delta_H} - \hat{b}_{2,V}^\dagger \hat{b}_{2,V}^\dagger \cos(\Theta_V) \sin(\Theta_V) e^{-i\delta_V} \right) |0, 0\rangle_{out} \quad (\text{E.7}) \end{aligned}$$

2.  $|\Phi^-\rangle_{in} \rightarrow$

$$\begin{aligned}
& \frac{1}{\sqrt{2}} \left( (\hat{b}_{1,H}^\dagger \cos(\Theta_H) - \hat{b}_{2,H}^\dagger \sin(\Theta_H) e^{i\delta_H}) (\hat{b}_{1,H}^\dagger \sin(\Theta_H) e^{-i\delta_H} + \hat{b}_2^\dagger \cos(\Theta_H)) \right. \\
& \left. - (\hat{b}_{1,V}^\dagger \cos(\Theta_V) - \hat{b}_{2,V}^\dagger \sin(\Theta_V) e^{i\delta_V}) (\hat{b}_{1,V}^\dagger \sin(\Theta_V) e^{-i\delta_V} + \hat{b}_{2,V}^\dagger \cos(\Theta_V)) \right) |0,0\rangle_{out} \\
& = \frac{1}{\sqrt{2}} \left( \hat{b}_{1,H}^\dagger \hat{b}_{1,H}^\dagger \cos(\Theta_H) \sin(\Theta_H) e^{-i\delta_H} - \hat{b}_{1,V}^\dagger \hat{b}_{1,V}^\dagger \cos(\Theta_V) \sin(\Theta_V) e^{-i\delta_V} \right. \\
& + \hat{b}_{1,H}^\dagger \hat{b}_{2,H}^\dagger \cos^2(\Theta_H) - \hat{b}_{2,H}^\dagger \hat{b}_{1,H}^\dagger \sin^2(\Theta_H) \\
& - \hat{b}_{1,V}^\dagger \hat{b}_{2,V}^\dagger \cos^2(\Theta_V) + \hat{b}_{2,V}^\dagger \hat{b}_{1,V}^\dagger \sin^2(\Theta_V) \\
& \left. - \hat{b}_{2,H}^\dagger \hat{b}_{2,H}^\dagger \sin(\Theta_H) \cos(\Theta_H) e^{i\delta_H} + \hat{b}_{2,V}^\dagger \hat{b}_{2,V}^\dagger \sin(\Theta_V) \cos(\Theta_V) e^{i\delta_V} \right) |0,0\rangle_{out} \quad (E.8)
\end{aligned}$$

3.  $|\Psi^+\rangle_{in} \rightarrow$

$$\begin{aligned}
& \frac{1}{\sqrt{2}} \left( (\hat{b}_{1,H}^\dagger \cos(\Theta_H) - \hat{b}_{2,H}^\dagger \sin(\Theta_H) e^{i\delta_H}) (\hat{b}_{1,V}^\dagger \sin(\Theta_V) e^{-i\delta_V} + \hat{b}_2^\dagger \cos(\Theta_V)) \right. \\
& \left. + (\hat{b}_{1,V}^\dagger \cos(\Theta_V) - \hat{b}_{2,V}^\dagger \sin(\Theta_V) e^{i\delta_V}) (\hat{b}_{1,H}^\dagger \sin(\Theta_H) e^{-i\delta_H} + \hat{b}_{2,H}^\dagger \cos(\Theta_H)) \right) |0,0\rangle_{out} \\
& = \frac{1}{\sqrt{2}} \left( \hat{b}_{1,H}^\dagger \hat{b}_{1,V}^\dagger \cos(\Theta_H) \sin(\Theta_V) e^{-i\delta_V} + \hat{b}_{1,V}^\dagger \hat{b}_{1,H}^\dagger \cos(\Theta_V) \sin(\Theta_H) e^{-i\delta_H} \right. \\
& + \hat{b}_{1,H}^\dagger \hat{b}_{2,V}^\dagger \cos(\Theta_H) \cos(\Theta_V) - \hat{b}_{2,V}^\dagger \hat{b}_{1,H}^\dagger \sin(\Theta_V) \sin(\Theta_H) e^{i(\delta_V - \delta_H)} \\
& + \hat{b}_{1,V}^\dagger \hat{b}_{2,H}^\dagger \cos(\Theta_V) \cos(\Theta_H) - \hat{b}_{2,H}^\dagger \hat{b}_{1,V}^\dagger \sin(\Theta_H) \sin(\Theta_V) e^{i(\delta_H - \delta_V)} \\
& \left. - \hat{b}_{2,H}^\dagger \hat{b}_{2,V}^\dagger \sin(\Theta_H) \cos(\Theta_V) e^{i\delta_H} - \hat{b}_{2,V}^\dagger \hat{b}_{2,H}^\dagger \sin(\Theta_V) \cos(\Theta_H) e^{i\delta_V} \right) |0,0\rangle_{out} \quad (E.9)
\end{aligned}$$

4.  $|\Psi^-\rangle_{in} \rightarrow$

$$\begin{aligned}
& \frac{1}{\sqrt{2}} \left( (\hat{b}_{1,H}^\dagger \cos(\Theta_H) - \hat{b}_{2,H}^\dagger \sin(\Theta_H) e^{i\delta_H}) (\hat{b}_{1,V}^\dagger \sin(\Theta_V) e^{-i\delta_V} + \hat{b}_2^\dagger \cos(\Theta_V)) \right. \\
& \left. - (\hat{b}_{1,V}^\dagger \cos(\Theta_V) - \hat{b}_{2,V}^\dagger \sin(\Theta_V) e^{i\delta_V}) (\hat{b}_{1,H}^\dagger \sin(\Theta_H) e^{-i\delta_H} + \hat{b}_{2,H}^\dagger \cos(\Theta_H)) \right) |0,0\rangle_{out} \\
& = \frac{1}{\sqrt{2}} \left( \hat{b}_{1,H}^\dagger \hat{b}_{1,V}^\dagger \cos(\Theta_H) \sin(\Theta_V) e^{-i\delta_V} - \hat{b}_{1,V}^\dagger \hat{b}_{1,H}^\dagger \cos(\Theta_V) \sin(\Theta_H) e^{-i\delta_H} \right. \\
& + \hat{b}_{1,H}^\dagger \hat{b}_{2,V}^\dagger \cos(\Theta_H) \cos(\Theta_V) + \hat{b}_{2,V}^\dagger \hat{b}_{1,H}^\dagger \sin(\Theta_V) \sin(\Theta_H) e^{i(\delta_V - \delta_H)} \\
& - \hat{b}_{1,V}^\dagger \hat{b}_{2,H}^\dagger \cos(\Theta_V) \cos(\Theta_H) - \hat{b}_{2,H}^\dagger \hat{b}_{1,V}^\dagger \sin(\Theta_H) \sin(\Theta_V) e^{i(\delta_H - \delta_V)} \\
& \left. - \hat{b}_{2,H}^\dagger \hat{b}_{2,V}^\dagger \sin(\Theta_H) \cos(\Theta_V) e^{i\delta_H} + \hat{b}_{2,V}^\dagger \hat{b}_{2,H}^\dagger \sin(\Theta_V) \cos(\Theta_H) e^{i\delta_V} \right) |0,0\rangle_{out} \quad (E.10)
\end{aligned}$$

With these results one can consider different values for the characteristic parameters  $\Theta_H$ ,  $\Theta_V$ ,  $\delta_H$ , and  $\delta_V$  of the beam splitter. Assuming two indistinguishable photons entering the beam splitter analog to the previous section, one can derive the interference behavior for different cases:

**Perfect polarization independent  $50/50$  beam splitter**

The characteristic parameters of a perfect polarization independent  $50/50$  beam splitter are  $\Theta_H = \frac{\pi}{4}$ ,  $\Theta_V = \frac{\pi}{4}$  and  $\delta_H = \delta_V = \delta$ :

$$\begin{aligned}
|\Phi^+\rangle_{in} &\rightarrow \frac{1}{\sqrt{2}} \left( \frac{1}{2} (\hat{b}_{1,H}^\dagger \hat{b}_{1,H}^\dagger + \hat{b}_{1,V}^\dagger \hat{b}_{1,V}^\dagger) e^{-i\delta} - \frac{1}{2} (\hat{b}_{2,H}^\dagger \hat{b}_{2,H}^\dagger + \hat{b}_{2,V}^\dagger \hat{b}_{2,V}^\dagger) e^{i\delta} \right) |0,0\rangle_{out} \\
&= \frac{1}{\sqrt{2}} \left( e^{-i\delta} \frac{1}{2} (|2_H,0\rangle_{out} + |2_V,0\rangle_{out}) - e^{i\delta} \frac{1}{2} (|0,2_H\rangle_{out} + |0,2_V\rangle_{out}) \right) \\
|\Phi^-\rangle_{in} &\rightarrow \frac{1}{\sqrt{2}} \left( \frac{1}{2} (\hat{b}_{1,H}^\dagger \hat{b}_{1,H}^\dagger - \hat{b}_{1,V}^\dagger \hat{b}_{1,V}^\dagger) e^{-i\delta} - \frac{1}{2} (\hat{b}_{2,H}^\dagger \hat{b}_{2,H}^\dagger e^{i\delta_H} - \hat{b}_{2,V}^\dagger \hat{b}_{2,V}^\dagger) e^{i\delta} \right) |0,0\rangle_{out} \\
&\frac{1}{\sqrt{2}} \left( e^{-i\delta} \frac{1}{2} (|2_H,0\rangle_{out} - |2_V,0\rangle_{out}) - e^{i\delta} \frac{1}{2} (|0,2_H\rangle_{out} - |0,2_V\rangle_{out}) \right) \\
|\Psi^+\rangle_{in} &\rightarrow \frac{1}{\sqrt{2}} \left( \frac{1}{2} (\hat{b}_{1,H}^\dagger \hat{b}_{1,V}^\dagger + \hat{b}_{1,V}^\dagger \hat{b}_{1,H}^\dagger) e^{-i\delta} - \frac{1}{2} (\hat{b}_{2,H}^\dagger \hat{b}_{2,V}^\dagger + \hat{b}_{2,V}^\dagger \hat{b}_{2,H}^\dagger) e^{i\delta} \right) |0,0\rangle_{out} \\
&= \frac{1}{\sqrt{2}} (e^{-i\delta} |1_H 1_V, 0\rangle_{out} - e^{i\delta} |0, 1_H 1_V\rangle_{out}) \\
|\Psi^-\rangle_{in} &\rightarrow \frac{1}{\sqrt{2}} \left( \frac{1}{2} (\hat{b}_{1,H}^\dagger \hat{b}_{2,V}^\dagger + \hat{b}_{2,V}^\dagger \hat{b}_{1,H}^\dagger) - \frac{1}{2} (\hat{b}_{1,V}^\dagger \hat{b}_{2,H}^\dagger + \hat{b}_{2,H}^\dagger \hat{b}_{1,V}^\dagger) \right) |0,0\rangle_{out} \\
&= \frac{1}{\sqrt{2}} (|1_H, 1_V\rangle_{out} - |1_V, 1_H\rangle_{out})
\end{aligned}$$

Two photons in the  $|\Phi^+\rangle_{in}$ ,  $|\Phi^-\rangle_{in}$ , and  $|\Psi^+\rangle_{in}$  state exhibit bunching and will be detected in the same output port. Two photons in the  $|\Psi^-\rangle_{in}$  state show perfect anti-bunching and will be detected each in a different output port. This type of beam splitter configuration is used in Bell state measurement in section 2.4.1.

**Perfect 50/50 beam splitter with a phase shift difference of  $\pi$  between polarizations**

Here the characteristic parameters are  $\Theta_H = \frac{\pi}{4}$ ,  $\Theta_V = \frac{\pi}{4}$  and  $\|\delta_H - \delta_V\| = \pi$ :

$$\begin{aligned}
|\Phi^+\rangle_{in} &\rightarrow \frac{1}{\sqrt{2}} \left( \frac{e^{-i\delta_H}}{2} (\hat{b}_{1,H}^\dagger \hat{b}_{1,H}^\dagger + \hat{b}_{1,V}^\dagger \hat{b}_{1,V}^\dagger e^{\pm i\pi}) - \frac{e^{i\delta_H}}{2} (\hat{b}_{2,H}^\dagger \hat{b}_{2,H}^\dagger + \hat{b}_{2,V}^\dagger \hat{b}_{2,V}^\dagger e^{\pm i\pi}) \right) |0,0\rangle_{out} \\
&= \frac{1}{\sqrt{2}} \left( \frac{e^{-i\delta_H}}{2} (|2_H,0\rangle_{out} + e^{\pm i\pi} |2_V,0\rangle_{out}) + \frac{e^{i\delta_H}}{2} (|0,2_H\rangle_{out} + e^{\pm i\pi} |0,2_V\rangle_{out}) \right) \\
|\Phi^-\rangle_{in} &\rightarrow \frac{1}{\sqrt{2}} \left( \frac{e^{-i\delta_H}}{2} (\hat{b}_{1,H}^\dagger \hat{b}_{1,H}^\dagger - e^{\pm i\pi} \hat{b}_{1,V}^\dagger \hat{b}_{1,V}^\dagger) - \frac{e^{i\delta_H}}{2} (\hat{b}_{2,H}^\dagger \hat{b}_{2,H}^\dagger - \hat{b}_{2,V}^\dagger \hat{b}_{2,V}^\dagger e^{\pm i\pi}) \right) |0,0\rangle_{out} \\
&\frac{1}{\sqrt{2}} \left( \frac{e^{-i\delta_H}}{2} (|2_H,0\rangle_{out} - e^{\pm i\pi} |2_V,0\rangle_{out}) + \frac{e^{i\delta_H}}{2} (|0,2_H\rangle_{out} - e^{\pm i\pi} |0,2_V\rangle_{out}) \right) \\
|\Psi^+\rangle_{in} &\rightarrow \frac{1}{\sqrt{2}} \left( \frac{1}{2} (\hat{b}_{1,H}^\dagger \hat{b}_{2,V}^\dagger + \hat{b}_{2,V}^\dagger \hat{b}_{1,H}^\dagger) + \frac{1}{\sqrt{2}} (\hat{b}_{1,V}^\dagger \hat{b}_{2,H}^\dagger + \hat{b}_{2,H}^\dagger \hat{b}_{1,V}^\dagger) \right) |0,0\rangle_{out} \\
&= \frac{1}{\sqrt{2}} (|1_H,1_V\rangle_{out} + |1_V,1_H\rangle_{out}) \\
|\Psi^-\rangle_{in} &\rightarrow \frac{1}{\sqrt{2}} \left( \frac{1}{2} e^{-i\delta_V} (\hat{b}_{1,H}^\dagger \hat{b}_{1,V}^\dagger - \hat{b}_{1,V}^\dagger \hat{b}_{1,H}^\dagger e^{\pm i\pi}) + \frac{1}{2} e^{i\delta_V} (-\hat{b}_{2,H}^\dagger \hat{b}_{2,V}^\dagger e^{\pm i\pi} + \hat{b}_{2,V}^\dagger \hat{b}_{2,H}^\dagger) \right) |0,0\rangle_{out} \\
&= \frac{1}{\sqrt{2}} (e^{-i\delta_V} |1_H 1_V, 0\rangle_{out} - e^{i\delta_V} |0, 1_H 1_V\rangle_{out})
\end{aligned}$$

Two photons in the  $|\Phi^+\rangle_{in}$ ,  $|\Phi^-\rangle_{in}$  state behave in the same way as in the previous case and bunch. In contrast two photons in the  $|\Psi^+\rangle_{in}$  and  $|\Psi^-\rangle_{in}$  show different behavior: now two photons in the  $|\Psi^-\rangle_{in}$  state show bunching and two photons in the  $|\Psi^+\rangle_{in}$  state show anti-bunching. This beam splitter configuration can also be used for the type of Bell state measurement from section 2.4.1.

**Polarization independent but not perfect <sup>50/50</sup> beam splitter**

For this beam splitter the characteristic parameters are  $\Theta_H = \Theta_V = \Theta$  and  $\delta_H = \delta_V = \delta$ :

$$\begin{aligned}
|\Phi^+\rangle_{in} &\rightarrow \frac{1}{\sqrt{2}} \left( \frac{\sin(2\Theta)}{2} \left( (\hat{b}_{1,H}^\dagger \hat{b}_{1,H}^\dagger + \hat{b}_{1,V}^\dagger \hat{b}_{1,V}^\dagger) e^{-i\delta} - (\hat{b}_{2,H}^\dagger \hat{b}_{2,H}^\dagger + \hat{b}_{2,V}^\dagger \hat{b}_{2,V}^\dagger) e^{i\delta} \right) \right. \\
&\quad \left. + \cos(2\Theta) (\hat{b}_{1,H}^\dagger \hat{b}_{2,H}^\dagger + \hat{b}_{1,V}^\dagger \hat{b}_{2,V}^\dagger) \right) |0,0\rangle_{out} \\
&= \frac{1}{\sqrt{2}} \frac{\sin(2\Theta)}{2} (e^{-i\delta} (|2_H,0\rangle_{out} + |2_V,0\rangle_{out}) - e^{i\delta} (|0,2_H\rangle_{out} + |0,2_V\rangle_{out})) \\
&\quad + \frac{1}{\sqrt{2}} \cos(2\Theta) (|1_H,1_H\rangle + |1_V,1_V\rangle_{out}) \\
|\Phi^-\rangle_{in} &\rightarrow \frac{1}{\sqrt{2}} \left( \frac{\sin(2\Theta)}{2} \left( (\hat{b}_{1,H}^\dagger \hat{b}_{1,H}^\dagger - \hat{b}_{1,V}^\dagger \hat{b}_{1,V}^\dagger) e^{-i\delta} - (\hat{b}_{2,H}^\dagger \hat{b}_{2,H}^\dagger - \hat{b}_{2,V}^\dagger \hat{b}_{2,V}^\dagger) e^{i\delta} \right) \right. \\
&\quad \left. + \cos(2\Theta) (\hat{b}_{1,H}^\dagger \hat{b}_{2,H}^\dagger - \hat{b}_{1,V}^\dagger \hat{b}_{2,V}^\dagger) \right) |0,0\rangle_{out} \\
&= \frac{1}{\sqrt{2}} \frac{\sin(2\Theta)}{2} (e^{-i\delta} (|2_H,0\rangle_{out} - |2_V,0\rangle_{out}) - e^{i\delta} (|0,2_H\rangle_{out} - |0,2_V\rangle_{out})) \\
&\quad + \frac{1}{\sqrt{2}} \cos(2\Theta) (|1_H,1_H\rangle - |1_V,1_V\rangle_{out}) \\
|\Psi^+\rangle_{in} &\rightarrow \frac{1}{\sqrt{2}} \left( \frac{\sin(2\Theta)}{2} \left( (\hat{b}_{1,H}^\dagger \hat{b}_{1,V}^\dagger + \hat{b}_{1,V}^\dagger \hat{b}_{1,H}^\dagger) e^{-i\delta} - (\hat{b}_{2,H}^\dagger \hat{b}_{2,V}^\dagger + \hat{b}_{2,V}^\dagger \hat{b}_{2,H}^\dagger) e^{i\delta} \right) \right. \\
&\quad \left. \cos(2\Theta) (\hat{b}_{1,H}^\dagger \hat{b}_{2,V}^\dagger - \hat{b}_{1,V}^\dagger \hat{b}_{2,H}^\dagger) \right) |0,0\rangle_{out} \\
&= \frac{1}{\sqrt{2}} \frac{\sin(2\Theta)}{2} (e^{-i\delta} |1_H 1_V, 0\rangle_{out} - e^{i\delta} |0, 1_H 1_V\rangle_{out}) \\
&\quad + \frac{1}{\sqrt{2}} \cos(2\Theta) (|1_H, 1_V\rangle_{out} - |1_V, 1_H\rangle_{out}) \\
|\Psi^-\rangle_{in} &\rightarrow \frac{1}{\sqrt{2}} \left( \frac{1}{2} (\hat{b}_{1,H}^\dagger \hat{b}_{2,V}^\dagger + \hat{b}_{2,V}^\dagger \hat{b}_{1,H}^\dagger) - \frac{1}{2} (\hat{b}_{1,V}^\dagger \hat{b}_{2,H}^\dagger + \hat{b}_{2,H}^\dagger \hat{b}_{1,V}^\dagger) \right) |0,0\rangle_{out} \\
&= \frac{1}{\sqrt{2}} (|1_H, 1_V\rangle_{out} - |1_V, 1_H\rangle_{out})
\end{aligned}$$

A not <sup>50/50</sup> beam splitter leads to reduced bunching. The anti bunching input state, in this case  $|\Psi^-\rangle_{in}$  sees no effect. For a Bell state measurement this reduced bunching leads to a mixing of the Bell states and reduces the fidelity for both detectable input states.

### A polarizing beam splitter

For a polarizing beam splitter the characteristic parameters  $\Theta_H = 0$ ,  $\Theta_V = \frac{\pi}{2}$  and  $\delta_H, \delta_V$  are free:

$$\begin{aligned} |\Phi^+\rangle_{in} &\rightarrow \frac{1}{\sqrt{2}} (\hat{b}_{1,H}^\dagger \hat{b}_{2,H}^\dagger - \hat{b}_{2,V}^\dagger \hat{b}_{1,V}^\dagger) |0,0\rangle_{out} \\ |\Phi^-\rangle_{in} &\rightarrow \frac{1}{\sqrt{2}} (\hat{b}_{1,H}^\dagger \hat{b}_{2,H}^\dagger + \hat{b}_{2,V}^\dagger \hat{b}_{1,V}^\dagger) |0,0\rangle_{out} \\ |\Psi^+\rangle_{in} &\rightarrow \frac{1}{\sqrt{2}} (\hat{b}_{1,H}^\dagger \hat{b}_{1,V}^\dagger e^{-i\delta_V} - \hat{b}_{2,V}^\dagger \hat{b}_{2,H}^\dagger e^{-i\delta_V}) \\ |\Psi^-\rangle_{in} &\rightarrow \frac{1}{\sqrt{2}} (\hat{b}_{1,H}^\dagger \hat{b}_{1,V}^\dagger e^{-i\delta_V} + \hat{b}_{2,V}^\dagger \hat{b}_{2,H}^\dagger e^{-i\delta_V}) \end{aligned}$$

A polarizing beam splitter shows the expected effect: for the input state with the same polarization for both photons  $|\Phi^+\rangle_{in}$  and  $|\Phi^-\rangle_{in}$  the photons are still in different ports. For the states with different polarization for the photons  $|\Psi^+\rangle_{in}$  and  $|\Psi^-\rangle_{in}$  are combined in one output.

## F. Technical Details of the Experimental Setup

### Laser System

All lasers used in the experiment are diode lasers.

#### Frequency stabilized lasers

The lasers used for laser cooling and addressing atomic states are frequency stabilized using Doppler-free saturation spectroscopy. Three stabilized diode lasers are used in each setup to create the fitting lasers light for the different purposes of cooling, pumping, excitation and read-out (Fig F.1).

**D2 transition from  $5S_{1/2}, F = 2$  (780 nm)** A laser stabilized to the transition from  $5S_{1/2}, F = 2$  to  $5P_{3/2}$  is used to create the “cooling”, “pump<sub>2→1</sub>”, and “cycling” light. For this the light is split up in 3 beam lines using polarizing beam splitters. The light in each beam line is shifted frequency using AOMs to the needed resonance and coupled into glass fibers going to the experiment.

**D2 transition from  $5S_{1/2}, F = 1$  (780 nm)** A laser stabilized to the transition from  $5S_{1/2}, F = 1$  to  $5P_{3/2}$  is used to create the “repump”, “pump<sub>1→1</sub>”, and “excitation” light.

**D1 transition (795 nm)** A laser stabilized to the transition from  $5S_{1/2}, F = 1$  to  $5P_{1/2}$  is used to create the “read-out” light.

#### Free running lasers

The ODT trap laser (850 nm) and the ionization laser (450 nm in lab 1 and 473 nm in lab 2) are free running single mode lasers. Due to the higher power demand of the ODT in lab 1 the laser is amplified using a tapered amplifier.

### Differences in the Trap Setups

#### Differences pumping and excitation beam path

The main difference in the two setups is the alignment of the pumping and excitation beam path: this is rotated by 90° for lab 2 (Fig. F.2). This does not lead to any change of the experimental procedure or the resulting atom-photon states.

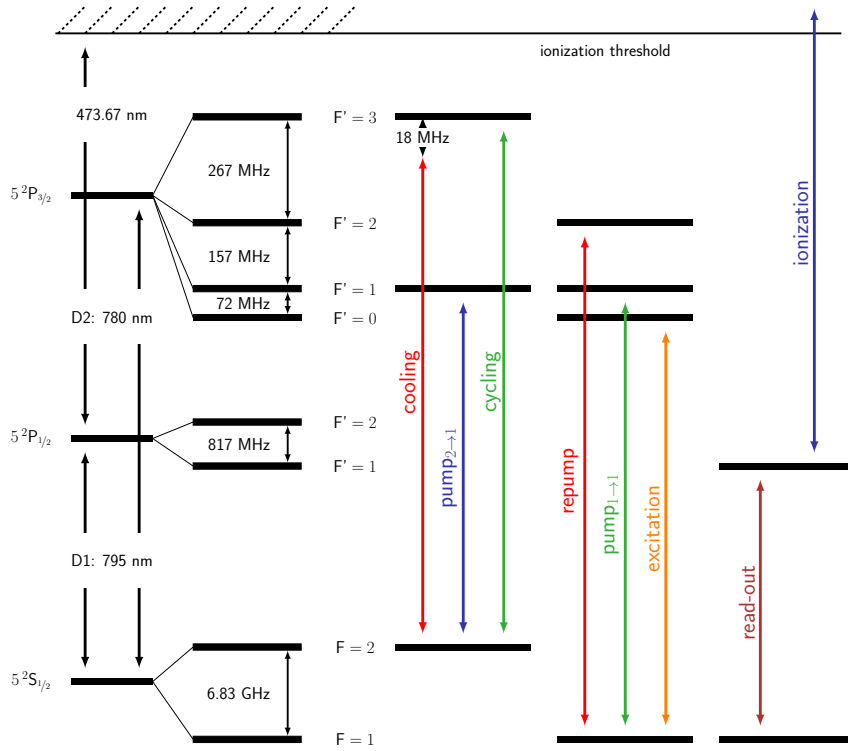


Figure F.1.: Laser light in the experiment

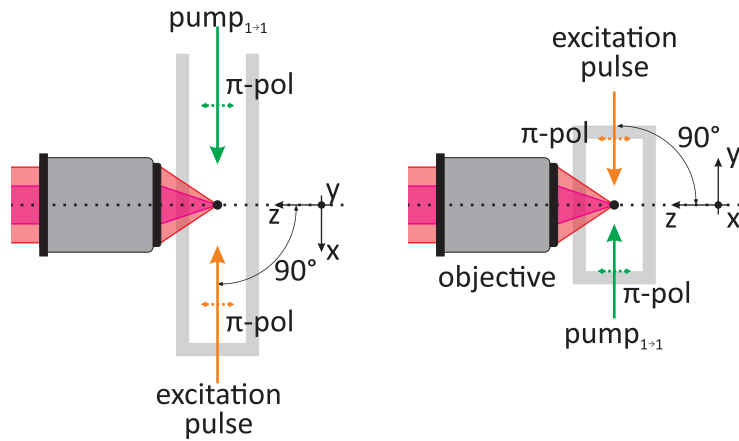
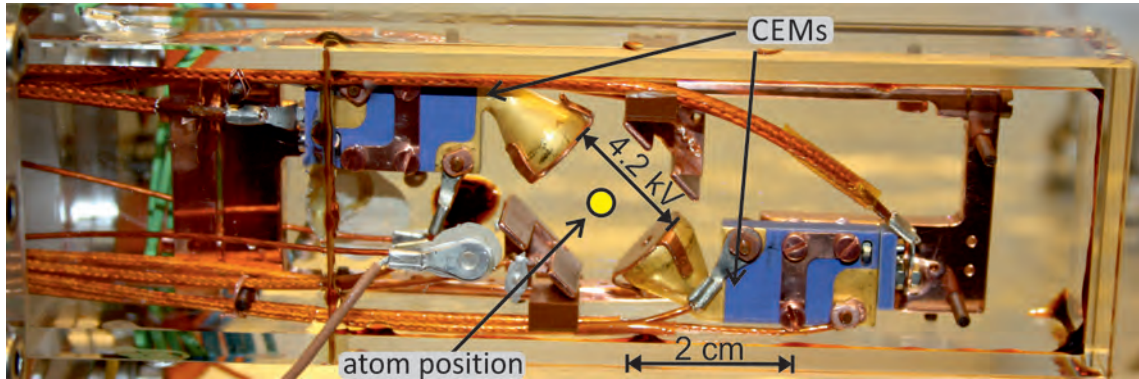
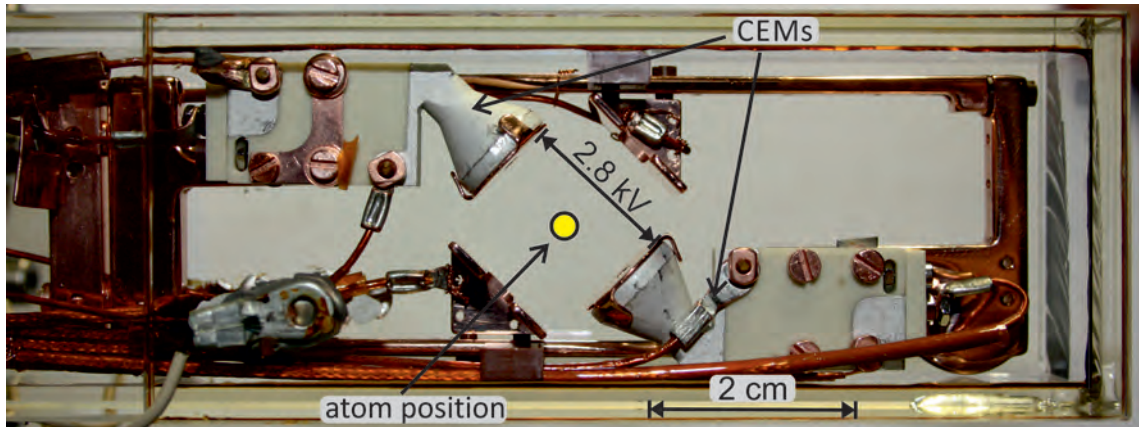


Figure F.2.: Excitation and pump $_{1 \rightarrow 1}$  beam path in both traps.



(a) CEM setup in Lab 1: The CEMs with gold coating show no background caused by the ionization laser. Stable operation with acceleration voltage of  $\Delta U_{acc} = 4.3$  kV possible.



(b) CEM setup in Lab 2: CEMs with silver coating show background caused by the ionization laser. An acceleration voltage  $\Delta U_{acc} \geq 2.8$  kV leads to very high background counts.

Figure F.3.: Differences of the channel electron multiplier setups in the trap setups.

### Differences in the CEM setup

The design of the CEM setup in both traps is identical, however the CEMs themselves are slightly different: in lab 1 gold coated CEMs and in lab 2 silver coated ones are used (Fig. F.3). Also the performance of the two setups is different. The setup in lab 1 performs as characterized in [37, 54]. However, the setup in lab 2 has a slightly higher fragment detection efficiency yet it suffers from background counts: with an acceleration voltage  $\Delta U_{acc} > 2800$  V field emission leads to background counts in the order of more than  $10^5$  counts/s. Thus, a lower voltage is used leading to a longer time of flight of the  $\text{Rb}^+$  ions to the detectors. Furthermore, the silver coating in combination with rubidium leads to electron emission caused by the ionization laser. The effect is stronger with shorter wave length blue laser but it can be reduced by “cleaning” the surfaces with UV light. After installing new silver coated CEMs in lab 1 the same problem occurred there.

## G. Formulary

### Bell state projection for entanglement swapping

$$\begin{aligned}
|\Psi_{all}\rangle &= |\Psi_1\rangle \otimes |\Psi_2\rangle \\
&= \frac{1}{\sqrt{2}} (|\uparrow\rangle_{A,1} |\downarrow\rangle_{P,1} + |\downarrow\rangle_{A,1} |\uparrow\rangle_{P,1}) \otimes \frac{1}{\sqrt{2}} (|\uparrow\rangle_{A,2} |\downarrow\rangle_{P,2} + |\downarrow\rangle_{A,2} |\uparrow\rangle_{P,2}) \\
&= \frac{1}{2} (|\uparrow\rangle_{A,1} |\downarrow\rangle_{P,1} |\uparrow\rangle_{A,2} |\downarrow\rangle_{P,2} + |\uparrow\rangle_{A,1} |\downarrow\rangle_{P,1} |\downarrow\rangle_{A,2} |\uparrow\rangle_{P,2}) \\
&\quad + \frac{1}{2} (|\downarrow\rangle_{A,1} |\uparrow\rangle_{P,1} |\uparrow\rangle_{A,2} |\downarrow\rangle_{P,2} + |\downarrow\rangle_{A,1} |\uparrow\rangle_{P,1} |\downarrow\rangle_{A,2} |\uparrow\rangle_{P,2}).
\end{aligned}$$

$$\begin{aligned}
\langle \Psi_P^- | \Psi_{all} \rangle &= \left\langle \frac{1}{\sqrt{2}} (|\uparrow\rangle_{P,1} \langle \downarrow|_{P,2} - \langle \downarrow|_{P,1} \langle \uparrow|_{P,2}) | \Psi_{all} \right\rangle \\
&= \frac{1}{2} \frac{1}{\sqrt{2}} (|\downarrow\rangle_{A,1} \langle \uparrow|_{A,2} - \langle \uparrow|_{A,1} \langle \downarrow|_{A,2}) \\
&= \frac{-1}{2} |\Psi_A^- \rangle
\end{aligned}$$

$$\begin{aligned}
\langle \Psi_P^+ | \Psi_{all} \rangle &= \left\langle \frac{1}{\sqrt{2}} (|\uparrow\rangle_{P,1} \langle \downarrow|_{P,2}) + \langle \downarrow|_{P,1} \langle \uparrow|_{P,2} | \Psi_{all} \right\rangle \\
&= \frac{1}{\sqrt{2}} \left( \frac{1}{2} |\downarrow\rangle_{A,1} \langle \uparrow|_{A,2} + \frac{1}{2} \langle \uparrow|_{A,1} \langle \downarrow|_{A,2} \right) \\
&= \frac{1}{2} |\Psi_A^+ \rangle
\end{aligned}$$

$$\begin{aligned}
\langle \Phi_P^- | \Psi_{all} \rangle &= \left\langle \frac{1}{\sqrt{2}} (|\uparrow\rangle_{P,1} \langle \uparrow|_{P,2} - \langle \downarrow|_{P,1} \langle \downarrow|_{P,2}) | \Psi_{all} \right\rangle \\
&= \frac{1}{\sqrt{2}} \left( \frac{1}{2} |\downarrow\rangle_{A,1} \langle \downarrow|_{A,2} - \frac{1}{2} \langle \uparrow|_{A,1} \langle \uparrow|_{A,2} \right) \\
&= \frac{-1}{2} |\Phi_A^- \rangle
\end{aligned}$$

$$\begin{aligned}
\langle \Phi_P^+ | \Psi_{all} \rangle &= \left\langle \frac{1}{\sqrt{2}} (|\uparrow\rangle_{P,1} \langle \uparrow|_{P,2} + \langle \downarrow|_{P,1} \langle \downarrow|_{P,2}) | \Psi_{all} \right\rangle \\
&= \frac{1}{\sqrt{2}} \left( \frac{1}{2} |\downarrow\rangle_{A,1} \langle \downarrow|_{A,2} + \frac{1}{2} \langle \uparrow|_{A,1} \langle \uparrow|_{A,2} \right) \\
&= \frac{1}{2} |\Phi_A^+ \rangle
\end{aligned}$$

**Lemma 1**

$\forall a, b \in [0, 1]$  is  $0 \leq |a + b - 1| + |a - b| \leq 1$ .

Proof:  $0 \leq |a + b - 1| + |a - b|$  follows directly from the definition. Now four cases that cover all combinations of  $a, b \in [0, 1]$  are considered:

1.  $b \leq a$  and  $a + b \leq 1$

$$\begin{aligned} |a + b - 1| + |a - b| &= 1 - a - b + a - b \\ &= 1 - 2b \leq 1 \end{aligned}$$

2.  $a \leq b$  and  $a + b \leq 1$

$$\begin{aligned} |a + b - 1| + |a - b| &= 1 - a - b - a + b \\ &= 1 - 2a \leq 1 \end{aligned}$$

3.  $b \leq a$  and  $a + b \geq 1$

$$\begin{aligned} |a + b - 1| + |a - b| &= a + b - 1 + a - b \\ &= 2a - 1 \leq 1 \end{aligned}$$

4.  $a \leq b$  and  $a + b \geq 1$

$$\begin{aligned} |a + b - 1| + |a - b| &= a + b - 1 - a + b \\ &= 2b - 1 \leq 1 \end{aligned}$$

$$\Rightarrow 0 \leq |a + b - 1| + |a - b| \leq 1 \quad \forall a, b \in [0, 1] \quad (\text{G.1})$$

**Bell-correlators for  $|\Psi^-\rangle$  and measurement operators from Tab.: 3.1**

An arbitrary state  $|\psi\rangle$  can be written as

$$|\psi\rangle = \begin{pmatrix} \cos(\theta/2) e^{-i\phi/2} \\ \sin(\theta/2) e^{i\phi/2} \end{pmatrix}$$

and an operator  $\hat{\sigma}$  as

$$\hat{\sigma} = \begin{pmatrix} \cos(\theta) & \sin(\theta) e^{-i\phi} \\ \sin(\theta) e^{i\phi} & -\cos(\theta) \end{pmatrix}. \quad (\text{G.2})$$

Using this for the operators  $\hat{A}_a$  and  $\hat{B}_b$  from Table 3.1 leads to

$$\begin{aligned} \hat{A}_a &= \begin{pmatrix} \cos(\theta_a) & \sin(\theta_a) \\ \sin(\theta_a) & -\cos(\theta_a) \end{pmatrix} \\ \hat{B}_b &= \begin{pmatrix} \cos(\theta_b) & \sin(\theta_b) \\ \sin(\theta_b) & -\cos(\theta_b) \end{pmatrix} \end{aligned}$$

with  $\phi_a = \phi_b = 0$  (since the operators have only real elements) and the  $\theta_a$  and  $\theta_b$  in Table G.1. Therefore, the correlator (3.7) takes the form

Input	operator	$\theta$ from (G.2)
$A = 1$	$\hat{A}_1 = \sigma_z$	$\theta_a = 0$
$A = 0$	$\hat{A}_0 = \sigma_x$	$\theta_a = \pi/2$
$B = 1$	$\hat{B}_1 = \frac{1}{\sqrt{2}}(\sigma_z + \sigma_x)$	$\theta_b = \pi/4$
$B = 0$	$\hat{B}_0 = \frac{1}{\sqrt{2}}(\sigma_z - \sigma_x)$	$\theta_b = -\pi/4$

Table G.1.:  $\theta_a$  and  $\theta_b$  for the measurement operators from Table 3.1

$$\begin{aligned}
E_{ab} &= \langle \hat{A}_a \hat{B}_b \rangle = \langle \Psi^- | \hat{A}_a \hat{B}_b | \Psi^- \rangle \\
&= \langle \Psi^- | \begin{pmatrix} \cos(\theta_a) & \sin(\theta_a) \\ \sin(\theta_a) & -\cos(\theta_a) \end{pmatrix}_A \begin{pmatrix} \cos(\theta_b) & \sin(\theta_b) \\ \sin(\theta_b) & -\cos(\theta_b) \end{pmatrix}_B | \Psi^- \rangle \\
&= \langle \Psi^- | \frac{1}{\sqrt{2}} \left[ \left| \begin{matrix} \cos(\theta_a) \\ \sin(\theta_a) \end{matrix} \right\rangle \left| \begin{matrix} \sin(\theta_b) \\ -\cos(\theta_b) \end{matrix} \right\rangle - \left| \begin{matrix} \sin(\theta_a) \\ -\cos(\theta_a) \end{matrix} \right\rangle \left| \begin{matrix} \cos(\theta_b) \\ \sin(\theta_b) \end{matrix} \right\rangle \right] \\
&= \frac{1}{2} (-\cos(\theta_a) \cos(\theta_b) - \sin(\theta_a) \sin(\theta_b) - \sin(\theta_a) \cos(\theta_b) - \cos(\theta_a) \cos(\theta_b)) \\
&= -\cos(\theta_a - \theta_b).
\end{aligned}$$

With the angles from Table G.1 the values of  $E_{ab}$  are

$$\begin{aligned}
E_{11} &= -\cos(-\pi/4) = -1/\sqrt{2}, \\
E_{10} &= -\cos(+\pi/4) = -1/\sqrt{2}, \\
E_{01} &= -\cos(+\pi/4) = -1/\sqrt{2}, \text{ and} \\
E_{00} &= -\cos(3\pi/4) = 1/\sqrt{2}.
\end{aligned}$$

Finally, (3.1) takes the value of

$$S = |-1/\sqrt{2} - 1/\sqrt{2}| + |-1/\sqrt{2} - 1/\sqrt{2}| = 2\sqrt{2}.$$

The according calculation can be done for  $|\Psi^+\rangle$ .

## Bibliography

- [1] A Einstein et al. Can Quantum-Mechanical Description of Physical Reality Be Considered Complete? PR, 47:777780, 1935. doi: 10.1103/PhysRev.47.777.
- [2] J. S. Bell. On the Einstein Podolsky Rosen paradox. PPF, 1:195, 1965.
- [3] R. P. Feynman. Simulating physics with computers. International Journal of Theoretical Physics, 21:467488, 1982. ISSN 1572-9575. doi: 10.1007/BF02650179.
- [4] F. Arute et al. Quantum supremacy using a programmable superconducting processor. Nature, 2019. ISSN 1476-4687. doi: 10.1038/s41586-019-1666-5.
- [5] A. K. Ekert. Quantum cryptography based on bell's theorem. PRL, 67:661663, 1991.
- [6] N. Bohr. Can quantum-mechanical description of physical reality be considered complete? PR, 48:696702, 1935.
- [7] A. Einstein. Physik und Realität. Journal of the Franklin Institute, 221:313347, 1936. ISSN 0016-0032.
- [8] A. Einstein. Quanten-Mechanik und Wirklichkeit. Dialectica, 2:320324, 1948. doi: 10.1111/j.1746-8361.1948.tb00704.x.
- [9] J. F. Clauser et al. Proposed Experiment to Test Local Hidden-Variable Theories. PRL, 23:880884, 1969. doi: 10.1103/PhysRevLett.23.880.
- [10] S. J. Freedman and J. F. Clauser. Experimental Test of Local Hidden-Variable Theories. PRL, 28:938941, 1972.
- [11] A. Aspect et al. Experimental Test of Bell's Inequalities Using Time-Varying Analyzers. PRL, 49:18041807, 1982.
- [12] A. Aspect et al. Experimental Realization of Einstein-Podolsky-Rosen-Bohm Gedankenexperiment: A New Violation of Bell's Inequalities. PRL, 49:9194, 1982.
- [13] J.-Å. Larsson. Loopholes in Bell inequality tests of local realism. Journal of Physics A: Mathematical and Theoretical, 47:424003, 2014. ISSN 1751-8121. doi: 10.1088/1751-8113/47/42/424003.
- [14] M. Jeng. A selected history of expectation bias in physics. American Journal of Physics, 74:578583, 2006. ISSN 0002-9505. doi: 10.1119/1.2186333.
- [15] J. Barrett. Quantum nonlocality, Bell inequalities, and the memory loophole. PRA, 66:042111, 2002.

- [16] R. D. Gill. Time, Finite Statistics, and Bell’s Fifth Position. In Proceedings of “Foundations of Probability and Physics - 2”, Ser. Math. Modelling in Phys., Engin., and Cogn. Sc., pages 179–206. Växjö University, 2003. URL <https://arxiv.org/abs/quant-ph/0301059v2>.
- [17] David Elkouss and Stephanie Wehner. (nearly) optimal P values for all Bell inequalities. *Npj Quantum Information*, 2:16026, 2016. doi: 10.1038/npjqi.2016.26.
- [18] B. Hensen et al. Loophole-free Bell inequality violation using electron spins separated by 1.3 kilometres. *Nature*, 526:682, 2015. doi: 10.1038/nature15759.
- [19] M. Giustina et al. Significant-Loophole-Free Test of Bell’s Theorem with Entangled Photons. *PRL*, 115:250401, 2015.
- [20] L. K. Shalm et al. Strong Loophole-Free Test of Local Realism. *PRL*, 115:250402, 2015.
- [21] D. Mayers and A. Yao. Quantum cryptography with imperfect apparatus. In FOCS ’98 Proceedings of the 39th Annual Symposium on Foundations of Computer Science, page 503. IEEE Computer Society, IEEE Computer Society Washington, DC, USA, 1998. ISBN 0-8186-9172-7.
- [22] D. Mayers and A. Yao. Self testing quantum apparatus. *Quantum Info. Comput.*, 4: 273286, 2004. doi: 10.26421/QIC4.4.
- [23] S. Pironio et al. Random numbers certified by Bell’s theorem. *Nature*, 464:1021, 2010. doi: 10.1038/nature09008.
- [24] H. J. Kimble. The quantum internet. *Nature*, 453:1023, 2008. doi: 10.1038/nature07127.
- [25] H.-J. Briegel et al. Quantum Repeaters: The Role of Imperfect Local Operations in Quantum Communication. *PRL*, 81:59325935, 1998.
- [26] R. Jozsa et al. Quantum Clock Synchronization Based on Shared Prior Entanglement. *PRL*, 85:20102013, 2000.
- [27] I. Šupić and J. Bowles. Self-testing of quantum systems: a review. arXiv:1904.10042, 2019. URL <https://arxiv.org/abs/1904.10042>.
- [28] M. Weber. Quantum optical experiments towards atom-photon entanglement. PhD thesis, Ludwig-Maximilians-Universität München, 2005. URL [http://xqp.physik.uni-muenchen.de/publications/theses\\_phd/phd\\_weber.html](http://xqp.physik.uni-muenchen.de/publications/theses_phd/phd_weber.html).
- [29] J. Volz et al. Observation of Entanglement of a Single Photon with a Trapped Atom. *PRL*, 96:030404, 2006.
- [30] Jürgen Volz. Atom-Photon Entanglement. PhD thesis, Ludwig-Maximilians-Universität München, 2006. URL [http://xqp.physik.uni-muenchen.de/publications/theses\\_phd/phd\\_volz.html](http://xqp.physik.uni-muenchen.de/publications/theses_phd/phd_volz.html).
- [31] M. Zukowski et al. “event-ready-detectors” Bell experiment via entanglement swapping. *PRL*, 71:4287, 1993.

- [32] J. Hofmann et al. Heralded Entanglement Between Widely Separated Atoms. *Science*, 337:72, 2012. URL <http://science.sciencemag.org/content/337/6090/72.abstract>.
- [33] Julian Hofmann. Heralded Atom-Atom Entanglement. PhD thesis, Ludwig-Maximilians-Universität München, 2014. URL [http://xqp.physik.uni-muenchen.de/publications/theses\\_phd/phd\\_hofmann.html](http://xqp.physik.uni-muenchen.de/publications/theses_phd/phd_hofmann.html).
- [34] Michael Krug. Ionization Based State Read Out of a single Rb-87 Atom. PhD thesis, Ludwig-Maximilians-Universität München, 2018. URL [http://xqp.physik.uni-muenchen.de/publications/theses\\_phd/phd\\_krug.html](http://xqp.physik.uni-muenchen.de/publications/theses_phd/phd_krug.html).
- [35] F. Henkel et al. Highly Efficient State-Selective Submicrosecond Photoionization Detection of Single Atoms. *PRL*, 105:253001, 2010. doi: 10.1103/PhysRevLett.105.253001.
- [36] Florian Henkel. Photoionisation detection of single Rb-87 atoms using channel electron multipliers. PhD thesis, Ludwig-Maximilians-Universität München, 2011. URL [http://xqp.physik.uni-muenchen.de/publications/theses\\_phd/phd\\_henkel.html](http://xqp.physik.uni-muenchen.de/publications/theses_phd/phd_henkel.html).
- [37] Norbert Ortegel. State readout of single Rubidium-87 atoms for a loophole-free test of Bell’s inequality. PhD thesis, Ludwig-Maximilians-Universität München, 2016. URL [http://xqp.physik.uni-muenchen.de/publications/theses\\_phd/phd\\_ortegel.html](http://xqp.physik.uni-muenchen.de/publications/theses_phd/phd_ortegel.html).
- [38] Daniel Burchardt. A Rigorous Test of Bell’s Inequality and Quantum Teleportation Employing Single Atoms. PhD thesis, Ludwig-Maximilians-Universität München, 2018. URL [http://xqp.physik.uni-muenchen.de/publications/theses\\_phd/phd\\_burchardt.html](http://xqp.physik.uni-muenchen.de/publications/theses_phd/phd_burchardt.html).
- [39] M. Fürst. High speed optical quantum random number generation. *Opt. Express*, 18:1302913037, 2010. URL <http://www.opticsexpress.org/abstract.cfm?URI=oe-18-12-13029>.
- [40] J. Gallicchio et al. Testing Bell’s Inequality with Cosmic Photons: Closing the Setting-Independence Loophole. *PRL*, 112:110405, 2014.
- [41] J. Handsteiner et al. Cosmic Bell Test: Measurement Settings from Milky Way Stars. *PRL*, 118:060401, 2017.
- [42] D. Rauch et al. Cosmic BellTest Using Random Measurement Settings from High-Redshift Quasars. *PRL*, 121:080403, 2018.
- [43] M.-H. Li et al. Test of Local Realism into the Past without Detection and Locality Loopholes. *PRL*, 121:080404, 2018.
- [44] J. S. Bell. Free variables and local causality. pages 100–104. Cambridge University Press, Cambridge, 2 edition, 2004. doi: 10.1017/cbo9780511815676.014.
- [45] The BIG Bell Test Collaboration. Challenging local realism with human choices. *Nature*, 557:212216, 2018. ISSN 1476-4687. doi: 10.1038/s41586-018-0085-3.
- [46] L.-M. Duan et al. Long-distance quantum communication with atomic ensembles and linear optics. *Nature*, 414:413418, 2001. ISSN 1476-4687. doi: 10.1038/35106500.
- [47] J.-D. Bancal et al. Device-independent certification of an elementary quantum network link. arXiv:1812.09117, 2018.

- [48] Wenjamin Rosenfeld. Experiments with an Entangled System of a Single Atom and a Single Photon. PhD thesis, Ludwig-Maximilians-Universität München, 2008. URL [http://xqp.physik.uni-muenchen.de/publications/theses\\_phd/phd\\_rosenfeld.html](http://xqp.physik.uni-muenchen.de/publications/theses_phd/phd_rosenfeld.html).
- [49] D. A. Steck. Rubidium 87 d line data. 01 2003. URL <https://steck.us/alkalidata/rubidium87numbers.1.6.pdf>.
- [50] S. Chu et al. Experimental observation of optically trapped atoms. PRL, 57:314, 1986. doi: 10.1103/PhysRevLett.57.314.
- [51] S. Chu et al. Three-dimensional viscous confinement and cooling of atoms by resonance radiation pressure. PRL, 55:48, 1985. doi: 10.1103/PhysRevLett.55.48.
- [52] T.W. Hänsch and A.L. Schawlow. Cooling of gases by laser radiation. Optics Communications, 13:68 – 69, 1975. ISSN 0030-4018. doi: [https://doi.org/10.1016/0030-4018\(75\)90159-5](https://doi.org/10.1016/0030-4018(75)90159-5).
- [53] E. L. Raab et al. Trapping of Neutral Sodium Atoms with Radiation Pressure. PRL, 59:2631, 1987. doi: 10.1103/PhysRevLett.59.2631.
- [54] K. Redeker. Detektion von Ionisationsfragmenten von Rb-87 Atomen, Diplomarbeit, 2012. URL [http://xqp.physik.uni-muenchen.de/publications/theses\\_diplom/diplom\\_redeker.html](http://xqp.physik.uni-muenchen.de/publications/theses_diplom/diplom_redeker.html).
- [55] J. Dalibard and C. Cohen-Tannoudji. Laser cooling below the Doppler limit by polarization gradients: simple theoretical models. Journal of the Optical Society of America B, 6(11):2023, 1989. doi: 10.1364/JOSAB.6.002023.
- [56] Paul Koschmieder. Efficient Control of Magnetic Fields in Single Atom Experiments. Master's thesis, Ludwig-Maximilians-Universität München, 2019. URL [https://xqp.physik.uni-muenchen.de/publications/files/theses\\_master/master\\_koschmieder.pdf](https://xqp.physik.uni-muenchen.de/publications/files/theses_master/master_koschmieder.pdf).
- [57] Optical Dipole Traps for Neutral Atoms.
- [58] N. Schlosser et al. Collisional blockade in microscopic optical dipole traps. Physical Review Letters, 89:023005, Jun 2002. doi: 10.1103/PhysRevLett.89.023005. URL <https://link.aps.org/doi/10.1103/PhysRevLett.89.023005>.
- [59] S. A. Lee et al. Doppler-free two-photon transitions to Rydberg levels: convenient, useful, and precise reference wavelengths for dye lasers. Opt. Lett., 3:141, 1978.
- [60] W Rosenfeld et al. Event-Ready Bell Test Using Entangled Atoms Simultaneously Closing Detection and Locality Loopholes. PRL, 119:010402, 2017. doi: 10.1103/PhysRevLett.119.010402.
- [61] K. L. Corwin et al. Spin-Polarized Atoms in a Circularly Polarized Optical Dipole Trap. PRL, 83:1311, 1999. doi: 10.1103/PhysRevLett.83.1311.
- [62] R. Dorn et al. The focus of light – linear polarization breaks the rotational symmetry of the focal spot. Journal of Modern Optics, 50:1917, 2003. doi: 10.1080/09500340308235246.

- [63] E. Wolf. Electromagnetic diffraction in optical systems - I. An integral representation of the image field. *Proceedings of the Royal Society of London A: Mathematical, Physical and Engineering Sciences*, 253:349, 1959. ISSN 0080-4630. doi: 10.1098/rspa.1959.0199.
- [64] B. Richards and E. Wolf. Electromagnetic diffraction in optical systems, II. Structure of the image field in an aplanatic system. *Proceedings of the Royal Society of London A: Mathematical, Physical and Engineering Sciences*, 253:358, 1959. ISSN 0080-4630. doi: 10.1098/rspa.1959.0200.
- [65] E. Thébault et al. International Geomagnetic Reference Field: the 12th generation. *Earth, Planets and Space*, 67:79, 2015. ISSN 1880-5981. doi: 10.1186/s40623-015-0228-9.
- [66] J.-W. Pan et al. Experimental Entanglement Swapping: Entangling Photons That Never Interacted. *PRL*, 80:3891, 1998.
- [67] W. Rosenfeld et al. Towards high-fidelity interference of photons emitted by two remotely trapped Rb-87 atoms. *Optics and Spectroscopy*, 111:535, 2011. ISSN 1562-6911. doi: 10.1134/S0030400X11110233.
- [68] C. K. Hong et al. Measurement of subpicosecond time intervals between two photons by interference. *PRL*, 59:2044, 1987.
- [69] R. A. Campos et al. Quantum-mechanical lossless beam splitter: SU(2) symmetry and photon statistics. *PRA*, 40:1371, 1989.
- [70] W. Rosenfeld et al. Towards Long-Distance Atom-Photon Entanglement. *PRL*, 101(26):260403, 2008.
- [71] J. von Neumann. *Mathematische Grundlagen der Quantenphysik*, chapter IV, pages 167–173. Verlag Julius Springer, 1932. ISBN 978-3-642-61409-5.
- [72] D. Bohm. A Suggested Interpretation of the Quantum Theory in Terms of "Hidden" Variables. i. *PR*, 85:166179, 1952.
- [73] D. Bohm. A Suggested Interpretation of the Quantum Theory in Terms of "Hidden" Variables. ii. *PR*, 85:180193, 1952.
- [74] J. Albertson. Von Neumann's Hidden-Parameter Proof. *American Journal of Physics*, 29:478484, 1961. ISSN 0002-9505. doi: 10.1119/1.1937816.
- [75] J.-M. Jauch and C. Piron. Can Hidden Variables be Excluded in Quantum Mechanics. *Helvetica Physica Acta*, 36:827, 1963. doi: 10.5169/seals-113402.
- [76] J. S. Bell. On the Problem of Hidden Variables in Quantum Mechanics. *RMP*, 38:447452, 1966.
- [77] B. S. Cirel'son. Quantum generalizations of Bell's inequality. *Letters in Mathematical Physics*, 4:93100, 1980. ISSN 1573-0530. doi: 10.1007/BF00417500.
- [78] P. M. Pearle. Hidden-Variable Example Based upon Data Rejection. *PRD*, 2:14181425, 1970.

- [79] J.-Å. Larsson and R. D. Gill. Bell's inequality and the coincidence-time loophole. *Europhysics Letters (EPL)*, 67:707713, 2004. ISSN 1286-4854. doi: 10.1209/epl/i2004-10124-7.
- [80] A. Garg and N. D. Mermin. Detector inefficiencies in the Einstein-Podolsky-Rosen experiment. *PRD*, 35:38313835, 1987.
- [81] J.-Å. Larsson. Bell's inequality and detector inefficiency. *PRA*, 57:33043308, 1998.
- [82] J. F. Clauser and M. A. Horne. Experimental consequences of objective local theories. *PRD*, 10:526535, 1974.
- [83] P. H. Eberhard. Background level and counter efficiencies required for a loophole-free Einstein-Podolsky-Rosen experiment. *PRA*, 47:R747, 1993. doi: 10.1103/PhysRevA.47.R747.
- [84] N. Brunner et al. Bell nonlocality. *RMP*, 86:419478, 2014.
- [85] R. A. Fisher. *The Design of Experiments*, chapter II., page 16. Hafner Publishing Company, ninth edition edition, 1971. ISBN 0-02-844690-9.
- [86] R. A. Fisher. *The Design of Experiments*. Hafner Publishing Company, New York, ninth edition edition, 1971. ISBN 0-02-844690-9.
- [87] H. C. Selvin and A. Stuart. Data-Dredging Procedures in Survey Analysis. *The American Statistician*, 20:2023, June 1966. ISSN 0003-1305. doi: 10.1080/00031305.1966.10480401.
- [88] R. A. Fisher. *Statistical methods for research workers*. Oliver & Boyd, Edinburgh, 1932.
- [89] J. T. Kost and M. P. McDermott. Combining dependent P-values. *Statistics & Probability Letters*, 60:183190, 2002. ISSN 0167-7152.
- [90] P. Bierhorst. A robust mathematical model for a loophole-free Clauser-Horne experiment. *Journal of Physics A: Mathematical and Theoretical*, 48:195302, 2015. ISSN 1751-8121.
- [91] J. Kofler. Requirements for a loophole-free photonic Bell test using imperfect setting generators. *PRA*, 93:032115, 2016.
- [92] Yanwu Gu, Weijun Li, Michael Evans, and Berthold-Georg Englert. Very strong evidence in favor of quantum mechanics and against local hidden variables from a Bayesian analysis. *PRA*, 99:022112, 2019.
- [93] G. Weihs et al. Violation of Bell's Inequality under Strict Einstein Locality Conditions. *PRL*, 81(23):5039–5043, 1998.
- [94] M. A. Rowe et al. Experimental violation of a Bell's inequality with efficient detection. *Nature*, 409:791, 2001. doi: 10.1038/35057215.
- [95] H. Bernien et al. Heralded entanglement between solid-state qubits separated by three metres. *Nature*, 497:86, 2013. doi: 10.1038/nature12016.

- [96] M. Giustina et al. Bell violation using entangled photons without the fair-sampling assumption. *Nature*, 497:227, 2013. doi: 10.1038/nature12012.
- [97] B. G. Christensen et al. Detection-Loophole-Free Test of Quantum nonlocality, and applications. *PRL*, 111:130406, 2013.
- [98] A. Lita et al. Counting near-infrared single-photons with 95% efficiency. *Opt. Express*, 16:30323040, 2008.
- [99] C. Abellán et al. Generation of Fresh and Pure Random Numbers for Loophole-Free Bell Tests. *PRL*, 115:250403, 2015.
- [100] B. Hensen et al. Loophole-free Bell test using electron spins in diamond: second experiment and additional analysis. *Scientific Reports*, 6:30289, 2016. URL <https://doi.org/10.1038/srep30289>.
- [101] Rodney Loudon. *The Quantum Theory of Light*. Oxford University Press, third edition, 2000. ISBN 0-19-850176-5.
- [102] M. Fox. *Quantum Optics*, chapter 2, pages 8–25. Oxford University Press, 2006. ISBN 9780198566731.
- [103] W. Hoeffding. Probability Inequalities for Sums of Bounded Random Variables. *Journal of the American Statistical Association*, 58:1330, 1963. ISSN 0162-1459. doi: 10.1080/01621459.1963.10500830.
- [104] K. Azuma. Weighted sums of certain dependent random variables. *Tohoku Math. J.* (2), 19:357367, 1967. ISSN 0040-8735.
- [105] C. McDiarmid. On the method of bounded differences. In J. Siemons, editor, *Surveys in Combinatorics*, London Mathematical Society Lecture Note Series, pages 148–188. Cambridge University Press, Cambridge, 1989. doi: 10.1017/cbo9781107359949.008.
- [106] G. Adenier and A. Yu. Khrennikov. Test of the no-signaling principle in the hensen loophole-free CHSH experiment. *Fortschr. Phys.*, 65:1600096, 2017. ISSN 0015-8208. doi: 10.1002/prop.201600096.
- [107] A. Bednorz. Analysis of assumptions of recent tests of local realism. *PRA*, 95:042118, 2017.
- [108] M. Jofre et al. True random numbers from amplified quantum vacuum. *Opt. Express*, 19:2066520672, 2011.
- [109] D. R. Williams. *Earth Fact Sheet*, 2019. URL <https://nssdc.gsfc.nasa.gov/planetary/factsheet/earthfact.html>.
- [110] F. Hocke. *Long Distance Atom Photon Entanglement*, Diplomarbeit, 2007. URL [https://xqp.physik.uni-muenchen.de/publications/files/theses\\_diplom/diplom\\_hocke.pdf](https://xqp.physik.uni-muenchen.de/publications/files/theses_diplom/diplom_hocke.pdf).
- [111] R. Gisin, N. and Thew. Quantum communication. *Nature Photonics*, 1:165, 2007. doi: 10.1038/nphoton.2007.22.

- [112] C. H. Bennett and G. Brassard. Quantum cryptography: Public key distribution and coin tossing. *Theoretical Computer Science*, 560:711, 2014. ISSN 0304-3975.
- [113] M. Caleffi et al. Quantum Internet: From Communication to Distributed Computing! In *Proceedings of the 5th ACM International Conference on Nanoscale Computing and Communication, NANOCOM '18*, pages 3:1–3:4, New York, NY, USA, 2018. ACM. ISBN 978-1-4503-5711-1. doi: 10.1145/3233188.3233224.
- [114] C. Elliott and H. Yeh. DARPA Quantum Network Testbed. Final technical report, BBN Technologies, 2007. URL <https://pdfs.semanticscholar.org/7394/14078534187ea756c0a52bf98fc43b1e35e5.pdf>.
- [115] C. Elliott. *Quantum Communications and Cryptography*, chapter Chapter 4, page 83. CRC Press, 2019.
- [116] ID Quantique. IDQ Celebrates 10-Year Anniversary of the World’s First Real-Life Quantum Cryptography Installation. Press release, 2017.
- [117] M. Peev et al. The SECOQC quantum key distribution network in vienna. *New Journal of Physics*, 11:075001, 2009. ISSN 1367-2630. doi: 10.1088/1367-2630/11/7/075001.
- [118] M. Sasaki. Field test of quantum key distribution in the Tokyo QKD Network. *Opt. Express*, 19:1038710409, 2011.
- [119] Q. Zhang et al. Large scale quantum key distribution: challenges and solutions. *Opt. Express*, 26:2426024273, 2018.
- [120] T. Schmitt-Manderbach et al. Experimental Demonstration of Free-Space Decoy-State Quantum Key Distribution over 144 km. *PRL*, 98:010504, 2007.
- [121] R. Ursin et al. Entanglement-based quantum communication over 144 km. *Nature Physics*, 3:481, 2007. URL <https://doi.org/10.1038/nphys629>.
- [122] S. Nauerth et al. Air-to-ground quantum communication. *Nature Photonics*, 7:382, 2013. doi: 10.1038/nphoton.2013.46.
- [123] S.-K. Liao et al. Satellite-to-ground quantum key distribution. *Nature*, 549:43, 2017. doi: 10.1038/nature23655.
- [124] Xinhua. China opens 2,000-km quantum communication line. Press release, 2017. URL [http://english.www.gov.cn/news/photos/2017/09/30/content\\_281475894651400.htm](http://english.www.gov.cn/news/photos/2017/09/30/content_281475894651400.htm).
- [125] J. Yin et al. Satellite-based entanglement distribution over 1200 kilometers. *Science*, 356:1140, 2017. URL <http://science.sciencemag.org/content/356/6343/1140.abstract>.
- [126] S.-K. Liao et al. Satellite-Relayed Intercontinental Quantum Network. *PRL*, 120:030501, 2018.
- [127] D. N. Matsukevich et al. Entanglement of Remote Atomic Qubits. *PRL*, 96:030405, 2006.

- [128] C.-W. Chou et al. Functional Quantum Nodes for Entanglement Distribution over Scalable Quantum Networks. *Science*, 316:1316, 2007. URL <http://science.sciencemag.org/content/316/5829/1316.abstract>.
- [129] Y. Yu et al. Entanglement of two quantum memories via fibres over dozens of kilometres. *Nature*, 578:240245, 2020. ISSN 1476-4687. doi: 10.1038/s41586-020-1976-7.
- [130] S. Ritter et al. An elementary quantum network of single atoms in optical cavities. *Nature*, 484:195200, 2012. ISSN 1476-4687. doi: 10.1038/nature11023.
- [131] D. N. Matsukevich et al. Bell Inequality Violation with Two Remote Atomic Qubits. *PRL*, 100:150404, 2008.
- [132] L. Slodička et al. Atom-Atom Entanglement by Single-Photon Detection. *PRL*, 110:083603, 2013.
- [133] N. Kalb et al. Entanglement distillation between solid-state quantum network nodes. *Science*, 356:928, 2017. URL <http://science.sciencemag.org/content/356/6341/928.abstract>.
- [134] A. Delteil et al. Generation of heralded entanglement between distant hole spins. *Nature Physics*, 12:218, 2015. doi: 10.1038/nphys3605.
- [135] A. Narla et al. Robust Concurrent Remote Entanglement Between Two Superconducting Qubits. *PRX*, 6:031036, 2016.
- [136] U. Vazirani and T. Vidick. Fully Device-Independent Quantum Key Distribution. *PRL*, 113:140501, 2014.
- [137] Y. Liu et al. High-Speed Device-Independent Quantum Random Number Generation without a Detection Loophole. *PRL*, 120:010503, 2018.
- [138] L. Shen. Randomness Extraction from Bell Violation with Continuous Parametric Down-Conversion. *PRL*, 121:150402, 2018.
- [139] P. Bierhorst et al. Experimentally generated randomness certified by the impossibility of superluminal signals. *Nature*, 556:223226, 2018. ISSN 1476-4687. doi: 10.1038/s41586-018-0019-0.
- [140] Y. Liu et al. Device-independent quantum random-number generation. *Nature*, 562:548551, 2018. ISSN 1476-4687. doi: 10.1038/s41586-018-0559-3.
- [141] D. Stucki et al. Fast and simple one-way quantum key distribution. *APL*, 87:194108, 2005. ISSN 0003-6951. doi: 10.1063/1.2126792.
- [142] H.-K. Lo et al. Secure quantum key distribution. *Nature Photonics*, 8:595, 2014. doi: 10.1038/nphoton.2014.149.
- [143] A. Acín et al. From Bell's Theorem to Secure Quantum Key Distribution. *PRL*, 97:120405, 2006. doi: 10.1103/PhysRevLett.97.120405.
- [144] A. Acín et al. Device-Independent Security of Quantum Cryptography against Collective Attacks. *PRL*, 98:230501, 2007.

- [145] E. A. Aguilar et al. Completely device-independent quantum key distribution. *PRA*, 94:022305, 2016.
- [146] S. Pironio. Device-independent quantum key distribution secure against collective attacks. *New Journal of Physics*, 11:045021, 2009. ISSN 1367-2630. doi: 10.1088/1367-2630/11/4/045021.
- [147] R. Arnon-Friedman et al. Practical device-independent quantum cryptography via entropy accumulation. *Nature Communications*, 9:459, 2018. ISSN 2041-1723. doi: 10.1038/s41467-017-02307-4.
- [148] G. Murta et al. Towards a realization of device-independent quantum key distribution. *Quantum Science and Technology*, 4:035011, 2019. ISSN 2058-9565. doi: 10.1088/2058-9565/ab2819.
- [149] T. Hummel. Increasing Photon Collection Efficiency for Generating Long-distance Entanglement of Atoms. Master's thesis, Ludwig-Maximilians-Universität München, 2018. URL [https://xqp.physik.uni-muenchen.de/publications/theses\\_master/master\\_hummel.html](https://xqp.physik.uni-muenchen.de/publications/theses_master/master_hummel.html).
- [150] E. Y.-Z. Tan et al. Advantage distillation for Device-Independent Quantum Key Distribution. *PRL*, 124:020502, 2020.
- [151] D. Gottesman and H.-K. Lo. Proof of security of quantum key distribution with two-way classical communications. *IEEE Transactions on Information Theory*, 49: 457475, 2003. ISSN 1557-9654.
- [152] M. Tomamichel et al. Tight finite-key analysis for quantum cryptography. *Nature Communications*, 3:634, 2012. ISSN 2041-1723. doi: 10.1038/ncomms1631.
- [153] Jędrzej Kaniewski. Analytic and Nearly Optimal Self-Testing Bounds for the Clauser-Horne-Shimony-Holt and Mermin Inequalities. *PRL*, 117:070402, 2016.
- [154] J. J. Sakurai. *Modern Quantum Mechanics*, chapter 3, page 181. Addison-Wesley Publishing, revised edition edition, 1994. ISBN 0-201-53929-2.
- [155] G. Lindblad. On the generators of quantum dynamical semigroups. *Communications in Mathematical Physics*, 48:119130, 1976. ISSN 1432-0916. doi: 10.1007/BF01608499.
- [156] T. van Leent et al. Long-Distance Distribution of Atom-Photon Entanglement at Telecom Wavelength. *PRL*, 124:010510, 2020.
- [157] M. Körber et al. Decoherence-protected memory for a single-photon qubit. *Nature Photonics*, 12:1821, 2018. ISSN 1749-4893. doi: 10.1038/s41566-017-0050-y.
- [158] M. Fox. *Quantum Optics*. Oxford University Press, 2006. ISBN 9780198566731.
- [159] C. Cohen-Tannoudji, B. Diu, and F. Laloë. *Quantum Mechanics*, chapter VI, page 659. Wiley, New York, 1977.
- [160] D. Taray. To be announced. Master's thesis, Ludwig-Maximilians-Universität München, 2020.

- [161] S. Feng and H. G. Winful. Physical origin of the gouy phase shift. *Opt. Lett.*, 26: 485–487, 2001.
- [162] N. Hodgson and H. Weber. *Laser Resonators and Beam Propagation*, chapter 5, page 243. Springer, 2005.

# Danksagung

Ich möchte mich bei all jenen bedanken, die mich bei dieser Arbeit unterstützt haben, sei es direkt in der wissenschaftlichen Arbeit oder bei der Aufrechterhaltung der Motivation und Moral über die ganze Zeit.

Zunächst möchte ich meinen Dank an Harald Weinfurter aussprechen. Durch die Aufnahme in seine Forschungsgruppe hat er mir die Arbeit an einem spannenden und herausfordernden Forschungsprojekt ermöglicht und damit meine Promotion. Als nächstes möchte ich Benjamin Rosenfeld danken. Ohne sein großes Engagement wäre das Bellprojekt noch viel schwerer geworden. Auch seine Geduld bei der Lösung von Problemen und dem Erklären von komplizierten Themen war unverzichtbar. Ein großen Dank geht auch an meine drei Kollegen Daniel Burchardt, Robert Garthoff und Norbert Ortegell, mit denen ich die meisten Experimente, die hier in der Arbeit beschrieben sind, durchgeführt habe. Trotz all der Rückschläge und Probleme haben wir es geschafft. Ein Dank erfolgt auch an meine Vorgänger und Nachfolger im Atomprojekt, Michael Krug und Julian Hofmann, sowie Tim van Leent, Florian Fertig und Wei Zhang. Ebenfalls bedanke ich mich bei unsere Masterstudenten für die gute Zeit und den Spaß an der Arbeit: Timon Hummel, Paul Koschmieder, Matthias Seubert, Derya Taray und Sebastian Eppelt. Auch den Kollegen aus Barcelona und Basel sei für die erfolgreichen Kooperationen gedankt.

Ich danke natürlich auch den anderen jetzigen und ehemaligen Mitgliedern der Arbeitsgruppe Weinfurter. Dank geht an Martin Zeitlmair, unseren letzten “Diamond Boy”, zusätzlich aber auch Computerexperte, Laserschutzmeister sowie Ersthelfer und die ehemaligen “Diamond Boys”, Lars Liebermeister, Lukas Worthmann und Toshiyuki Tashima. Dank geht an die Cryptogruppe aka Cryptonellen (ich hoffe der Peter ist nicht mehr böse), angefangen mit Sebastian Nauert, Markus Rau, Gwen Vest, Stefan Frick bis Peter Freiwang, Leonhard Mayr, Jakob Brikmann und Rengaraj Aparajithan. Sowie an die Garching Christian Schwemmer, Daniel Richart, Lukas Knips, Jan Dziewior und Jasmin Meinecke mit ihren sehr komplizierten Themen, die einem immer wieder gezeigt haben, dass man die Physik doch noch nicht so gut versteht, wie man dachte. Dank dafür und für die gute Kameradschaft. Einen Dank natürlich auch an Daniel Schlenk und Markus Weber für die gute Zeit und an meine Bürogenossen Lukas Fuchs und Tina Ogriseg, sowie all die anderen! Außerdem möchte ich dem Team des Lehrstuhls von Professor T.W. Hänsch, Nicole Schmidt, Anton Scheich und natürlich Gabriele Gschwendtner, für die Unterstützung unserer Arbeit danken.

Zu guter Letzt möchte ich noch meiner Familie und meinen Freunden danken, die mich immer wieder aufgebaut haben, wenn mal wieder das Vakuum, Laserdioden oder Klimaanlage kaputt gegangen sind.